

# CRYSTAL SYMMETRY AND SPIN-ORBIT TORQUES

A Dissertation

Presented to the Faculty of the Graduate School  
of Cornell University

in Partial Fulfillment of the Requirements for the Degree of  
Doctor of Philosophy

by

Gregory Mark Stiehl

August 2018

© 2018 Gregory Mark Stiehl  
ALL RIGHTS RESERVED

# CRYSTAL SYMMETRY AND SPIN-ORBIT TORQUES

Gregory Mark Stiehl, Ph.D.

Cornell University 2018

Recent discoveries regarding current-induced spin-orbit torques produced by heavy-metal/ferromagnet and topological insulator/ferromagnet bilayers provide the potential for dramatically improved efficiency in the manipulation of magnetic devices. However, spin-orbit torques have an important limitation – in the vast majority of samples, the current-generated spin direction is required by symmetry to lie in the sample plane and perpendicular to an in-plane applied current, i.e., a Rashba-like symmetry. This means, for example, that spin-orbit torques can drive the most current-efficient type of magnetic reversal (antidamping switching) only for magnetic devices with in-plane anisotropy, not the devices with perpendicular magnetic anisotropy that are needed for high-density applications. In this dissertation, I outline a promising approach for reducing those symmetry requirements: using a single crystalline spin-source material with low structural symmetry to alter the symmetry constraints of the generated spin-orbit torques.

## BIOGRAPHICAL SKETCH

Greg Stiehl attended the University of Denver, obtaining a B.S. in Physics and Mathematics in 2010. Prior to coming to Cornell University, he spent a year conducting research at the National Institute of Standards and Technology in Boulder, Colorado. Greg joined the Ralph Group in the summer of 2011, a decision he looks back on fondly. He obtained his M.S. in Physics from Cornell in 2014 and completed his degree requirements for the Ph.D. in 2018. Greg will next be working as a postdoc in Professors Kin Fai Mak and Jie Shan's group.

To my parents,  
for their constant and continued love and support.

## ACKNOWLEDGEMENTS

First and foremost, I would like to thank my adviser Dan Ralph. I have relished learning from you these past years. Your keen eye for physics, and your constant and ever-present scientific diligence and integrity, will be held as ideals throughout my career. Thank you for helping to guide me through the many pitfalls of research, towards a project I really enjoyed digging into. I would also like to thank you for being a kind, welcoming, and humble human being in a scientific world where there are too few. It has fostered a wonderfully friendly, open, and productive group environment that I have greatly appreciated.

I would also like to thank Bob Buhrman. Your vast knowledge of physics and materials science, healthy skepticism, and willingness to tell it like you see it have all been invaluable to me. I am inspired by the success you've had in moving through many different subfields of condensed matter physics. I will strive to live by the bit of advice you gave me — never ignore the seemingly small things in your data that you don't understand, that's usually where the good stuff is. Thank you for letting me on occasion join your group as an adopted member.

I would also like to thank Craig Fennie for being on my committee, always having an open door, and having an interest in my work. I hope to continue to work with, and learn from, you.

Although Greg Fuchs is not on my committee, he has always been generous with his time: listening to my ideas, making useful suggestions, and helping to guide me in the next steps of my career. It has been great getting to know both branches of the Buhrman Cornell progeny! Thank you.

I also must thank the person that started me on my journey into physics, my undergraduate adviser Barry Zink. He has continued to guide, push and

encourage me throughout my graduate school years, even though his call to duty has long since ended. Thank you very much! I would have given up long ago if not for you.

There are a great many Ralph group members, past and present, that I must thank for their time, energy, help, guidance and friendship. To Takahiro Moriyama and Ted Gudmundsen, thank you for helping me settle into the Ralph group, teaching me some tricks of the cleanroom and starting me down the path of antiferromagnet spintronics. Taka, your strong work ethic set the tone for my Ph.D. Chen Wang, thank you for taking the time to teach me about your beautiful work on magnetic nanoparticles. Sufei Shi has been a constant presence over the years even though we only overlapped for one. You have always been generous with your time, advice and encouragement as we've run into each other in the CNF and conferences, thanks!

I got to know Eugenia Tam through running, playing soccer and the occasional beverage. She quickly became a good friend and useful mentor on the Sharon evaporator. Since you've graduated things haven't been quite as fun, and I'm definitely in worse shape! Colin Heikes introduced me to some of my favorite parts of Ithaca, and helped me organize the short lived Ralph group happy hours. Your knowledge of materials (and beer) will always be appreciated! Alex Mellnik, thank you for showing me how to do ST-FMR measurements and tolerating my constant questions while you were trying to finish up. To Neal Reynolds, thank you for your boundless optimism and constant vigilance in keeping things in the Ralph group running. Good luck on your exciting next steps!

John Heron deserves a special thanks for the time and energy he put into working with this then-excited-but-still-green graduate student. Thank you for

entertaining my crazy ideas and pushing me to pursue them. What little I know about materials growth is thanks to you. Thanks for being a compatriot on the lonely road of antiferromagnetic spintronics and I'm sorry that none of our lofty projects came to fruition!

For years, David MacNeill and I passed in the hallways with nothing but silent acknowledgement, having never had overlapping work to bring us together. Deciding to work on 2D spintronics together was a great decision and a blind dive into the deep end for both of us. Working together with Marcos Guimarães to come up with the core ideas for this thesis, and the explanation behind the "Huh, that's weird..." moment of our work on  $WTe_2$  has been one of the most exciting scientific experiences of my career thus far. It has been great sharing the beauty of these symmetry induced effects with you. Thank you for your knowledge of 2D materials, and setting such a high bar in terms of work ethic. I have very much enjoyed our conversations about the scientific enterprise and job hunting. I am happy to call you a friend and hope to work together again in the future!

Without the guidance of the postdoc Marcos Guimarães, the work in this thesis would not have happened. Thank you for helping to bring 2D materials and such a jovial attitude into the Ralph group. Marcos, you're the best!

To Ruofan Li and Vishakha Gupta, thank you for taking up the mantle of the many projects I've left behind, and for tolerating the sporadic assistance I've offered while trying to finish up. Ruofan, your staunch practicality, persistence on "why?" and steadfast work ethic will serve you very well. Vishakha, your diligence and determination will see you rise to the top. Thank you both for being so nice to work with, and I look forward to continue working together over the next year!

To the rest of the Ralph group members: Yongtao, Wan, Lin, Jen, Colin J., Jonathan, Peter, Sam, Saba, and Joseph, and to all of you, thank you for making the Ralph group such a wonderful place to call home for these past years.

I must also thank many members of my research home away from home, the Buhrman group. To Luqiao Liu and Chi-Feng Pai, though we didn't overlap very much at Cornell, our chats at conferences have been invaluable. To Junbo Park, thanks for showing me the nitty-gritty of the cleanroom, helping me increase my paranoia until my fabrication processes worked, and for showing me the ways of the ion mill. Your willingness to help out is greatly appreciated, and I'm glad we got to play some soccer together too! To the two Buhrman postdocs that helped shape the formative years of my time here, Graham Rowlands and Sriharsha Aradhya, thank you for your generosity, sage advice and friendship. You two rock.

In particular, I must thank my good friend Praveen Gowtham for taking me under his wing. It is through working with him that I found my way towards a solid footing in research. Thank you for listening to my ideas, answering my ceaseless questions and telling me when I'm being dumb. Your penchant for working on what you find interesting, regardless of the trends, will serve you well in the long run. Thank you for sharing your vast knowledge on life, science, philosophy and more. You are deeply curious, a friend-mentor, and jester-sage.

To the rest of the Buhrman group, Minh-Hai, Yongxi, Luis, Shengjie, Ryan and Lijun, thank you for making me feel welcome and keeping the ion mill going!

Outside of lab, there are a great many people that have kept me sane and made graduate school fun. To my "Fallen Creek Family": Edward Lochocki, Evan MacQuarrie, Jason Bartell, Lena Bartell, Sam Ahles, Jessica Abueg, Coralie

Salesse-Smith and Éamonn O'Shea, thank you for being wonderful friends, compatriots, and commiserators. Thank you for listening to me blab about science when I was excited, and encouraging me when things weren't working. And of course, thanks for adding an all-important balance to my life.

To Sam Kachuck and Kacey Wochna, thank you both for being a beacon of light, life and friendship. I love you both. To Dan Gonnella, thank you for perennially hosting friendsgiving and a cottage get-away – much needed respites – and being a good friend. You're awesome. To the many folks in the Ithaca soccer and jazz communities, thank you for welcoming and challenging me!

I must also thank my parents, my sister and my extended family, for their constant, continued and ever-present love and support. Thank you for cheering me on when I was down, having faith in me when I did not, and providing me the chances I have had in life. You guys are the best and I love you all!

Finally, I would like to thank Summer Saraf. Your love and support has powered me through graduate school. You have kept me sane, helped me find a balance, and pushed me to grow as a person. You have truly brightened up my life! What's more, you've always freely lent your technical wizardry, LaTeX expertise, Word hacks and Python tricks whenever needed – as well as your actual technical equipment, I think the laptop count is up to three? You always have something interesting on your mind, about technology, biology, politics or life. Thanks for keeping us engaged in the academic pursuit! You are a great partner-in-life, and I look forward to the countless adventures ahead!

## TABLE OF CONTENTS

Biographical Sketch . . . . .	iii
Dedication . . . . .	iv
Acknowledgements . . . . .	v
Table of Contents . . . . .	x
List of Tables . . . . .	xiii
List of Figures . . . . .	xiv
<b>1 Introduction</b>	<b>1</b>
1.1 Potential Applications . . . . .	2
1.2 Some History and Definitions . . . . .	4
1.2.1 The Spin Hall Effect . . . . .	5
1.2.2 The Rashba-Edelstein Effect . . . . .	7
1.3 Symmetry of Spin-Orbit Torques . . . . .	10
1.4 Breaking the Symmetry Requirements . . . . .	12
1.4.1 Asymmetric Device Geometries . . . . .	13
1.4.2 Local Magnetic Moment . . . . .	14
1.4.3 Single Crystal Materials . . . . .	15
1.5 Transition Metal Dichalcogenides . . . . .	17
1.5.1 Previous work on MoS <sub>2</sub> / Ferromagnet Heterostructures .	19
1.6 Outline . . . . .	21
<b>2 Crystal Symmetry and Spin-Orbit Torques in Tungsten Ditelluride</b>	<b>32</b>
2.1 Introduction . . . . .	33
2.2 Device Fabrication . . . . .	34
2.3 Spin-Torque Ferromagnetic Resonance Measurements . . . . .	38
2.4 ST-FMR Dependence on Applied In-Plane Field Angle . . . . .	40
2.5 Dependence of the Torques on the WTe <sub>2</sub> Crystal Axis . . . . .	45
2.6 Magnetic anisotropy of WTe <sub>2</sub> /Py bilayers . . . . .	48
2.7 Conclusion . . . . .	49
2.8 Supplemental information . . . . .	50
2.8.1 Comparison of mechanisms for current-induced switching of magnetic layers with perpendicular magnetic anisotropy (PMA) . . . . .	50
2.8.2 Analysis of ST-FMR measurements . . . . .	52
2.8.3 Determination of the in-plane magnetic anisotropy . . . . .	54
2.8.4 Data from additional devices . . . . .	57
2.8.5 Torques in WTe <sub>2</sub> /CoFeB bilayers . . . . .	60
2.8.6 Symmetry analysis for current generated torques . . . . .	61
2.8.7 Higher harmonics in the ST-FMR angular dependence . . . . .	64
2.8.8 On why there can be no contribution to the out-of-plane antidamping torque from the bulk of a WTe <sub>2</sub> layer . . . . .	65

2.8.9	Some comments on the microscopic origin of an out-of-plane antidamping torque in $WTe_2/Py$ bilayers . . . . .	67
2.8.10	Second-harmonic Hall measurements . . . . .	70
<b>3</b>	<b>Thickness Dependence of Spin-Orbit Torques in Tungsten Ditelluride</b>	<b>82</b>
3.1	Introduction . . . . .	82
3.2	Device Fabrication . . . . .	84
3.3	Second-harmonic Hall measurements . . . . .	86
3.4	$WTe_2$ Thickness Dependence . . . . .	91
3.5	Conclusion . . . . .	98
3.6	Appendix . . . . .	99
3.6.1	Derivation of Eq. 3.1 from the Landau-Lifshitz-Gilbert-Slonczewski equation . . . . .	99
3.6.2	Determination of the magnetic easy-axis from first-harmonic Hall measurements . . . . .	101
3.6.3	Comparison between ST-FMR data in nitrogen and vacuum exfoliated $WTe_2$ . . . . .	102
<b>4</b>	<b>Spin-Orbit Torques in Niobium Diselenide</b>	<b>109</b>
4.1	Introduction . . . . .	109
4.2	Device Fabrication . . . . .	112
4.3	Spin-Torque Ferromagnetic Resonance Measurements . . . . .	113
4.4	Dependence on $NbSe_2$ thickness . . . . .	118
4.5	Conclusion . . . . .	122
4.6	Supplemental Information . . . . .	123
4.6.1	Estimation of spin pumping contributions . . . . .	123
4.6.2	Anisotropic Magnetoresistance Measurements . . . . .	125
4.6.3	Temperature Dependence of the Measured Spin-Orbit Torques . . . . .	126
4.6.4	Resistance as a function of $NbSe_2$ thickness and the Oersted field contribution . . . . .	127
<b>5</b>	<b>Current-Induced Torques in Tantalum Ditelluride with Dresselhaus Symmetry.</b>	<b>135</b>
5.1	Introduction . . . . .	135
5.2	Device Fabrication . . . . .	137
5.3	ST-FMR measurements . . . . .	138
5.4	Crystal Axis Dependence . . . . .	142
5.5	Microscopic Mechanism . . . . .	145
5.6	Conclusions . . . . .	148
5.7	Supplemental Information . . . . .	149
5.7.1	Analysis of ST-FMR measurements . . . . .	149
5.7.2	Second harmonic Hall measurements . . . . .	150
5.7.3	Cross-sectional HAADF-STEM . . . . .	154

5.7.4	Measurement of the in-plane magnetic anisotropy . . . . .	155
5.7.5	Determination of TaTe <sub>2</sub> crystal axes . . . . .	158
5.7.6	In-plane torques in TaTe <sub>2</sub> /Py bilayers . . . . .	159
5.7.7	Model for C/A . . . . .	161
5.7.8	Thickness dependence of the torques . . . . .	162
5.7.9	Dresselhaus-like torque in WTe <sub>2</sub> /Py bilayers . . . . .	163
<b>6</b>	<b>Spin-Orbit Torques in Molybdenum Ditelluride</b>	<b>170</b>
6.1	Introduction . . . . .	170
6.2	Spin-Torque Ferromagnetic Resonance Measurements . . . . .	173
6.3	Dependence on Crystallographic Orientation . . . . .	177
6.4	MoTe <sub>2</sub> Thickness Dependence . . . . .	179
6.5	Dresselhaus-like Torques . . . . .	184
6.6	In-plane Field-like Torque . . . . .	186
6.7	Determination of Crystal Orientation . . . . .	187
6.7.1	Magnetic Easy Axis . . . . .	188
6.7.2	Raman Spectroscopy . . . . .	190
6.8	Determining the Crystal Phase in the Few-Layer Limit . . . . .	191
6.9	Discussion and Concluding Remarks . . . . .	192
<b>7</b>	<b>Final Thoughts and Future Directions</b>	<b>199</b>

## LIST OF TABLES

1.1	Crystal structure and space groups for the transition metal dichalcogenides studied in this dissertation. . . . .	18
2.1	Comparison of torque measurements for 26 WTe <sub>2</sub> /Py ST-FMR devices . . . . .	57
3.1	Comparison of WTe <sub>2</sub> /Py device parameters and torques as measured by second-harmonic Hall. . . . .	93
5.1	Comparison of torque measurements for 19 TaTe <sub>2</sub> /Py ST-FMR devices . . . . .	154
5.2	Comparison of torque measurements for select WTe <sub>2</sub> /Py ST-FMR devices with Dresselhaus torque. . . . .	164
6.1	Comparison of torque measurements for 14 MoTe <sub>2</sub> /Py ST-FMR devices . . . . .	182

## LIST OF FIGURES

1.1	Depiction of the spin Hall effect . . . . .	5
1.2	Thickness dependence of spin Hall effect. . . . .	6
1.3	Depiction of Rashba spin texture. . . . .	8
1.4	Transition metal dichalcogenides with trigonal and octahedral coordination. . . . .	17
1.5	Crystal structures of the various transition metal dichalcogenides (TMDs) highlighted in this dissertation. . . . .	20
2.1	Sample geometry and selected ST-FMR traces . . . . .	35
2.2	Atomic force microscopy of a WTe <sub>2</sub> /Py bilayer . . . . .	36
2.3	Polarized Raman spectroscopy of a WTe <sub>2</sub> /Py bilayer . . . . .	37
2.4	Cross-sectional HAADF-STEM image of a WTe <sub>2</sub> /Py device. . . . .	39
2.5	Angular dependence of ST-FMR signals . . . . .	42
2.6	Spin-orbit torque for current along the WTe <sub>2</sub> <i>b</i> -axis . . . . .	44
2.7	Dependence of the spin-orbit torques on the angle of applied current and the thickness of WTe <sub>2</sub> . . . . .	46
2.8	Anisotropic magnetoresistance of a WTe <sub>2</sub> /Py bilayer . . . . .	53
2.9	Applied magnetic field at ferromagnetic resonance versus angle of the applied field, for WTe <sub>2</sub> /Py bilayers . . . . .	55
2.10	Hall resistance as a function of external field for a WTe <sub>2</sub> /Py bilayer Hall bar . . . . .	56
2.11	Plots of the symmetric and antisymmetric components of the ST-FMR mixing voltage for multiple WTe <sub>2</sub> /Py bilayers . . . . .	58
2.12	Summary of calibrated torque conductivity measurements . . . . .	59
2.13	Plots of the symmetric and antisymmetric components of the ST-FMR mixing voltage for a WTe <sub>2</sub> /CoFeB device . . . . .	61
2.14	Higher harmonics in ST-FMR angular dependence of WTe <sub>2</sub> /Py bilayers . . . . .	65
2.15	ST-FMR measurements on a WTe <sub>2</sub> /Py bilayer with a monolayer step . . . . .	66
2.16	Second harmonic Hall measurements on a WTe <sub>2</sub> /Py Hall bar . . . . .	72
3.1	Geometry of our WTe <sub>2</sub> Hall bars . . . . .	85
3.2	Second-harmonic Hall signal for a WTe <sub>2</sub> /Py device as a function applied field angle and magnitude. . . . .	87
3.3	Torque measurements across a monolayer step, for monolayer and bilayer WTe <sub>2</sub> . . . . .	90
3.4	Out-of-plane field-like torque compared to Oersted field. . . . .	92
3.5	Out-of-plane antidamping torque as a function of WTe <sub>2</sub> thickness. . . . .	95
3.6	Comparison of torque ratios as measured by second-harmonic Hall and ST-FMR as a function of WTe <sub>2</sub> thickness. . . . .	97
3.7	First-harmonic Hall measurement for a WTe <sub>2</sub> /Py device. . . . .	101

3.8	Comparison of torques in vacuum and nitrogen exfoliated WTe <sub>2</sub> samples. . . . .	102
4.1	NbSe <sub>2</sub> device geometry and select ST-FMR traces. . . . .	114
4.2	Antisymmetric and Symmetric mixing voltage as a function of applied field angle in NbSe <sub>2</sub> /Py devices. . . . .	117
4.3	NbSe <sub>2</sub> /Py spin torque conductivities as a function of thickness. . . . .	120
4.4	NbSe <sub>2</sub> /Py ST-FMR measurements at a temperature of 4.2 K. . . . .	121
4.5	Anisotropic magnetoresistance for NbSe <sub>2</sub> /Py . . . . .	125
4.6	NbSe <sub>2</sub> /Py torque ratios as a function of temperature. . . . .	126
4.7	Inverse sheet resistance as a function of NbSe <sub>2</sub> thickness. . . . .	128
5.1	Sample geometries and ST-FMR mixing voltage. . . . .	139
5.2	Angular dependence of out-of-plane torques in TaTe <sub>2</sub> . . . . .	141
5.3	Dependence on crystal axis for the out-of-plane Dresselhaus-like torques in TaTe <sub>2</sub> and WTe <sub>2</sub> . . . . .	143
5.4	Angular dependence of out-of-plane torques in WTe <sub>2</sub> with Dresselhaus-like contribution. . . . .	144
5.5	Extracted resistivities as a function of crystal axis and modeled current streamlines . . . . .	146
5.6	First harmonic Hall measurement of a TaTe <sub>2</sub> /Py device . . . . .	150
5.7	Second harmonic Hall measurement of the torques in a TaTe <sub>2</sub> /Py device . . . . .	152
5.8	Resonant field for ST-FMR devices as a function of applied magnetic field angle. . . . .	155
5.9	Polarized Raman spectroscopy for TaTe <sub>2</sub> . . . . .	156
5.10	Cross-sectional HAADF-STEM images along and perpendicular to the TaTe <sub>2</sub> mirror plane. . . . .	157
5.11	In-plane torques in our TaTe <sub>2</sub> /Py devices. . . . .	160
5.12	Resistivity and torques as a function of TMD thickness for select TaTe <sub>2</sub> /Py devices. . . . .	162
6.1	MoTe <sub>2</sub> crystal structure, device geometry and ST-FMR mixing voltage for a MoTe <sub>2</sub> monolayer interfaced with Permalloy . . . . .	171
6.2	Dependence on the applied field angle for both the antisymmetric and symmetric component of the mixing voltage. . . . .	174
6.3	Crystal axis dependence for out-of-plane antidamping torque and standard antidamping torques. . . . .	178
6.4	Inverse sheet resistance and torque conductivity $\propto \hat{m} \times \hat{y}$ as a function of MoTe <sub>2</sub> thickness . . . . .	179
6.5	Torque ratios and torque conductivities as a function of MoTe <sub>2</sub> thickness. . . . .	183
6.6	Dresselhaus-like torques as a function of MoTe <sub>2</sub> crystal axis alignment. . . . .	185

6.7	Symmetric and antisymmetric component of the mixing voltage for a device with shows an in-plane field-like torque $\propto \hat{m} \times \hat{z}$ . . .	186
6.8	Thickness and crystal axis dependence of the in-plane field-like torque $\propto \hat{m} \times \hat{z}$ . . . . .	188
6.9	Polarized Raman spectra for MoTe <sub>2</sub> . . . . .	189

# CHAPTER 1

## INTRODUCTION

The coupling of spin to the orbital degree of freedom in condensed matter systems has puzzled and intrigued physicists for well over fifty years. Although this coupling exists at a relatively small energy scale, spin-orbit interactions can have dramatic ramifications for the optical and transport properties of real materials. In this dissertation, we will look at how spin-orbit interactions can be leveraged to manipulate magnetic moments for potential magnetic memory applications. Specifically, we will study how crystal symmetry influences the spin-orbit generated torques exerted on a magnet, and will ultimately end by posing the question: how can the symmetries of a crystal be manipulated in order to control, and perhaps eventually engineer, spin-orbit torques in future materials?

This dissertation focuses on the collection of phenomena known as “spin-orbit torques”. The use of the phrase “spin-orbit torque” has evolved in the literature over the past fifteen years, and, in an effort to avoid confusion, we will use it agnostically. That is, we use it without reference to a particular microscopic mechanism, to refer to the torque exerted on a magnetic moment generated by flowing a charge current through a material with large spin-orbit coupling. The spin-orbit material could be interfaced with a ferromagnet to form a heterostructure, relying on the spin Hall effect to exert a torque. Or, the spin-orbit material might itself have a magnetic moment, and rely on local Rashba-Edelstein spin-orbit fields to exert a torque on its own magnetization. Here, we refer to all such effects as “spin-orbit torques”.

## 1.1 Potential Applications

To motivate our study we provide some context on the potential applications, though we wish to make clear that the focus of this dissertation will be on the physics, and not a particular application. We do hope that future researchers will build off of this work in such a way that might lead to a realistic (scalable) implementation, and we will give some of our thoughts on this matter in the last chapter.

Magnetic based memories are poised to be the next non-volatile memory technology of choice, with unlimited read and write endurance, low write energy, and low standby power [1]. However, an efficient method for writing the memory, i.e. controlling the direction of a magnetic moment, is still needed. For example, it is difficult to apply a localized magnetic field so that a magnetic bit can be switched without destabilizing a neighboring bit  $< 100$  nm away. Not only is this cumbersome, it is also inefficient. Magnetic dynamics are governed by the Landau-Lifshitz-Gilbert-Slonczewski (LLGS) equation:

$$\frac{\partial \hat{m}}{\partial t} = -\gamma \hat{m} \times H_{\text{eff}}^{\vec{}} + \alpha_G \hat{m} \times \frac{\partial \hat{m}}{\partial t} + \vec{\tau}, \quad (1.1)$$

where  $\hat{m}$  is the magnetization unit vector,  $\gamma$  is the gyromagnetic ratio,  $H_{\text{eff}}$  is the effective magnetic field which includes any external field ( $H_{\text{ext}}$ ), anisotropy field ( $H_{\text{an}}$ ) or dipole field,  $\alpha_G$  is the Gilbert damping and  $\tau$  is the applied torque. For the magnets with the perpendicular magnetic anisotropy (PMA) required for high density applications, a field induced switch must apply a torque  $\vec{\tau} = -\gamma H_{\text{ext}}(\hat{m} \times \hat{z})$ , where the field is applied along the  $\hat{z}$  direction and must exceed the anisotropy value,  $H_{\text{ext}} > H_{\text{an}}$ .

At present, commercial magnetic memories manipulate their magnetic state

through the transfer of angular momentum with spin-polarized electrons, where the electrons are polarized by flowing a charge current through a metallic ferromagnet layer. This technique, known as spin-transfer torque, is a step in the right direction. Instead of using an inefficient field-like torque<sup>1</sup> for manipulating the magnet, it instead supplies what is called a damping-like<sup>2</sup>, or antidamping, torque - a component of torque that directly compensates the damping of the magnetic layer,  $\alpha_G$ . When out-of-plane spins are injected into a magnet with PMA, they will induce an antidamping torque  $\vec{\tau} = \tau_0 \hat{m} \times (\hat{m} \times \hat{z})$ . In order to switch the magnet, that torque must be  $\tau_0 > \gamma \alpha_G H_{an}$ , a factor of  $\alpha_G$  ( $\approx 0.01$ ) smaller than a field induced switch!

However, schemes that use a ferromagnetic layer to polarize the current are generally limited to transferring one unit of angular momentum ( $\hbar/2$ ) per electron due to the device geometry (current must flow from the polarizer to magnet that is to be switched, generally in the out-of-plane direction). One promising solution uses a similar angular momentum transfer scheme, but instead the angular momentum is generated by (for example) the spin Hall effect in a spin-orbit material interfaced with a ferromagnet. Here, current flows along the heterostructure (in the device plane), where an electron can interact multiple times with both the magnetic moment and spin-orbit material as it diffuses back and forth across the interface. Recent reports [2–5] showing best-in-class switching speeds and low write error rates using such spin-orbit driven torques have continued to generate considerable excitement for this approach.

There is, however, a problem with the spin-orbit torques in commonly-studied materials. They are prevented by their structural symmetry from gener-

---

<sup>1</sup>Any torque that is odd in magnetization is defined as ‘field-like’.

<sup>2</sup>An ‘antidamping’ or ‘damping-like’ torque is defined as a torque even in magnetization.

ating out-of-plane spins with current applied in the plane, precisely the configuration necessary to generate that efficient antidamping torque  $\vec{\tau} = \tau_0 \hat{m} \times (\hat{m} \times \hat{z})!$  The symmetry constraints are discussed in the next few sections, and the remainder of this dissertation is centered around probing one method of removing (or more precisely, altering) this limitation.

## 1.2 Some History and Definitions

As is often the case when rapid scientific progress is made on one topic, the body of work on spin-orbit torques is somewhat muddled, particularly in regards to the microscopic mechanisms and magnitudes of the observed effects. Unfortunately for the eager novices beginning to immerse themselves in the literature, the mechanisms and magnitudes themselves are still muddled, though we are beginning to converge on a common language with which to discuss them. I have tried to collect the relevant references and provide a brief introduction to these topics here. What is clear is that the implications of surface inversion symmetry breaking [6, 7], bulk inversion symmetry breaking [8], and even the spin Hall effect [9–11] in spin-orbit materials had been considered long before any such effect was used to exert a torque on a ferromagnet. Following the experimental detection of the spin Hall effect in a crystalline semiconductor in 2004 [12], the pace of experimental progress quickened significantly and was rapidly followed by the spin Hall effect in metals [13–16], the observation of torque generation by the inverse spin galvanic effect [17–19], the first switching of a ferromagnet by spin-orbit torque [20], and finally the measurement of gigantic spin-orbit torques in more exotic materials such as  $\text{Bi}_2\text{Se}_3$  [21] and  $\text{BiSbTe}_3$  [22].

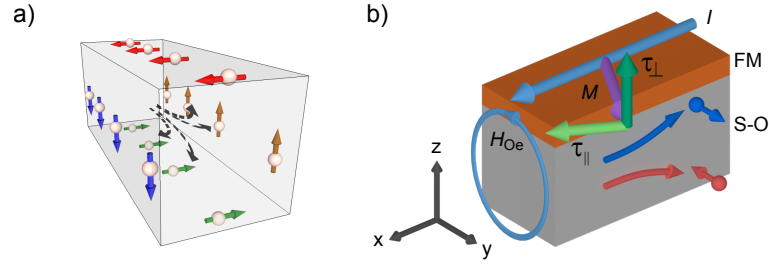


Figure 1.1: a) An unpolarized charge current in a spin Hall material is preferentially deflected by its spin orientation, forming a spin accumulation along the surfaces perpendicular to the current. Image adapted from [23]. b) Depiction of a current ( $I$ ) applied to a spin Hall material (S-O) / ferromagnet (FM) heterostructure. The generated spins that diffuse towards the FM interface may exert a torque ( $\tau$ ) on the moment ( $M$ ).

For the purposes of this text, it is helpful to understand something about the respective mechanisms that generate spin-orbit torques, but it is not necessary to delve into the details of each model. We will divide things into two primary mechanisms: (1) the spin Hall effect, and (2) the Rashba-Edelstein effect.

## 1.2.1 The Spin Hall Effect

The spin Hall effect (SHE) generates a transverse spin current in response to a longitudinal charge current, as depicted in Fig. 1.1a. It is a process that exists within the bulk of a material, and is similar in nature to the anomalous Hall effect in magnetic materials [24]. In materials with a SHE, the (initially unpolarized) carriers of the applied current are preferentially deflected based on the direction of their spin. When the material has inversion and time reversal symmetry, spins of opposite sign are deflected in opposing directions in strictly equal proportions. This deflection can be intrinsic in nature, owing to an anomalous velocity in momentum space (*i.e.* the Berry curvature), or extrinsic in nature, due to a skew scattering or side jump scattering process.

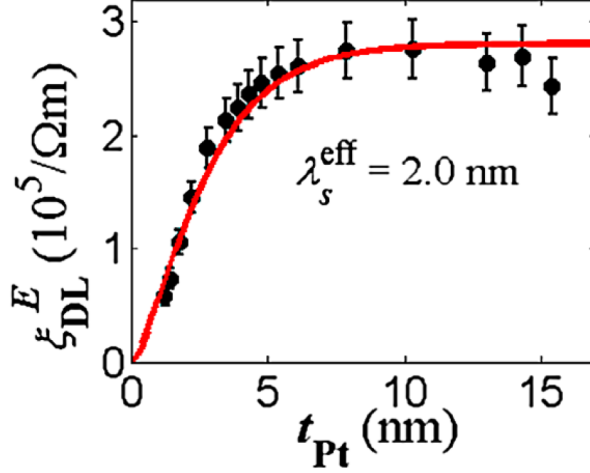


Figure 1.2: The torque efficiency normalized by the applied electric field as a function of platinum thickness. The fit allows the extraction of an effective spin diffusion length of 2 nm. Figure adapted from [25].

In a finite material, such as the square bar shown in Fig. 1.1a, spin polarized electrons will accumulate at the boundaries giving rise to the aptly named spin accumulation. This spin accumulation exists within roughly one spin diffusion length – the length over which a spin travels prior to reorienting in a material – of the surface. It is important to note, though, that if we average over the cross-section of the bar there is no net spin accumulation and no net spin polarization within the material. Throughout this dissertation, we will use *spin polarization* to refer to a real-space spin density, and *spin texture* to refer to  $k$ -space.

The situation changes when a spin Hall material is interfaced with another material into which the generated spins can diffuse, say a ferromagnet (Fig. 1.1b). Here, there can be a net flow of spins into the ferromagnet, which if not aligned with the magnetization, will dephase and deposit their angular momentum, inducing a torque. The mechanism by which angular momentum is transferred from the spin to the ferromagnetic moment, regardless of how the spin is polarized, is called “spin-transfer torque” [26]. The magnitude of the

torque generated by the spin Hall effect depends on a number of material parameters such as interface transparency [27, 28], spin diffusion length [25, 29, 30] and intrinsic spin Hall efficiency [16, 21, 22, 31, 32]. Further details can be found in these reviews [33, 34] and in the provided references.

We conclude our brief overview of the spin Hall effect with the observation that because the SHE is a bulk effect with a finite spin diffusion length, the induced torques will have a dependence on the thickness of the spin Hall material (note that the thickness dependence of the torques is also complicated by a thickness dependence in the resistivity of a spin hall material [25]). In materials such as Pt, perhaps the most widely studied spin Hall material [14, 16, 20, 25, 27, 29, 30, 35], a strong thickness dependence is observed. Figure 1.2 shows the dependence of the spin Hall torque efficiency normalized by the applied electric field as a function of platinum thickness. The observed dependence is strongest within a just a few times the spin diffusion length,  $\lambda_s \sim 2$  nm.

## 1.2.2 The Rashba-Edelstein Effect

When inversion symmetry is locally broken, say at the interface of two materials, a non-equilibrium spin polarization confined to that interface is allowed by symmetry. The effects of spin-orbit coupling at that interface can be modeled by the Rashba Hamiltonian:

$$\hat{H}_R = (\alpha_R/\hbar) (\hat{n} \times \vec{k}) \cdot \vec{\sigma}, \quad (1.2)$$

where  $\alpha_R$  is the Rashba parameter,  $\hat{n}$  is the symmetry breaking direction (say, normal to an interface,  $\hat{z}$ ) and  $\vec{\sigma}$  are the Pauli spin matrices. This results in a

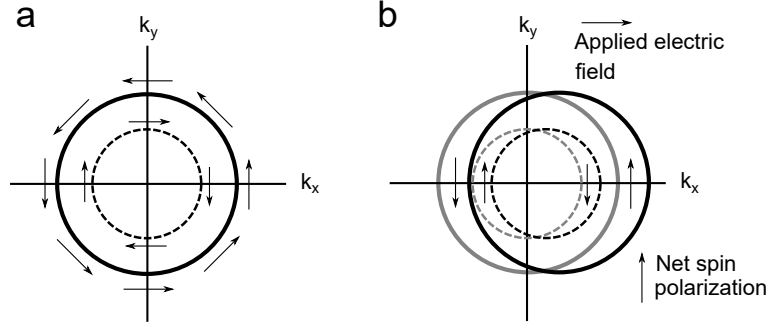


Figure 1.3: Depiction of Rashba spin texture from a symmetry breaking in the  $\hat{z}$  direction showing the two spin-split bands (a) without and (b) with an applied in-plane electric field. A net spin polarization is present in (b).

$k$ -space spin texture as shown in Fig. 1.3a, where the two spin-split bands have spins perpendicular to both the symmetry breaking direction and the  $k$ -space vector. When an in-plane electric field is applied (Fig. 1.3b), a net spin polarization is generated that is localized to that interface. The Rashba spin-orbit interaction has been probed in a variety of systems, such as two-dimensional electron gases [36], gold surface states [37] and the Bi/Ag surface [38, 39], and forms the basis of several modern subfields [40, 41]. Although many researchers have claimed to observe an interfacial Rashba-Edelstein spin-orbit torque, these effects are often difficult to distinguish from other mechanisms such as the spin Hall effect. For example, the first observation of spin-orbit torque switching by Miron *et al.* was originally claimed to be Rashba in nature [20], but was later determined to be due to the spin Hall effect by researchers at Cornell [35].

The situation changes when inversion symmetry is instead broken in the bulk of a spin-generation material. In this case, a current-induced spin polarization is not limited to a symmetry-breaking interface, but can instead exist within the bulk. These spin polarizations have been observed in materials with broken inversion symmetry such as single crystal GaAs [17]. Many researchers will use the phrases “Rashba-Edelstein effect” and “inverse spin galvanic effect” inter-

changeably. However, we feel it is important to distinguish between surface and bulk inversion symmetry breaking, as that determines precisely where a spin polarization can exist. We will use the phrase “Rashba-Edelstein effect” to refer to *surface* inversion breaking spin-orbit effects and “inverse spin galvanic effect” to refer to *bulk*.

When interfaced with a ferromagnet, such as in GaAs/Fe heterostructures [42], these bulk spin polarizations can exert a torque on the ferromagnet. However, the inverse spin galvanic effect often co-exists with other spin-orbit effects, such as the spin Hall effect [17], making distinguishing the source of the torque difficult. Perhaps more interestingly, an inverse spin galvanic effect can exert a torque on a local moment – that is, a moment contained within the spin-generation material itself - such as in Ga(Mn)As [19] and NiMnSb [43]. In this situation spin Hall torques are typically ruled out as a source, as the spin Hall effect generates equal magnitudes of spins with opposite signs, which cannot exert a net torque on a local moment.

To close this section we note that traditionally the Rashba-Edelstein effect and inverse spin galvanic effects are thought to generate primarily field-like torques with minimal dependence on the thickness of the spin-generation material. The reasoning is that these spin polarizations are localized to the inversion symmetry breaking sites, and thus primarily couple to an external moment as an effective field. However, recent work has suggested that this may not necessarily be the case, with additional complications coming from interactions with ferromagnetic interfaces [44–47] or the local moments in an inverse spin galvanic material [48].

### 1.3 Symmetry of Spin-Orbit Torques

For a current or electric field to generate a torque, global inversion symmetry must be broken. To see that this is the case, consider how the inversion operator acts on the linear response equation

$$\vec{\tau} = \zeta \cdot \vec{E}, \quad (1.3)$$

where  $\vec{E}$  is the electric field generating the torque,  $\vec{\tau}$ , which are related by the axial (pseudo-) tensor  $\zeta$ . The torque is a pseudovector and transforms under a symmetry operation,  $S$ , as  $\vec{\tau}' = \det(R)R\vec{\tau}$ , where  $R$  is the matrix representation of  $S$ .  $\vec{E}$ , however, is a vector and thus transforms under symmetry operation  $S$  as  $\vec{E}' = R\vec{E}$ . If  $S$  is a good symmetry operation of the crystal<sup>3</sup>, we may use the transformation properties of  $\vec{\tau}$  and  $\vec{E}$  to derive the relation  $\zeta = \det(R)R\zeta R^{-1}$ . This relation does not allow a nontrivial solution under the inversion operator, and therefore inversion symmetry must be broken if Eq. 1.3 is to hold. This same argument is also precisely why a net current induced spin polarization cannot exist in the presence of inversion symmetry.

In materials with inversion symmetry (such as the polycrystalline spin Hall metals Pt, Ta, and W or the topological insulators Bi<sub>2</sub>Se<sub>3</sub> and BiSbTe<sub>3</sub>) this symmetry breaking is accomplished solely by the presence of an interface, such as the interface with a ferromagnet. However, if this is the only additional symmetry breaking present the spins or fields generated must follow a Rashba-like symmetry regardless of the microscopic mechanism, similar to the one shown in Fig. 1.3. To see that this is the case, let us consider just a simple cubic Bravais lattice interfaced with a ferromagnet in the  $x - y$  plane. Again using a linear

---

<sup>3</sup>By which we mean transforms the atomic sites onto themselves.

response formalism, we can consider the spin polarization at that interface,

$$\vec{s} = \chi \cdot \vec{E}, \quad (1.4)$$

where  $\vec{s}$  is the spin polarization related to  $\vec{E}$  by  $\chi$ . The shape of  $\chi$  must also satisfy the relation  $\chi = \det(R)R\chi R^{-1}$  for all of the symmetry operations,  $S$ , in the space group of the crystal. Even though the interface removes the  $x - y$  mirror plane and all rotational symmetries but those about  $\hat{z}$ , we find that these symmetries are sufficient to constrain  $\chi$  to:

$$\chi^{\text{Rashba}} = \begin{pmatrix} 0 & \chi_{ab} & 0 \\ -\chi_{ab} & 0 & 0 \\ 0 & 0 & 0 \end{pmatrix}, \quad (1.5)$$

which is consistent with the spin polarization in Fig. 1.3. However, if we break the four-fold rotational symmetry about  $\hat{z}$  by applying an in-plane uniaxial strain (for example along the  $\hat{x}$  direction), we will further reduce our constraints on  $\chi$ , obtaining:

$$\chi^{\text{R+D}} = \begin{pmatrix} 0 & \chi_{ab} & 0 \\ \chi_{ba} & 0 & 0 \\ 0 & 0 & 0 \end{pmatrix}, \quad (1.6)$$

where the two non-zero elements are no longer related. This effectively allows for both a Rashba-like spin polarization, and a spin-polarization known as a ‘Dresselhaus’ spin polarization. A pure Dresselhaus spin polarization would be given by

$$\chi^{\text{Dresselhaus}} = \begin{pmatrix} \chi_{aa} & 0 & 0 \\ 0 & -\chi_{aa} & 0 \\ 0 & 0 & 0 \end{pmatrix}. \quad (1.7)$$

To see that Eq. 1.6 is a combination of Rashba and Dresselhaus spin polarization,

consider a  $\pi/4$  rotation<sup>4</sup>. If we could further reduce the symmetry of our lattice down to a single mirror plane, say in the  $y - z$  plane, then the allowed spin polarization would be

$$\chi^{y-z\text{mirror}} = \begin{pmatrix} 0 & \chi_{ab} & \chi_{ac} \\ \chi_{ba} & 0 & 0 \\ \chi_{ca} & 0 & 0 \end{pmatrix}, \quad (1.8)$$

where the element  $\chi_{ca}$  represents an out-of-plane spin in response to an in-plane electric field applied perpendicular to the mirror plane. This is the same geometry of spin generation that has not been observed in previous studies, and the one required for efficient antidamping switching of magnets with PMA discussed in Section 1.1! This means that in order to generate such a torque, we need to limit the symmetries of our system down to a single mirror plane. For more details on this type of linear response symmetry analysis for the spin polarizations induced in nonmagnetic, ferromagnetic and antiferromagnetic materials, see the excellent work by Železný *et al.* [43, 49]. An analogous symmetry analysis of the spin Hall generated spins shows that the spin Hall materials are similarly constrained by their crystal symmetry [50]. The next section discusses methods of reducing the symmetry in real materials.

## 1.4 Breaking the Symmetry Requirements

In order to generate different geometries of spin-orbit torques, it is necessary to alter or break the constraining symmetry requirements. Here we will review three different methods of changing the symmetry requirements for spin-orbit

---

<sup>4</sup>Note that Eq. 1.6 also allows for a constant in-plane term in addition to a Rashba and Dresselhaus, see [43, 49] for details.

torque generation and comment on the utility of each method: (1) asymmetric device geometries, (2) a local moment in the spin-generation material, and (3) a low-symmetry single crystal material.

### 1.4.1 Asymmetric Device Geometries

As mentioned in the previous section, the asymmetry in device geometry that is introduced by the presence of an interface (*i.e.* a spin-orbit material / ferromagnet interface) can be the only breaking of inversion symmetry that is necessary for the generation of a net torque. In this sense, asymmetric device geometries are often crucial. However, the concept of breaking the symmetries in this way can be taken too far.

In 2014, Yu *et al.* observed a field-like torque  $\propto \hat{m} \times \hat{z}$  in stacks of the trilayer heterostructure Ta/CoFeB/TaO<sub>x</sub>, grown with a wedge (variation of thickness across the wafer) in the TaO<sub>x</sub> layer [51]. Such a torque requires reducing the symmetries of a device down to a single mirror plane and flowing the current perpendicular to that plane. Consistent with this symmetry requirement, the torque  $\propto \hat{m} \times \hat{z}$  is observed when current is flowed perpendicular to the wedge direction, with the claim being that the asymmetry of the wedge is sufficient to break the required symmetries. The problem with this is that when you calculate the thickness gradient of the wedge across their device, a total difference of only  $< 0.5$  pm (or just 0.002 of an atom!!!) across their entire 20  $\mu\text{m}$  wide sample, such a small breaking of structural symmetry seems highly non-physical. We suggest that the average surface roughness of similarly grown films is often 100 to 1000 times larger than this difference. That being said, their data does suggest

the presence of a torque  $\propto \hat{m} \times \hat{z}$ , with other research groups having replicated this effect [52]. While we do not question the validity of the data that suggests the presence of this torque, we emphasize that the microscopic mechanism by which this torque is generated, and indeed the mechanism of symmetry breaking, is still unknown.

### 1.4.2 Local Magnetic Moment

The presence of a local magnetic moment in the spin-generating material can also reduce the symmetry requirements on the allowed spin-orbit torques. While a ferromagnetic moment cannot itself break inversion symmetry, when coupled with an interface it may reduce the constraining symmetries down to a single mirror plane. Numerous groups have recently started investigating such effects, like the spins generated from the anomalous Hall effect [53–56]. We particularly note the exciting developments in studying spin-orbit torques generated in the presence of a ferromagnetic interface [44–47, 57] and in spin-orbit materials with a local moment [48]. Here, spin-orbit filtering and precession effects, as well as exchange torques, can significantly complicate the relatively simple pictures drawn in sections 1.2 and 1.3. We also note that while ferromagnetic ordering cannot break inversion symmetry, an antiferromagnetic order can. There are some very interesting recent developments in the spin-orbit manipulation and generation of spins in antiferromagnets [49, 58, 59].

While this approach to lowering the symmetry requirements of a spin-orbit torque system is scalable, at present the novel spin-orbit torques observed in these systems are small, particularly in the polycrystalline materials. Further, it

is perhaps a more difficult system in which to probe specific symmetry breaking and model the microscopic mechanisms generating these low-symmetry torques due to the disordered and polycrystalline nature of the system. It is this author's opinion that pursuing both the path laid out in this section and in the next section in parallel is the most advantageous for the field.

### 1.4.3 Single Crystal Materials

Another approach is to explicitly lower the symmetry requirements on spin-orbit torques by growing single crystal materials with low crystalline symmetry. Previous work on spin-orbit torques in single crystalline materials include  $\text{Bi}_2\text{Se}_3$  and  $\text{BiSbTe}_3$  / ferromagnet heterostructures,  $\text{Ga}(\text{Mn})\text{As}$ ,  $\text{GaAs}/\text{Fe}$  heterostructures and  $\text{NiMnSb}$ <sup>5</sup>. In the case of the two topological insulators, the crystalline symmetry allows only Rashba-like torques, consistent with what is observed [21, 22]. However, in  $\text{Ga}(\text{Mn})\text{As}$  [19, 48],  $\text{GaAs}/\text{Fe}$  heterostructures [42] and  $\text{NiMnSb}$  [43] torques due to additional symmetry breaking by the crystal structure are present.

$\text{GaAs}$  crystallizes in a zinc blend structure and  $\text{NiMnSb}$  as a cubic half-Heusler lattice both with point group  $\bar{4}3m$ , which lacks inversion symmetry. In the presence of an epitaxial growth strain commonly present in the films, the point group is reduced to  $\bar{4}2m$ . This point group allows for a Dresselhaus-like spin polarization due to the inverse spin galvanic effect, with  $\chi$  having the

---

<sup>5</sup>Note also the single crystalline  $\text{CuMnAs}$  [58] and  $\text{IrMn}_3$  [59] referenced in section 1.4.2, however we do not include them here as it is local magnetic order, not the crystal symmetry, that alters the allowed torques

shape:

$$\chi = \begin{pmatrix} \chi_{aa} & 0 & 0 \\ 0 & -\chi_{aa} & 0 \\ 0 & 0 & 0 \end{pmatrix}. \quad (1.9)$$

Consistent with this symmetry, large Dresselhaus-like spin-orbit torques are observed in all three systems.

If one could grow single crystals of materials with even lower symmetry, it would be possible to generate spin with additional directions, such as an out-of-plane spin. In practice, low symmetry single crystal thin-films are difficult to grow by methods requiring epitaxial substrates (*e.g.*, pulsed laser deposition and molecular beam epitaxy techniques). This limitation is primarily a reflection of the dearth of suitable substrates with the necessary lattice constants and symmetries from which a single crystal thin-film can crystallize.

One way around this problem is to start with a low-symmetry bulk crystal that can be thinned down to nanometer scale thicknesses without causing much damage to the surface. Van der Waals materials fit this requirement nicely, due to the ease with which they can be cleaved along the van der Waals bond plane, while also providing a wide range of materials properties and crystal structures from which to draw on. In this thesis, we will draw on one of the most widely studied subclasses of van der Waals materials called the transition metal dichalcogenides.

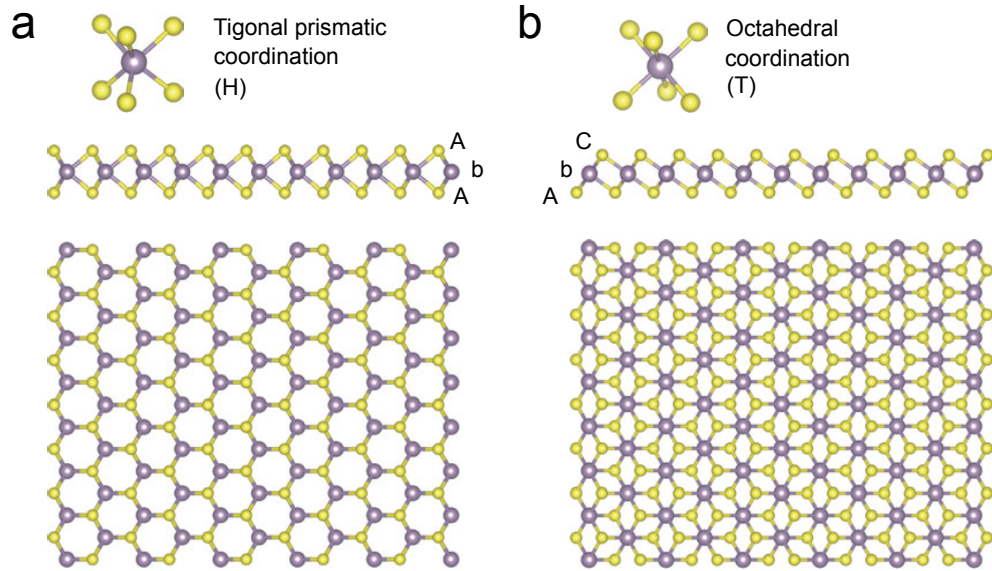


Figure 1.4: Monolayers of (a) hexagonal and (b) octahedral transition metal dichalcogenides. Top panel shows the metal atom coordination in each phase. Figure adapted from [60].

## 1.5 Transition Metal Dichalcogenides

Transition metal dichalcogenides (TMDs) can broadly be defined as taking the chemical formula  $MX_2$ , where M is a transition metal (some common ones are  $M = \text{Mo}, \text{W}, \text{Ta}, \text{Pt}, \text{Re}, \text{Ir}, \text{and Ti}$ ) and X is a chalcogenide (typically  $X = \text{S}, \text{Se}$  or  $\text{Te}$ ). These materials can be a semiconductor, semimetal or metal, with a variety of crystal structures, and are widely available from bulk crystal vendors (such as HQ graphene). They can readily be thinned into the mono- or few-layer regime through mechanical exfoliation, *i.e.* the scotch tape method.

Although TMDs have been studied in detail for nearly 60 years, they have experienced a dramatic resurgence in interest over the past decade following the exfoliation of single layer graphene and the discovery of the direct gap monolayer semiconductor  $\text{MoS}_2$ . While much of the recent interest in these materials is related to the optical and transport properties of the semiconducting

Material	MoS <sub>2</sub>	NbSe <sub>2</sub>	WTe <sub>2</sub> $\gamma$ -MoTe <sub>2</sub>	$\beta$ -MoTe <sub>2</sub>	TaTe <sub>2</sub>
Type	Semiconductor	Metal	Semimetal	Semimetal	Metal
Bulk Structure	Hexagonal	Hexagonal	Orthorhombic	Monoclinic	Monoclinic
Bulk Space Group	P6 <sub>3</sub> /mmc	P6 <sub>3</sub> /mmc	Pmn2 <sub>1</sub>	P2 <sub>1</sub> /m	C2/m
Number	194	194	31	11	12
Inversion?	Yes	Yes	No	Yes	Yes
Monolayer Structure	Hexagonal	Hexagonal	Monoclinic	Monoclinic	Monoclinic
Monolayer Space Group	P $\bar{6}$ m2	P $\bar{6}$ m2	P2 <sub>1</sub> /m	P2 <sub>1</sub> /m	C2/m
Number	187	187	11*	11	12
Inversion?	No	No	Yes	Yes	Yes

Table 1.1: Crystal structure and space groups for the transition metal dichalcogenides studied in this dissertation. Data taken from the Springer Materials database. \* There is a very recent paper that indicates WTe<sub>2</sub> monolayer may actually be space group 6, which lacks inversion symmetry [61].

TMDs, we will limit ourselves in this dissertation to the semimetal and metallic TMDs, with the exception of one brief mention of the previous work on spin-orbit torques in the semiconductor MoS<sub>2</sub>.

The crystal structures for TMDs come in two flavors, trigonal (H phase) and octahedral (T phase). The bond coordination for each phase is shown in Fig. 1.4, and forms the base unit for the hexagonal and octahedral crystal structures (also shown in Fig. 1.4). These two structures serve as the starting point for many of the TMD crystals. Small distortions to these base structures, such as dimerizations or trimerizations of the metal atoms, serve to alter the stable crystal structures in the available TMDs, and provides us with a rich pallet of low-symmetry materials from which to draw on.

I will not summarize the structures and electrical properties of all the possible TMDs here, and instead refer the interested reader to an exquisite review by Wilson and Yoffe from 1969 [62]. Instead, I will give the structures and symmetries of the TMDs studied in this dissertation, NbSe<sub>2</sub>, WTe<sub>2</sub>, TaTe<sub>2</sub> and MoTe<sub>2</sub>,

as well as one of the most ubiquitous TMDs, MoS<sub>2</sub>. Table 1.1 summarizes the structures and Fig. 1.5 shows a quadlayer of each material. We note that although we show two 2H crystal structures with the same space groups (MoS<sub>2</sub> and NbSe<sub>2</sub>), the native stacking of the layers differs.

### 1.5.1 Previous work on MoS<sub>2</sub> / Ferromagnet Heterostructures

The work presented in this thesis was not the first to look for spin-orbit torques in TMD/ferromagnet heterostructures. The first that we are aware of was performed by Zhang *et al.* [63]. This work studies spin-orbit torques generated by the semiconductor TMD, MoS<sub>2</sub>. They use chemical vapor deposited (CVD) MoS<sub>2</sub> monolayers interfaced with the ferromagnet Permalloy (Ni<sub>80</sub>Fe<sub>20</sub>), and report a large component of antidamping torque. While we question the quality of these devices (due to poor interface quality from a liftoff process, clear misalignment of the lithography and unetched MoS<sub>2</sub>), there is no doubt this work was influential in inspiring the work presented here. We have tried reproducing their results using CVD deposited semiconducting TMDs (MoS<sub>2</sub>, WS<sub>2</sub> and WSe<sub>2</sub>) with mixed results, finding that the antidamping component was only significant when the films were damaged in lithography or had a large surface roughness. We have also tried exfoliated samples of MoS<sub>2</sub> and WSe<sub>2</sub> with mixed results, largely due to difficulty with fabrication. Additional follow up work on this might be merited.

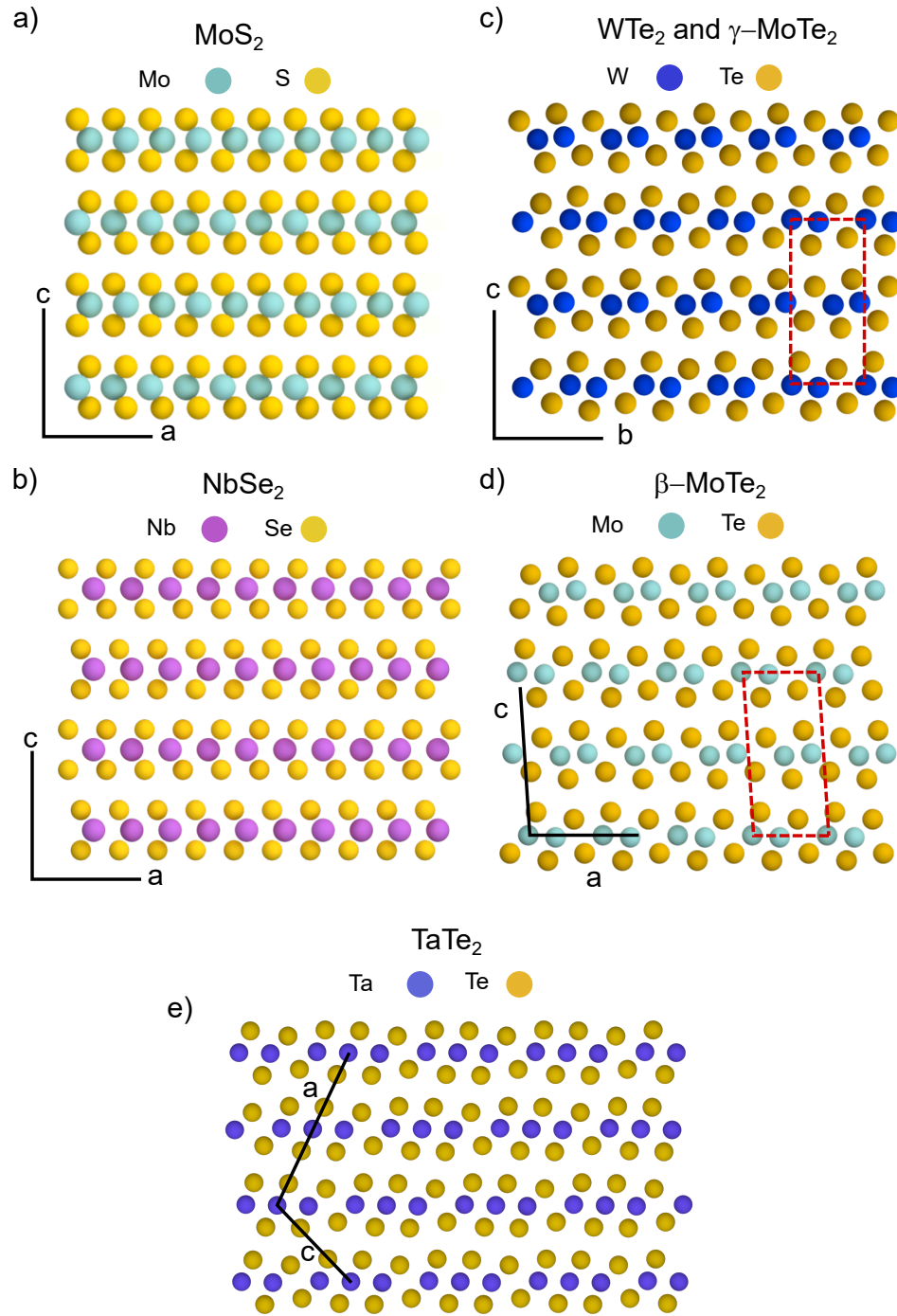


Figure 1.5: Crystal structures of the various transition metal dichalcogenides (TMDs) highlighted in this dissertation. All views are looking down the metal chain (or zigzag) direction. In the monoclinic structures, this is defined as the unique axis.

## 1.6 Outline

This thesis is roughly organized by the spin-generation material studied. In the next two chapters, we will focus on the spin-orbit torques generated in  $WTe_2$ /ferromagnet heterostructures. In Chapter 2, we will outline our initial discovery of a spin-orbit generated out-of-plane antidamping torque, discuss the specific symmetry requirements for the  $WTe_2$  system, provide detailed measurements of the torques dependence on the  $WTe_2$  crystal axes, and present a preliminary thickness dependence. This chapter is adapted from our publication in *Nature Physics* [64], and appears here with minor modifications.

In Chapter 3, we focus on a specific crystalline orientation of the  $WTe_2$ , and give a detailed study of the  $WTe_2$  thickness dependence for the observed torques. We find contrasting results in the thickness dependence for one of the torques in initial study [64], the out-of-plane field-like torque, and now correctly ascribe the origin of this torque to the Oersted field. Additionally, we report initial measurements in the few-layer regime, and conclusively show that the sign of the out-of-plane antidamping torque changes across a monolayer step in the  $WTe_2$  – consistent with the non-symmorphic symmetries of the  $WTe_2$  crystal. This work is adapted from our publication in *Physical Review B* [65].

Chapter 4 focuses on the TMD  $NbSe_2$ .  $NbSe_2$  is a high symmetry metallic TMD, and in its idealized crystal structure should only show torques similar to materials such as Pt, torques  $\propto \hat{m} \times \hat{y}$  and  $\propto \hat{m} \times (\hat{m} \times \hat{y})$ . In this chapter we report our measurements of the torques in  $NbSe_2$ /ferromagnet heterostructures down to the monolayer limit. We show that in most samples we observe only torques  $\propto \hat{m} \times \hat{y}$  and  $\propto \hat{m} \times (\hat{m} \times \hat{y})$ , and show that the torque  $\propto \hat{m} \times \hat{y}$  is dominated

by the Oersted field in thick NbSe<sub>2</sub>. However, in some samples we observe a large torque  $\propto \hat{m} \times \hat{z}$ , which is inconsistent with the symmetries of the NbSe<sub>2</sub> crystal, and we suggest the presence of a uniaxial strain that arises during the fabrication process as the potential source of symmetry breaking. This work is adapted from our publication in *Nano Letters* [66].

In Chapter 5 we discuss the presence of Dresselhaus-like torques in our TMD/ferromagnet heterostructure devices, using both TaTe<sub>2</sub> and WTe<sub>2</sub> as our torque-generating material. We find a Dresselhaus field-like torque,  $\propto \hat{m} \times \hat{x}$ , in both materials. However, we suggest that the observed torques are dominated by an interesting artifact that is ubiquitous to low symmetry materials – the Oersted torque arising from a non-uniform current flow due to an anisotropy of the resistivity with respect to the crystal axis.

In Chapter 6 we present our initial measurements of the spin-orbit torques in octahedrally coordinated ( $\beta$  and  $\gamma$ ) MoTe<sub>2</sub>/ferromagnet heterostructures at room temperature. We find an out-of-plane antidamping torque present when current is flowed perpendicular to the MoTe<sub>2</sub> mirror plane, as well as a standard antidamping torque present in all devices. We also present a detailed study of the MoTe<sub>2</sub> thickness dependence for the observed torques, and show that the torque  $\propto \hat{m} \times \hat{y}$  is dominated by the Oersted field in MoTe<sub>2</sub>. Similar to WTe<sub>2</sub>, both the in-plane and out-of-plane antidamping torques are relatively unaffected by the TMD thickness, suggesting an interfacial mechanism. Future experiments will probe the dependence of the observed torques on the expected phase transition of octahedrally coordinated MoTe<sub>2</sub>, from  $\beta$ -MoTe<sub>2</sub> at room temperature to  $\gamma$ -MoTe<sub>2</sub> below 250 K.

In Chapter 7 we give a wider outlook on this work and discuss possible

future experiments.

## References

- [1] A. D. Kent and D. C. Worledge. “A new spin on magnetic memories.” *Nature Nanotechnology* **10**, 187 (2015).
- [2] C. Zhang, S. Fukami, H. Sato, F. Matsukura, and H. Ohno. “Spin-orbit torque induced magnetization switching in nano-scale Ta/CoFeB/MgO.” *Applied Physics Letters* **107**, 012401 (2015).
- [3] S. V. Aradhya, G. E. Rowlands, J. Oh, D. C. Ralph, and R. A. Buhrman. “Nanosecond-Timescale Low Energy Switching of In-Plane Magnetic Tunnel Junctions through Dynamic Oersted-Field-Assisted Spin Hall Effect.” *Nano Letters* **16**, 5987 (2016).
- [4] M. Baumgartner, K. Garello, J. Mendil, C. O. Avci, E. Grimaldi, C. Murer, J. Feng, M. Gabureac, C. Stamm, Y. Acremann, S. Finizio, S. Wintz, J. Raabe, and P. Gambardella. “Spatially and time-resolved magnetization dynamics driven by spin-orbit torques.” *Nature Nanotechnology* **12**, 980 (2017).
- [5] S. Shi, Y. Ou, S. V. Aradhya, D. C. Ralph, and R. A. Buhrman. “Fast Low-Current Spin-Orbit-Torque Switching of Magnetic Tunnel Junctions through Atomic Modifications of the Free-Layer Interfaces.” *Phys. Rev. Applied* **9**, 011002 (2018).
- [6] Y. A. Bychkov and E. I. Rashba. “Oscillatory effects and the magnetic susceptibility of carriers in inversion layers.” *Journal of Physics C: Solid State Physics* **17**, 6039 (1984).

- [7] V. Edelstein. "Spin polarization of conduction electrons induced by electric current in two-dimensional asymmetric electron systems." *Solid State Communications* **73**, 233 (1990).
- [8] G. Dresselhaus. "Spin-Orbit Coupling Effects in Zinc Blende Structures." *Phys. Rev.* **100**, 580 (1955).
- [9] M. I. D'Yakonov and V. I. Perel. "Possibility of Orienting Electron Spins with Current." *Soviet Journal of Experimental and Theoretical Physics Letters* **13**, 467 (1971).
- [10] J. E. Hirsch. "Spin Hall Effect." *Phys. Rev. Lett.* **83**, 1834 (1999).
- [11] J. Sinova, D. Culcer, Q. Niu, N. A. Sinitsyn, T. Jungwirth, and A. H. MacDonald. "Universal Intrinsic Spin Hall Effect." *Phys. Rev. Lett.* **92**, 126603 (2004).
- [12] Y. K. Kato, R. C. Myers, A. C. Gossard, and D. D. Awschalom. "Observation of the Spin Hall Effect in Semiconductors." *Science* **306**, 1910 (2004).
- [13] S. O. Valenzuela and M. Tinkham. "Direct electronic measurement of the spin Hall effect." *Nature* **442**, 176 (2006).
- [14] T. Kimura, Y. Otani, T. Sato, S. Takahashi, and S. Maekawa. "Room-Temperature Reversible Spin Hall Effect." *Phys. Rev. Lett.* **98**, 156601 (2007).
- [15] T. Seki, Y. Hasegawa, S. Mitani, S. Takahashi, H. Imamura, S. Maekawa, J. Nitta, and K. Takanashi. "Giant spin Hall effect in perpendicularly spin-polarized FePt/Au devices." *Nature Materials* **7**, 125 (2008).
- [16] L. Liu, T. Moriyama, D. C. Ralph, and R. A. Buhrman. "Spin-Torque Fer-

- romagnetic Resonance Induced by the Spin Hall Effect." *Physical Review Letters* **106**, 036601 (2011).
- [17] Y. K. Kato, R. C. Myers, A. C. Gossard, and D. D. Awschalom. "Current-Induced Spin Polarization in Strained Semiconductors." *Phys. Rev. Lett.* **93**, 176601 (2004).
- [18] J. Wunderlich, B. Kaestner, J. Sinova, and T. Jungwirth. "Experimental Observation of the Spin-Hall Effect in a Two-Dimensional Spin-Orbit Coupled Semiconductor System." *Phys. Rev. Lett.* **94**, 047204 (2005).
- [19] D. Fang, H. Kurebayashi, J. Wunderlich, K. Výborný, L. P. Zârbo, R. P. Campion, A. Casiraghi, B. L. Gallagher, T. Jungwirth, and A. J. Ferguson. "Spin-orbit-driven ferromagnetic resonance." *Nature Nanotechnology* **6**, 413 (2011).
- [20] I. M. Miron, K. Garello, G. Gaudin, P.-J. Zermatten, M. V. Costache, S. Auffret, S. Bandiera, B. Rodmacq, A. Schuhl, and P. Gambardella. "Perpendicular switching of a single ferromagnetic layer induced by in-plane current injection." *Nature* **476**, 189 (2011).
- [21] A. R. Mellnik, J. S. Lee, A. Richardella, J. L. Grab, P. J. Mintun, M. H. Fischer, A. Vaezi, A. Manchon, E.-A. Kim, N. Samarth, and D. C. Ralph. "Spin-transfer torque generated by a topological insulator." *Nature* **511**, 449 (2014).
- [22] Y. Fan, P. Upadhyaya, X. Kou, M. Lang, S. Takei, Z. Wang, J. Tang, L. He, L.-T. Chang, M. Montazeri, G. Yu, W. Jiang, T. Nie, R. N. Schwartz, Y. Tserkovnyak, and K. L. Wang. "Magnetization switching through giant spin-orbit torque in a magnetically doped topological insulator heterostructure." *Nature Materials* **13**, 699 (2014).

- [23] C.-F. Pai. "The spin hall effect induced spin transfer torque in magnetic heterostructures." *Ph.D. Dissertation* Cornell University (2014).
- [24] N. Nagaosa, J. Sinova, S. Onoda, A. H. MacDonald, and N. P. Ong. "Anomalous Hall effect." *Rev. Mod. Phys.* **82**, 1539 (2010).
- [25] M.-H. Nguyen, D. C. Ralph, and R. A. Buhrman. "Spin Torque Study of the Spin Hall Conductivity and Spin Diffusion Length in Platinum Thin Films with Varying Resistivity." *Phys. Rev. Lett.* **116**, 126601 (2016).
- [26] D. Ralph and M. Stiles. "Spin transfer torques." *Journal of Magnetism and Magnetic Materials* **320**, 1190 (2008).
- [27] W. Zhang, W. Han, X. Jiang, S.-H. Yang, and S. S. P. Parkin. "Role of transparency of platinum-ferromagnet interfaces in determining the intrinsic magnitude of the spin Hall effect." *Nature Physics* **11**, 496 (2015).
- [28] C.-F. Pai, Y. Ou, L. H. Vilela-Leão, D. C. Ralph, and R. A. Buhrman. "Dependence of the efficiency of spin Hall torque on the transparency of Pt/ferromagnetic layer interfaces." *Phys. Rev. B* **92**, 064426 (2015).
- [29] L. Liu, R. Buhrman, and D. Ralph. "Review and Analysis of Measurements of the Spin Hall Effect in Platinum." arXiv1111.3702 (2011).
- [30] V. Castel, N. Vlietstra, J. Ben Youssef, and B. J. van Wees. "Platinum thickness dependence of the inverse spin-Hall voltage from spin pumping in a hybrid yttrium iron garnet/platinum system." *Applied Physics Letters* **101**, 132414 (2012).
- [31] L. Liu, C.-F. Pai, Y. Li, H. W. Tseng, D. C. Ralph, and R. A. Buhrman. "Spin-Torque Switching with the Giant Spin Hall Effect of Tantalum." *Science* **336**, 555 (2012).

- [32] C. F. Pai, L. Liu, Y. Li, H. W. Tseng, D. C. Ralph, and R. A. Buhrman. "Spin transfer torque devices utilizing the giant spin Hall effect of tungsten." *Applied Physics Letters* **101**, 122404 (2012).
- [33] A. Hoffmann. "Spin Hall Effects in Metals." *IEEE Transactions on Magnetics* **49**, 5172 (2013).
- [34] J. Sinova, S. O. Valenzuela, J. Wunderlich, C. H. Back, and T. Jungwirth. "Spin Hall effects." *Rev. Mod. Phys.* **87**, 1213 (2015).
- [35] L. Liu, O. J. Lee, T. J. Gudmundsen, D. C. Ralph, and R. A. Buhrman. "Current-Induced Switching of Perpendicularly Magnetized Magnetic Layers Using Spin Torque from the Spin Hall Effect." *Phys. Rev. Lett.* **109**, 096602 (2012).
- [36] J. Nitta, T. Akazaki, H. Takayanagi, and T. Enoki. "Gate Control of Spin-Orbit Interaction in an Inverted  $\text{In}_{0.53}\text{Ga}_{0.47}\text{As}/\text{In}_{0.52}\text{Al}_{0.48}\text{As}$  Heterostructure." *Phys. Rev. Lett.* **78**, 1335 (1997).
- [37] S. LaShell, B. A. McDougall, and E. Jensen. "Spin Splitting of an Au(111) Surface State Band Observed with Angle Resolved Photoelectron Spectroscopy." *Phys. Rev. Lett.* **77**, 3419 (1996).
- [38] J. C. R. Sánchez, L. Vila, G. Desfonds, S. Gambarelli, J. P. Attané, J. M. De Teresa, C. Magén, and A. Fert. "Spin-to-charge conversion using Rashba coupling at the interface between non-magnetic materials." *Nature Communications* **4**, 2944 (2013).
- [39] M. B. Jungfleisch, W. Zhang, J. Sklenar, W. Jiang, J. E. Pearson, J. B. Ketterson, and A. Hoffmann. "Interface-driven spin-torque ferromagnetic res-

- onance by Rashba coupling at the interface between nonmagnetic materials." *Phys. Rev. B* **93**, 224419 (2016).
- [40] A. Manchon, H. C. Koo, J. Nitta, S. M. Frolov, and R. A. Duine. "New perspectives for Rashba spin-orbit coupling." *Nature Materials* **14**, 871 (2015).
- [41] A. Soumyanarayanan, N. Reyren, A. Fert, and C. Panagopoulos. "Emergent phenomena induced by spin-orbit coupling at surfaces and interfaces." *Nature* **539**, 509 (2016).
- [42] T. D. Skinner, K. Olejník, L. K. Cunningham, H. Kurebayashi, R. P. Campion, B. L. Gallagher, T. Jungwirth, and A. J. Ferguson. "Complementary spin-Hall and inverse spin-galvanic effect torques in a ferromagnet/semiconductor bilayer." *Nature Communications* **6**, 6730 (2015).
- [43] C. Ciccarelli, L. Anderson, V. Tshitoyan, A. J. Ferguson, F. Gerhard, C. Gould, L. W. Molenkamp, J. Gayles, J. Železný, L. Šmejkal, Z. Yuan, J. Sinova, F. Freimuth, and T. Jungwirth. "Room-temperature spin-orbit torque in NiMnSb." *Nature Physics* **12**, 855 (2016).
- [44] V. P. Amin and M. D. Stiles. "Spin transport at interfaces with spin-orbit coupling: Phenomenology." *Physical Review B* **94**, 104420 (2016).
- [45] V. P. Amin and M. D. Stiles. "Spin transport at interfaces with spin-orbit coupling: Formalism." *Physical Review B* **94**, 104419 (2016).
- [46] K.-W. Kim, K.-J. Lee, J. Sinova, H.-W. Lee, and M. D. Stiles. "Spin-orbit torques from interfacial spin-orbit coupling for various interfaces." *Phys. Rev. B* **96**, 104438 (2017).
- [47] S.-h. C. Baek, V. P. Amin, Y.-W. Oh, G. Go, S.-J. Lee, G.-H. Lee, K.-J. Kim,

- M. D. Stiles, B.-G. Park, and K.-J. Lee. "Spin currents and spin-orbit torques in ferromagnetic trilayers." *Nature Materials* **17**, 509 (2018).
- [48] H. Kurebayashi, J. Sinova, D. Fang, A. C. Irvine, T. D. Skinner, J. Wunderlich, V. Novák, R. P. Campion, B. L. Gallagher, E. K. Vehstedt, L. P. Zârbo, K. Výborný, A. J. Ferguson, and T. Jungwirth. "An antidamping spinorbit torque originating from the Berry curvature." *Nature Nanotechnology* **9**, 211 (2014).
- [49] J. Železný, H. Gao, A. Manchon, F. Freimuth, Y. Mokrousov, J. Zemen, J. Mašek, J. Sinova, and T. Jungwirth. "Spin-orbit torques in locally and globally noncentrosymmetric crystals: Antiferromagnets and ferromagnets." *Physical Review B* **95**, 014403 (2017).
- [50] M. Seemann, D. Ködderitzsch, S. Wimmer, and H. Ebert. "Symmetry-imposed shape of linear response tensors." *Phys. Rev. B* **92**, 155138 (2015).
- [51] G. Yu, P. Upadhyaya, Y. Fan, J. G. Alzate, W. Jiang, K. L. Wong, S. Takei, S. A. Bender, L.-T. Chang, Y. Jiang, M. Lang, J. Tang, Y. Wang, Y. Tserkovnyak, P. K. Amiri, and K. L. Wang. "Switching of perpendicular magnetization by spin-orbit torques in the absence of external magnetic fields." *Nature Nanotechnology* **9**, 548 (2014).
- [52] C.-F. Pai, M. Mann, A. J. Tan, and G. S. D. Beach. "Determination of spin torque efficiencies in heterostructures with perpendicular magnetic anisotropy." *Phys. Rev. B* **93**, 144409 (2016).
- [53] T. Taniguchi, J. Grollier, and M. D. Stiles. "Spin-Transfer Torques Generated by the Anomalous Hall Effect and Anisotropic Magnetoresistance." *Phys. Rev. Applied* **3**, 044001 (2015).

- [54] A. M. Humphries, T. Wang, E. R. J. Edwards, S. R. Allen, J. M. Shaw, H. T. Nembach, J. Q. Xiao, T. J. Silva, and X. Fan. "Observation of spin-orbit effects with spin rotation symmetry." *Nature Communications* **8**, 911 (2017).
- [55] A. Bose, D. D. Lam, S. Bhuktare, S. Dutta, H. Singh, Y. Jibiki, M. Goto, S. Miwa, and A. A. Tulapurkar. "Observation of Anomalous Spin Torque Generated by a Ferromagnet." *Phys. Rev. Applied* **9**, 064026 (2018).
- [56] J. D. Gibbons, D. MacNeill, R. A. Buhrman, and D. C. Ralph. "Reorientable Spin Direction for Spin Current Produced by the Anomalous Hall Effect." *Phys. Rev. Applied* **9**, 064033 (2018).
- [57] F. Hellman, A. Hoffmann, Y. Tserkovnyak, G. S. D. Beach, E. E. Fullerton, C. Leighton, A. H. MacDonald, D. C. Ralph, D. A. Arena, H. A. Dürr, P. Fischer, J. Grollier, J. P. Heremans, T. Jungwirth, A. V. Kimel, B. Koopmans, I. N. Krivorotov, S. J. May, A. K. Petford-Long, J. M. Rondinelli, N. Samarth, I. K. Schuller, A. N. Slavin, M. D. Stiles, O. Tchernyshyov, A. Thiaville, and B. L. Zink. "Interface-induced phenomena in magnetism." *Rev. Mod. Phys.* **89**, 025006 (2017).
- [58] P. Wadley, B. Howells, J. Železný, C. Andrews, V. Hills, R. P. Campion, V. Novák, K. Olejník, F. Maccherozzi, S. S. Dhesi, S. Y. Martin, T. Wagner, J. Wunderlich, F. Freimuth, Y. Mokrousov, J. Kuneš, J. S. Chauhan, M. J. Grzybowski, A. W. Rushforth, K. W. Edmonds, B. L. Gallagher, and T. Jungwirth. "Electrical switching of an antiferromagnet." *Science* **351**, 587 (2016).
- [59] W. Zhang, W. Han, S.-H. Yang, Y. Sun, Y. Zhang, B. Yan, and S. S. P. Parkin. "Giant facet-dependent spin-orbit torque and spin Hall conductivity in the triangular antiferromagnet IrMn<sub>3</sub>." *Science Advances* **2** (2016).

- [60] M. Chhowalla, H. S. Shin, G. Eda, L.-J. Li, K. P. Loh, and H. Zhang. "The chemistry of two-dimensional layered transition metal dichalcogenide nanosheets." *Nature Chemistry* **5**, 263 (2013).
- [61] S.-Y. Xu, Q. Ma, H. Shen, V. Fatemi, S. Wu, T.-R. Chang, G. Chang, A. M. M. Valdivia, C.-K. Chan, Q. D. Gibson, J. Zhou, Z. Liu, K. Watanabe, T. Taniguchi, H. Lin, R. J. Cava, L. Fu, N. Gedik, and P. Jarillo-Herrero. "Electrically switchable Berry curvature dipole in the monolayer topological insulator  $\text{WTe}_2$ ." *Nature Physics AOP* (2018).
- [62] J. Wilson and A. Yoffe. "The transition metal dichalcogenides discussion and interpretation of the observed optical, electrical and structural properties." *Advances in Physics* **18**, 193 (1969).
- [63] W. Zhang, J. Sklenar, B. Hsu, W. Jiang, M. B. Jungfleisch, J. Xiao, F. Y. Fradin, Y. Liu, J. E. Pearson, J. B. Ketterson, Z. Yang, and A. Hoffmann. "Research Update: Spin transfer torques in permalloy on monolayer  $\text{MoS}_2$ ." *APL Materials* **4**, 032302 (2016).
- [64] D. MacNeill, G. M. Stiehl, M. H. D. Guimarães, R. A. Buhrman, J. Park, and D. C. Ralph. "Control of spinorbit torques through crystal symmetry in  $\text{WTe}_2$ /ferromagnet bilayers." *Nature Physics* **13**, 300 (2017).
- [65] D. MacNeill, G. M. Stiehl, M. H. D. Guimarães, N. D. Reynolds, R. A. Buhrman, and D. C. Ralph. "Thickness dependence of spin-orbit torques generated by  $\text{WTe}_2$ ." *Physical Review B* **96**, 054450 (2017).
- [66] M. H. D. Guimarães, G. M. Stiehl, D. MacNeill, N. D. Reynolds, and D. C. Ralph. "SpinOrbit Torques in  $\text{NbSe}_2$ /Permalloy Bilayers." *Nano Letters* **18**, 1311 (2018).

CHAPTER 2  
CRYSTAL SYMMETRY AND SPIN-ORBIT TORQUES IN TUNGSTEN  
DITELLURIDE

Recent discoveries regarding current-induced spin-orbit torques produced by heavy-metal/ferromagnet and topological insulator/ferromagnet bilayers provide the potential for dramatically improved efficiency in the manipulation of magnetic devices. However, in experiments performed to date, spin-orbit torques have an important limitation – the component of torque that can compensate magnetic damping is required by symmetry to lie within the device plane. This means that spin-orbit torques can drive the most current-efficient type of magnetic reversal (antidamping switching) only for magnetic devices with in-plane anisotropy, not the devices with perpendicular magnetic anisotropy that are needed for high-density applications. In this chapter, we show experimentally that this state of affairs is not fundamental, but rather one can change the allowed symmetries of spin-orbit torques in spin-source/ferromagnet bilayer devices by using a spin-source material with low crystalline symmetry. We use  $WTe_2$ , a transition-metal dichalcogenide whose surface crystal structure has only one mirror plane and no two-fold rotational invariance. Consistent with these symmetries, we generate an out-of-plane antidamping torque when current is applied along a low-symmetry axis of  $WTe_2$ /Permalloy bilayers, but not when current is applied along a high-symmetry axis. Controlling spin-orbit torques by crystal symmetries in multilayer samples provides a new strategy for optimizing future magnetic technologies. This chapter is based on work published in *Nature Physics* with D. MacNeill, M.H.D. Guimarães, R.A. Buhrman, J. Park and D.C. Ralph (Ref. [1]), and appears here with modifications and additional data.

## 2.1 Introduction

Current-induced torques generated by materials with strong spin-orbit (S-O) interactions are a promising approach for energy-efficient manipulation of non-volatile magnetic memory and logic technologies [2]. However, S-O torques observed to date are limited by their symmetry so that they cannot efficiently switch the nanoscale magnets with perpendicular magnetic anisotropy (PMA) that are required for high-density applications [3]. S-O torques generated either in conventional heavy metal/ferromagnet thin-film bilayers[4–14], or in topological insulator/ferromagnet bilayers [15, 16], are restricted by symmetry to have a particular form: an “antidamping-like” component oriented in the sample plane that is even upon reversal of the magnetization direction [17],  $\hat{m}$ , plus an “effective field” component that is odd in  $\hat{m}$ . The fact that the antidamping torque lies in-plane means that the most efficient mechanism of S-O-torque-driven magnetic reversal for small devices (antidamping switching) [18, 19], is available only for magnetic samples with in-plane magnetic anisotropy [9, 10], and not PMA samples (see also Section 2.8.1). S-O torques can also arise from broken crystalline inversion symmetry, even within single layers of ferromagnets [20–23] or antiferromagnets [24], but the antidamping torques that have been measured to date are still limited to lie in the sample plane [22, 23, 25]. Here we demonstrate that the allowed symmetries of S-O torques in spin source/ferromagnet bilayer samples can be changed by using a spin source material with reduced crystalline symmetry. We generate an out-of-plane antidamping S-O torque when current is applied along a low-symmetry axis of the bilayer. This previously-unobserved form of S-O torque is quenched when current is applied along a high symmetry axis.

As our low-symmetry spin source material, we use the semi-metal  $\text{WTe}_2$ , a layered orthorhombic transition metal dichalcogenide (TMD) with strong S-O coupling [26–29]. TMD materials are attractive for use as sources of S-O torque because they can be prepared as monocrystalline thin films with atomically-flat surfaces down to the single-layer level. They provide a broad palette of crystal symmetries, S-O coupling strengths, and electrical conductivities [30, 31]. Other research groups have demonstrated recently the generation of S-O torques in devices made with the TMD  $\text{MoS}_2$  [32], and the Onsager reciprocal process (voltage generation from spin pumping) in  $\text{MoS}_2/\text{Al}/\text{Co}$  heterostructures [33]. Compared to  $\text{MoS}_2$ , the crystal structure of  $\text{WTe}_2$  has lower symmetry, with the space group  $Pmn2_1$  for bulk  $\text{WTe}_2$  crystals [34]. In a  $\text{WTe}_2$ /ferromagnet bilayer sample, the screw-axis and glide plane symmetries of this space group are broken at the interface, so that  $\text{WTe}_2$ /ferromagnet bilayers have only one symmetry, a mirror symmetry relative to the  $bc$  plane depicted in Fig. 2.1a. There is no mirror symmetry in the  $ac$  plane, and therefore no  $180^\circ$  rotational symmetry about the  $c$ -axis (perpendicular to the sample plane).

## 2.2 Device Fabrication

Our device fabrication starts with high quality artificially-grown crystals of  $\text{WTe}_2$  (from HQ Graphene) which we exfoliate onto a high-resistivity silicon wafer with  $1\ \mu\text{m}$  of thermal oxide. The exfoliation is performed in flowing dry nitrogen in the load-lock chamber of our sputtering system, so that the exfoliated samples can be transferred into the sputter system with minimal exposure to air. We have also carried out measurements on samples exfoliated in vacuum with largely similar results, though there are some important differences (see

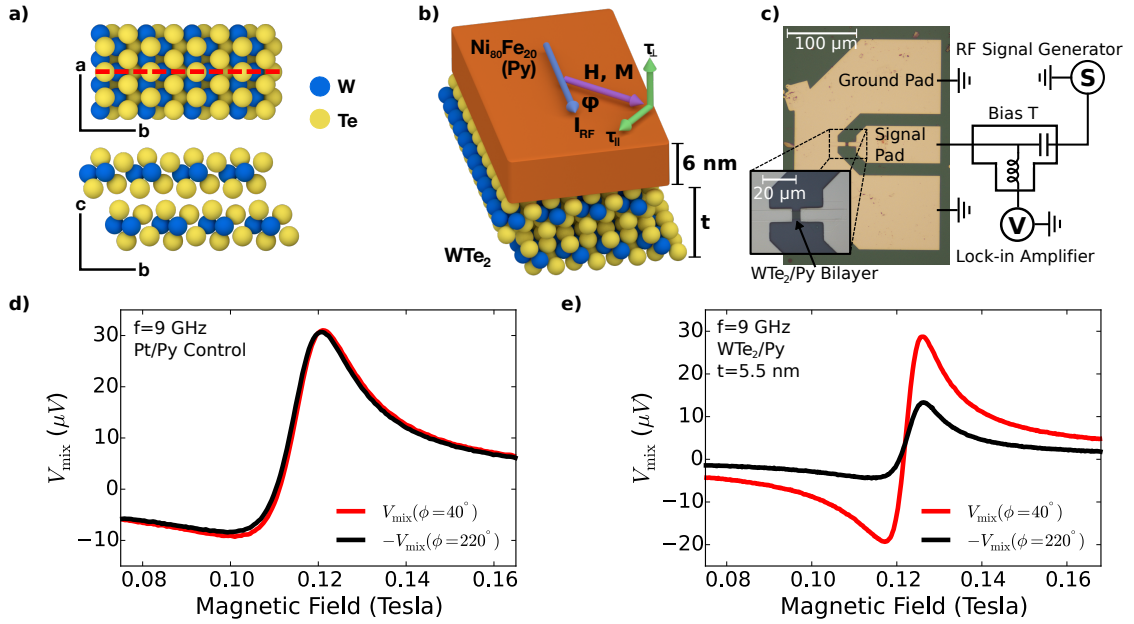


Figure 2.1: **a)** Crystal structure near the surface of WTe<sub>2</sub>. The surface possesses mirror symmetry with respect to the bc plane (dashed line), but not with respect to the ac plane, and therefore it is also not symmetric relative to a 180° rotation about the c-axis. **b)** Schematic of the bilayer WTe<sub>2</sub>/Permalloy sample geometry. **c)** Optical images of the sample geometry including contact pads, with the circuit used for spin-torque FMR measurements. **d)** ST-FMR resonances for Pt(6 nm)/Py(6 nm) control samples, with the magnetization oriented at 40° and 220° relative to the current direction. The applied microwave power is 0 dBm. **e)** ST-FMR resonances for a WTe<sub>2</sub>(5.5 nm)/Py(6 nm) sample with current applied along the *a*-axis, with the magnetization oriented at 40° and 220° relative to the current direction. The applied microwave power is 5 dBm.

Section 3.6.3). The exfoliation results in the deposition of single-crystal flakes of WTe<sub>2</sub> up to 40 μm in lateral extent and with a distribution of thicknesses. To minimize damage to the WTe<sub>2</sub> flakes, we use grazing-angle magnetron sputtering to deposit 6 nm of permalloy (Py=Ni<sub>81</sub>Fe<sub>19</sub>) onto the WTe<sub>2</sub>. The Py deposition rates are kept below 0.2 Å/s and are performed in an ambient Ar background pressure of 4 mtorr while the substrate rotates at 3 rotations per minute. We then deposit a protective aluminum oxide cap in situ onto the WTe<sub>2</sub>/Py bilayer by sputter deposition of 1 nm aluminum which is subsequently oxidized

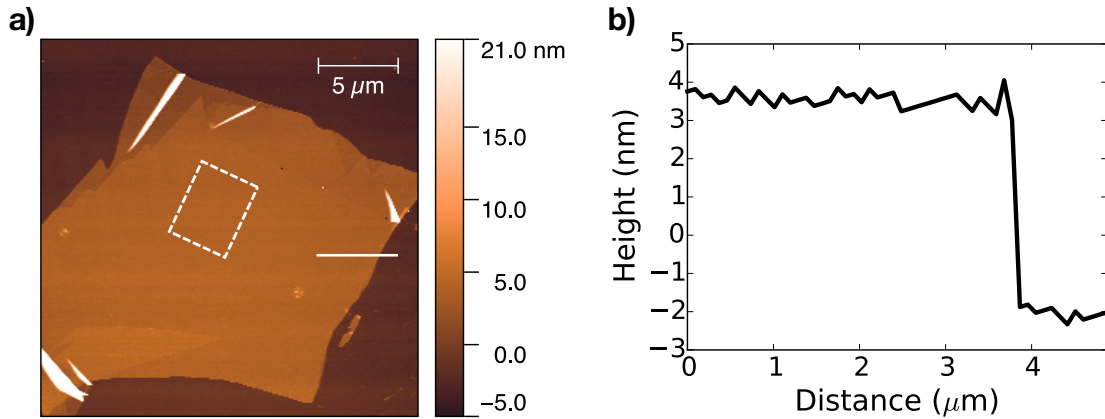


Figure 2.2: **a)** An atomic force microscopy image of the  $WTe_2$  flake used for fabrication of Device 15 after deposition of the Permalloy layer and aluminum oxide cap but before any lithographic processing. The active region used for the device (dashed white box) has a RMS surface roughness  $< 300 \text{ pm}$ . **b)** A linecut [white line in **a)**] from the edge of the  $WTe_2$  flake, showing an average thickness of 5.5 nm.

in a dry  $N_2/O_2$  mixture. The Py magnetic moment is in-plane for all devices studied.

After deposition of the ferromagnet and aluminum oxide cap, we use optical contrast and atomic force microscopy (AFM) to select  $WTe_2$  flakes for further study. Flakes are chosen to ensure an active region with homogenous thickness (i.e. no monolayer steps or tape residue) and minimal roughness (typically  $< 300 \text{ pm RMS}$ ). An AFM image of a typical  $WTe_2/Py$  bilayer prior to patterning is shown in Fig. 2.2.

The  $WTe_2/Py$  bilayers are patterned into bars of width 3-4  $\mu\text{m}$ . The bars are defined via Ar ion milling, using either a hard mask (silicon or aluminum oxide) or an e-beam exposed PMMA/HSQ bilayer. After etching, another step of e-beam lithography is used to make electrical contact to the bars with Ti/Pt contact pads, which have a ground-signal-ground geometry compatible with

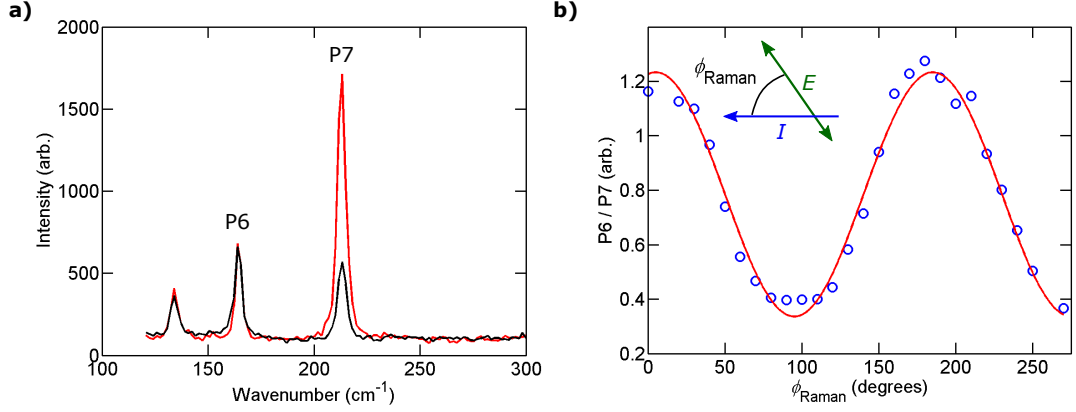


Figure 2.3: **a)** Polarized Raman spectra with the orientation of the electric field of the excitation,  $E$ , parallel to the  $\text{WTe}_2$  a-axis (black) and parallel to the  $\text{WTe}_2$  b-axis (red) for Device 4. Traces are normalized by the silicon substrate peak for ease of comparison (not shown).  $P6 = 165.7 \text{ cm}^{-1}$  and  $P7 = 211.3 \text{ cm}^{-1}$  (as defined by Ref. [35]) **b)** The ratio of intensities for P6/P7 (blue circles) plotted as a function of angle between the current (lithographically defined bar) direction and the linearly polarized Raman excitation as defined in the inset. The orientation of the  $\text{WTe}_2$  a-axis is determined from the angle that maximizes the fit (red) to a  $\cos^2(\phi_{\text{Raman}})$  type dependence [35]. The directions  $\hat{b}$  and  $-\hat{b}$  are not differentiated by Raman scattering.

microwave probes (Fig. 2.1c). The active region between the contacts is  $3\text{-}6 \mu\text{m}$  long. For hard-mask devices, an additional reactive-ion etching (RIE) or wet etch step is used prior to the Ti/Pt deposition to remove the mask in the contact region. The Py resistivity in our devices is  $(100 \pm 20) \mu\Omega\text{cm}$ . The  $\text{WTe}_2$  bulk resistivity value is  $(380 \pm 10) \mu\Omega\text{cm}$  with the current flowing along the  $a$ -axis and is likely higher in thinner flakes [29].

The crystal axes of  $\text{WTe}_2$  are determined by polarized Raman measurements using a Renishaw inVia confocal Raman microscope with a linearly polarized 488 nm wavelength excitation and a co-linear polarizer placed in front of the spectrometer entrance slit (see Fig. 2.3a). The  $\text{WTe}_2$  sample is positioned such that the light is incident normal to the sample surface and the excitation electric field is in the sample plane. Previous calculations and measurements have

shown that the  $165.7\text{ cm}^{-1}$  (P6) and  $211.3\text{ cm}^{-1}$  (P7) Raman peaks of  $\text{WTe}_2$  are sensitive to the alignment of the electric field and the crystal axes [35]. We measure the intensity of the P6 and P7 Raman peaks as a function of angle by rotating the sample from  $0^\circ$  to  $180^\circ$  in steps of  $10^\circ$  or  $20^\circ$  (keeping the electric field in the sample plane). The angle for which the ratio of peak intensities,  $P6/P7$ , is maximized identifies the  $a$ -axis, allowing determination of the angle between the  $a$ -axis and current direction,  $\phi_{a-I}$  (see Fig. 2.3b). This has been confirmed by high-angle annular dark-field scanning transmission electron microscopy (HAADF-STEM) imaging (see Fig. 2.4). We have measured a total of 15 devices with bars oriented at a variety of alignments to the  $\text{WTe}_2$  crystal axes and with  $\text{WTe}_2$  thicknesses ranging from 1.8 nm to 15.0 nm.

### 2.3 Spin-Torque Ferromagnetic Resonance Measurements

To measure the S-O torques produced by our  $\text{WTe}_2/\text{Py}$  bilayers, we use the technique of spin-torque ferromagnetic resonance (ST-FMR) [7, 22], performed at room temperature. In ST-FMR, an in-plane alternating current is applied through the bilayer at a frequency characteristic of ferromagnetic resonance (here, 5-12 GHz). The torques generated by the current excite the magnetic moment away from equilibrium and cause it to precess, creating a time-dependent change in the resistance of the bilayer due to the anisotropic magnetoresistance (AMR) in the ferromagnet. This change in resistance mixes with the alternating current to create a DC voltage across the bar,  $V_{\text{mix}}$ . The circuit used to measure  $V_{\text{mix}}$  is depicted in Fig. 2.1c. By sweeping an applied in-plane magnetic field we tune the ferromagnetic resonance through the applied frequency, giving rise to a resonance feature in  $V_{\text{mix}}$  (Figs. 2.1d). The in-plane ( $\tau_{\parallel}$ ) and out-of-plane

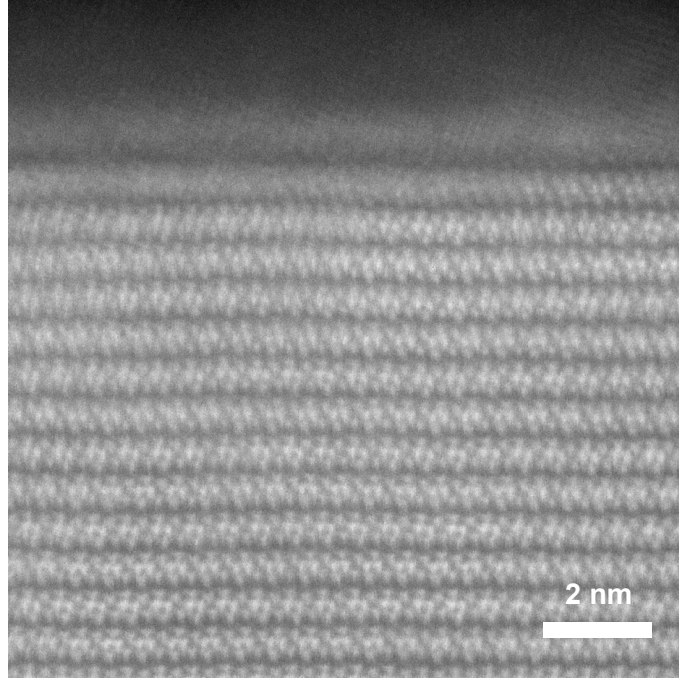


Figure 2.4: Cross-sectional HAADF-STEM image of WTe<sub>2</sub>/Py Device 2 looking down the WTe<sub>2</sub> a-axis. Note that this device was exfoliated under nitrogen (and not vacuum) which could explain the slightly increased disorder at the interface when compared to TaTe<sub>2</sub> (see Chapter 5). This is likely due to mild oxygen exposure at the interface, which is not present in our vacuum exfoliated devices. Beyond the damage in the first two layers, the quality of underlying WTe<sub>2</sub> film is notable. Imaging courtesy of Ismail El Baggari.

( $\tau_{\perp}$ ) torque amplitudes defined in Fig. 2.1b contribute to the symmetric and antisymmetric parts of the lineshape, respectively. This allows determination of the torque components by fitting  $V_{\text{mix}}$  as a function of applied magnetic field to a sum of symmetric and antisymmetric Lorentzians (see Section 2.8.2). The amplitudes of the Lorentzians are related to the two components of torque by:

$$V_S = -\frac{I_{\text{RF}} dR}{2} \frac{d\phi}{d\phi} \frac{1}{\alpha_G \gamma (2B_0 + \mu_0 M_{\text{eff}})} \tau_{\parallel} \quad (2.1)$$

$$V_A = -\frac{I_{\text{RF}} dR}{2} \frac{d\phi}{d\phi} \frac{\sqrt{1 + \mu_0 M_{\text{eff}}/B_0}}{\alpha_G \gamma (2B_0 + \mu_0 M_{\text{eff}})} \tau_{\perp}, \quad (2.2)$$

where  $R$  is the device resistance,  $\phi$  is the angular orientation of the magnetization relative to the direction of applied current in the sample,  $dR/d\phi$  is due to the AMR in the Py,  $\mu_0 M_{\text{eff}}$  is the out-of-plane demagnetization field,  $B_0$  is the resonance field,  $I_{\text{RF}}$  is the microwave current in the bilayer,  $\alpha_G$  is the Gilbert damping coefficient and  $\gamma$  is the gyromagnetic ratio. In our devices,  $\mu_0 M_{\text{eff}} = 0.7$  Tesla and  $\alpha_G = 0.011$  as determined by the ST-FMR resonance frequency and linewidth, respectively, and  $R(\phi)$  is measured directly by rotating the magnetic field using a projected-field apparatus.

## 2.4 ST-FMR Dependence on Applied In-Plane Field Angle

During a ST-FMR measurement, the applied magnetic field fixes the average angle of the magnetization at a given value,  $\phi$ . The strengths of the current-induced torques for different angles of the magnetization are related to the symmetries of the device. For example, in a Pt/Py structure, the two-fold rotational symmetry requires that the S-O torque change sign when the magnetization is rotated in-plane by  $180^\circ$ , correspondingly changing the sign of  $V_{\text{mix}}$  but maintaining the same magnitude. This is illustrated in Fig. 2.1d where we plot ST-FMR traces for a Pt(6 nm)/Py(6 nm) bilayer at  $\phi = 40^\circ$  and  $220^\circ$ , showing nearly identical lineshapes after multiplying the  $\phi = 220^\circ$  trace by -1.

Figure 2.1e shows the results of the same experiment carried out on a WTe<sub>2</sub>/Py bilayer with the current applied along the low-symmetry crystal axis of WTe<sub>2</sub>, parallel to the  $a$ -axis (Device 1). In this case, we find that  $V_{\text{mix}}(40^\circ)$  and  $-V_{\text{mix}}(220^\circ)$  differ significantly in both amplitude and shape, indicating that the current-induced torques in the two cases differ in both magnitude and direction.

This observation is incompatible with two-fold rotational symmetry, indicating that the current-induced torques are affected by the reduced symmetry of the  $\text{WTe}_2$  surface.

To analyze this result in more detail, we consider the full angular dependence of the ST-FMR signal as an external magnetic field is used to rotate the direction of the magnetization within the sample plane. In a simple heavy metal/ferromagnet bilayer with no broken lateral symmetries, the current-induced torque amplitudes (due to the spin Hall effect, the Rashba-Edelstein effect, or the Oersted field) have a  $\cos \phi$  dependence [7, 15]. The AMR in Permalloy has an angular dependence that scales as  $\cos^2 \phi$ , which enters  $V_{\text{mix}}$  as  $dR/d\phi \propto \sin 2\phi$ . The product of these two contributions then yields the same angular dependence for the symmetric and antisymmetric ST-FMR components:  $V_S = S \cos \phi \sin 2\phi$  and  $V_A = A \cos \phi \sin 2\phi$ . Our Pt/Py control samples are well described by this behavior (Fig. 2.5a; the parameter  $\phi_0$  accounts for any misalignment between the sample and the electro-magnet, and is typically  $< 5^\circ$ ).

For our  $\text{WTe}_2$ /Permalloy samples with current along the  $a$ -axis, the symmetric component of the ST-FMR signal also has this form (Fig. 2.5b top panel). The non-zero symmetric component indicates that S-O torques are present in the  $\text{WTe}_2$ /Permalloy bilayer, since the symmetric component corresponds to an in-plane torque and cannot be generated by an Oersted field. However, the more striking result is that the angular dependence of the antisymmetric component is very different from  $\cos \phi \sin 2\phi$  (Fig. 2.5b bottom panel). The variations in the absolute values of signal amplitudes reflect the broken symmetries of the  $\text{WTe}_2$  surface: the absence of mirror symmetry in the  $ac$  plane (corresponding to  $\phi \rightarrow 180^\circ - \phi$ , since  $\hat{m}$  is a pseudovector) and the absence of twofold rotational

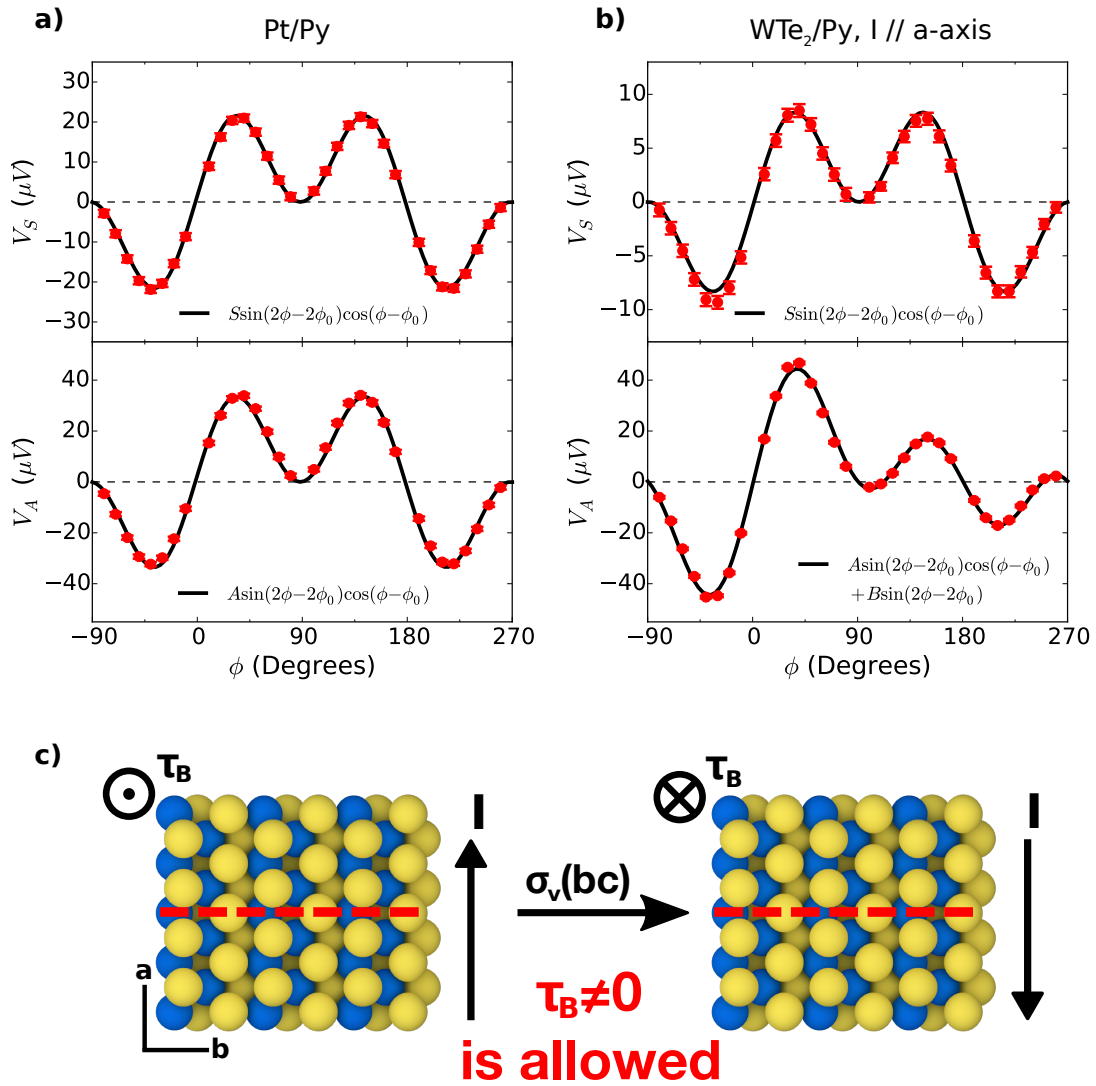


Figure 2.5: **a)** Symmetric and antisymmetric ST-FMR resonance components for a Pt(6 nm)/Py (6 nm) control sample as a function of in-plane magnetic-field angle. The microwave frequency is 9 GHz and the applied microwave power is 0 dBm. The parameter  $\phi_0$  accounts for any misalignment between the sample and the magnet. **b)** Symmetric and antisymmetric ST-FMR resonance components for a WTe<sub>2</sub>(5.5 nm)/Py (6 nm) device (Device 1) as a function of in-plane magnetic-field angle, with current applied parallel to the  $a$ -axis. The microwave frequency is 9 GHz and the applied microwave power is 5 dBm. The error bars in **a** and **b** represent the estimated standard deviations from the least-squares fitting procedure used to determine  $V_A$  and  $V_S$ . **c)** Illustration that a magnetization-independent, linear-in-current out-of-plane S-O torque is allowed by symmetry for current applied along the  $a$ -axis of a WTe<sub>2</sub>/Py bilayer.

symmetry about the  $c$ -axis ( $\phi \rightarrow 180^\circ + \phi$ ). This result indicates the existence of a source of out-of-plane torque not previously observed in any S-O torque experiment.

The unusual angular dependence we measure for the antisymmetric ST-FMR signal with current applied along the  $a$ -axis can be well fit by the simple addition of a term proportional to  $\sin 2\phi$ :

$$V_A = A \cos \phi \sin 2\phi + B \sin 2\phi \quad (2.3)$$

where  $A$  and  $B$  are constants independent of the field angle (see the solid line in Fig. 2.5 bottom panel). To quantitatively translate the measured angular dependence of  $V_S$  and  $V_A$  to torques, we can use Eqs. 2.1 and 2.2 to remove the contribution from the angular dependence of the AMR. The fits in Fig. 2.5b then correspond to angular dependences for the in-plane and perpendicular torque amplitudes of the form

$$\tau_{\parallel}(\phi) = \tau_S \cos(\phi) \quad (2.4)$$

$$\tau_{\perp}(\phi) = \tau_A \cos(\phi) + \tau_B \quad (2.5)$$

where  $\tau_S$ ,  $\tau_A$ , and  $\tau_B$  are independent of  $\phi$ . The terms proportional to  $\cos \phi$  are the usual terms observed previously, and in the Pt/Py control samples. The new term ( $\tau_B$ ) corresponds to an out-of-plane torque that is independent of the in-plane magnetization orientation; i.e., it is even in  $\hat{m}$  and therefore an antidamping-like torque. It is consistent with predictions [36] that broken lateral mirror symmetry can allow an out-of-plane torque of the form  $\tau_{AD} \propto \hat{m} \times (\hat{m} \times \hat{c})$ . That an out-of-plane antidamping-like torque with the form of  $\tau_B$  could exist has also been discussed in an analysis of the allowed symmetries for S-O torques in GaMnAs/Fe samples [25], but this torque has not previously been identified in experiment.

In commonly studied bilayer systems without any broken in-plane symmetries, a linear-in-current out-of-plane torque that is independent of the in-plane magnetization angle cannot exist by symmetry. For example, the presence of a twofold rotation disallows  $\tau_B$ . In samples with twofold rotational symmetry, rotating the sample by  $180^\circ$  is equivalent to changing the sign of an in-plane current without changing the sign of  $\tau_B$ , which violates the linear-in-current requirement. However,  $WTe_2/Py$  bilayers do not have two-fold rotational symmetry. The only symmetry in our  $WTe_2/Py$  bilayers is the  $bc$  plane mirror,  $\sigma_v(bc)$ . The effect of  $\sigma_v(bc)$  on a  $WTe_2/Py$  bilayer with current flowing along the  $a$ -axis is illustrated in Fig. 2.5c. Both the out-of-plane torque (a pseudovector) and the current change sign under  $\sigma_v(bc)$ ,  $\tau_B \rightarrow -\tau_B$  and  $I \rightarrow -I$ , which is the expected behavior for a current-generated S-O torque: the sign of torque must change with the sign of the current. A torque with the symmetry of  $\tau_B$  is therefore allowed for  $WTe_2/Py$  bilayers with current along the  $a$ -axis.

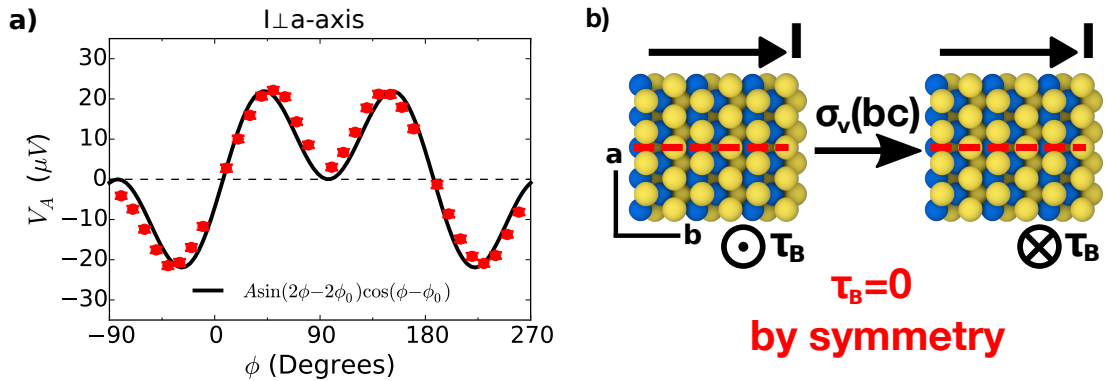


Figure 2.6: **a)** Antisymmetric ST-FMR resonance component for a  $WTe_2(15\text{ nm})/Py(6\text{ nm})$  device (Device 2) as a function of in-plane magnetic-field angle, with current applied parallel to the  $b$ -axis. The microwave frequency is 9 GHz and the applied microwave power is 5 dBm. The error bars in **a)** represent the estimated standard deviations from the least-squares fitting procedure used to determine  $V_A$ . **b)** Illustration that a magnetization-independent, linear-in-current out-of-plane S-O torque is forbidden by symmetry for current applied along the  $b$ -axis.

## 2.5 Dependence of the Torques on the WTe<sub>2</sub> Crystal Axis

We observe that  $\tau_B$  goes to zero when the current is applied parallel to the  $b$ -axis of WTe<sub>2</sub>. Figure 2.6a shows the antisymmetric ST-FMR component  $V_A$  (red circles) as a function of  $\phi$  for Device 2, in which the current is applied along the  $b$ -axis. The angular fit to Eq. 2.3 yields a value of  $B$  equal to 0 within experimental uncertainty. This result is again consistent with the symmetries of the WTe<sub>2</sub> surface layer. When the mirror symmetry operation  $\sigma_v(bc)$  is applied in this case (Fig. 2.6b), the out-of-plane torque is inverted but the current is not, and therefore  $\tau_B$  is forbidden by symmetry. Higher-order angular terms are symmetry-allowed for current along the  $b$ -axis, and can be included in fits of  $V_A$  versus  $\phi$  to improve the quantitative agreement (Section 2.8.7). We also continue to observe a nonzero symmetric ST-FMR signal when the current is aligned with the  $b$ -axis, which has the same functional form as the symmetric ST-FMR signal in the devices with current along the  $a$ -axis (Section 2.8.4).

We further investigated the symmetry dependence of  $\tau_B$  by studying devices with different angles,  $\phi_{a-I}$ , between the  $a$ -axis of the WTe<sub>2</sub> and the applied current direction. We fabricated 26 devices with different  $\phi_{a-I}$  and performed full angle-dependent ST-FMR measurements on each in order to extract  $A$ ,  $B$  and  $S$  (see Table 2.1). Figure 2.7a shows the ratio of  $\tau_B/\tau_A$  at a given frequency ( $f = 9$  GHz) as a function of  $\phi_{a-I}$  for the first 15 of these devices (those for which the crystalline axes were identified via Raman spectroscopy). We consistently see that the ratio of  $\tau_B/\tau_A$  is large when current is aligned with the  $a$ -axis, and is gradually quenched as the projection of the current along the  $b$ -axis grows. This provides strong additional evidence that the observed magnetization-independent out-of-plane torque is correlated with the symme-

tries present in the  $\text{WTe}_2$  crystal.

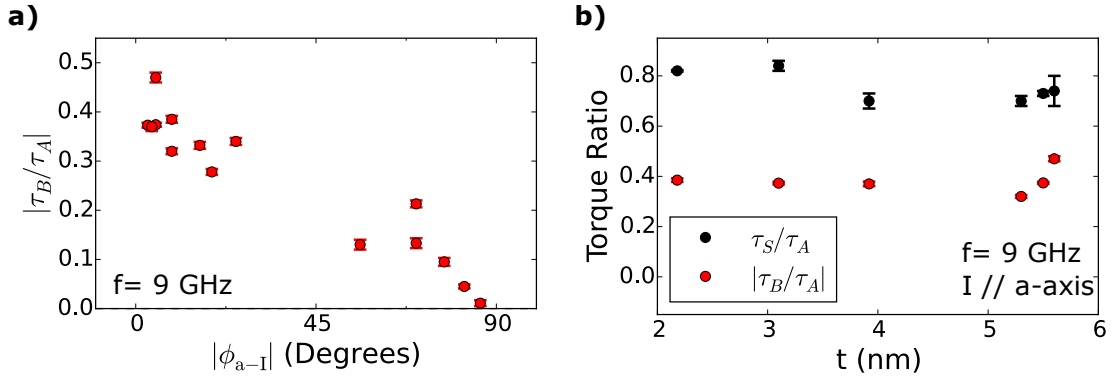


Figure 2.7: **a)** Ratio of the out-of-plane antidamping torque  $\tau_B$  to the out-of-plane effective-field torque  $\tau_A$  as a function of the angle between the  $a$ -axis and the applied current. **b)** Torque ratios as a function of the thickness of the  $\text{WTe}_2$  layer for current applied along the  $a$ -axis. Here  $\tau_S$  is the in-plane current-induced torque. The error bars in **a)** and **b)** represent estimated standard deviations calculated via error propagation from the least-squares fitting procedure used to determine  $\tau_A$ ,  $\tau_B$ , and  $\tau_S$ .

The dependence of the measured torques on  $\text{WTe}_2$  thickness provides insight into the mechanism of torque generation. If the torques arise through bulk mechanisms, clear thickness dependences should be expected; however, if the torques are generated by interface effects they should not depend on  $\text{WTe}_2$  thickness. Figure 2.7b shows the dependence of the torque ratios  $\tau_B/\tau_A$  and  $\tau_S/\tau_A$  on  $\text{WTe}_2$  thickness for devices that have current along the  $a$ -axis and are exfoliated in flowing nitrogen. (The individual dependences of  $\tau_A$ ,  $\tau_B$ , and  $\tau_S$  on  $\text{WTe}_2$  thickness and on the angle of the current relative to the  $a$ -axis are plotted in Section 2.8.4.) While neither  $\tau_B/\tau_A$  nor  $\tau_S/\tau_A$  show any significant dependence on  $\text{WTe}_2$  thickness in these devices, in a later study with vacuum exfoliated devices and a much larger data set (Chapter 3) we found that  $\tau_A$  has a strong thickness dependence due to the Oersted torque, though  $\tau_B$  and  $\tau_S$  remain relatively independent of thickness.

A bulk contribution to  $\tau_B$  is forbidden by the screw symmetry of the  $\text{WTe}_2$  crystal structure. The bulk  $\text{WTe}_2$  structure is mapped onto itself if it is rotated by  $180^\circ$  about an axis normal to the layers ( $c$ -axis) and translated by half a unit cell along both the  $c$  and  $a$ -axis (in the  $c$  direction, half a unit cell is one layer spacing). A bulk contribution to  $\tau_B$  would be left unaltered by this operation, while the direction of an in-plane charge current is reversed. This implies that there can be no net bulk contribution to that is linear in the applied in-plane current (see also Section 2.8.8). We have verified the surface origin of  $\tau_B$  experimentally using a sample containing a single-layer step; the strength of is suppressed because contributions from two surfaces with opposite symmetry largely cancel (Section 2.8.8). The symmetry constraints on  $\tau_B$ , together with the lack of dependence on  $\text{WTe}_2$  thickness for  $\tau_B$  and  $\tau_S$  (see Chapter 3), suggests that  $\tau_B$  and  $\tau_S$  arise from interfacial effects in the  $\text{WTe}_2/\text{Py}$  bilayer.

The strength of the individual components of torque can be determined quantitatively from Eqs. 2.1 and 2.2, using independently-measured values of the resistance as a function of magnetization angle ( $dR/d\phi$ ) and the transmitted and reflected microwave power ( $S_{21}$  and  $S_{11}$ ) in order to determine  $I_{\text{RF}}$  (Section 2.8.2). We will express these strengths as torque conductivities ( $\sigma_S, \sigma_A, \sigma_B$ ; torques per unit area per unit electric field) because the electric field applied across the device can be determined accurately, while the division of current density flowing in the different layers has larger uncertainties. We find for current along the  $a$ -axis that  $\sigma_S = (8 \pm 2) \times 10^3 (\hbar/2e)(\Omega\text{m})^{-1}$ ,  $\sigma_A = (9 \pm 3) \times 10^3 (\hbar/2e)(\Omega\text{m})^{-1}$ , and  $\sigma_B = (3.6 \pm 0.8) \times 10^3 (\hbar/2e)(\Omega\text{m})^{-1}$ , where the uncertainties give the standard deviation across our devices.

We find it interesting that although a broken lateral mirror symmetry should

also allow additional terms for the in-plane S-O torque when current is applied along the  $a$ -axis, for example an effective-field torque of the form  $\hat{m} \times \hat{c}$ , we detect no such contributions. A term  $\propto \hat{m} \times \hat{c}$  would add a  $\phi$ -independent contribution to Eq. 2.4,  $\tau_{\parallel}(\phi) \rightarrow \tau_S \cos \phi + \tau_T$  that would cause the absolute values of the amplitudes for the symmetric part of the ST-FMR resonance (Fig. 2.5b, upper panel) to be asymmetric under the operations  $\phi \rightarrow 180^\circ + \phi$  and  $\phi \rightarrow 180^\circ - \phi$ . We can set a limit for our devices that  $|\tau_T| < 0.05\tau_S$ . Our results are therefore opposite a report about S-O torques in “wedge,” [36] samples, which claimed that the breaking of lateral mirror symmetry by the wedge structure generated an effective field torque, but no out-of-plane antidamping torque. We question whether the extremely small thickness gradient in Ref. [36] (a difference in average thickness of  $\leq 0.5$  picometers, or 0.002 of an atom, between the two sides of a 20- $\mu\text{m}$ -wide sample) actually provides a meaningful breaking of structural mirror symmetry.

## 2.6 Magnetic anisotropy of WTe<sub>2</sub>/Py bilayers

We note one additional consequence of strong S-O coupling at the WTe<sub>2</sub>/Py interface – the magnetic anisotropy easy axis of the Py is determined by the crystal lattice of the WTe<sub>2</sub>. The magnetic anisotropy can be determined from our ST-FMR data via the  $\phi$  dependence of the magnetic resonance frequency and by direct AMR measurements (Sections 2.8.2 and 2.8.3). Regardless of the orientation of the sample channel with respect to the WTe<sub>2</sub> crystal lattice, we find that the magnetic easy axis is always parallel to the  $b$ -axis of WTe<sub>2</sub>. The effective anisotropy field in different devices ranges from 4.9 to 17.3 mT for 6 nm of Py (Table 2.1).

## 2.7 Conclusion

In summary, we have demonstrated that it is possible to generate an out-of-plane antidamping-like S-O torque in spin-source/ferromagnet bilayers by using a spin-source material whose surface crystal structure has a broken lateral mirror symmetry. This is important as it provides a strategy for achieving efficient manipulation of magnetic devices with perpendicular magnetic anisotropy. Compared to in-plane-magnetized devices, PMA devices are of interest because they can be scaled to smaller sizes and higher density while maintaining thermal stability. PMA devices can be switched much more efficiently using an out-of-plane antidamping torque,  $\tau_{AD}$ , compared to an effective field torque,  $\tau_{FL}$ , since the effective field torque required for switching in the macrospin limit is  $\tau_{FL} \approx \gamma H_{an}$ , where  $H_{an}$  is the anisotropy field, while the antidamping torque required is much smaller:  $\tau_{AD} \approx \alpha_G \gamma H_{an}$ , with  $\alpha_G \approx 0.01$  (Ref. [19]). Previously, because S-O torques could generate an antidamping-like component only in the sample plane, they have been incapable of switching PMA devices by this efficient antidamping process[37–42] – an in-plane anti-damping torque switches PMA devices through a mechanism involving domain nucleation and domain-wall propagation that becomes inefficient at small size scales [3]. Our results therefore suggest a strategy, based on control of broken crystal symmetry in materials with strong S-O coupling, that has the potential to enable efficient antidamping switching of PMA memory and logic devices at the 10’s of nm size scale.

Acknowledgments: We thank N. D. Reynolds for experimental assistance, R. De Alba for help with the graphics, and G. D. Fuchs and P. G. Gowtham for comments on the manuscript. This work was supported by the National

Science Foundation (DMR-1406333) and the Army Research Office (W911NF-15-1-0447). G.M.S. acknowledges support by a National Science Foundation Graduate Research Fellowship under Grant No. DGE-1144153. M.H.D.G. acknowledges support by the Netherlands Organization for Scientific Research (NWO 680-50-1311) and the Kavli Institute at Cornell for Nanoscale Science. This work made use of the NSF-supported Cornell Nanoscale Facility (ECCS-1542081), the Cornell Center for Materials Research Shared Facilities, which are supported through the NSF MRSEC Program (DMR-1120296), and the NSF-supported Platform for the Accelerated Realization, Analysis, and Discovery of Interface Materials (PARADIM) (DMR-1539918).

## **2.8 Supplemental information**

### **2.8.1 Comparison of mechanisms for current-induced switching of magnetic layers with perpendicular magnetic anisotropy (PMA)**

In principle, spin-orbit torques with three different symmetries can drive switching of PMA magnetic layers, each associated with different reversal mechanisms and yielding different values for the critical torque required for switching. [Note that in this discussion we will consider all torques per unit magnetization, so that  $\tau$  has the same units as  $d\hat{m}/dt$ , where  $\hat{m}$  is the magnetic orientation.] (i) If the current can produce an effective field in the vertical ( $\hat{z}$ ) direction, yielding a torque of the form  $\tau_{\text{FL}} = -\gamma H_{\text{FL}}(\hat{m} \times \hat{z})$ , then in a macrospin

approximation switching will occur at a critical value  $H_{FL} = H_{an}$ , where  $H_{an}$  is the perpendicular anisotropy field. (ii) If the current produces an in-plane antidamping torque of the form  $\tau_{AD,\parallel} = \gamma\tau_{AD,\parallel}^0 \hat{m} \times (\hat{m} \times \hat{y})$ , then deterministic switching can be achieved if there is also a symmetry-breaking effective field with a component along the current direction [8, 43], but the switching mechanism in this case is not actually based on a change in the magnetic layer's effective damping because the antidamping torque is perpendicular to the magnetization. The torque in this case must still overcome the anisotropy field, so that the critical value of the torque in the macrospin limit is  $\tau_{AD,\parallel}^0 \approx \gamma H_{an}/2$  (Refs. [43, 44]). In samples larger than a few tens of nm diameter, an in-plane antidamping torque can, alternatively, drive a more efficient non-macrospin reversal process involving current-generated domain wall motion [38], but measurements indicate that this becomes ineffective for the highly-scaled PMA devices that are desired for applications [3]. (iii) If the current produces an out-of-plane antidamping torque of the form  $\tau_{AD,\perp} = \gamma\tau_{AD,\perp}^0 \hat{m} \times (\hat{m} \times \hat{z})$ , then in this case the direction of the torque is parallel to the magnetization so that it does have the ability to change the effective damping of the magnetic layer. Switching occurs when the effective damping is driven negative, resulting in a critical value of torque  $\tau_{AD,\perp}^0 = \gamma\alpha_G H_{an}$  [18, 19]. Because the Gilbert damping is typically on the order of 0.01, an out-of-plane antidamping component has the ability to drive switching of PMA magnetic devices at much lower values of torque than the other two mechanisms, for sample sizes smaller than a few 10's of nm.

## 2.8.2 Analysis of ST-FMR measurements

We model the ST-FMR measurements by using the Landau-Lifshitz-Gilbert-Slonczewski (LLGS) equation to calculate the precessional dynamics of the magnetization direction,  $\hat{m}(t)$ , in the macrospin approximation in response to the in-plane and out-of-plane torque amplitudes,  $\tau_{\parallel}$  and  $\tau_{\perp}$  [7, 18]. This determines the ST-FMR mixing voltage as

$$V_{\text{mix}} = \langle I(t)R[m(t)] \rangle_t = V_S \frac{\Delta^2}{(B_{\text{app}} - B_0)^2 + \Delta^2} + V_A \frac{\Delta(B_{\text{app}} - B_0)}{(B_{\text{app}} - B_0)^2 + \Delta^2} \quad (2.6)$$

where  $B_{\text{app}}$  is the applied magnetic field and  $\Delta$  is the linewidth. The  $\hat{m}(t)$  dependence of the device resistance arises from the anisotropic magnetoresistance (AMR) of the ferromagnet Permalloy. We determine the symmetric and anti-symmetric amplitudes,  $V_S$  and  $V_A$ , by fitting Eq. to measurements of the mixing voltage as a function of applied magnetic field. These amplitudes are related to the torque amplitudes  $\tau_{\parallel}$  and  $\tau_{\perp}$  by Eqs. 2.1 and 2.2. We note  $\tau_{\parallel}$  and  $\tau_{\perp}$  are normalized by the total angular momentum of the magnet, and so have dimensions of frequency. We determine torque ratios from the ratio of Eqs. 2.1 and 2.2 together with measured values for  $B_0$  and  $M_{\text{eff}}$ . We obtain the value of  $B_0$  via fits of the resonance lineshape, and we estimate  $M_{\text{eff}}$  from the frequency dependence of  $B_0$  using the Kittel formula  $2\pi f = \gamma \sqrt{B_0(B_0 + \mu_0 M_{\text{eff}})}$ . As we discuss in Section 2.8.3,  $B_0$  and  $M_{\text{eff}}$  depend on  $\phi$  due to the in-plane magnetic anisotropy of our samples. For our analysis we use angle-averaged values for these quantities; the error in doing so is less than 5% due to the small degree of angular variation.

To obtain quantitative measurements of the individual torque components using Eq. 2.1 or Eq. 2.2 (i.e. not just their ratios), it is also necessary to determine  $\alpha_G$ ,  $R(\phi)$ , and  $I_{\text{RF}}$ . The Gilbert damping is estimated from the frequency dependence of the linewidth via  $\Delta = 2\pi f \alpha_G / \gamma + \Delta_0$ , where  $\Delta_0$  is the inhomoge-

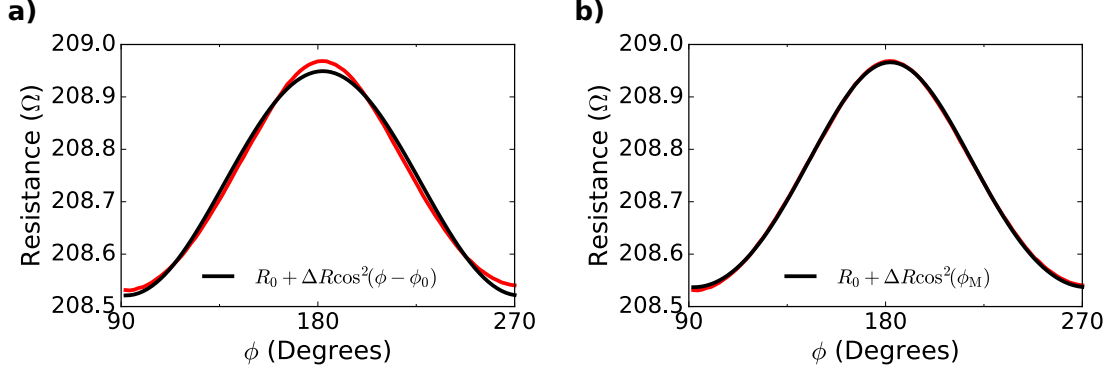


Figure 2.8: **a)** Resistance of Device 1 (red) as a function of the in-plane applied magnetic field angle. Measurements are made in a Wheatstone bridge configuration with a static magnetic field of 0.08 T. The fit (black) is used to extract  $dR/d\phi$ . **b)** Resistance of Device 1 (red) as a function of applied in-plane magnetic field angle. The fit here (black) takes into account the in-plane magnetic anisotropy via  $\phi_M = \phi - \phi_0 + \frac{H_A}{2H} \sin 2(\phi - \phi_0)$  corresponding to an easy-axis perpendicular to the current flow direction (along the  $WTe_2$   $b$ -axis). The fit gives  $H_A = 120 \pm 20$  Oe. We have not accounted for the non-saturated nature of  $R(\phi)$  in our ST-FMR measurements.

neous broadening. To obtain the AMR we measure the device resistance as a function of a rotating in-plane magnetic field (with magnitude 0.08 T) applied via a projected-field magnet. Fitting these data to  $R_0 + \Delta R \cos^2(\phi - \phi_0)$  allows calculation of  $dR/d\phi$  (Fig. 2.8). To measure the RF current, we use a vector network analyzer to estimate the reflection coefficients of our devices ( $S_{11}$ ) and the transmission coefficient of our RF circuit ( $S_{21}$ ). These calibrations allow calculation of the RF current flowing in the device as a function of applied microwave power and frequency:

$$I_{\text{RF}} = 2 \sqrt{1\text{mW} \cdot 10^{\frac{P_{\text{source}}(\text{dBm}) + S_{21}(\text{dBm})}{10}} (1 - |\Gamma|)^2 / 50\Omega} \quad (2.7)$$

where  $P_{\text{source}}$  is the power sourced by the microwave generator and  $\Gamma = 10^{S_{11}(\text{dBm})/20}$ .

The torque conductivity, defined as the angular momentum absorbed by the

magnet per second per unit interface area per unit electric field, provides an absolute measure of the torques produced in a spin source/ferromagnet bilayer independent of geometric factors. For a torque  $\tau_K$  (where  $K = A, B, S, \text{ or } T$ ) we calculate the corresponding torque conductivity via

$$\sigma_K = \frac{M_s l w t_{\text{magnet}}}{\gamma} \frac{\tau_K}{(l w) E} = \frac{M_s l t_{\text{magnet}}}{\gamma} \frac{\tau_K (1 - \Gamma)}{(1 + \Gamma) I_{\text{RF}} \cdot 50 \Omega} \quad (2.8)$$

where  $M_s$  is the saturation magnetization,  $E$  is the electric field,  $l$  and  $w$  are the length and width of the WTe<sub>2</sub>/Permalloy bilayer, and  $t_{\text{magnet}}$  is the thickness of the Permalloy. The factor  $M_s l w t_{\text{magnet}} / \gamma$  is the total angular momentum of the magnet, which converts the normalized torque into units of angular momentum per second. Due to the unavailability of mm-scale WTe<sub>2</sub>/Permalloy bilayers, we are unable to measure  $M_s$  directly via magnetometry, and instead approximate  $M_s \approx M_{\text{eff}}$ , which we have found to be accurate in other Permalloy bilayer systems [7].

### 2.8.3 Determination of the in-plane magnetic anisotropy

Figure 2.9 shows the magnetic field at ferromagnetic resonance as a function of the in-plane magnetization angle for Devices 1 and 2. For Device 1 the current flows nearly parallel to the  $a$ -axis ( $\phi_{a-I} = -3^\circ$ ), and for Device 2 it is nearly parallel to the  $b$ -axis ( $\phi_{a-I} = 86^\circ$ ). The data from both samples indicate the presence of a uniaxial magnetic anisotropy within the sample plane, with an easy axis along the  $b$ -axis of the WTe<sub>2</sub>. The angular dependence of the resonance field is described well by the form

$$B_0 = B_{\text{Kittel}} - B_A \cos(2\phi - 2\phi_{\text{Easy-I}} - 2\phi_0) \quad (2.9)$$

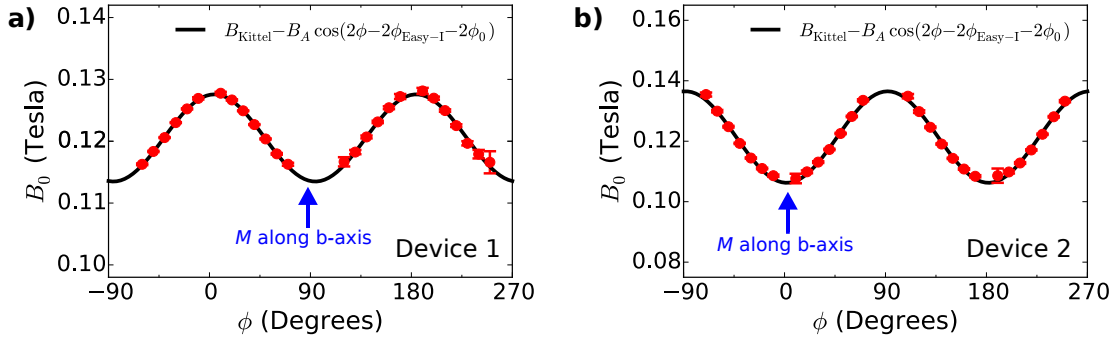


Figure 2.9: Ferromagnetic resonance field as a function of the in-plane magnetization angle for **a)** Device 1 and **b)** Device 2. The data are represented by red circles and the black lines are the indicated fits. In both cases the applied microwave frequency is 9 GHz and the power is 5 dBm. The blue arrows indicates the values of  $\phi$  for which the magnetization lies along the  $b$ -axis. Error bars represent estimated standard deviations from the least-squares fitting procedure.

where  $B_A$  is the in-plane anisotropy field, related to the anisotropy energy  $K_A$  via  $B_A = 2\mu_0 K_A / M_s$ ,  $B_{\text{Kittel}}$  is the resonance field without any in-plane anisotropy,  $\phi_{\text{Easy-I}}$  is the angle from the current direction to the magnetic easy-axis and  $\phi_0$  is the angular misalignment extracted from the angular dependence of the mixing voltage. This equation also assumes  $B_A, B_{\text{Kittel}} \ll \mu_0 M_{\text{eff}}$  which are valid approximations for our experiment. We find values for  $B_A$  of 7 mT and 15 mT for Device 1 and Device 2, respectively. We observe no unidirectional component to the magnetic anisotropy.

We performed similar fits for all of the devices listed in Table 2.1. In all cases the magnetic easy axis was along the  $b$ -axis within experimental uncertainty; i.e.  $\phi_{a-I} = \phi_{\text{Easy-I}} + 90^\circ$ . Over all of our devices we find  $B_A$  to be in the range 2.4-17.3 mT. Some, but likely not all, of the device-to-device variation may be explained by differences in the sample shape and exfoliation environment.

To check that the Permalloy has a magnetic anisotropy that is entirely in the

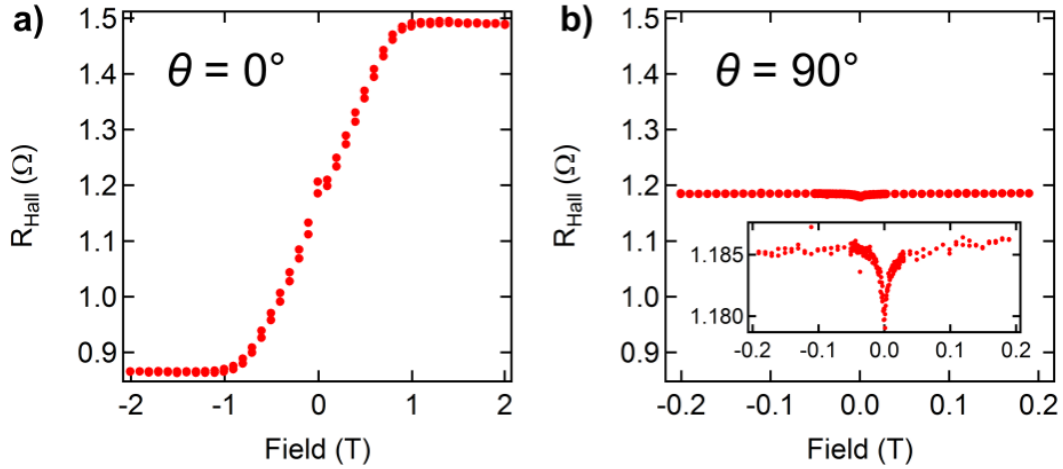


Figure 2.10: Measurements of transverse resistance,  $R_{\text{Hall}}$ , for a  $\text{WTe}_2/\text{Py}(6 \text{ nm})$  Hall bar with the magnetic field oriented perpendicular to the sample plane (a) and parallel to the  $\text{WTe}_2$   $b$ -axis in the sample plane (b) with current directed along the  $\text{WTe}_2$   $a$ -axis. The contribution of the ordinary Hall effect in a has been subtracted. The peak-to-peak anomalous Hall effect contribution to  $R_{\text{Hall}}$ ,  $R_{\text{AHE}}$ , is  $0.62 \Omega$ , as extracted from a. The inset to b shows  $R_{\text{Hall}}$  versus the applied field along the  $b$ -axis with an expanded vertical scale. The small variation ( $0.007 \Omega$ ) in b is consistent with a planar Hall effect.

sample plane we fabricated a  $\text{WTe}_2/\text{Py}$  bilayer Hall bar using the same sample fabrication techniques and Py thickness as our ST-FMR devices. The Hall bar is oriented with the current along the  $\text{WTe}_2$   $a$ -axis ( $\phi_{a-I} = -1^\circ$ ), with a length and width of  $26 \mu\text{m}$  and  $4 \mu\text{m}$  respectively. Hall measurements with the magnetic field applied perpendicular to the sample plane are shown in and in Fig. 2.10a and Hall measurements with the field parallel to the  $\text{WTe}_2$   $b$ -axis (the in-plane magnetic easy axis) are shown in Fig. 2.10b. In Fig. 2.10a, the contribution of the ordinary Hall effect has been removed by subtraction of the linear portion of the curve at large fields. Saturation of the Py moment is achieved in out-of-plane fields above 0.9 T and the extracted peak-to-peak value of the anomalous Hall contribution,  $R_{\text{AHE}}$ , is  $0.62 \Omega$ . If there were any tilting of the anisotropy axis out-of-plane, this should give an antisymmetric signal in the  $b$ -axis scan about

zero field. Instead, we observe only a very small, approximately-symmetric Hall signal in Fig. 2.10b ( $\approx 1\%$  of the saturated anomalous Hall signal). The small signal that we see has an angular dependence (not shown) consistent with a planar Hall effect, and not an out-of-plane tilt. These results show that the overall magnetic anisotropy is in-plane, without any significant out-of-plane tilt of the equilibrium magnetization direction.

## 2.8.4 Data from additional devices

Device Name	Device Number	$t$ (nm) $\pm 0.3$ nm	$L \times W$ ( $\mu\text{m}$ ) $\pm 0.2$ $\mu\text{m}$	$\tau_B/\tau_A$	$\tau_S/\tau_A$	$B_A$ (0.1 mT)	$\phi_{\text{Easy-I}} + 90^\circ$	$\phi_{a-I}$ $\pm 2^\circ$
B11D5	1	5.5	$4.8 \times 4$	0.373(4)	0.72(1)	70.1(7)	3.4(3)	-5
B13D2	2	15.0	$6 \times 4$	0.011(7)	0.77(3)	151(2)	84.9(6)	86
B11D3	3	3.1	$3.5 \times 4$	-0.372(6)	0.84(2)	62(4)	4.2(9)	-3
B12D1	4	5.6	$4 \times 4$	-0.47(1)	0.74(6)	49(12)	2(3)	-5
B13D1	5	8.2	$6 \times 4$	0.133(8)	0.99(3)	150(1)	74.7(5)	70
B13D3	6	3.9	$6 \times 4$	0.372(9)	0.70(3)	98(2)	2.7(7)	-4
B14D3	7	3.4	$4 \times 3$	0.207(8)	1.20(3)	153(1)	75.1(4)	70
B14D4	8	2.2	$4 \times 3$	0.385(7)	0.83(3)	74(1)	-0.3(5)	-9
B16D6	9	6.7	$5 \times 4$	0.278(6)	0.70(2)	173(1)	24.7(5)	19
B14D2	10	2.8	$4 \times 3$	0.095(8)	1.42(3)	116(2)	80.2(4)	77
B16D7	11	14.0	$5 \times 4$	-0.13(1)	0.72(4)	138(2)	-58(1)	-56
B16D8	12	5.3	$5 \times 4$	-0.320(6)	0.70(2)	156(3)	-6.0(3)	-9
B16D10	13	1.8	$5 \times 4$	-0.045(4)	0.79(2)	172(2)	83.4(4)	82
B16D4	14	5.3	$5 \times 4$	0.340(7)	0.78(3)	140(1)	-20.9(5)	-25
B16D5	15	5.5	$5 \times 4$	0.332(7)	0.74(2)	155(1)	-14.8(5)	-16
B16D12	16	3.4	$5 \times 4$	0.236(8)	1.35(3)	132(1)	-60.6(4)	-
B17D8	17	2.6	$5 \times 4$	0.020(8)	1.50(4)	20(2)	88(2)	-
B17D5	18	5.0	$5 \times 4$	-0.451(7)	0.83(2)	20(3)	-16(3)	-
B18D1	19	15.0 (S)	$5 \times 4$	-0.080(6)	0.35(2)	40(2)	6(1)	-1.6
B18D3	20	2.0	$5 \times 4$	0.74(2)	1.27(5)	31(2)	2.7(9)	-
B18D6	21	5.4 (S)	$4 \times 3$	0.033(5)	0.64(2)	38(1)	-1.8(6)	3.7
B18D7	22	6.9	$5 \times 4$	-0.331(6)	0.59(2)	33(2)	-2(1)	-
B18D11	23	9.0	$5 \times 4$	-0.287(7)	0.49(3)	32(3)	5(1)	-
B18D13	24	0.6	$5 \times 4$	-0.60(2)	1.46(6)	24(6)	5(4)	-
B19D6	25	6.9 (S)	$4 \times 3$	-0.240(6)	0.44(3)	44(2)	2.2(0.7)	-
B19D7	26	6.8 (S)	$5 \times 4$	-0.008(7)	0.51(3)	40(2)	2(1)	-
Pt/Py	Pt/Py	6	$10 \times 5$	0.000(4)	1.79(2)	42(2)	85.5(8)	-

Table 2.1: Comparison of device parameters, torque ratios, and magnetic anisotropy parameters for  $\text{WTe}_2/\text{Py}$  bilayers discussed in the main text and a Pt/Py control device. Here  $\phi_{\text{Easy-I}}$  is the angle of the magnetic easy-axis with respect to the current flow direction, and  $B_A$  is the anisotropy field. A label “S” in the thickness column indicates a device with a monolayer step dividing the active region. Devices 17-26 were cleaved under vacuum.

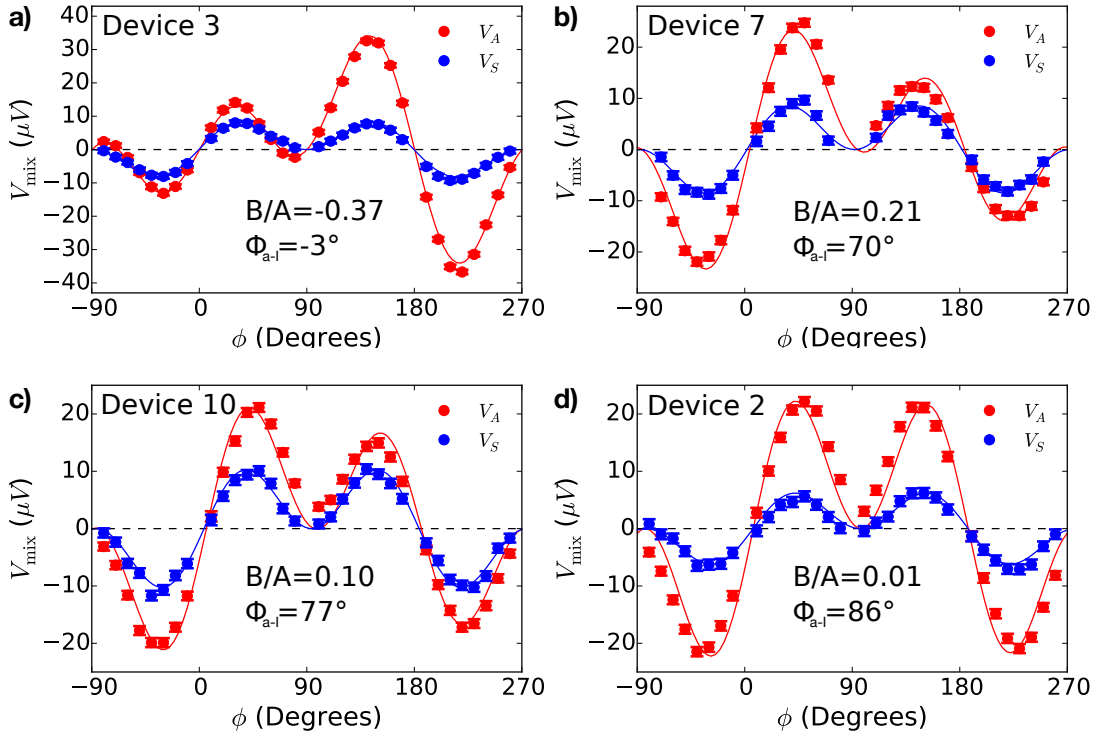


Figure 2.11: Plots of the symmetric (blue circles) and antisymmetric (red circles) components of the ST-FMR mixing voltage for **a)** Device 3, **b)** Device 7, **c)** Device 10, and **d)** Device 2. The current in Device 3 is applied approximately along the  $a$ -axis of the  $\text{WTe}_2$ , with the angle turning increasingly toward the  $b$ -axis for Devices 7, 10, and 2. The microwave frequency is 9 GHz and the microwave power is 5 dBm. The solid blue lines are fits of  $S \sin(2\phi - 2\phi_0) \cos(\phi - \phi_0)$  to  $V_S(\phi)$  and the solid red lines are fits of  $\sin(2\phi - 2\phi_0)[B + A \cos(\phi - \phi_0)]$  to  $V_A(\phi)$ . Error bars represent estimated standard deviations from the least-squares fitting procedure.

In Table 2.1, we provide device parameters, torque ratios, and magnetic anisotropy parameters for 26  $\text{WTe}_2$ /Permalloy bilayers, and a Pt/Permalloy control device. Only the first 15 devices were used for Figs. 2.7a and 2.7b. Devices 1-16 were cleaved in the sputter system load lock while dry nitrogen was flowing, whereas 17-26 were cleaved in the load lock under vacuum (below  $10^{-5}$  Torr). In Fig. 2.11, we plot  $V_S$  and  $V_A$  as a function of  $\phi$  for four devices, along with fits to  $S \sin(2\phi - 2\phi_0) \cos(\phi - \phi_0)$  and  $\sin(2\phi - 2\phi_0)[B + A \cos(\phi - \phi_0)]$

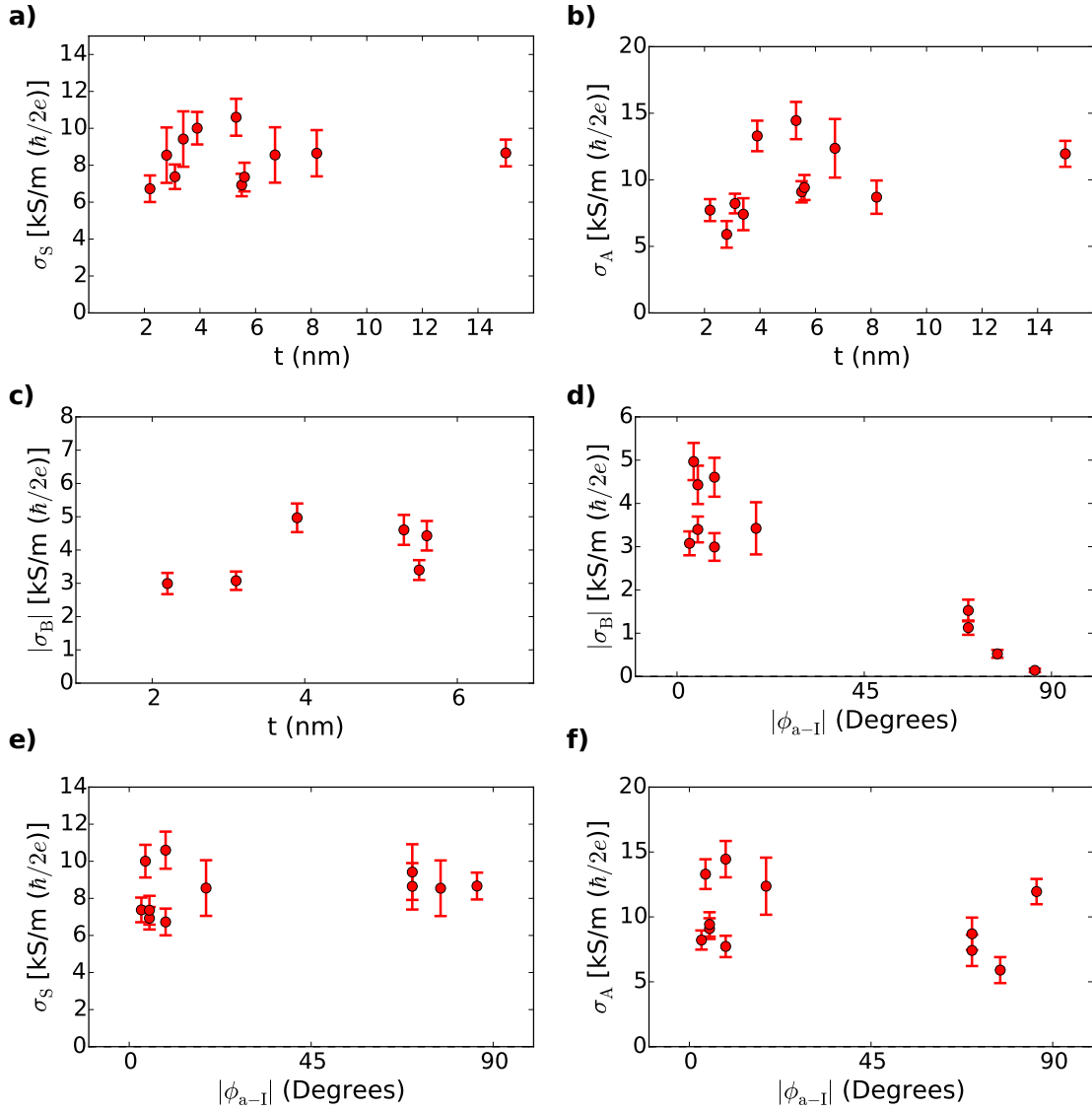


Figure 2.12: **a)** Torque conductivity  $\sigma_S$  as a function of WTe<sub>2</sub> thickness for the 11 devices on which we used a vector network analyzer to perform fully-calibrated measurements. The current is applied at various angles to the WTe<sub>2</sub>  $a$ -axis. **b)** Torque conductivity  $\sigma_A$  as a function of WTe<sub>2</sub> thickness for these 11 devices. **c)** Torque conductivity  $|\sigma_B|$  as a function of WTe<sub>2</sub> thickness for 6 fully-calibrated devices with  $|\phi_{a-l}| < 10^\circ$ . **d)**  $|\sigma_B|$  as a function of  $|\phi_{a-l}|$  for the 11 devices used in panels **a)** and **b)**. **e)**  $\sigma_S$  as a function of  $|\phi_{a-l}|$  for the 11 devices used in panels **a)** and **b)**. **f)**  $\sigma_A$  as a function of  $|\phi_{a-l}|$  for the 11 devices used in panels **a)** and **b)**. For the data shown in panels **a)**-**f)**, the applied microwave power is 5 dBm, and the torque conductivities are averaged over the frequency range 8-11 GHz. Error bars represent estimated standard deviations based on error propagation including uncertainties in calibrating the microwave voltage applied across each device and uncertainties derived from least-squares fits to ST-FMR data.

for the symmetric and antisymmetric data respectively. The sign of the parameter  $B$  varies apparently randomly between devices. This is to be expected because Raman scattering does not allow us to distinguish between the  $\hat{b}$  and  $-\hat{b}$  directions, which are physically distinct for the  $\text{WTe}_2$  surface crystal structure (a consequence of broken two-fold rotational symmetry). Essentially, the sign of  $B$  depends on whether the positive  $\hat{b}$  direction lies along  $0^\circ < \phi < 180^\circ$  or  $180^\circ < \phi < 360^\circ$ . Since interchanging the ground and signal leads rotates the definition of  $\phi$  by  $180^\circ$ , the sign of  $B$  is determined by the decision of which end of the bilayer is connected to the signal lead.

We carried out calibrated torque conductivity measurements (using a vector network analyzer to determine  $I_{\text{RF}}$ ) for 11 of our devices. The device-averaged torque conductivities for devices with current applied along the  $a$ -axis are reported in the main text. The torque conductivity data from all 11 devices is summarized in Fig. 2.12. In Fig. 2.12a and Fig. 2.12b we plot  $\sigma_S$  and  $\sigma_A$  respectively as a function of thickness. In Fig. 2.12c we plot  $|\sigma_B|$  as a function of thickness for the subset of the 11 devices where current is applied along the  $a$ -axis, and in Fig. 2.12d we plot  $|\sigma_B|$  as a function of  $|\phi_{a-l}|$  for all 11 devices.

### 2.8.5 Torques in $\text{WTe}_2/\text{CoFeB}$ bilayers

Throughout the work in this dissertation, we have made use of the same ferromagnetic material, Permalloy, and the same thickness of the ferromagnet,  $t_{\text{magnet}} = 6 \text{ nm}$ , simply to reduce the number of variables. Here, we briefly report measurements on a device in which we have used  $\text{Co}_{40}\text{Fe}_{40}\text{B}_{20}$  as the ferromagnetic layer in order to show the generality of the out-of-plane antidamp-

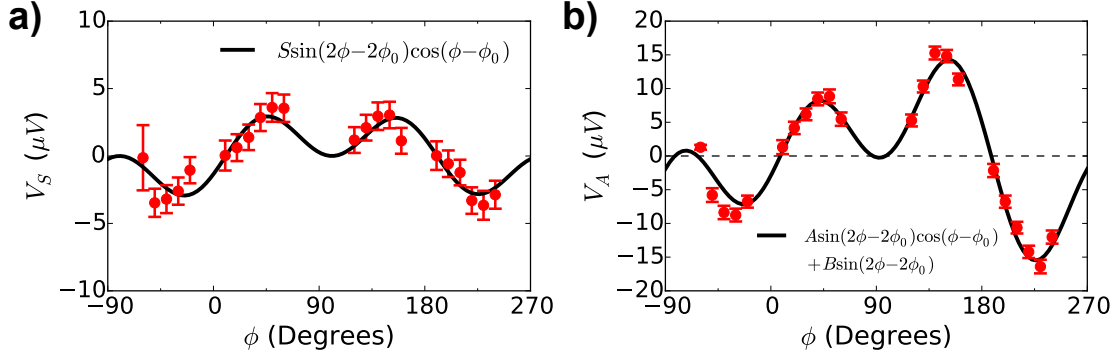


Figure 2.13: **a)** and **b)** Plots of the symmetric and antisymmetric components of the ST-FMR mixing voltage for a  $\text{WTe}_2(12.5 \text{ nm})/\text{Co}_{40}\text{Fe}_{40}\text{B}_{20}(6 \text{ nm})$  device respectively. The applied microwave power is 10 dBm at 10 GHz.

ing spin-orbit torque generated in the  $\text{WTe}_2$ . We have fabricated these devices in an identical fashion as our  $\text{WTe}_2/\text{Py}$  bilayers, using grazing-angle incidence sputtering to deposit 6 nm of  $\text{Co}_{40}\text{Fe}_{40}\text{B}_{20}$ . The  $\text{WTe}_2$  is 12.5 nm thick and is patterned into a  $4 \times 3 \mu\text{m}$  ( $l \times w$ ) ST-FMR device. The applied current is along the  $\text{WTe}_2$  a-axis. We find an angle and frequency averaged effective magnetization of  $\mu_0 M_{eff} \approx 1.3 \text{ T}$ , in agreement with the larger intrinsic magnetization of  $\text{Co}_{40}\text{Fe}_{40}\text{B}_{20}$  as compared to Py. The values of  $V_S$  and  $V_A$  as a function of applied field angle at a frequency of 10 GHz are shown in Fig. 2.13. From the fits we extract a value of  $\tau_B/\tau_A = -0.26 \pm 0.02$  and  $\tau_S/\tau_A = 1.0 \pm 0.1$ . Note that the voltage amplitudes of the signals for all the torques in these devices are smaller than those of our  $\text{WTe}_2/\text{Py}$  devices, which may be due to the smaller AMR and larger resistivity in  $\text{Co}_{40}\text{Fe}_{40}\text{B}_{20}$ .

## 2.8.6 Symmetry analysis for current generated torques

The torques acting on an in-plane magnetization can be written as  $\tau_{\parallel}(\hat{m}, E) = \tau_{\parallel}(\phi, E)\hat{m} \times \hat{c}$  and  $\tau_{\perp}(\hat{m}, E) = \tau_{\perp}(\phi, E)\hat{c}$ , where we have explicitly included the de-

pendence of the torques on the electric field,  $E$ , in the bilayer. These expressions are generic, since  $\hat{m} \times \hat{c}$  and  $\hat{c}$  are unit vectors forming a basis for the vectors perpendicular to  $\hat{m}$ . The pre-factors,  $\tau_{\parallel}(\phi, E)$  and  $\tau_{\perp}(\phi, E)$ , can be Fourier expanded:

$$\begin{aligned}\tau_{\parallel}(\phi, E) &= E (S_0 + S_1 \cos \phi + S_2 \sin \phi + S_3 \cos 2\phi + S_4 \sin 2\phi + S_5 \cos 3\phi + \dots) \\ \tau_{\perp}(\phi, E) &= E (A_0 + A_1 \cos \phi + A_2 \sin \phi + A_3 \cos 2\phi + A_4 \sin 2\phi + A_5 \cos 3\phi + \dots)\end{aligned}\tag{2.10}$$

First, we consider the case of an electric field applied along the  $\text{WTe}_2$  crystal  $a$ -axis. In this case, applying the  $\sigma_v(bc)$  symmetry operation to the device flips the direction of the electric field (since  $\mathbf{E}$  is a vector perpendicular to the  $bc$  plane) and reverses the component of the magnetization perpendicular to the  $a$ -axis (since  $\hat{m}$  is a pseudovector). This is equivalent to the transformations  $\phi \rightarrow -\phi$  and  $E \rightarrow -E$ .

The torques must also transform as pseudovectors under  $\sigma_v(bc)$ , which constrains the dependence of  $\tau_{\parallel}(\phi, E)$  and  $\tau_{\perp}(\phi, E)$  on  $\phi$  and  $E$ . The nature of these constraints can be understood by re-writing  $\tau_{\perp}(\phi, E) = \hat{c} \cdot \boldsymbol{\tau}_{\perp}$  and  $\tau_{\parallel}(\phi, E) = (\hat{m} \times \hat{c}) \cdot \boldsymbol{\tau}_{\perp}$ . Since  $\hat{c}$  is a vector and  $\boldsymbol{\tau}_{\perp}$  is a pseudovector,  $\hat{c} \cdot \boldsymbol{\tau}_{\perp}$  transforms as a pseudoscalar (i.e. changes sign under inversion and mirror operations but is invariant under rotations) as the dot product of a vector and a pseudovector is a pseudoscalar. Consistency of the transformations  $\phi \rightarrow -\phi$ ,  $E \rightarrow -E$ , and  $\hat{c} \cdot \boldsymbol{\tau}_{\perp} \rightarrow -\hat{c} \cdot \boldsymbol{\tau}_{\perp}$  under  $\sigma_v(bc)$  then requires that  $\tau_{\perp}(-\phi, -E) = -\hat{c} \cdot \boldsymbol{\tau}_{\perp} = -\tau_{\perp}(\phi, E)$ . One can also show that the cross product of a vector and a pseudovector transforms as a vector, and so  $\hat{m} \times \hat{c}$  is a vector. This implies that  $(\hat{m} \times \hat{c}) \cdot \boldsymbol{\tau}_{\perp}$  transforms as a pseudoscalar so that  $(\hat{m} \times \hat{c}) \cdot \boldsymbol{\tau}_{\perp} \rightarrow -(\hat{m} \times \hat{c}) \cdot \boldsymbol{\tau}_{\perp}$  under  $\sigma_v(bc)$ , and therefore  $\tau_{\parallel}(-\phi, -E) = -\tau_{\parallel}(\phi, E)$ . We have considered only torques linear in  $E$  so that the symmetry requirement becomes  $\tau_{\parallel(\perp)}(-\phi, E) = \tau_{\parallel(\perp)}(\phi, E)$ . Keeping only the

terms in Eq. 2.10 that comply with this symmetry requirement leaves

$$\begin{aligned}\tau_{\parallel}^a(\phi, E) &= E(S_0 + S_1 \cos \phi + S_3 \cos 2\phi + S_5 \cos 3\phi + \dots) \\ \tau_{\perp}^a(\phi, E) &= E(A_0 + A_1 \cos \phi + A_3 \cos 2\phi + A_5 \cos 3\phi + \dots).\end{aligned}\tag{2.11}$$

The measured angular dependence discussed in the main text for  $\mathbf{E}$  along the  $a$ -axis can be fit accurately with just the low-order terms  $S_1$ ,  $A_0$ , and  $A_1$ . Notably, we do not experimentally observe the term  $S_0$ , although it is allowed by symmetry.

For an electric field applied along the  $b$ -axis, applying  $\sigma_v(bc)$  to the device flips the projection of the magnetization along the  $b$ -axis direction, and leaves the electric field unchanged i.e.  $\phi \rightarrow \pi - \phi$  and  $E \rightarrow E$ . From this, one can derive the symmetry constraints  $\tau_{\parallel(\perp)}(\pi - \phi, E) = -\tau_{\parallel(\perp)}(\phi, E)$ . Therefore the allowed angular dependencies of the torques for an electric field along the  $b$ -axis are

$$\begin{aligned}\tau_{\parallel}^b(\phi, E) &= E(S_1 \cos \phi + S_4 \sin 2\phi + S_5 \cos 3\phi + \dots) \\ \tau_{\perp}^b(\phi, E) &= E(A_1 \cos \phi + A_4 \sin 2\phi + A_5 \cos 3\phi + \dots).\end{aligned}\tag{2.12}$$

In this case, with  $\mathbf{E}$  along the  $b$ -axis, the lowest order terms ( $S_1$  and  $A_1$ ) dominate our measurements for both the symmetric and antisymmetric amplitudes, although better agreement is obtained when we include the coefficient  $A_5$  as shown in Fig. 2.14. The expansion for  $\mathbf{E}$  applied at an arbitrary angle  $\phi_{a-E}$  from the  $a$ -axis can be determined from the linearity of the torques:

$$\tau_{\parallel(\perp)}(\phi, \mathbf{E}) = \tau_{\parallel(\perp)}^a(\phi - \phi_{a-E}, |\mathbf{E}| \cos \phi_{a-E}) + \tau_{\parallel(\perp)}^b(\phi - \phi_{a-E} - \pi/2, -|\mathbf{E}| \sin \phi_{a-E})\tag{2.13}$$

where  $\tau_{\parallel(\perp)}^a$  and  $\tau_{\parallel(\perp)}^b$  are the expansions for electric field along the  $a$  and  $b$  axes respectively.

### 2.8.7 Higher harmonics in the ST-FMR angular dependence

Based on the symmetry analysis in Section 2.8.6, we may expect that the angular dependence of the in- and out-of-plane torques can be more general than  $\tau_{\parallel} = S \cos \phi$  and  $\tau_{\perp} = A \cos \phi + B$ . We examined fits of our data to the most general symmetry-allowed Fourier expansion, up to the third harmonic. We find significant values for  $A_5$  (i.e., the term proportional to  $\cos 3\phi$ ) with the largest magnitudes occurring for current flowing close to the  $b$ -axis direction. Figure 2.14 shows  $V_A$  as a function of  $\phi$  for two devices, along with fits to  $\sin(2\phi - 2\phi_0)[B + A \cos(\phi - \phi_0)]$  and  $\sin(2\phi - 2\phi_0)[B + A \cos(\phi - \phi_0) + C \cos(3\phi - 3\phi_0)]$ ; the  $\cos 3\phi$  term significantly improves the fit, corresponding to a non-zero value of  $A_5$ . We also find significant values for  $S_5$  of a similar magnitude. For our Pt/Py control device  $S_5/A_1 = -0.10 \pm 0.02$  and  $A_5/A_1 = -0.077 \pm 0.008$ . All other coefficients up to the third harmonic – except for  $A_0$ ,  $A_1$ , and  $S_1$  – are zero within our experimental uncertainty.

The  $\cos 3\phi$  term might arise either from a true angular dependence of the torque or from a lack of full saturation for the in-plane anisotropic magnetoresistance  $R(\phi)$  due to in-plane magnetic anisotropy. Our initial analyses suggest that this in-plane anisotropy can account at least partially, but perhaps not completely, for our measured  $\cos 3\phi$  term. This mechanism cannot affect our determination of the  $\tau_B$  torque.

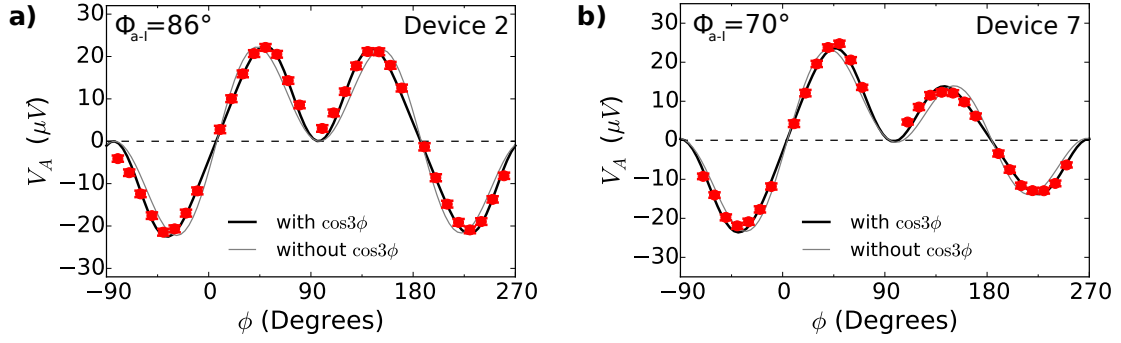


Figure 2.14: Plots of the antisymmetric part of the mixing voltage (red circles) versus the in-plane magnetization angle for **a)** Device 2 and **b)** Device 7. The microwave frequency is 9 GHz and the microwave power is 5 dBm. The black lines show fits to  $\sin(2\phi - 2\phi_0) [B + A \cos(\phi - \phi_0) + C \cos(3\phi - 3\phi_0)]$  giving  $C/A = 0.24 \pm 0.01$  for Device 2 and  $C/A = 0.20 \pm 0.01$  for Device 7. The light grey lines show fits to  $\sin(2\phi - 2\phi_0) [B + A \cos(\phi - \phi_0)]$ . Error bars represent estimated standard deviations from the least-squares fitting procedure.

## 2.8.8 On why there can be no contribution to the out-of-plane antidamping torque from the bulk of a $WTe_2$ layer

Bulk crystals of  $WTe_2$  have a screw symmetry: the crystal structure is mapped onto itself if it is rotated by  $180^\circ$  about an axis normal to the layers ( $c$ -axis) and translated by half a unit cell along both the  $c$  and  $a$ -axis (in the  $c$  direction, half a unit cell is one layer spacing). If there is any net bulk spin polarization or spin current with a component perpendicular to the plane, that spin component will be left unaltered by this operation, while the direction of an in-plane charge current will be reversed. This implies that there can be no bulk contribution to the current-induced antidamping spin torque that is linear in the applied in-plane current. This screw symmetry is broken at the  $WTe_2/Py$  interface, so a surface-generated out-of-plane antidamping torque is allowed by symmetry. This surface contribution might come entirely from a single  $WTe_2$  layer at the

interface or from imperfect cancellations between more than one WTe<sub>2</sub> layer near the interface (e.g., if there is surface-induced band banding).

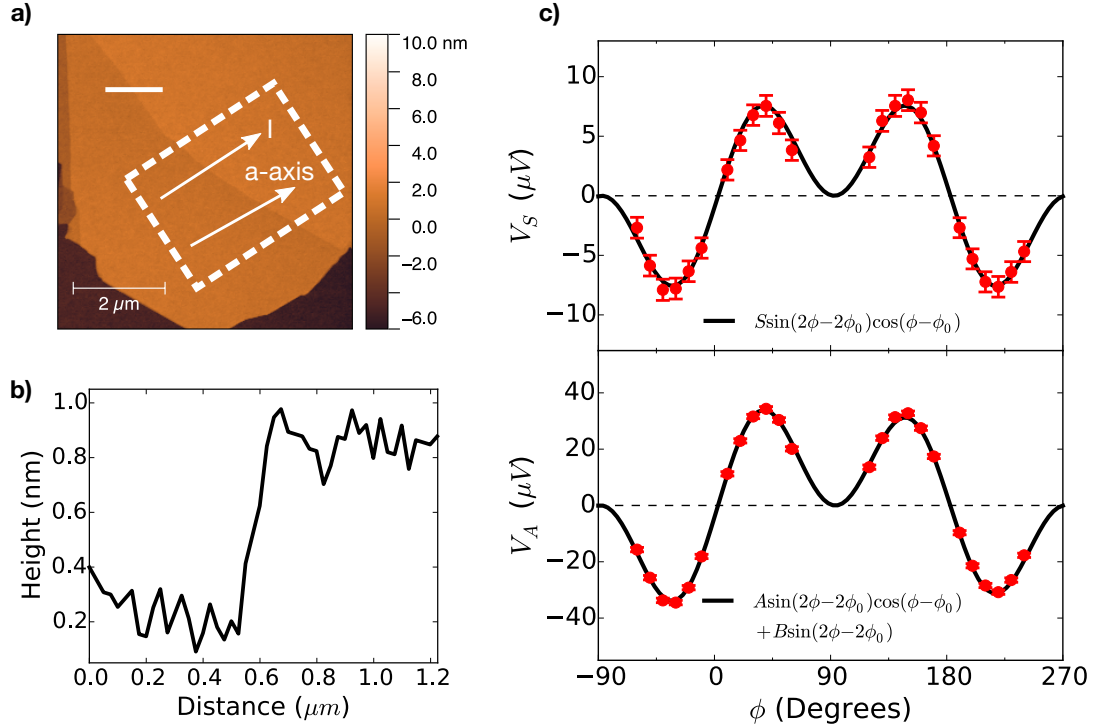


Figure 2.15: **a)** An atomic force microscopy image of the WTe<sub>2</sub> flake used for fabrication of Device S1 after deposition of the Permalloy layer and aluminum oxide cap. The dashed white rectangle shows the approximate placement of the device active region (the uncertainty in the lateral location is about 500 nm due to the alignment procedure for the lithography steps). **b)** A linecut [white solid line in **a**] showing a step height of about 0.7 nm corresponding to a monolayer step in the WTe<sub>2</sub> crystal. **c)** Plot of the symmetric (top, red circles) and antisymmetric parts (bottom, red circles) of the mixing voltage versus the versus the in-plane magnetization angle. The magnitude of the symmetric part indicates a spin-orbit torque comparable to other *a*-axis aligned WTe<sub>2</sub> devices, but the antisymmetric part shows  $B/A=0.033$  indicating that  $\tau_B$  is much smaller here than in devices without a monolayer step. Error bars represent estimated standard deviations from the least-squares fitting procedure.

We have checked that adjacent layers generate  $\tau_B$  of opposite sign by studying a sample (Device S1) in which the sample region contains a single-layer

step, so that the Permalloy is exposed to two  $\text{WTe}_2$  surfaces with opposite symmetry (Fig. 2.15). Device S1 was fabricated with the bar aligned at  $3.7^\circ$  from the  $a$ -axis and with a monolayer step dividing the channel into two regions of approximately equal area, as shown by the atomic force microscopy data in Figs. 2.15a and 2.15b. The angular dependences of  $V_S$  and  $V_A$  are shown in Fig. 2.15c. The non-zero value of  $V_S$  implies the existence of spin-orbit torque and a clean  $\text{WTe}_2/\text{Py}$  interface. However, we measure  $B/A = 0.033$  for this device, in contrast to our finding that  $|B/A| > 0.32$  for all devices measured with  $|\phi_{a-I}| < 10^\circ$  and an atomically flat channel. We interpret this low value of  $B/A$  in device S1 as arising from cancellation of the torques from the two  $\text{WTe}_2/\text{Py}$  interface regions of opposite surface symmetry, providing strong evidence that  $\tau_B$  arises from an interface effect. Similar results were obtained on two additional devices containing a monolayer step and with the bar direction aligned to the  $\text{WTe}_2$   $a$ -axis.

### 2.8.9 Some comments on the microscopic origin of an out-of-plane antidamping torque in $\text{WTe}_2/\text{Py}$ bilayers

In this section, we discuss a few possible microscopic mechanisms for generation of out-of-plane antidamping torques, with the understanding that these possibilities are not exhaustive. We focus on mechanisms that can generate transport and accumulation of spins polarized in the  $c$ -direction, since absorption of  $c$ -axis polarized spins is expected to lead to a  $\hat{m} \times (\hat{m} \times \hat{c})$  torque. To start, we show that symmetry constraints forbid a nonzero contribution from two well-known effects generating spin-orbit torques: a bulk spin-Hall conductivity, and a bulk-averaged inverse spin galvanic effect. We then consider possible

mechanisms for which non-zero contributions are allowed.

To generate a  $\hat{m} \times (\hat{m} \times \hat{c})$  torque via the bulk spin-Hall effect, we must have  $c$ -axis polarized spins flowing towards the  $\text{WTe}_2/\text{Py}$  interface in response to an in-plane electric field. The total current of  $c$ -axis polarized spins,  $\mathbf{j}_s^c$ , can be written as  $\mathbf{j}_s^c = \boldsymbol{\sigma}^c \cdot \mathbf{E}$ , where  $\boldsymbol{\sigma}^c$  is the  $c$ -axis polarized part of the spin-Hall conductivity tensor. The form of this tensor is constrained by the point group of the crystal [45]. For the  $mm2$  point group operations of  $\text{WTe}_2$ , the most general form is:

$$\boldsymbol{\sigma}^c = \begin{pmatrix} 0 & \sigma_{ab}^c & 0 \\ \sigma_{ba}^c & 0 & 0 \\ 0 & 0 & 0 \end{pmatrix}. \quad (2.14)$$

Notably, the terms  $\sigma_{ca}^c$  and  $\sigma_{cb}^c$ , corresponding to  $c$ -axis polarized spins flowing in the  $c$ -direction (towards the  $\text{WTe}_2/\text{Py}$  interface) in response to in-plane electric fields, are zero. Therefore, there can be no contribution to a  $\hat{m} \times (\hat{m} \times \hat{c})$  torque from the bulk spin Hall effect in  $\text{WTe}_2$ .

When an electric field is applied to a non-centrosymmetric crystal we expect a non-equilibrium spin-density to be generated in the crystal due to the inverse spin galvanic effect. This spin polarization can also be written in terms of a linear response tensor:  $\mathbf{s} = \boldsymbol{\chi} \cdot \mathbf{E}$ . The tensor  $\boldsymbol{\chi}$  must satisfy the relation  $\boldsymbol{\chi} = \det(S)S^{-1}\boldsymbol{\chi}S$  for any symmetry operation  $S$  in the point group of the crystal [46]. The point group rather than the space group is relevant here because we assume the spin density to have a nonzero component that is spatially uniform. For  $\text{WTe}_2$ , the most general form is:

$$\boldsymbol{\chi} = \begin{pmatrix} 0 & \chi_{ab} & 0 \\ \chi_{ba} & 0 & 0 \\ 0 & 0 & 0 \end{pmatrix}. \quad (2.15)$$

Since  $\chi_{cb}$  and  $\chi_{ca}$  are zero, the bulk inverse spin galvanic effect of  $\text{WTe}_2$  cannot generate a  $\hat{m} \times (\hat{m} \times \hat{c})$  torque.

The symmetry of  $\text{WTe}_2$  does, however, allow for local accumulations of  $c$ -axis polarized spins in response to an in-plane electric field, provided these accumulations switch sign between atomic sites related by the screw-axis and glide-plane symmetries. This is similar to recent work on  $\text{CuMnAs}$ , where the absence of local inversion symmetry allows for current-induced exchange fields that change sign between atomic sites related by the global inversion symmetry [24]. The  $\text{WTe}_2$  crystal can be partitioned into adjacent  $A$  and  $B$  type layers, where  $B$  layers are rotated by  $180^\circ$  with respect to  $A$  layers. The symmorphic  $bc$  mirror plane maps every layer back onto itself, while the non-symmorphic symmetries (screw-axis and glide-plane) map each layer onto an adjacent one of the opposite type. If we define layer specific spin accumulations  $s^A = \chi^A \mathbf{E}$  and  $s^B = \chi^B \mathbf{E}$ , the respective tensors obey:

$$\chi^A = \begin{pmatrix} 0 & \chi^A_{ab} & \chi^A_{ac} \\ \chi^A_{ba} & 0 & 0 \\ \chi^A_{ca} & 0 & 0 \end{pmatrix}, \chi^B = \begin{pmatrix} 0 & \chi^A_{ab} & -\chi^A_{ac} \\ \chi^A_{ba} & 0 & 0 \\ -\chi^A_{ca} & 0 & 0 \end{pmatrix}. \quad (2.16)$$

Therefore, it is possible to generate local  $c$ -axis spin polarizations in the bulk  $\text{WTe}_2$  crystal via an in-plane current, but the local  $c$ -axis spin polarizations change sign between layers. In a real crystal the surface will terminate on either an  $A$  or  $B$  type layer, leading to a  $c$ -axis spin polarization on the surface when current is applied along the  $a$ -axis. This mechanism is expected to lead to a  $\hat{m} \times (\hat{m} \times \hat{c})$  torque, along with a  $\hat{m} \times \hat{c}$  torque due to exchange coupling of the ferromagnet to the  $\text{WTe}_2$  surface spins.

Another approach is to consider the torques generated in an interface layer

formed by hybridization between electronic states of the  $\text{WTe}_2$  and Py, *i.e.* in a region at the  $\text{WTe}_2/\text{Py}$  interface with electronic properties differing from the bulk of either layer. These interface states could generate  $c$ -axis polarized spin accumulations via the inverse spin galvanic effect. For example, the spin-orbit coupling Hamiltonian  $H_{\text{SOC}} \propto \hat{n} \cdot (\mathbf{k} \times \boldsymbol{\sigma})$ , where  $\hat{n}$  lies in the  $bc$  plane, is consistent with the symmetry of the  $\text{WTe}_2/\text{Py}$  interface, and leads to a non-zero  $\langle \sigma_c \rangle$  in response to electric fields applied along the  $a$ -axis. This is a generalization of the usual Rashba-Edelstein effect discussed in the context heavy metal/ferromagnet bilayers, which corresponds to  $\hat{n} = \hat{z}$ . Such a  $\langle \sigma_c \rangle$  can generate both  $\hat{m} \times (\hat{m} \times \hat{c})$  and  $\hat{m} \times \hat{c}$  torques, with their relative magnitude depending on microscopic details. Magnetic anisotropy associated with this mechanism has been predicted to arise at the interface between ferromagnets and low-symmetry materials with strong spin-orbit coupling [47].

Recent theoretical work suggests that it may also be possible that the spin-polarized electrons flowing within a metallic ferromagnet layer may generate spin-transfer torque when they scatter from an interface with a material possessing strong spin-orbit coupling, without necessarily requiring charge current flow within the spin-orbit material [48, 49]. This mechanism is attractive because it might provide a natural explanation for the apparent lack of dependence on the  $\text{WTe}_2$  thickness for the torque components  $\tau_B$  and  $\tau_S$ .

### 2.8.10 Second-harmonic Hall measurements

Second-harmonic measurements of Hall voltage as a function of the angle of an in-plane applied magnetic field,  $B$ , provide an alternative method to measure an

out-of-plane antidamping torque independent of ST-FMR measurements. We performed this measurement using a Hall bar device discussed in Section 2.8.3, for which the Permalloy thickness is 6 nm and the WTe<sub>2</sub> thickness is 16 nm. The Hall bar has a length and width of 26  $\mu\text{m}$  and 4  $\mu\text{m}$ , respectively, and is oriented so that the current is along the WTe<sub>2</sub> *a*-axis ( $\phi_{a-I} = -1$ ); the voltage probes used for the Hall measurements are 2  $\mu\text{m}$  wide. The active region of the Hall bar has a uniform WTe<sub>2</sub> thickness, with no monolayer steps, over better than 90% of its area. We apply a current  $I(t) = I_0 \sin(2\pi ft)$  at a frequency  $f = 340$  Hz with  $I_0 = 0.66$  mA, and measure the Hall voltage at the second harmonic frequency. The angle of the in-plane magnetic field,  $\phi$ , is defined relative to the direction of current flow. Generalizing the argument in Ref. [50] to include the effects of an in-plane uniaxial anisotropy  $B_A$  with the easy axis parallel to the *b*-axis of the WTe<sub>2</sub> (in addition to the shape anisotropy of the thin film  $\mu_0 M_{\text{eff}}$ ), and allowing for in-plane and out-of-plane current-induced torques with the angular dependence  $\tau_{\parallel} = \tau_S \cos \phi_M$  and  $\tau_{\perp} = \tau_A \cos \phi_M + \tau_B$ , the second harmonic signal has the form:

$$R_{xy}^{2\omega} = \frac{R_{\text{PHE}} \cos 2\phi_M (\tau_A \cos \phi_M + \tau_B)}{\gamma (B - B_A \cos 2\phi_M)} + \frac{R_{\text{AHE}} \tau_S \cos \phi_M}{2\gamma (B + \mu_0 M_{\text{eff}} + B_A \sin^2 \phi_M)} + \frac{V_{\text{ANE}}}{I_0} \cos \phi_M, \quad (2.17)$$

where  $R_{\text{PHE}}$  and  $R_{\text{AHE}}$  are the planar and anomalous Hall resistances of the device, and  $V_{\text{ANE}}$  is the anomalous Nernst voltage arising from an out-of-plane thermal gradient proportional to the Joule power  $I^2 R$ . This expression neglects terms above first order in  $B_A/B$ , which is an accurate approximation over the range of fields studied for our second harmonic measurements. Here  $\phi_M$  is the angle of the magnetization relative to the direction of current flow, which differs from  $\phi$  for low-fields due to the in-plane magnetic anisotropy. To first order in  $B_A/B$ , the equilibrium magnetization angle is  $\phi_M = \phi + B_A \sin 2\phi / 2B$ . Equation

2.17 shows that the second harmonic signal associated with  $\tau_B$  has an angular dependence distinct from  $\tau_A$ ,  $\tau_S$  and the magneto-thermopower voltage ( $V_{ANE}$ ).

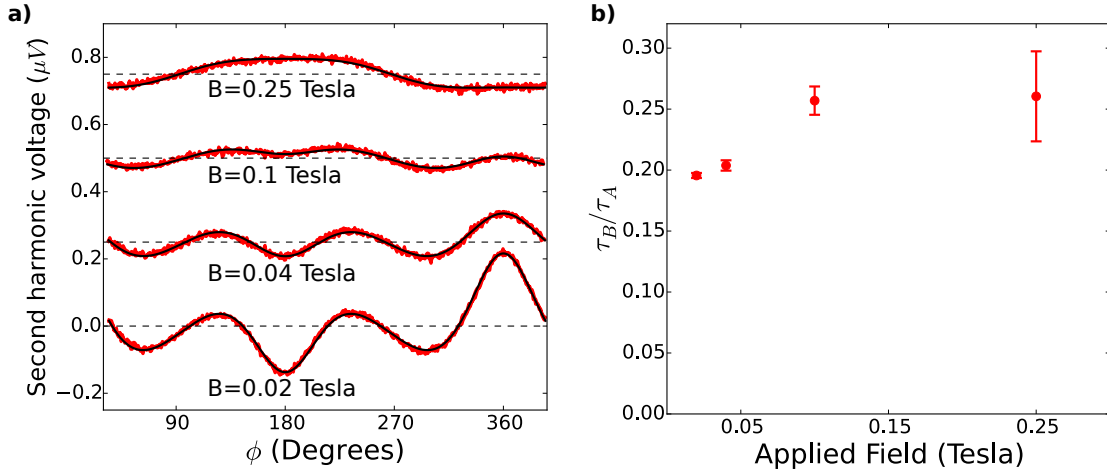


Figure 2.16: **a)** Second harmonic Hall voltage for a  $WTe_2/Py$  bilayer (with current along the  $a$ -axis) as a function of the angle between the in-plane applied magnetic field and the current flow direction. The data (red) are plotted for different magnitudes of the applied magnetic field ( $B=0.25$  T, 0.1 T, 0.04 T, and 0.02 T, from top to bottom). Data for different values of the applied field have been vertically offset for clarity. The black lines show fits to Eq. 2.17. **b)** The torque ratio  $\tau_B/\tau_A$  extracted from the angular dependence of the second harmonic Hall voltage, as a function of the magnitude of the applied magnetic field used for the angular sweep. Error bars represent estimated standard deviations from the least-squares fitting procedure.

Fig. 2.16 shows measurements of the second-harmonic Hall voltage in the  $WTe_2/Py$  Hall bar as a function of  $\phi$  for selected magnitudes of applied magnetic field  $B$ ; the red lines indicate the data, while the black lines are fits to Eq. 2.17. Even without any fitting, it is clear that the out-of-plane antidamping torque  $\tau_B$  is indeed non-zero, as the magnitude of the second-harmonic signal is significantly different for  $\phi = 180^\circ$  and  $360^\circ$  [when  $\tau_B = 0$ , Eq. 2.17 predicts simply that  $R_{xy}^{2\omega}(\phi = 180^\circ) = -R_{xy}^{2\omega}(\phi = 360^\circ)$ ]. To fit the data, we use a simplified version of Eq. 2.17, valid when  $B \ll \mu_0 M_{\text{eff}}$ :

$$R_{xy}^{2\omega} = \frac{\cos 2\phi_M}{(B - B_A \cos 2\phi_M)} (A_1 \cos \phi_M + A_0) + R_\phi \cos \phi_M, \quad (2.18)$$

where  $A_0 = R_{\text{PHE}}\tau_{\text{B}}/\gamma$ ,  $A_1 = R_{\text{PHE}}\tau_{\text{A}}/\gamma$ , and  $R_\phi$  is a constant combining the contributions of the in-plane antidamping torque and the anomalous Nernst voltage. For each value of  $B$  we fit the data using the parameters  $A_0$ ,  $A_1$ ,  $R_\phi$ , and  $B_{\text{A}}$ , along with an additional overall  $\phi$ -independent offset. For the fits, we used the first-order expression for  $\phi_{\text{M}}(\phi)$  discussed above. We find that Eq. 2.8.10 fits the data well with  $B_{\text{A}} \approx 3mT$ . The torque ratio  $\tau_{\text{B}}/\tau_{\text{A}}$  can then be determined independent of any other sample parameters at each value of the field magnitude,  $A_0/A_1 = \tau_{\text{B}}/\tau_{\text{A}}$ . In figure 2.16b we plot  $\tau_{\text{B}}/\tau_{\text{A}}$  as a function of  $B$ , showing that  $\tau_{\text{B}}/\tau_{\text{A}} \approx 0.2 - 0.25$ . These values are similar to, albeit slightly lower than, the values of  $|\tau_{\text{B}}|/\tau_{\text{A}}$  determined by ST-FMR for different devices ( $|\tau_{\text{B}}|/\tau_{\text{A}} = 0.32 - 0.385$ ; see Fig. 2.11 or Table 2.1).

We determine the individual torque conductivities  $\sigma_{\text{A}}$  and  $\sigma_{\text{B}}$  from the second harmonic Hall measurements according to (here the subscript  $K = A$  or  $B$ ):

$$\sigma_{\text{K}} = \frac{M_{\text{s}}lwt_{\text{magnet}}}{\hbar\gamma/2e} \frac{\tau_{\text{K}}}{(lw)E} \left( \frac{\hbar}{2e} \right) = \frac{eM_{\text{s}}lt_{\text{magnet}}}{\mu_{\text{B}}} \frac{\tau_{\text{K}}}{V} \left( \frac{\hbar}{2e} \right). \quad (2.19)$$

Using  $R_{\text{PHE}} = 0.14 \Omega$ , for the harmonic Hall measurement with  $B = 1000 \text{ Oe}$  we find  $\tau_{\text{A}} = 8.3 \pm 0.2 \text{ MHz}$  and  $\tau_{\text{B}} = 2.12 \pm 0.09 \text{ MHz}$ . To estimate the applied electric field we divide the applied voltage (566 mV peak-to-peak) by the length of the Hall device, and to estimate the saturation magnetization  $M_{\text{s}} \approx M_{\text{eff}}$  we fit to the anomalous Hall effect data of Fig. 2.10 finding  $\mu_0 M_{\text{eff}} = 0.81 \text{ T} \pm 0.01 \text{ T}$ . From Eq. 2.19 we then find  $\sigma_{\text{B}} = (6 \pm 1) \times 10^3 (\hbar/2e)(\Omega m)^{-1}$  and  $\sigma_{\text{A}} = (25 \pm 4) \times 10^3 (\hbar/2e)(\Omega m)^{-1}$ , where the errors are primarily due to the uncertainty in the thickness of the Permalloy. These values can be compared with the calibrated ST-FMR measurements presented in Fig. 2.12. The calibrated ST-FMR measurements for devices with  $|\phi_{\text{a-I}}| \leq 10^\circ$  give a range of  $\sigma_{\text{B}} = (3 - 5) \times 10^3 (\hbar/2e)(\Omega m)^{-1}$  and  $\sigma_{\text{A}} = (8 - 14) \times 10^3 (\hbar/2e)(\Omega m)^{-1}$ . The second-

harmonic value for  $\sigma_B$  agrees with the ST-FMR measurements within the range of reasonable experimental uncertainty. The value of  $\sigma_A$  as determined from the second-harmonic measurements is approximately twice as large as the typical ST-FMR value. This discrepancy in  $\sigma_A$  is not presently understood but there may be differences in the  $WTe_2$  crystal quality or the cleanliness of the  $WTe_2/Py$  interface, as the Py film used for the Hall bar device was grown in a different round of sputtering depositions than those used for the ST-FMR devices.<sup>1</sup> We conclude that the second-harmonic Hall measurements confirm the existence of a nonzero out-of-plane antidamping torque  $\tau_B$  and give a value for its strength in agreement with the ST-FMR measurements.

## References

- [1] D. MacNeill, G. M. Stiehl, M. H. D. Guimaraes, R. A. Buhrman, J. Park, and D. C. Ralph. “Control of spinorbit torques through crystal symmetry in  $WTe_2$ /ferromagnet bilayers.” *Nature Physics* **13**, 300 (2017).
- [2] A. Brataas, A. D. Kent, and H. Ohno. “Current-induced torques in magnetic materials.” *Nat. Mater.* **11**, 372 (2012).
- [3] C. Zhang, S. Fukami, H. Sato, F. Matsukura, and H. Ohno. “Spin-orbit torque induced magnetization switching in nano-scale Ta/CoFeB/MgO.” *Applied Physics Letters* **107**, 012401 (2015).
- [4] K. Ando, S. Takahashi, K. Harii, K. Sasage, J. Ieda, S. Maekawa, and E. Saitoh. “Electric Manipulation of Spin Relaxation Using the Spin Hall Effect.” *Phys. Rev. Lett.* **101**, 036601 (2008).

---

<sup>1</sup>We have recently determined this is likely due to exfoliation conditions, see Section 3.6.3.

- [5] U. H. Pi, K. W. Kim, J. Y. Bae, S. C. Lee, Y. J. Cho, K. S. Kim, and S. Seo. "Tilting of the spin orientation induced by Rashba effect in ferromagnetic metal layer." *Applied Physics Letters* **97**, 162507 (2010).
- [6] I. Mihai Miron, G. Gaudin, S. Auffret, B. Rodmacq, A. Schuhl, S. Pizzini, J. Vogel, and P. Gambardella. "Current-driven spin torque induced by the Rashba effect in a ferromagnetic metal layer." *Nat. Mater.* **9**, 230 (2010).
- [7] L. Liu, T. Moriyama, D. C. Ralph, and R. A. Buhrman. "Spin-Torque Ferromagnetic Resonance Induced by the Spin Hall Effect." *Phys. Rev. Lett.* **106**, 036601 (2011).
- [8] I. M. Miron, K. Garello, G. Gaudin, P.-J. Zermatten, M. V. Costache, S. Auffret, S. Bandiera, B. Rodmacq, A. Schuhl, and P. Gambardella. "Perpendicular switching of a single ferromagnetic layer induced by in-plane current injection." *Nature* **476**, 189 (2011).
- [9] L. Liu, C.-F. Pai, Y. Li, H. W. Tseng, D. C. Ralph, and R. A. Buhrman. "Spin-Torque Switching with the Giant Spin Hall Effect of Tantalum." *Science* **336**, 555 (2012).
- [10] C.-F. Pai, L. Liu, Y. Li, H. W. Tseng, D. C. Ralph, and R. A. Buhrman. "Spin transfer torque devices utilizing the giant spin Hall effect of tungsten." *Applied Physics Letters* **101**, 122404 (2012).
- [11] J. Kim, J. Sinha, M. Hayashi, M. Yamanouchi, S. Fukami, T. Suzuki, S. Mitani, and H. Ohno. "Layer thickness dependence of the current-induced effective field vector in Ta|CoFeB|MgO." *Nat. Mater.* **12**, 240 (2013).
- [12] P. P. J. Haazen, E. Murè, J. H. Franken, R. Lavrijsen, H. J. M. Swagten, and

- B. Koopmans. "Domain wall depinning governed by the spin Hall effect." *Nat. Mater.* **12**, 299 (2013).
- [13] S. Emori, U. Bauer, S.-M. Ahn, E. Martinez, and G. S. D. Beach. "Current-driven dynamics of chiral ferromagnetic domain walls." *Nat. Mater.* **12**, 611 (2013).
- [14] K.-S. Ryu, L. Thomas, S.-H. Yang, and S. Parkin. "Chiral spin torque at magnetic domain walls." *Nat. Nano.* **8**, 527 (2013).
- [15] A. R. Mellnik, J. S. Lee, A. Richardella, J. L. Grab, P. J. Mintun, M. H. Fischer, A. Vaezi, A. Manchon, E. A. Kim, N. Samarth, and D. C. Ralph. "Spin-transfer torque generated by a topological insulator." *Nature* **511**, 449 (2014).
- [16] Y. Fan, P. Upadhyaya, X. Kou, M. Lang, S. Takei, Z. Wang, J. Tang, L. He, L.-T. Chang, M. Montazeri, G. Yu, W. Jiang, T. Nie, R. N. Schwartz, Y. Tserkovnyak, and K. L. Wang. "Magnetization switching through giant spin-orbit torque in a magnetically doped topological insulator heterostructure." *Nat. Mater.* **13**, 699 (2014).
- [17] K. Garello, I. M. Miron, C. O. Avci, F. Freimuth, Y. Mokrousov, S. Blugel, S. Auffret, O. Boulle, G. Gaudin, and P. Gambardella. "Symmetry and magnitude of spin-orbit torques in ferromagnetic heterostructures." *Nat. Nano.* **8**, 587 (2013).
- [18] J. C. Slonczewski. "Current-driven excitation of magnetic multilayers." *Journal of Magnetism and Magnetic Materials* **159**, L1 (1996).
- [19] J. Z. Sun. "Spin-current interaction with a monodomain magnetic body: A model study." *Phys. Rev. B* **62**, 570 (2000).

- [20] A. Chernyshov, M. Overby, X. Liu, J. K. Furdyna, Y. Lyanda-Geller, and L. P. Rokhinson. "Evidence for reversible control of magnetization in a ferromagnetic material by means of spin-orbit magnetic field." *Nat. Phys.* **5**, 656 (2009).
- [21] M. Endo, F. Matsukura, and H. Ohno. "Current induced effective magnetic field and magnetization reversal in uniaxial anisotropy (Ga,Mn)As." *Applied Physics Letters* **97**, 222501 (2010).
- [22] D. Fang, H. Kurebayashi, J. Wunderlich, K. Výborný, L. P. Zârbo, R. P. Campion, A. Casiraghi, B. L. Gallagher, T. Jungwirth, and A. J. Ferguson. "Spin-orbit-driven ferromagnetic resonance." *Nature Nanotechnology* **6**, 413 (2011).
- [23] H. Kurebayashi, J. Sinova, D. Fang, A. C. Irvine, T. D. Skinner, J. Wunderlich, V. Novak, R. P. Campion, B. L. Gallagher, E. K. Vehstedt, L. P. Zarbo, K. Vyborny, A. J. Ferguson, and T. Jungwirth. "An antidamping spin-orbit torque originating from the Berry curvature." *Nat. Nano.* **9**, 211 (2014).
- [24] P. Wadley, B. Howells, J. Železný, C. Andrews, V. Hills, R. P. Campion, V. Novák, K. Olejník, F. Maccherozzi, S. S. Dhesi, S. Y. Martin, T. Wagner, J. Wunderlich, F. Freimuth, Y. Mokrousov, J. Kuneš, J. S. Chauhan, M. J. Grzybowski, A. W. Rushforth, K. W. Edmonds, B. L. Gallagher, and T. Jungwirth. "Electrical switching of an antiferromagnet." *Science* **351**, 587 (2016).
- [25] T. D. Skinner, K. Olejník, L. K. Cunningham, H. Kurebayashi, R. P. Campion, B. L. Gallagher, T. Jungwirth, and A. J. Ferguson. "Complementary spin-Hall and inverse spin-galvanic effect torques in a ferromagnet/semiconductor bilayer." *Nat. Commun.* **6**, 6730 (2015).
- [26] M. N. Ali, J. Xiong, S. Flynn, J. Tao, Q. D. Gibson, L. M. Schoop, T. Liang,

- N. Haldolaarachchige, M. Hirschberger, N. P. Ong, and R. J. Cava. "Large, non-saturating magnetoresistance in  $WTe_2$ ." *Nature* **514**, 205 (2014).
- [27] J. Jiang, F. Tang, X. C. Pan, H. M. Liu, X. H. Niu, Y. X. Wang, D. F. Xu, H. F. Yang, B. P. Xie, F. Q. Song, P. Dudin, T. K. Kim, M. Hoesch, P. K. Das, I. Vobornik, X. G. Wan, and D. L. Feng. "Signature of Strong Spin-Orbital Coupling in the Large Nonsaturating Magnetoresistance Material  $WTe_2$ ." *Phys. Rev. Lett.* **115**, 166601 (2015).
- [28] Z. Zhu, X. Lin, J. Liu, B. Fauqué, Q. Tao, C. Yang, Y. Shi, and K. Behnia. "Quantum Oscillations, Thermoelectric Coefficients, and the Fermi Surface of Semimetallic  $WTe_2$ ." *Phys. Rev. Lett.* **114**, 176601 (2015).
- [29] L. Wang, I. Gutiérrez-Lezama, C. Barreteau, N. Ubrig, E. Giannini, and A. F. Morpurgo. "Tuning magnetotransport in a compensated semimetal at the atomic scale." *Nat. Commun.* **6**, 8892 (2015).
- [30] J. A. Wilson and A. D. Yoffe. "The transition metal dichalcogenides discussion and interpretation of the observed optical, electrical and structural properties." *Advances in Physics* **18**, 193 (1969).
- [31] Q. H. Wang, K. Kalantar-Zadeh, A. Kis, J. N. Coleman, and M. S. Strano. "Electronics and optoelectronics of two-dimensional transition metal dichalcogenides." *Nat. Nano.* **7**, 699 (2012).
- [32] W. Zhang, J. Sklenar, B. Hsu, W. Jiang, M. B. Jungfleisch, J. Xiao, F. Y. Fradin, Y. Liu, J. E. Pearson, J. B. Ketterson, Z. Yang, and A. Hoffmann. "Research Update: Spin transfer torques in permalloy on monolayer  $MoS_2$ ." *APL Mater.* **4**, 032302 (2016).

- [33] C. Cheng, M. Collet, J.-C. Rojas Sánchez, V. Ivanovskaya, B. Dlubak, P. Seineor, A. Fert, H. Kim, G. H. Han, Y. H. Lee, H. Yang, and A. Anane. "Spin to charge conversion in MoS<sub>2</sub> monolayers with spin pumping." Preprint at arXiv:1510.03451 [cond-mat.mes-hall] (2015).
- [34] B. E. Brown. "The crystal structures of WTe<sub>2</sub> and high-temperature MoTe<sub>2</sub>." *Acta Crystallographica* **20**, 268 (1966).
- [35] W.-D. Kong, S.-F. Wu, P. Richard, C.-S. Lian, J.-T. Wang, C.-L. Yang, Y.-G. Shi, and H. Ding. "Raman scattering investigation of large positive magnetoresistance material WTe<sub>2</sub>." *Applied Physics Letters* **106**, 081906 (2015).
- [36] G. Yu, P. Upadhyaya, Y. Fan, J. G. Alzate, W. Jiang, K. L. Wong, S. Takei, S. A. Bender, L.-T. Chang, Y. Jiang, M. Lang, J. Tang, Y. Wang, Y. Tserkovnyak, P. K. Amiri, and K. L. Wang. "Switching of perpendicular magnetization by spin-orbit torques in the absence of external magnetic fields." *Nat. Nano.* **9**, 548 (2014).
- [37] T. Taniguchi, J. Grollier, and M. D. Stiles. "Spin-Transfer Torques Generated by the Anomalous Hall Effect and Anisotropic Magnetoresistance." *Phys. Rev. Applied* **3**, 044001 (2015).
- [38] O. J. Lee, L. Q. Liu, C. F. Pai, Y. Li, H. W. Tseng, P. G. Gowtham, J. P. Park, D. C. Ralph, and R. A. Buhrman. "Central role of domain wall depinning for perpendicular magnetization switching driven by spin torque from the spin Hall effect." *Phys. Rev. B* **89**, 024418 (2014).
- [39] G. Yu, P. Upadhyaya, K. L. Wong, W. Jiang, J. G. Alzate, J. Tang, P. K. Amiri, and K. L. Wang. "Magnetization switching through spin-Hall-

- effect-induced chiral domain wall propagation." *Phys. Rev. B* **89**, 104421 (2014).
- [40] K. Garello, C. O. Avci, I. M. Miron, M. Baumgartner, A. Ghosh, S. Auffret, O. Boulle, G. Gaudin, and P. Gambardella. "Ultrafast magnetization switching by spin-orbit torques." *Applied Physics Letters* **105**, 212402 (2014).
- [41] N. Mikuszeit, O. Boulle, I. M. Miron, K. Garello, P. Gambardella, G. Gaudin, and L. D. Buda-Prejbeanu. "Spin-orbit torque driven chiral magnetization reversal in ultrathin nanostructures." *Phys. Rev. B* **92**, 144424 (2015).
- [42] J.-C. Rojas-Sánchez, P. Laczkowski, J. Sampaio, S. Collin, K. Bouzehouane, N. Reyren, H. Jaffrès, A. Mougin, and J.-M. George. "Perpendicular magnetization reversal in Pt/[Co/Ni]<sub>3</sub>/Al multilayers via the spin Hall effect of Pt." *Applied Physics Letters* **108**, 082406 (2016).
- [43] L. Liu, O. J. Lee, T. J. Gudmundsen, D. C. Ralph, and R. A. Buhrman. "Current-Induced Switching of Perpendicularly Magnetized Magnetic Layers Using Spin Torque from the Spin Hall Effect." *Phys. Rev. Lett.* **109**, 096602 (2012).
- [44] K.-S. Lee, S.-W. Lee, B.-C. Min, and K.-J. Lee. "Threshold current for switching of a perpendicular magnetic layer induced by spin Hall effect." *Applied Physics Letters* **102**, 112410 (2013).
- [45] M. Seemann, D. Ködderitzsch, S. Wimmer, and H. Ebert. "Symmetry-imposed shape of linear response tensors." *Phys. Rev. B* **92**, 155138 (2015).
- [46] C. Ciccarelli, L. Anderson, V. Tshitoyan, A. J. Ferguson, F. Gerhard, C. Gould, L. W. Molenkamp, J. Gayles, J. Zelezny, L. Smejkal, Z. Yuan,

- J. Sinova, F. Freimuth, and T. Jungwirth. "Room-temperature spin-orbit torque in NiMnSb." *Nat. Phys.* **12**, 855 (2016).
- [47] J. Li and P. M. Haney. "Interfacial magnetic anisotropy from a 3-dimensional Rashba substrate." *Applied Physics Letters* **109**, 032405 (2016).
- [48] V. P. Amin and M. D. Stiles. "Spin transport at interfaces with spin-orbit coupling: Formalism." *Phys. Rev. B* **94**, 104419 (2016).
- [49] V. P. Amin and M. D. Stiles. "Spin transport at interfaces with spin-orbit coupling: Phenomenology." *Phys. Rev. B* **94**, 104420 (2016).
- [50] C. O. Avci, K. Garello, M. Gabureac, A. Ghosh, A. Fuhrer, S. F. Alvarado, and P. Gambardella. "Interplay of spin-orbit torque and thermoelectric effects in ferromagnet/normal-metal bilayers." *Phys. Rev. B* **90**, 224427 (2014).

## CHAPTER 3

### THICKNESS DEPENDENCE OF SPIN-ORBIT TORQUES IN TUNGSTEN DITELLURIDE

In this Chapter, we perform a more detailed study of the current-induced torques in  $WTe_2$ /permalloy bilayers as a function of  $WTe_2$  thickness, following up on our measurements in Chapter 2. We measure the torques using both second-harmonic Hall and spin-torque ferromagnetic resonance measurements for samples with  $WTe_2$  thicknesses that span from 16 nm down to a single monolayer. We confirm the existence of an out-of-plane antidamping torque, and show directly that the sign of this torque component is reversed across a monolayer step in the  $WTe_2$ . The magnitude of the out-of-plane antidamping torque depends only weakly on  $WTe_2$  thickness, such that even a single-monolayer  $WTe_2$  device provides a strong torque that is comparable to much thicker samples. In contrast, the out-of-plane field-like torque has a significant dependence on the  $WTe_2$  thickness. We demonstrate that this field-like component originates predominantly from the Oersted field, correcting an inference drawn in our initial work on  $WTe_2$  [1]. This chapter is adapted from our work originally published in *Physical Review B* with D. MacNeill, M.H.D. Guimarães, N.D. Reynolds, R.A. Buhrman and D.C. Ralph [2].

### 3.1 Introduction

Current-induced torques in materials with strong spin-orbit coupling provide an attractive approach for efficiently manipulating nanomagnets [3]. Spin-orbit torques are most commonly studied in polycrystalline ferromagnet/heavy-metal bilayers[4–11], but several groups have also investigated crystalline spin-

orbit materials [1, 12–18]. Using non-centrosymmetric crystals, researchers have demonstrated spin-orbit torques within a single ferromagnetic layer [12, 13, 15, 18] and electrical switching of an antiferromagnet [16]. For some low-symmetry crystal structures, it is possible to generate out-of-plane polarized spin injection in response to an in-plane applied current [1]. This is an important capability for applications. Out-of-plane spin injection could enable efficient antidamping switching of high-density magnetic memory devices with perpendicular magnetic anisotropy that is not possible with conventional spin-orbit torques [1].

Recently, our group has measured current-induced torques acting on a ferromagnetic layer (permalloy, Py = Ni<sub>80</sub>Fe<sub>20</sub>) deposited on single crystals of the layered material WTe<sub>2</sub> [1] (outlined in Chapter 2). WTe<sub>2</sub> is an intriguing choice of spin-source material, due to its strong spin-orbit coupling [19, 20], surface states [21, 22], high mobility [23–25], and low-symmetry crystal structure [26, 27]. The crystal structure of WTe<sub>2</sub> is such that when current is applied along the WTe<sub>2</sub> *a*-axis, a spin-orbit torque consistent with transfer of spins oriented partially along the *z*-axis (out of the sample plane) is observed in the permalloy. The geometry is illustrated in Fig. 3.1. We refer to this torque as the out-of-plane antidamping torque,  $\tau_B$ . As discussed in our previous work, the dependence of  $\tau_B$  on the current flow direction reflects the symmetries of the WTe<sub>2</sub> surface in a detailed way.

While the existence of  $\tau_B$  is consistent with symmetry constraints, its microscopic origin is not understood. Even the conventional current-induced torques in the WTe<sub>2</sub>/Py system (an in-plane antidamping torque,  $\tau_S$ , and an out-of-plane field-like torque,  $\tau_A$ ) have not yet been assigned concrete mechanisms. Known mechanisms such as the Rashba-Edelstein effect (REE) [12, 28] and the spin

Hall effect (SHE) [29, 30] have distinct thickness dependencies once the layer thickness is comparable to the spin diffusion length. For this reason, varying the spin-source thickness can provide clues as to the origin of current-induced torques [7, 31–34].

Here, we report measurements of current-induced torques in  $\text{WTe}_2/\text{Py}$  bilayers for a wide range of  $\text{WTe}_2$  thicknesses, down to the previously-unexplored monolayer limit. We employ second-harmonic Hall [5, 35] and spin-torque ferromagnetic resonance (ST-FMR) [7, 14] measurements as complementary techniques for studying current-induced torques, and report good agreement between the two. We find that the magnitude of the out-of-plane antidamping torque component  $|\tau_B|$  depends only weakly on the  $\text{WTe}_2$  thickness  $t$  for  $t > 4$  nm, and remains significant even for thinner samples all the way to the monolayer (0.7 nm) limit for  $\text{WTe}_2$ . We also demonstrate by direct measurements that the sign of  $\tau_B$  reverses across a monolayer step. In contrast to a conclusion we made previously based on a much smaller data set [1], we find that the out-of-plane field-like torque varies as a function of  $\text{WTe}_2$  thickness with a form in quantitative agreement with a dominant contribution from the current-induced Oersted field.

## 3.2 Device Fabrication

Our  $\text{WTe}_2/\text{Py}$  stack is shown in Fig. 3.1a. To prepare the stack, we take a commercially-available  $\text{WTe}_2$  crystal (from HQgraphene), and exfoliate it onto a high-resistivity Si/SiO<sub>2</sub> wafer using Scotch tape. The final step of exfoliation, where the tape is removed from the substrate to cleave the  $\text{WTe}_2$  crystals, is car-

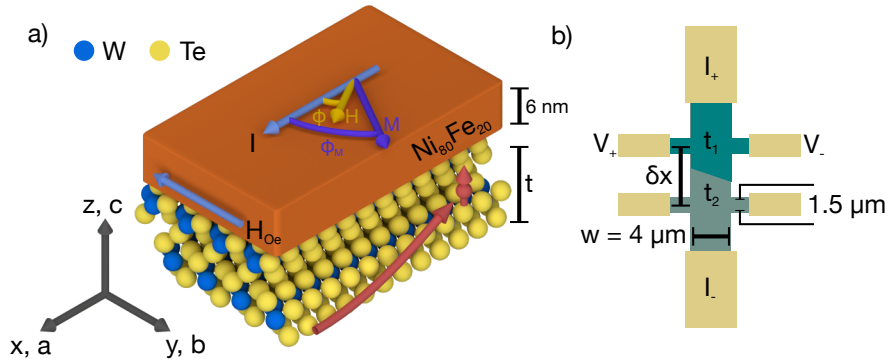


Figure 3.1: a) Illustration of our  $\text{WTe}_2/\text{Py}$  bilayers. The Py thickness is 6 nm, and the  $\text{WTe}_2$  thickness,  $t$ , varies between devices. For all devices we study, the  $\text{WTe}_2$   $c$ -axis is normal to the sample plane, and the current flow direction is chosen to be approximately aligned to the  $\text{WTe}_2$   $a$ -axis. We carry out our measurements with the magnetic field applied at a variable angle,  $\phi$  from the current flow direction. The red arrow depicts injection of out-of-plane spins into the permalloy, which can account for an out-of-plane antidamping torque. b) Illustration of the device geometry and electrical connections. For some devices, we used  $\text{WTe}_2$  with mono- or bi-layer steps in the channel, allowing for multiple thickness data points from a single device. To eliminate cross talk, we keep  $\delta x > 4 \mu\text{m}$ .

ried out in the load-lock chamber of our sputter system. The pressure at this step is well below  $1 \times 10^{-5}$  Torr. This preparation differs from our previous work (Ref. [1]), where the samples were exfoliated in flowing nitrogen after purging the load-lock. The samples are then moved to the process chamber without breaking vacuum, where we deposit 6 nm of Py by glancing angle ( $\sim 5^\circ$ ) sputtering and 2 nm of Al to prevent oxidation of the ferromagnet. The Py moment lies in the sample plane. Before further processing, the topography and thickness of the chosen flakes are characterized by atomic force microscopy (AFM). We are careful to position devices only in regions that are atomically smooth (less than 200 pm roughness) and contain no steps in the  $\text{WTe}_2$  layer, except for devices in which steps are positioned intentionally between different sets of Hall contacts (see below). The films are then patterned into Hall bars using e-beam

lithography and argon ion-milling (where we use  $\text{SiO}_2$  as the etch mask). The current-flow direction is chosen to lie along the direction of long straight edges in the cleaved  $\text{WTe}_2$  flakes, which typically corresponds to the  $\text{WTe}_2$   $a$ -axis. The angle between the current flow direction and the  $a$ -axis is later checked using planar Hall effect measurements on the completed devices (see below). This angle is always less than  $20^\circ$  and typically less than  $5^\circ$ . Contact pads of 5 nm Ti/75 nm Pt are also defined using e-beam lithography and sputtering.

### 3.3 Second-harmonic Hall measurements

We will first discuss second-harmonic Hall measurements of the spin-orbit torques. Second-harmonic Hall measurements allow for a precise calibration of the current flowing in the device (more easily than, *e.g.*, ST-FMR) and therefore provide a convenient method for making an accurate comparison between devices. When the equilibrium magnetization is in the sample plane, this technique is most easily used for measuring out-of-plane torques because in this geometry the signals for in-plane torques must be disentangled from an artifact due to the anomalous Nernst effect [36]. Our Hall bar design is shown in Fig. 3.1b. We keep the width of the channel ( $w = 4 \mu\text{m}$ ) and the voltage probes ( $1.5 \mu\text{m}$ ) consistent across all devices. This helps prevent artifacts in the thickness series due to changes in the current distribution. For the second-harmonic Hall measurements, we apply a voltage of 400 mV RMS at 1.317 kHz to the device and a series resistor, and measure the first- and second-harmonic Hall voltages simultaneously. We calibrate the current flowing through the device by measuring the voltage across the series resistor. For some of our devices we placed multiple Hall contact pairs (up to three) on the same device, with each pair

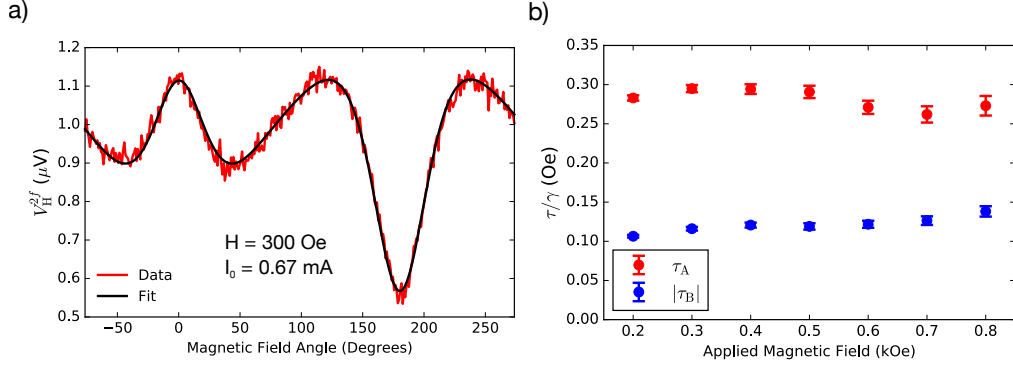


Figure 3.2: a) Second-harmonic Hall voltage for a  $\text{WTe}_2$  (5.6 nm)/Py (6 nm) bilayer as a function of the in-plane angle of the applied magnetic field (the magnitude of the applied field is 300 Oe). The red curve represents measured data, and the black line is a fit to Eq. 3.2. The lack of odd symmetry under  $\phi \rightarrow \phi + 180^\circ$  indicates the presence of an out-of-plane antidamping torque,  $\tau_B$ . b) Dependence of the measured out-of-plane field-like ( $\tau_A$ , red circles) and out-of-plane antidamping torque ( $\tau_B$ , blue circles) on the magnitude of applied magnetic field. The negligible field dependence is evidence that the signals arise from current-induced torques.

sensing regions of different  $\text{WTe}_2$  thickness. Since the transverse voltages are expected to decay as  $e^{-\pi\delta x/w}$  (see Fig. 3.1b) [37], we placed the contacts at least  $4 \mu\text{m}$  apart to avoid cross-talk. This allows for direct thickness comparisons within the same device.

The Hall resistance of a  $\text{WTe}_2/\text{Py}$  bilayer can be modeled as  $R_H = R_{\text{PHE}} \sin(2\phi_M) \sin^2(\theta_M) + R_{\text{AHE}} \cos(\theta_M)$ , where  $\phi_M$  is the angle between the Py moment and the current flow direction,  $\theta_M$  is the angle of the Py moment from the  $z$ -axis,  $R_{\text{PHE}}$  is the planar Hall resistance, and  $R_{\text{AHE}}$  is the anomalous Hall resistance. When a current  $I(t) = I_0 \sin(\omega t)$  is applied to the bilayer, any out-of-plane current-induced torques will rotate the moment in-plane,  $\phi_M \rightarrow \phi_M + \delta\phi_M \sin(\omega t)$ . In-plane torques will rotate the moment out-of-plane:  $\theta_M \rightarrow \theta_M + \delta\theta_M \sin(\omega t)$ . The Hall voltage is therefore  $V_H(t) = I(t)R_H(t) = I_0 R_H \sin(\omega t) + I_0 \frac{dR_H}{d\phi_M} \delta\phi_M \sin^2(\omega t) + I_0 \frac{dR_H}{d\theta_M} \delta\theta_M \sin^2(\omega t)$ , where the last two terms represent the response from current induced torques. Calculating  $\delta\phi_M$  and  $\delta\theta_M$  as a function of the in-plane and out-

of-plane torques,  $\tau_\phi$  and  $\tau_z$ , gives the second-harmonic ( $2\omega$ ) voltage component (see Section 3.6.1):

$$V_H^{2\omega} \approx I_0 R_{\text{PHE}} \cos(2\phi_M) \frac{\tau_z/\gamma}{H + H_A \cos(2\phi_M - 2\phi_E)} - \frac{1}{2} I_0 R_{\text{AHE}} \frac{\tau_\phi/\gamma}{H + M_s + H_A \cos^2(\phi_M - \phi_E)}, \quad (3.1)$$

where  $H$  is the applied field magnitude,  $M_s$  is the effective magnetization,  $H_A$  is the in-plane uniaxial anisotropy field, and  $\phi_E$  is the angle of the anisotropy axis relative to the current flow direction. We have previously shown that the in-plane easy-axis always lies along the  $\text{WTe}_2$   $b$ -axis in  $\text{WTe}_2/\text{Py}$  bilayers (so that  $\phi_E \approx 90^\circ$ ). We determine  $H_A$  and  $\phi_E$  for each sample by analyzing the dependence of the first-harmonic planar Hall voltage on the angle of an applied magnetic field (see Section 3.6.2). The results of this determination are given in Table 3.1. We find that the current-flow direction is always aligned with the  $\text{WTe}_2$   $a$ -axis to within better than  $20^\circ$ , and  $H_A$  has values in the range 48-96 Oe.

To complete our model, we note that torques from the Oersted field and ordinary REE and SHE will be proportional to  $\hat{m} \times \hat{y}$  and  $\hat{m} \times (\hat{m} \times \hat{y})$  respectively. Then  $\tau_{z,\text{Oe}}(\phi_M) = \tau_A \cos(\phi_M)$  and  $\tau_{\phi,\text{SHE}}(\phi_M) = \tau_S \cos(\phi_M)$ . When a magnet absorbs out-of-plane spins the resulting torque is  $\propto \hat{m} \times (\hat{m} \times \hat{z})$  [38], so that the out-of-plane antidamping torque gives an angle-independent contribution,  $\tau_z(\phi_M) = \tau_B$ , for an in-plane magnetic moment. For our fits, we also add an angle-independent voltage offset,  $C$ , and a term  $\propto \cos(\phi_M)$  to account for the anomalous Nernst effect resulting from an out-of-plane thermal gradient [36]. The resulting model for the field and angle dependence of our second-harmonic Hall data is:

$$V_H^{2\omega} = I_0 R_{\text{PHE}} \cos(2\phi_M) \frac{[\tau_A \cos(\phi_M) + \tau_B]/\gamma}{H + H_A \cos(2\phi_M - 2\phi_E)} - \frac{1}{2} I_0 R_{\text{AHE}} \frac{\tau_S \cos(\phi_M)/\gamma}{H + M_s + H_A \cos^2(\phi_M - \phi_E)} + V_{\text{ANE}} \cos(\phi_M) + C \quad (3.2)$$

where  $V_{\text{ANE}}$  is the anomalous Nernst voltage. In our system  $H_A \ll M_s$ , which

means the anomalous Nernst effect and the in-plane torques give second-harmonic Hall voltages with indistinguishable  $\phi$  dependence. We fit them with a single term  $\propto \cos(\phi_M)$ . There are six other fit parameters:  $I_0 R_{\text{PHE}} \tau_A$ ,  $I_0 R_{\text{PHE}} \tau_B$ ,  $H_A$ ,  $\phi_E$ ,  $C$ , and an overall angular offset not shown here which accounts for any misalignment of the device from the axes of the measurement apparatus.  $I_0 R_{\text{PHE}}$  is determined independently using the  $\phi$ -dependence of the first-harmonic Hall voltage, allowing measurements of  $\tau_A$  and  $\tau_B$  from data for  $V_{\text{H}}^{2\omega}$  as a function of  $\phi$ .

Figure 3.2a shows  $V_{\text{H}}^{2\omega}(\phi)$  data from one of our WTe<sub>2</sub>/Py bilayers. The WTe<sub>2</sub> is 5.6 nm thick and the current flows along the WTe<sub>2</sub>  $a$ -axis ( $\phi_E \approx 90^\circ$ ). The red line shows measured data, and the black line is a fit to Eq. 3.2. The existence of a non-zero value of  $\tau_B$  is apparent from the lack of  $\phi \rightarrow \phi + 180^\circ$  symmetry; in particular, the different-sized peaks at  $\phi = 0$  and  $\phi = 180^\circ$  relate to the cooperation  $\tau_z = \tau_B + \tau_A$  or competition  $\tau_z = \tau_B - \tau_A$  of the different out-of-plane torques. This asymmetry reflects the absence of rotational symmetry at the WTe<sub>2</sub> surface. Figure 3.2b shows  $\tau_A$  and  $\tau_B$  (from fits to Eq. 3.2) as a function of the applied magnetic field. The extracted torques are to a good approximation independent of the magnitude of the applied field, confirming that they originate from current-induced torques.

A key prediction of our symmetry arguments in Ref. [1] is that the sign of  $\tau_B$  should change across a monolayer step in WTe<sub>2</sub> thickness, if this step occurs at the Py/WTe<sub>2</sub> interface. This is because adjacent WTe<sub>2</sub> layers are related by a  $180^\circ$  rotation around the  $c$ -axis (see Fig. 3.3), and  $\tau_B$  is not two-fold symmetric –  $\tau_B$  changes sign with a  $180^\circ$  rotation about the  $c$ -axis. In Ref. [1] we presented indirect evidence for this conclusion, in which a sample whose de-

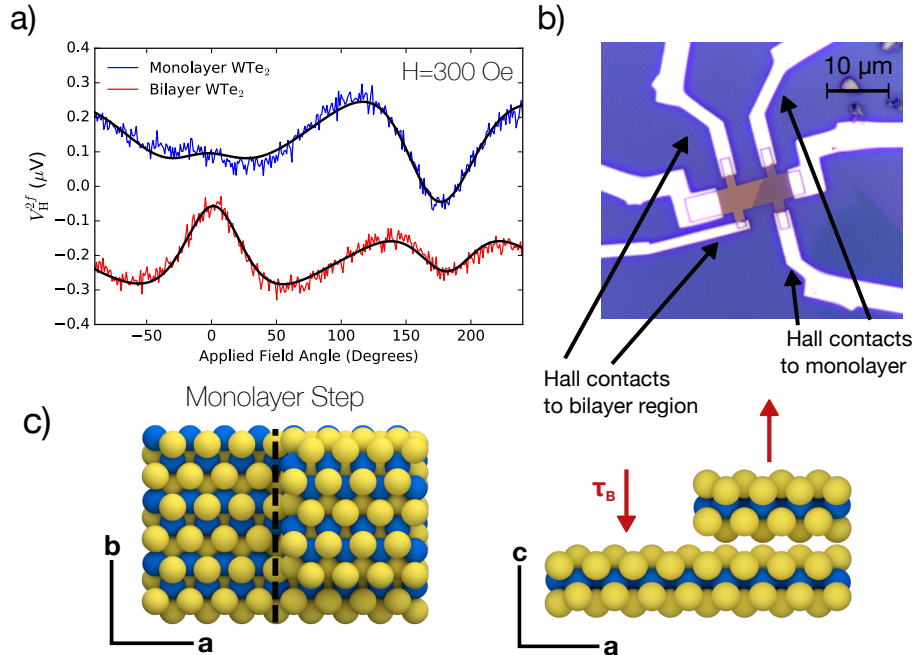


Figure 3.3: a) Second-harmonic Hall data for a  $\text{WTe}_2/\text{Py}$  device for a region of the sample with a monolayer-thick  $\text{WTe}_2$  layer (top curve, blue) and for a different region of the same sample with bilayer  $\text{WTe}_2$  (bottom curve, red), as a function of the angle of the applied magnetic field (defined relative to the current flow direction). The lines are fits to Eq. 3.2. The sign reversal of  $\tau_B$  is reflected in the different angles at which the peak signals are found. A vertical offset is added to the data for ease of viewing. b) Optical micrograph of the device measured for panel a), showing the monolayer and bilayer  $\text{WTe}_2$  regions in false color. c) Schematic of the crystal structure of  $\text{WTe}_2$ , showing that the surface structure is rotated by  $180^\circ$  across a monolayer step.

vice area spanned across a single-monolayer step in the  $\text{WTe}_2$  layer exhibited a suppressed value of  $\tau_B$  due to partial cancellations of the contributions from the two crystal faces. Here we provide a direct test by fabricating devices containing multiple Hall contacts so that we can separately measure the values of  $\tau_B$  produced by different regions of the same sample separated by steps of known height (see Fig. 3.1). We have fabricated 6 devices with Hall contacts on either side of a monolayer step, as determined by AFM measurements showing a step height  $0.7 \pm 0.3 \text{ nm}$ . Fig. 3.3 shows second-harmonic Hall data for a device where the  $\text{WTe}_2$  thickness increases from a monolayer to a bilayer in the mid-

dle of the channel. For the monolayer side we found  $\tau_B/\gamma = -0.093 \pm 0.002$  Oe whereas for the bilayer side  $\tau_B/\gamma = 0.049 \pm 0.002$  Oe. The out-of-plane field-like component  $\tau_A$  has the same sign on both sides of the step ( $\tau_A/\gamma = 0.103 \pm 0.004$  Oe and  $\tau_A/\gamma = 0.123 \pm 0.003$  Oe for the monolayer and bilayer respectively). In 5/6 devices with Hall contacts on opposite sides of a monolayer step, we found that  $\tau_B$  changes sign between contacts (see Table 3.1). In principle, the monolayer step we observe by AFM could be on either the top (Py/WTe<sub>2</sub>) or bottom (WTe<sub>2</sub>/SiO<sub>2</sub>) interface of the WTe<sub>2</sub>, and we do not expect that a step at the WTe<sub>2</sub>/SiO<sub>2</sub> interface would affect the sign of  $\tau_B$ . Therefore it is somewhat surprising that we observe sign changes in more than 50% of samples. It may be that the mechanics of exfoliation cause steps in the WTe<sub>2</sub> to be more likely on the top surface of the flake than the bottom. In devices with a bilayer step dividing two sets of Hall contacts,  $\tau_B$  never changes sign (3/3 devices).

### 3.4 WTe<sub>2</sub> Thickness Dependence

We now turn to our thickness series over multiple devices. In total, we measured torques from 12 distinct devices, some with multiple Hall contacts per device. The resulting data are shown in Fig. 3.4a, where we plot  $|\tau_B|w/I_0$  (blue points) and  $\tau_A w/I_0$  (red points) as a function of WTe<sub>2</sub> thickness. The complete data set is given in Table 3.1. We normalize the torques by the current density  $I_0/w$  since we can measure the current flowing in the channel more easily than the electric field. We observe in Fig. 3.4a that the out-of-plane field-like torque  $\tau_A/I_0$  has a significant dependence on the WTe<sub>2</sub> thickness, increasing by a factor of over 4.8 between the monolayer sample and 16 nm, while the out-of-plane antidamping torque has a much weaker dependence.

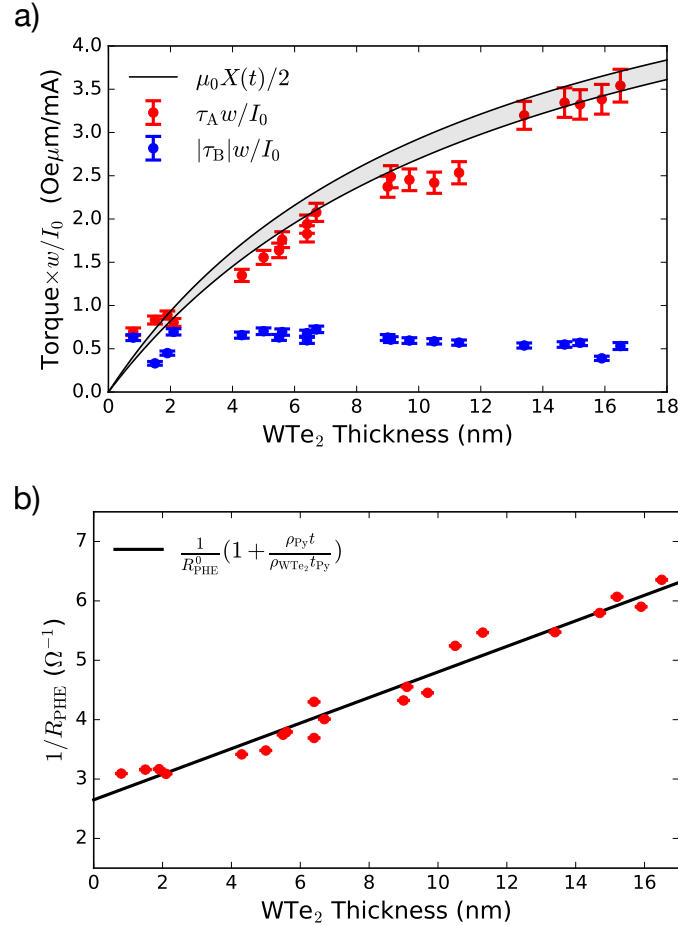


Figure 3.4: a) Torques normalized per unit  $I_0/w$  for (red circles) the out-of-plane field-like component  $\tau_A w / I_0$  and (blue circles) the out-of-plane antidamping component  $|\tau_B| w / I_0$ , as a function of  $\text{WTe}_2$  thickness, for all devices measured. The shaded region shows a  $\pm 1\sigma$  estimate for the torque from the magnetic field generated by the current flowing in the  $\text{WTe}_2$ . b) (red circles) Dependence of the inverse of the first-harmonic planar Hall resistance on the  $\text{WTe}_2$  thickness. Current shunting through the  $\text{WTe}_2$  leads to a linear increase in  $1/R_{\text{PHE}}$  as  $t$  is increased. The black line is a linear fit, which gives an estimate of the shunt factor  $X(t)$  as a function of  $\text{WTe}_2$  thickness.

Device Name	$t$ (nm) $\pm 0.3$ nm	$L$ ( $\mu\text{m}$ ) $\pm 0.2$ $\mu\text{m}$	$\tau_A$ (Oe)	$\tau_B$ (Oe)	$H_A$ (Oe)	$\phi_E - 90^\circ$ (Degrees)	$I_0$ ( $\mu\text{A}$ ) $\pm 0.1$ $\mu\text{A}$
SH4D10S1	5.6	13	0.295(4)	-0.116(2)	57.6(4)	2.9(2)	670.0
SH4D10S2	6.4	13	0.325(7)	0.100(3)	61.8(5)	2.7(2)	670.0
SH4D7S1	0.8	12.5	0.103(4)	-0.093(2)	48(4)	-2.6(2)	591.3
SH4D7S2	1.5	12.5	0.123(3)	0.049(2)	54.4(5)	-1.9(3)	591.3
SH4D6S1	16.5	23.5	0.473(9)	-0.071(4)	60.9(5)	1.7(2)	534.3
SH4D6S2	15.9	23.5	0.452(4)	0.052(2)	54.3(5)	2.0(2)	534.3
SH4D6S3	15.2	23.5	0.444(5)	-0.076(2)	58.9(5)	2.9(2)	534.3
SH5D12S1	6.7	9.5	0.410(3)	0.143(2)	64.7(9)	-1.7(4)	789.7
SH5D18S1	2.1	8.5	0.155(4)	-0.134(2)	57.7(5)	18.8(2)	770.8
SH5D26S1	5.5	14.5	0.249(3)	0.096(2)	63.1(8)	4.2(4)	608.3
SH5D26S2	4.3	14.5	0.205(3)	0.100(2)	60.6(2)	4.6(4)	608.3
SH5D25S1	11.3	10.0	0.506(4)	0.114(2)	57.5(7)	2.6(3)	798.6
SH5D25S2	10.5	10.0	0.483(4)	0.117(2)	56.9(7)	1.8(3)	798.6
SH5D29S1	6.4	17.1	0.242(3)	0.090(1)	61.1(8)	2.7(4)	529.4
SH5D29S2	5.0	17.1	0.206(3)	0.093(2)	64.6(8)	2.3(3)	529.4
SH5D28S1	9.7	17.5	0.367(4)	-0.089(2)	68.1(6)	2.1(2)	598.4
SH5D28S2	9.0	17.5	0.355(4)	0.094(2)	69.3(9)	2.4(4)	598.4
SH5D32S1	1.7	7.0	0.192(3)	0.097(2)	77.4(9)	-2.4(3)	862.9
SH5D33S1	13.4	14.0	0.565(4)	-0.095(2)	72(1)	0.5(4)	706.7
SH5D33S2	14.7	14.0	0.591(6)	-0.097(3)	67.9(7)	0.3(3)	706.7
SH5D36S1	9.1	8.5	0.530(6)	0.129(3)	96(2)	-16.1(4)	851.8

Table 3.1: Device parameters, torques measured by the second-harmonic Hall technique (for the values of applied current  $I_0$  listed in the last column), and measured magnetic anisotropy parameters for the  $\text{WTe}_2/\text{Py}$  bilayers analyzed in the main text. Here  $\phi_E$  is the angle of the magnetic easy-axis with respect to the current flow direction, and  $H_A$  is the anisotropy field. The number after ‘‘S,’’ in each device name indexes the sets of contacts on the same device.

In many spin-orbit torque systems (but not all [14, 17, 18, 39]), the out-of-plane field-like torque  $\tau_A$  is dominated by a contribution from the Oersted field. The Oersted torque is related to the fraction of current flowing in the non-magnetic underlayer,  $X(t) \equiv I_{\text{WTe}_2}/I_0$ , by  $\tau_{\text{Oe}} = \mu_0 X(t) I_0 / 2w$  where  $I_0 = I_{\text{Py}} + I_{\text{WTe}_2}$ . To determine the factor  $X(t)$  for our devices, we examine the planar Hall resistance extracted from the first-harmonic Hall voltage as a function of  $t$  (shown in Fig. 3.4b). The observed linear dependence on  $\text{WTe}_2$  thickness is consistent with a reduction in the planar Hall resistance due to shunting through the  $\text{WTe}_2$ , and an approximately-constant  $\text{WTe}_2$  resistivity:

$$\frac{1}{R_{\text{PHE}}} = \frac{I_{\text{Py}} + I_{\text{WTe}_2}}{V_{\text{PHE}}} = \frac{1}{R_{\text{PHE}}^0} \left[ 1 + \frac{\rho_{\text{Py}} t}{\rho_{\text{WTe}_2} t_{\text{Py}}} \right], \quad (3.3)$$

where  $1/R_{\text{PHE}}^0 \equiv I_{\text{Py}}/V_{\text{PHE}}$  when  $I_{\text{Py}} = I_0$ . The fit yields a normalized WTe<sub>2</sub> conductivity of  $\rho_{\text{Py}}/(\rho_{\text{WTe}_2}t_{\text{Py}}) = 0.081 \pm 0.006 \text{ nm}^{-1}$  and a planar Hall coefficient of  $R_{\text{PHE}}^0 = 0.38 \pm 0.1 \text{ } \Omega$  for the Py. The normalized WTe<sub>2</sub> conductivity can be used to estimate:

$$X(t) \approx \frac{1}{1 + \frac{\rho_{\text{WTe}_2}t_{\text{Py}}}{\rho_{\text{Py}}t}}. \quad (3.4)$$

The shaded black area of Fig. 3.4a shows the range of the expected Oersted torque (times  $w/I_0$ ) within one standard deviation of the best-fit value for  $\rho_{\text{Py}}/(\rho_{\text{WTe}_2}t_{\text{Py}})$ . The measured points for  $\tau_{\text{A}}w/I_0$  all fall close to this area, indicating that  $\tau_{\text{A}}$  is dominated by the current-generated Oersted field. This result differs from a conclusion we drew based on a more limited data set of devices with  $\phi_{a-1} < 20^\circ$  in Ref. [1]. Of course, our data can not rule out additional spin-orbit contributions, which may be detected by more precise calibration of the Oersted field.

As noted above, compared to  $\tau_{\text{A}}w/I_0$ , the out-of-plane antidamping torque  $|\tau_{\text{B}}|w/I_0$  displays a much weaker dependence on WTe<sub>2</sub> thickness. The form of this weaker dependence is displayed in Fig. 3.5, which shows a zoomed-in plot of the same data as in Fig. 3.4a (blue points). For WTe<sub>2</sub> thicknesses greater than 4 nm,  $|\tau_{\text{B}}|w/I_0$  decreases slightly as the WTe<sub>2</sub> thickness is increased. This slight decrease is consistent with current shunting, if one assumes that  $|\tau_{\text{B}}|$  is proportional to the applied electric field within the device. In this case  $|\tau_{\text{B}}|w/I_0$  should be proportional to  $X(t)/t$ . This proportionality occurs because for a given applied current  $I_0$  the total electric field will decrease with increasing WTe<sub>2</sub> thickness due a decreased overall device resistance. The black line in Fig. 3.5 shows  $X(t)/t$  estimated from the PHE data of Fig. 3.4b, re-scaled to fit the  $|\tau_{\text{B}}|w/I_0$  data for WTe<sub>2</sub> thicknesses above 4 nm. This good agreement, however, tells us little about the origin of  $\tau_{\text{B}}$ , since the total electric field in the device, the charge

current density in the  $\text{WTe}_2$ , and the charge current density in the Py are all proportional to this factor.

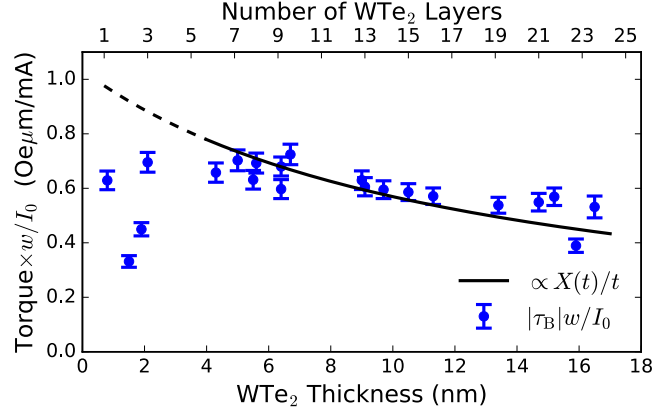


Figure 3.5:  $|\tau_B|w/I_0$  as a function of  $\text{WTe}_2$  thickness (blue circles), along with a curve proportional to  $X(t)/t$  as estimated from our planar Hall effect data (black solid and dashed lines). The proportionality constant is chosen to fit the data above 4 nm of  $\text{WTe}_2$  thickness.

For  $t < 4$  nm, the measurements of  $|\tau_B|$  exhibit significantly increased scatter, but even in this regime  $|\tau_B|$  can remain large. For the one sample with a single-monolayer  $\text{WTe}_2$  that we have been able to study, we find  $|\tau_B|w/I_0 = 0.63 \pm 0.03$  Oe  $\mu\text{m}/\text{mA}$ , very comparable to the values measured for much thicker  $\text{WTe}_2$  layers, and fully 65% of the value expected simply by scaling the results from the thicker layers by the factor  $X(t)/t$  (see Fig. 3.5). Our observation that the torque for monolayer  $\text{WTe}_2$  samples is not suppressed close to zero suggests that either the spin diffusion length in  $\text{WTe}_2$  is very short, comparable to the layer spacing, or else the out-of-plane antidamping torque results from a spin current generated in the Py layer that reflects off of the  $\text{WTe}_2$  surface [40–42]. Our data for very thin  $\text{WTe}_2$  layers also provides a hint that there might be an even-odd effect in the number of  $\text{WTe}_2$  layers, in that  $|\tau_B|$  for a bilayer sample is the smallest for any of our devices, and in particular it is smaller than for either the monolayer sample or trilayer samples.

To confirm the results of Fig. 3.4a using an independent measurement technique, we also performed ST-FMR measurements using two-terminal devices fabricated from our vacuum-exfoliated  $\text{WTe}_2/\text{Py}$  bilayers. The ST-FMR technique has the advantage that it can provide reliable measurements of both out-of-plane and in-plane current-induced torques, although the current calibration has greater uncertainty because this calibration must be performed using network-analyzer reflectance measurements [39]. For this reason, we will present our ST-FMR results in terms of ratios for the different torque components, in which case the current calibration does not enter.

For the ST-FMR samples, the  $\text{WTe}_2/\text{Py}$  bilayers were etched into bars and contacted in a ground-signal-ground geometry compatible with microwave probes. The device geometry and protocol for our ST-FMR measurements are detailed in Ref. [1]; for the data shown here, the applied frequency was 9 GHz. Figure 3.6a compares the torque ratios  $|\tau_B/\tau_A|$  measured with ST-FMR to those from second-harmonic Hall measurements as a function of  $\text{WTe}_2$  thickness. The ratio  $|\tau_B/\tau_A|$  shows good agreement with the second-harmonic Hall measurements.

Figure 3.6b displays the in-plane torques measured with ST-FMR. Consistent with the results in Ref. [1] we measure a significant in-plane antidamping torque of the form  $\tau_S \hat{m} \times (\hat{m} \times \hat{y})$ . We find that  $|\tau_S/\tau_B| > 1$  and that  $|\tau_S/\tau_B|$  does not depend strongly on thickness. As in Ref. [1], we again note that although symmetry allows for an in-plane field-like torque of the form  $\tau_T \hat{m} \times \hat{z}$ , we find that  $\tau_T = 0$  within our measurement uncertainty.

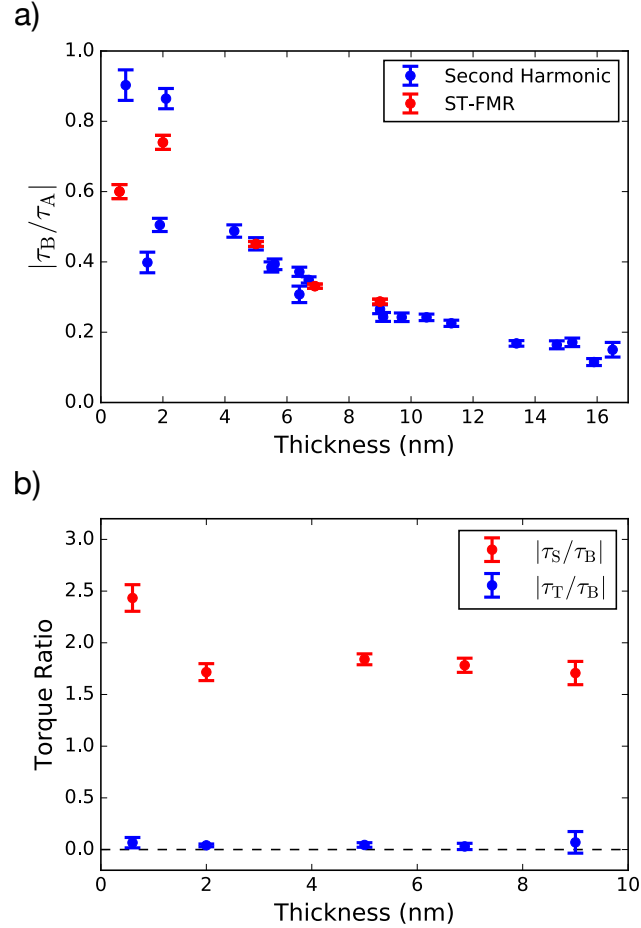


Figure 3.6: a) Comparison of the torque ratios  $|\tau_B/\tau_A|$  from ST-FMR and second-harmonic Hall measurements for WTe<sub>2</sub>/Py bilayers, as a function of thickness. The blue circles give  $|\tau_B/\tau_A|$  from the second-harmonic Hall measurements, and the red circles are the values from ST-FMR. For all ST-FMR measurements, the applied frequency was 9 GHz, and for the second-harmonic measurements, the applied magnetic field was 300 Oe. b) (red circles) Ratios of the in-plane antidamping torque  $\tau_S$  to the out-of-plane antidamping torque  $\tau_B$  as a function of WTe<sub>2</sub> thickness. (blue circles) Ratios of the in-plane field-like torque  $\tau_T$  to the out-of-plane antidamping torque  $\tau_B$  as a function of WTe<sub>2</sub> thickness. The latter ratio is zero within our measurement uncertainty.

### 3.5 Conclusion

In summary, we measure current-induced torques in  $WTe_2/Py$  bilayers as a function of  $WTe_2$  thickness. We provide direct confirmation that the out-of-plane antidamping torque  $\tau_B$  changes sign across a monolayer step in the  $WTe_2$ , consistent with the non-symmorphic symmetries in bulk  $WTe_2$ . For  $WTe_2$  thicknesses  $t$  greater than 4 nm,  $|\tau_B|$  decreases slowly with increasing thickness consistent with simple current shunting within the bilayer. For  $t$  less than 4 nm,  $|\tau_B|$  exhibits significant device-to-device variations, which might be associated with finite size effects, interfacial charge transfer, or electronic structure changes. Nevertheless,  $\tau_B$  remains large even for a single-monolayer of  $WTe_2$ . The out-of-plane field-like torque  $\tau_A$  displays a much stronger dependence on  $WTe_2$  thickness, that is quantitatively consistent with the effect of the Oersted field produced by current flowing within the  $WTe_2$  layer. This conclusion regarding the dependence of field-like torque component on  $WTe_2$  thickness represents a correction of our previous report based on a more limited data set of devices with  $\phi_{a-I} < 20^\circ$  [1].

Acknowledgements: This work was supported by the National Science Foundation (DMR-1406333), and by the NSF MRSEC program through the Cornell Center for Materials Research (DMR-1120296). G.M.S. acknowledges support by a National Science Foundation Graduate Research Fellowship under Grant No. DGE-1144153. M.H.D.G. acknowledges support by the Netherlands Organization for Scientific Research (NWO 680-50-1311) and the Kavli Institute at Cornell for Nanoscale Science. This work made use of the Cornell Nanoscale Facility, which is supported by the NSF (ECCS-1542081) and the Cornell Center for Materials Research Shared Facilities.

## 3.6 Appendix

### 3.6.1 Derivation of Eq. 3.1 from the Landau-Lifshitz-Gilbert-Slonczewski equation

Our derivation of Eq. 3.1 in the main text is an adaptation of the analysis in Ref. [35]. To calculate the displacement of the permalloy magnetic moment in response to the current-induced torque,  $\tau$ , we solve the Landau-Lifshitz-Gilbert-Slonczewski (LLGS) equation in the static limit; that is, with  $d\hat{m}/dt = 0$ , where  $\hat{m}$  is a unit vector pointing along the macrospin magnetization direction. This reduces to the condition that the net torque (current-induced torque plus the torques from the magnetic anisotropy and applied field) on the magnet vanishes:

$$0 = -\gamma\hat{m} \times \left[ H\hat{h} - M_s(\hat{m} \cdot \hat{z})\hat{z} + H_A(\hat{m} \cdot \hat{b})\hat{b} \right] + \tau, \quad (3.5)$$

where  $\hat{b}$  points along the  $\text{WTe}_2$   $b$ -axis (the magnetic easy axis), and  $\hat{z}$  points out of the sample plane. We also introduce vectors for the direction of the in-plane applied field ( $\hat{h}$ ) and the total current induced torque ( $\tau$ ).

To solve Eq. 3.5 for the current-induced reorientation of the magnetization, we linearize the equation around the equilibrium (zero-current) magnetization direction  $\hat{r}$ , setting  $\hat{m} \approx \hat{r} + m_z\hat{z} + m_\phi\hat{z} \times \hat{r}$ . Here  $\hat{z} \times \hat{r}$  gives an in-plane unit vector orthogonal to the equilibrium magnetization. In equilibrium the magnetization will point along the total anisotropy field, leading to a self-consistency condition:

$$\hat{r} = \left[ H\hat{h} + H_A(\hat{r} \cdot \hat{b})\hat{b} \right] / H_{\text{eq}}, \quad (3.6)$$

where we have introduced  $H_{\text{eq}}$ , which is the total anisotropy field evaluated at

the equilibrium position of the magnetization and so equals  $|H\hat{h} + H_A \cos \phi_{M-E}\hat{b}|$ .  $\phi_{M-E}$  is the angle between the magnetic moment and the magnetic easy axis in equilibrium.

We can conveniently regroup the terms in the anisotropy field using the consistency condition and  $\hat{m} \cdot \hat{b} = \hat{r} \cdot \hat{b} + m_\phi(\hat{z} \times \hat{r}) \cdot \hat{b}$ :

$$\boldsymbol{\tau}/\gamma = \hat{m} \times \left[ H_{\text{eq}}\hat{r} - M_s m_z \hat{z} - H_A m_\phi \sin \phi_{M-E} \hat{b} \right], \quad (3.7)$$

where we use  $\hat{b} = \cos \phi_{M-E} \hat{r} - \sin \phi_{M-E} \hat{z} \times \hat{r}$  to evaluate  $(\hat{z} \times \hat{r}) \cdot \hat{b}$ . Substituting in the approximation for  $\hat{m}$  and expanding the cross-product gives:

$$\begin{aligned} \boldsymbol{\tau}/\gamma = & (M_s + H_{\text{eq}}) m_z \hat{z} \times \hat{r} \\ & - (H_{\text{eq}} - H_A \sin^2 \phi_{M-E}) m_\phi \hat{z}, \end{aligned} \quad (3.8)$$

where we have dropped all terms at second order in the small deviations  $m_\phi$  and  $m_z$ . This equation is decoupled in  $m_\phi$  and  $m_z$  and so can trivially be solved to find  $\delta\phi_M = m_\phi$  and  $\delta\theta_M = -m_z$  required for Eq. 3.1.

The final ingredient is an approximation for  $H_{\text{eq}}$ , which proceeds from Eq. 3.6

$$\begin{aligned} H_{\text{eq}}^2 = & \left| H\hat{h} + H_A \cos \phi_{M-E} \hat{b} \right|^2, \\ H_{\text{eq}} \approx & H + H_A \cos^2 \phi_{M-E}, \end{aligned} \quad (3.9)$$

where we assume  $H_A \ll H$  and keep terms to first order in  $H_A/H$ . This approximation together with Eq. 3.8 yields the denominators of Eq. 3.1.

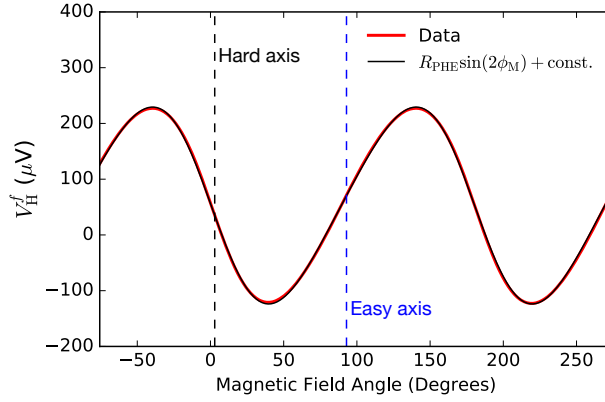


Figure 3.7:  $V_H^f$  versus  $\phi$  for a  $WTe_2/Py$  bilayer with a 5.6 nm  $WTe_2$  underlayer (red). The applied field is 300 Oe. The presence of in-plane magnetic anisotropy is apparent from the lack of symmetry around  $\phi = 45^\circ$ . The solid black line is a fit assuming an in-plane uniaxial field of magnitude  $H_A$  with an easy-axis at  $\phi_E$  from the current-flow direction. The values for  $\phi_E$  and  $H_A$  determined from the fit are recorded in the “SH4D10S1” row of Table 3.1. The dotted black and blue lines give the estimated angles of the magnetic hard and easy axes respectively. These are equivalent to the  $WTe_2$  crystal  $a$  and  $b$  axes.

### 3.6.2 Determination of the magnetic easy-axis from first-harmonic Hall measurements

To confirm the alignment of the current flow direction to the  $WTe_2$   $a$ -axis, we use first-harmonic Hall measurements. This is possible since the  $WTe_2$   $a$ -axis is always along the hard direction of the in-plane uniaxial magnetic anisotropy. We previously established this fact through comparison of ST-FMR, second-harmonic Hall, and polarized Raman scattering measurements [1]. Because of the in-plane uniaxial anisotropy, the magnetization angle of the permalloy,  $\phi_M$ , will deviate slightly from the applied field angle,  $\phi$ . The equilibrium magnetization angle satisfies the condition:

$$\sin(\phi_M - \phi) = -\frac{H_A}{2H} \sin(2\phi_M - 2\phi_E). \quad (3.10)$$

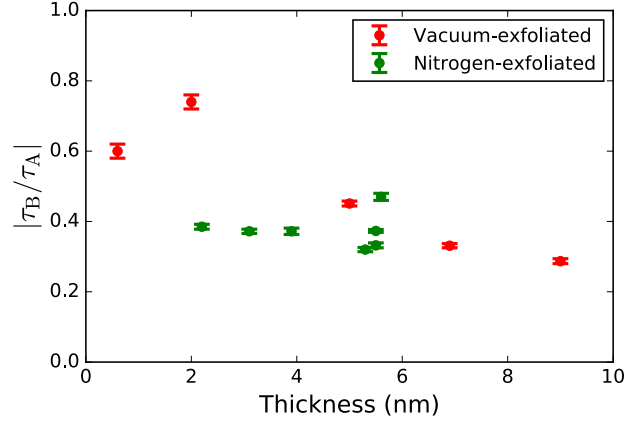


Figure 3.8:  $|\tau_B/\tau_A|$  extracted from ST-FMR measurements on (green points) devices from Ref. [1] exfoliated in flowing nitrogen and (red points) devices from this paper exfoliated in vacuum.

Assuming that  $H_A \ll H$  we can solve this equation up to first order in  $H_A/H$  giving:

$$\phi_M = \phi - \frac{H_A}{2H} \sin(2\phi - 2\phi_E). \quad (3.11)$$

Fitting the first-harmonic Hall data to  $R_H = R_{\text{PHE}} \sin(2\phi_M)$  (and a constant offset), then allows a measurement of  $\phi_E$  and  $H_A$ . Data for  $V_H^f$  versus  $\phi$ , along with a fit, are given in Fig. 3.7.

### 3.6.3 Comparison between ST-FMR data in nitrogen and vacuum exfoliated $\text{WTe}_2$ .

As discussed in the main text, for the ST-FMR data in Ref. [1] we exfoliated  $\text{WTe}_2$  flakes in flowing nitrogen in the load-lock chamber of our sputter system. For both the second-harmonic Hall and ST-FMR data in this paper, we exfoliated the  $\text{WTe}_2$  flakes in the load-lock under vacuum better than  $1 \times 10^{-5}$  Torr. The ratio  $|\tau_B/\tau_A|$  extracted via ST-FMR on the two device types is compared in Fig. 3.8. For

WTe<sub>2</sub> films around 4 nm, the vacuum exfoliated (red) and nitrogen-exfoliated (green) devices are in good agreement, whereas there is apparent disagreement for thinner flakes. We are not certain whether this apparent disagreement arises from low statistics, or from reaction of the WTe<sub>2</sub> during the nitrogen exfoliation. The effects of oxygen/water exposure on the WTe<sub>2</sub> surface merit further study.

## References

- [1] D. MacNeill, G. M. Stiehl, M. H. D. Guimaraes, R. A. Buhrman, J. Park, and D. C. Ralph. "Control of spin-orbit torques through crystal symmetry in WTe<sub>2</sub>/ferromagnet bilayers." *Nat. Phys.* **13**, 300 (2017).
- [2] D. MacNeill, G. M. Stiehl, M. H. D. Guimarães, N. D. Reynolds, R. A. Buhrman, and D. C. Ralph. "Thickness dependence of spin-orbit torques generated by WTe<sub>2</sub>." *Physical Review B* **96**, 054450 (2017).
- [3] A. Brataas, A. D. Kent, and H. Ohno. "Current-induced torques in magnetic materials." *Nat. Mater.* **11**, 372 (2012).
- [4] K. Ando, S. Takahashi, K. Harii, K. Sasage, J. Ieda, S. Maekawa, and E. Saitoh. "Electric Manipulation of Spin Relaxation Using the Spin Hall Effect." *Phys. Rev. Lett.* **101**, 036601 (2008).
- [5] U. H. Pi, K. W. Kim, J. Y. Bae, S. C. Lee, Y. J. Cho, K. S. Kim, and S. Seo. "Tilting of the spin orientation induced by Rashba effect in ferromagnetic metal layer." *App. Phys. Lett.* **97**, 162507 (2010).
- [6] I. Mihai Miron, G. Gaudin, S. Auffret, B. Rodmacq, A. Schuhl, S. Pizzini, J. Vogel, and P. Gambardella. "Current-driven spin torque induced by the Rashba effect in a ferromagnetic metal layer." *Nat. Mater.* **9**, 230 (2010).

- [7] L. Liu, T. Moriyama, D. C. Ralph, and R. A. Buhrman. "Spin-Torque Ferromagnetic Resonance Induced by the Spin Hall Effect." *Phys. Rev. Lett.* **106**, 036601 (2011).
- [8] I. M. Miron, K. Garello, G. Gaudin, P.-J. Zermatten, M. V. Costache, S. Auffret, S. Bandiera, B. Rodmacq, A. Schuhl, and P. Gambardella. "Perpendicular switching of a single ferromagnetic layer induced by in-plane current injection." *Nature* **476**, 189 (2011).
- [9] L. Liu, O. J. Lee, T. J. Gudmundsen, D. C. Ralph, and R. A. Buhrman. "Current-Induced Switching of Perpendicularly Magnetized Magnetic Layers Using Spin Torque from the Spin Hall Effect." *Phys. Rev. Lett.* **109**, 096602 (2012).
- [10] L. Liu, C.-F. Pai, Y. Li, H. W. Tseng, D. C. Ralph, and R. A. Buhrman. "Spin-Torque Switching with the Giant Spin Hall Effect of Tantalum." *Science* **336**, 555 (2012).
- [11] C.-F. Pai, L. Liu, Y. Li, H. W. Tseng, D. C. Ralph, and R. A. Buhrman. "Spin transfer torque devices utilizing the giant spin Hall effect of tungsten." *App. Phys. Lett.* **101**, 122404 (2012).
- [12] A. Chernyshov, M. Overby, X. Liu, J. K. Furdyna, Y. Lyanda-Geller, and L. P. Rokhinson. "Evidence for reversible control of magnetization in a ferromagnetic material by means of spin-orbit magnetic field." *Nat. Phys.* **5**, 656 (2009).
- [13] M. Endo, F. Matsukura, and H. Ohno. "Current induced effective magnetic field and magnetization reversal in uniaxial anisotropy (Ga,Mn)As." *App. Phys. Lett.* **97**, 222501 (2010).

- [14] D. Fang, H. Kurebayashi, J. Wunderlich, K. Vyborny, L. P. Zarbo, R. P. Campion, A. Casiraghi, B. L. Gallagher, T. Jungwirth, and A. J. Ferguson. "Spin-orbit-driven ferromagnetic resonance." *Nat. Nano.* **6**, 413 (2011).
- [15] H. Kurebayashi, J. Sinova, D. Fang, A. C. Irvine, T. D. Skinner, J. Wunderlich, V. Novak, R. P. Campion, B. L. Gallagher, E. K. Vehstedt, L. P. Zarbo, K. Vyborny, A. J. Ferguson, and T. Jungwirth. "An antidamping spin-orbit torque originating from the Berry curvature." *Nat. Nano.* **9**, 211 (2014).
- [16] P. Wadley, B. Howells, J. Železný, C. Andrews, V. Hills, R. P. Campion, V. Novák, K. Olejník, F. Maccherozzi, S. S. Dhesi, S. Y. Martin, T. Wagner, J. Wunderlich, F. Freimuth, Y. Mokrousov, J. Kuneš, J. S. Chauhan, M. J. Grzybowski, A. W. Rushforth, K. W. Edmonds, B. L. Gallagher, and T. Jungwirth. "Electrical switching of an antiferromagnet." *Science* **351**, 587 (2016).
- [17] T. D. Skinner, K. Olejník, L. K. Cunningham, H. Kurebayashi, R. P. Campion, B. L. Gallagher, T. Jungwirth, and A. J. Ferguson. "Complementary spin-Hall and inverse spin-galvanic effect torques in a ferromagnet/semiconductor bilayer." *Nat. Comm.* **6**, 6730 (2015).
- [18] C. Ciccarelli, L. Anderson, V. Tshitoyan, A. J. Ferguson, F. Gerhard, C. Gould, L. W. Molenkamp, J. Gayles, J. Zelezny, L. Smejkal, Z. Yuan, J. Sinova, F. Freimuth, and T. Jungwirth. "Room-temperature spin-orbit torque in NiMnSb." *Nat. Phys.* **12**, 855 (2016).
- [19] D. Rhodes, S. Das, Q. R. Zhang, B. Zeng, N. R. Pradhan, N. Kikugawa, E. Manousakis, and L. Balicas. "Role of spin-orbit coupling and evolution of the electronic structure of WTe<sub>2</sub> under an external magnetic field." *Phys. Rev. B* **92**, 125152 (2015).

- [20] P. K. Das, D. Di Sante, I. Vobornik, J. Fujii, T. Okuda, E. Bruyer, A. Gyenis, B. E. Feldman, J. Tao, R. Ciancio, G. Rossi, M. N. Ali, S. Picozzi, A. Yadzani, G. Panaccione, and R. J. Cava. "Layer-dependent quantum cooperation of electron and hole states in the anomalous semimetal  $WTe_2$ ." *Nat. Comm.* **7**, 10847 (2016).
- [21] Y. Wu, D. Mou, N. H. Jo, K. Sun, L. Huang, S. L. Bud'ko, P. C. Canfield, and A. Kaminski. "Observation of Fermi arcs in the type-II Weyl semimetal candidate  $WTe_2$ ." *Phys. Rev. B* **94**, 121113 (2016).
- [22] L. Huang, T. M. McCormick, M. Ochi, Z. Zhao, M.-T. Suzuki, R. Arita, Y. Wu, D. Mou, H. Cao, J. Yan, N. Trivedi, and A. Kaminski. "Spectroscopic evidence for a type II Weyl semimetallic state in  $MoTe_2$ ." *Nat. Mater.* **15**, 1155 (2016).
- [23] M. N. Ali, J. Xiong, S. Flynn, J. Tao, Q. D. Gibson, L. M. Schoop, T. Liang, N. Haldolaarachchige, M. Hirschberger, N. P. Ong, and R. J. Cava. "Large, non-saturating magnetoresistance in  $WTe_2$ ." *Nature* **514**, 205 (2014).
- [24] V. Fatemi, Q. D. Gibson, K. Watanabe, T. Taniguchi, R. J. Cava, and P. Jarillo-Herrero. "Magnetoresistance and quantum oscillations of an electrostatically tuned semimetal-to-metal transition in ultrathin  $WTe_2$ ." *Phys. Rev. B* **95**, 041410 (2017).
- [25] L. Wang, I. Gutiérrez-Lezama, C. Barreteau, N. Ubrig, E. Giannini, and A. F. Morpurgo. "Tuning magnetotransport in a compensated semimetal at the atomic scale." *Nat. Comm.* **6**, 8892 (2015).
- [26] B. E. Brown. "The crystal structures of  $WTe_2$  and high-temperature  $MoTe_2$ ." *Acta Crystallographica* **20**, 268 (1966).

- [27] L. Muechler, A. Alexandradinata, T. Neupert, and R. Car. "Topological Nonsymmorphic Metals from Band Inversion." *Phys. Rev. X* **6**, 041069 (2016).
- [28] V. Edelstein. "Spin polarization of conduction electrons induced by electric current in two-dimensional asymmetric electron systems." *Solid State Comm.* **73**, 233 (1990).
- [29] M. Dyakonov and V. Perel. "Current-induced spin orientation of electrons in semiconductors." *Phys. Lett. A* **35**, 459 (1971).
- [30] J. E. Hirsch. "Spin Hall Effect." *Phys. Rev. Lett.* **83**, 1834 (1999).
- [31] L. Liu, R. A. Buhrman, and D. C. Ralph. "Review and Analysis of Measurements of the Spin Hall Effect in Platinum." *Preprint at arXiv:1111.3702 [cond-mat.mes-hall]* (2011).
- [32] J. C. R. Sánchez, L. Vila, G. Desfonds, S. Gambarelli, J. P. Attané, J. M. De Teresa, C. Magén, and A. Fert. "Spin-to-charge conversion using Rashba coupling at the interface between non-magnetic materials." *Nat. Comm.* **4**, 2944 (2013).
- [33] J. Kim, J. Sinha, M. Hayashi, M. Yamanouchi, S. Fukami, T. Suzuki, S. Mitani, and H. Ohno. "Layer thickness dependence of the current-induced effective field vector in Ta|CoFeB|MgO." *Nat. Mater.* **12**, 240 (2013).
- [34] M.-H. Nguyen, D. C. Ralph, and R. A. Buhrman. "Spin Torque Study of the Spin Hall Conductivity and Spin Diffusion Length in Platinum Thin Films with Varying Resistivity." *Phys. Rev. Lett.* **116**, 126601 (2016).

- [35] M. Hayashi, J. Kim, M. Yamanouchi, and H. Ohno. “Quantitative characterization of the spin-orbit torque using harmonic Hall voltage measurements.” *Phys. Rev. B* **89**, 144425 (2014).
- [36] C. O. Avci, K. Garello, M. Gabureac, A. Ghosh, A. Fuhrer, S. F. Alvarado, and P. Gambardella. “Interplay of spin-orbit torque and thermoelectric effects in ferromagnet/normal-metal bilayers.” *Phys. Rev. B* **90**, 224427 (2014).
- [37] D. A. Abanin, A. V. Shytov, L. S. Levitov, and B. I. Halperin. “Nonlocal charge transport mediated by spin diffusion in the spin Hall effect regime.” *Phys. Rev. B* **79**, 035304 (2009).
- [38] D. Ralph and M. Stiles. “Spin transfer torques.” *J. Magn. Magn. Mater.* **320**, 1190 (2008).
- [39] A. R. Mellnik, J. S. Lee, A. Richardella, J. L. Grab, P. J. Mintun, M. H. Fischer, A. Vaezi, A. Manchon, E. A. Kim, N. Samarth, and D. C. Ralph. “Spin-transfer torque generated by a topological insulator.” *Nature* **511**, 449 (2014).
- [40] V. P. Amin and M. D. Stiles. “Spin transport at interfaces with spin-orbit coupling: Formalism.” *Phys. Rev. B* **94**, 104419 (2016).
- [41] V. P. Amin and M. D. Stiles. “Spin transport at interfaces with spin-orbit coupling: Phenomenology.” *Phys. Rev. B* **94**, 104420 (2016).
- [42] A. M. Humphries, T. Wang, E. R. J. Edwards, S. R. Allen, J. M. Shaw, H. T. Nembach, J. Q. Xiao, T. J. Silva, and X. Fan. “Observation of spin-orbit effects with spin rotation symmetry.” *Nature Communications* **8**, 911 (2017).

## CHAPTER 4

### SPIN-ORBIT TORQUES IN NIOBIUM DISELENIDE

In this chapter, we present measurements of current-induced spin-orbit torques generated in NbSe<sub>2</sub>, a fully-metallic hexagonal transition-metal dichalcogenide. We measure the spin-orbit torques in NbSe<sub>2</sub>/Permalloy heterostructures using the spin-torque ferromagnetic resonance (ST-FMR) technique. In addition to the out-of-plane Oersted torque expected from current flow in the metallic NbSe<sub>2</sub> layer, we observe an in-plane antidamping torque with torque conductivity  $\sigma_S \approx 10^3(\hbar/2e)(\Omega\text{m})^{-1}$  and indications of a weak field-like contribution to the out-of-plane torque oriented opposite to the Oersted torque. In some samples we also measure an in-plane field-like torque with the form  $\hat{m} \times \hat{z}$ . The size of this component varies strongly between samples and is not correlated with the NbSe<sub>2</sub> thickness. A torque of this form is not allowed by the bulk symmetries of NbSe<sub>2</sub>, but is consistent with symmetry breaking by a uniaxial strain that might result during device fabrication. This chapter is adapted from work originally published in *Nano Letters* with M.H.D. Guimarães, D. MacNeill, N. Reynolds and D.C. Ralph [1].

#### 4.1 Introduction

Current-induced spin torques generated by materials with large spin-orbit coupling (SOC), such as heavy metals [2–4] and topological insulators [5, 6], are candidates to enable a new generation of efficient non-volatile magnetic memories. Several research groups have recently considered the possibility that some 2-dimensional (2D) materials might also be used as sources of spin-orbit torque

(SOT) [7–11]. For example, 2D transition metal dichalcogenides [12] (TMDs) can possess strong SOC and are easily incorporated into device heterostructures with clean, atomically-precise interfaces. Initial studies of the SOT originating from the TMD semiconductors MoS<sub>2</sub> [7–9] and WSe<sub>2</sub> [8], grown by chemical vapor deposition, reported nonzero spin-torque conductivities, but disagreed as to whether the dominant torque is field-like or antidamping-like. Our research group has measured SOTs in WTe<sub>2</sub>/permalloy samples in which semi-metallic WTe<sub>2</sub> layers were prepared by exfoliation, and observed an out-of-plane anti-damping SOT component made possible by the low crystal symmetry of WTe<sub>2</sub>, as well as a more-conventional in-plane anti-damping SOT and an out-of-plane field-like torque due to the Oersted field [10, 11].

For magnetic memory applications it is of particular interest to explore materials which combine high electrical conductivity,  $\sigma$ , and strong SOC,  $\lambda_{SOC}$ . Here we report the first measurements of SOTs generated by a fully-metallic TMD, NbSe<sub>2</sub>, with  $\sigma \approx 6 \times 10^5 (\Omega\text{m})^{-1}$  in our devices and  $\lambda_{SOC} = 76$  meV [13]. For comparison, the previously-measured semiconducting TMDs MoS<sub>2</sub> and WS<sub>2</sub> have typical electrical conductivities  $\sigma \approx 10^{-6} (\Omega\text{m})^{-1}$  and SOC energies  $\lambda_{SOC} = 0 - 40$  meV in the conduction band and  $\lambda_{SOC} = 150 - 430$  meV in the valence band [14–16], while for semi-metallic WTe<sub>2</sub>  $\sigma \approx 10^4 (\Omega\text{m})^{-1}$  and  $\lambda_{SOC} = 15$  meV [10, 11, 17].

Our spin-torque ferromagnetic resonance (ST-FMR) measurements on NbSe<sub>2</sub>/Permalloy (Py) bilayers reveal small but nonzero SOTs, corresponding to spin-torque conductivities of order or less than  $10^3(\hbar/2e)(\Omega\text{m})^{-1}$ , about a factor of 100 weaker than the spin-torque conductivities generated by Pt or Bi<sub>2</sub>Se<sub>3</sub> at room temperature [6, 18]. To probe the mechanisms of these SOTs we per-

form systematic studies as a function of the NbSe<sub>2</sub> thickness,  $t$ , and the angle of applied magnetic field. We measure an in-plane antidamping SOT component that is only weakly dependent on  $t$ , remaining sizable down to a single NbSe<sub>2</sub> layer – suggesting an interfacial origin. We also observe a field-like out-of-plane torque that scales linearly with  $t$  for sufficiently thick ( $t > 5$  nm) samples, indicating that in this regime the torque is dominated by a current-generated Oersted field. However, for devices with smaller number of NbSe<sub>2</sub> layers ( $t < 5$  nm), the out-of-plane torque is weaker than the value expected from the field alone, and, for a single NbSe<sub>2</sub> layer we observe a reversal of the direction of the field-like out-of-plane torque. These deviations could be the result of either an interfacial out-of-plane field-like SOT directed opposite to the Oersted torque, or possibly to non-uniform charge current flow in the Py layer such that the current within the Py generates a nonzero net Oersted field acting on the Py.

Interestingly, by performing systematic measurements as a function of the angle of an in-plane magnetic field we detect in some samples the presence of an additional in-plane torque that is field-like with the form  $\hat{m} \times \hat{z}$ , where  $\hat{m}$  is the Py magnetization direction. This torque is not allowed by symmetry considerations for the bulk NbSe<sub>2</sub> crystal structure [10]. We propose that the presence of this torque component is due to a strain-induced symmetry breaking, e.g., a unidirectional strain in the NbSe<sub>2</sub> layer generated during the process of exfoliation and sample fabrication [19].

## 4.2 Device Fabrication

We prepare our samples by mechanically exfoliating a bulk synthetic NbSe<sub>2</sub> crystal (HQgraphene) onto an intrinsic Si wafer with a 1- $\mu\text{m}$ -thick SiO<sub>2</sub> layer thermally grown on the surface. The mechanical exfoliation is performed under vacuum (at pressures below  $10^{-6}$  Torr) in the load-lock chamber of our sputter system, and the samples are loaded into the sputtering chamber without breaking vacuum. We then deposit 6 nm of Py by grazing angle ( $\sim 5^\circ$ ) sputtering followed by 1.2 nm of Al, which oxidizes completely upon contact with atmosphere and serves as a capping layer. We have previously demonstrated that the grazing angle sputter deposition causes little to no damage to our TMD crystals [10]. The NbSe<sub>2</sub> flakes are identified by optical contrast, and their thicknesses and morphology are determined by atomic force microscopy (AFM). In order to avoid artifacts in our measurements due to roughness of the ferromagnetic layer, we selected only flat flakes with RMS surface roughness below 0.4 nm, measured by AFM in an area of  $1 \times 1 \mu\text{m}^2$ , and with no steps in the TMD crystals over the device area. We then pattern the NbSe<sub>2</sub>/Py heterostructures into a bar shape with a well-defined length and width by using electron beam lithography followed by Ar<sup>+</sup> ion milling. As a final step, we define Ti/Pt (5/75 nm) contacts in the shape of a coplanar waveguide using electron beam lithography followed by metal sputtering deposition. An optical micrograph of a finished device is shown in Figure 4.1a.

### 4.3 Spin-Torque Ferromagnetic Resonance Measurements

To measure the SOTs, we use the ST-FMR technique [2, 6, 10] in which an alternating microwave-frequency current ( $I_{RF}$ ) (with frequencies  $f = 7 - 12$  GHz) is applied within the sample plane. Current-induced torques cause the magnetization  $M$  of the ferromagnet to precess. By applying an external magnetic field  $H$  at an angle  $\phi$  with respect to  $I_{RF}$ , we set the direction of  $\vec{M}$  and the characteristic ferromagnetic resonance frequency of the ferromagnet (Figure 4.1b). The precession of the magnetization creates a time-dependent change of the device resistance due to the anisotropic magnetoresistance (AMR) of the ferromagnetic layer. This change in resistance mixes with  $I_{RF}$  generating a DC voltage across the NbSe<sub>2</sub>/Py bar ( $V_{mix}$ ). The signal-to-noise ratio is maximized by modulating the amplitude of  $I_{RF}$  at low frequencies and detecting  $V_{mix}$  using a lock-in amplifier. The circuit geometry is shown in Figure 4.1a. All measurements are performed at room temperature unless indicated.

When the ferromagnetic resonance frequency matches  $f$ ,  $V_{mix}$  shows a resonance peak with a lineshape that can be described as:  $V_{mix}(H) = V_S(H) + V_A(H)$ , where  $V_S$  is a symmetric Lorentzian with amplitude proportional to the in-plane component of the torque ( $\tau_{\parallel}$ ), and  $V_A$  an antisymmetric Lorentzian with amplitude proportional to the out-of-plane component of the torque ( $\tau_{\perp}$ ). This allows the separation of the two torque components by fitting a measurement of  $V_{mix}$  as a function of  $H$ . The two torques components are related to the amplitudes of the Lorentzians by [2, 6]:

$$V_S = -\frac{I_{RF}}{2} \left( \frac{dR}{d\phi} \right) \frac{1}{\alpha\gamma\mu_0 (2H_0 + M_{eff})} \tau_{\parallel}, \quad (4.1)$$

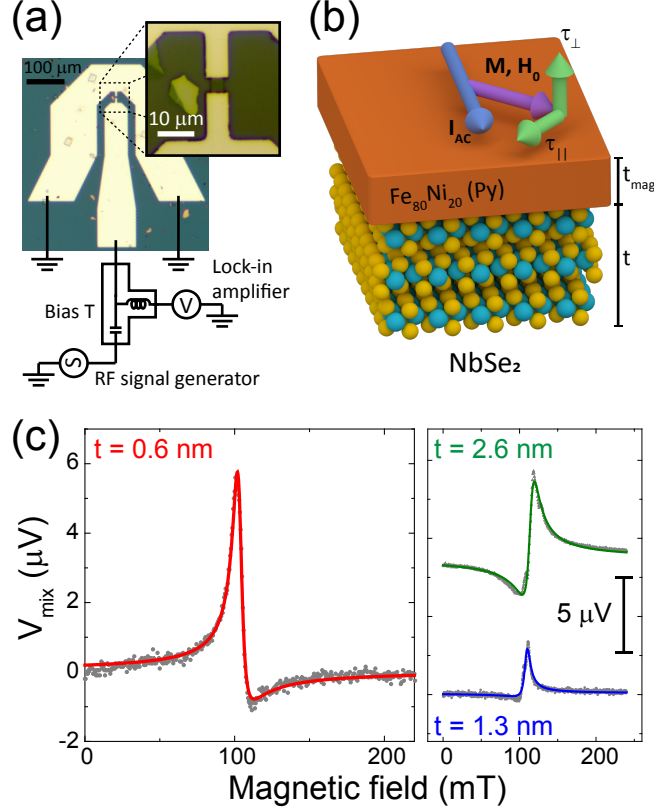


Figure 4.1: (a) Micrograph of a typical device with the measuring circuit schematic. (b) Schematic of the NbSe<sub>2</sub>/Py structure. (c) ST-FMR resonances for  $\phi = 130^\circ$ ,  $f = 9$  GHz, and  $P_{RF} = 5$  dBm for different thicknesses of the NbSe<sub>2</sub> layer: 0.6 nm (red), 1.3 nm (blue), and 2.6 nm (green). The gray points are the measured data and the solid lines show the fits to a symmetric plus antisymmetric Lorentzian.

$$V_A = -\frac{I_{RF}}{2} \left( \frac{dR}{d\phi} \right) \frac{\sqrt{1 + M_{eff}/H_0}}{\alpha\gamma\mu_0(2H_0 + M_{eff})} \tau_{\perp}, \quad (4.2)$$

where  $R$  is the device resistance,  $\phi$  is the angle between  $H$  and  $I_{RF}$ ,  $M_{eff}$  is the effective magnetization of the Py layer, composed by the saturation magnetization and anisotropy terms,  $\alpha$  is the Gilbert damping of the Py,  $\gamma$  is the gyromagnetic ratio,  $\mu_0$  is the vacuum permittivity, and  $H_0$  is the resonance field. The term  $dR/d\phi$  is due to the AMR in the Py layer. For our devices we have  $\mu_0 M_{eff} \approx 0.8$  T and  $\alpha \approx 0.01$  as obtained by the ST-FMR resonance frequency and linewidth,

respectively, and  $R(\phi)$  is measured directly by measuring the devices resistance as a function of  $\phi$ . The current  $I_{RF}$  is calibrated by using a network analyzer to measure transmitted and reflected microwave powers ( $S_{11}$  and  $S_{21}$ ).

Resonance curves for one, two, and four NbSe<sub>2</sub> monolayers devices ( $t = 0.6, 1.3, \text{ and } 2.6 \text{ nm}$ , respectively) with  $f = 9 \text{ GHz}$ , applied RF power  $P_{RF} = 5 \text{ dBm}$  and  $\phi = 130^\circ$  are shown in Fig. 4.1c, where the gray points represent experimental data and the fits are shown by the solid lines. Two important features are illustrated by these curves: the ratio between the amplitude of the symmetric and antisymmetric Lorentzians decreases with the increase of  $t$ , and the sign of the antisymmetric component flips sign between the mono- and bi- layer devices. For both the one and two layer-thick devices, the lineshape is dominated by the symmetric component of the Lorentzian, meaning that the in-plane SOT is dominant over the out-of-plane component.

Our observation of both symmetric and antisymmetric components in the ST-FMR resonance is qualitatively similar to the results of Ref. 6 on MoS<sub>2</sub>/Py devices. The presence of both field-like and damping-like interfacial torques is consistent with general considerations of interfacial spin-orbit torques [20–22]. However, a more recent measurement on MoS<sub>2</sub>/CoFeB and WSe<sub>2</sub>/CoFeB structures using a second harmonic Hall technique was unable to measure any in-plane SOT and attributed the large symmetric Lorentzian measured in Ref. 6 to spin-pumping combined with an inverse Rashba-Edelstein effect, rather than a spin-orbit torque [8]. We can tell that the symmetric ST-FMR resonance signal we observe is not due primarily to a spin-pumping effect because this would require an unphysically-large spin-to-charge conversion factor (see Section 4.6.1).

The symmetries and mechanisms of the SOTs can be analyzed in more de-

tail by performing ST-FMR measurements as a function of the magnetic-field angle as  $\tau_{\parallel}$  and  $\tau_{\perp}$  both depend upon  $\phi$ . The contributions to the expected angular dependence can be understood as follows. Part of the angular dependence arises from the AMR in the bilayer, which contributes the dependence  $dR/d\phi \propto \sin(2\phi)$  (see Eqs. 4.1 and 4.2). Many current-induced torques have a  $\cos(\phi)$  dependence (e.g. in-plane antidamping torques due to standard spin Hall or Rashba-Edelstein Effects, and the field-like out-of-plane torque due to the Oersted field), leading to an overall angular dependence  $V_{mix} \propto \cos(\phi) \sin(2\phi)$ . However, additional torque components can arise in systems with lower symmetry [23, 24], such as  $\text{WTe}_2$  [10, 11] and some semiconductor alloys [25–29].

The angular dependence we measure for the antisymmetric and symmetric components of the ST-FMR resonances of  $\text{NbSe}_2/\text{Py}$  samples are shown in Fig. 4.2 for devices with monolayer (a,b) and bilayer (c,d)  $\text{NbSe}_2$ . The angular dependence of the antisymmetric components for both samples is consistent with a simple  $\cos(\phi) \sin(2\phi)$  form, illustrating that the out-of-plane torque has the usual  $\cos(\phi)$  dependence expected for a field-like out-of-plane torque. However, the symmetric ST-FMR components deviate from this form. We have performed more general fits (black lines in Fig. 4.2) for both components to the forms:

$$V_S = S \cos(\phi) \sin(2\phi) + T \sin(2\phi), \quad (4.3)$$

$$V_A = A \cos(\phi) \sin(2\phi) + B \sin(2\phi), \quad (4.4)$$

corresponding to the inclusion of additional angle-independent torques  $\tau_T \propto T$  and  $\tau_B \propto B$  such that the in-plane torque is  $\tau_{\parallel} = \tau_S \cos(\phi) + \tau_T$  and the out-of-

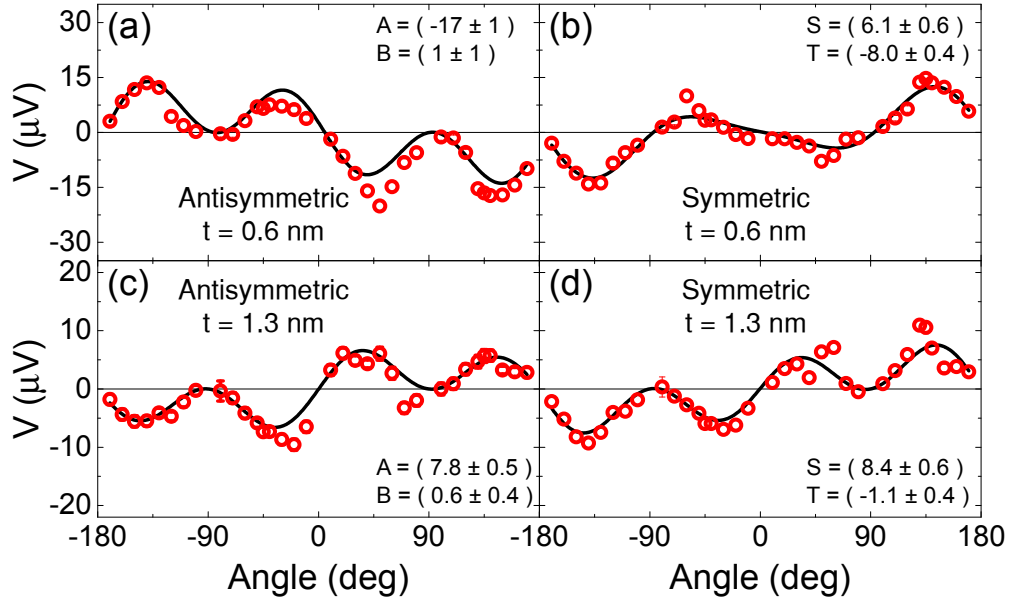


Figure 4.2: Antisymmetric and symmetric components of the ST-FMR resonance fits for  $V_{mix}$  as a function of the magnetic field angle for devices with (a, b) one and (c, d) two NbSe<sub>2</sub> monolayers for  $f = 9$  GHz and  $P_{RF} = 5$  dBm. The data are shown by the red circles and the fits using equations 4.3 and 4.4 are shown by the black lines.

plane torque is  $\tau_{\perp} = \tau_A \cos(\phi) + \tau_B$  (where  $\tau_S$ ,  $\tau_T$ ,  $\tau_A$ , and  $\tau_B$  are independent of  $\phi$ ). The vector forms of these additional torque components correspond to  $\vec{\tau}_T \propto \hat{m} \times \hat{z}$  and  $\vec{\tau}_B \propto \hat{m} \times (\hat{m} \times \hat{z})$ . We find that this generalization greatly improves the fits for the symmetric ST-FMR components, with nonzero values for both  $S$  and  $T$ , and with the results for the monolayer sample indicating  $|\tau_T| > \tau_S$ . For the bilayer sample the contribution from  $\tau_T$  is less prominent but still clearly nonzero, while for both samples the fits to the antisymmetric component gives  $\tau_B = 0$  within the experimental resolution.

This result is curious in several ways. First, for the usual 2H-NbSe<sub>2</sub> structure (space group P6<sub>3</sub>/mmc) [30], the NbSe<sub>2</sub>/Py interface reduces to the space group P3m1 containing the identity, two 3-fold rotations, and three mirror planes. This set of symmetries forbids the presence of both of the torque terms  $\vec{\tau}_T \propto \hat{m} \times \hat{z}$  and

$\vec{\tau}_B \propto \hat{m} \times (\hat{m} \times \hat{z})$ . However, any uniaxial strain will break the three-fold rotational symmetry and reduce the mirror symmetries to a single mirror plane or lower, depending on the alignment of the strain axis to the crystal axes. If there is a uniaxial strain, the torque terms  $\propto \hat{m} \times \hat{z}$  or  $\propto \hat{m} \times (\hat{m} \times \hat{z})$  become symmetry-allowed, and in the case of a remaining mirror plane the applied electrical current must have a component perpendicular to this plane. This situation is analogous to the strain-induced valley magnetoelectric effect observed in MoS<sub>2</sub> monolayers [19].

We note, though, that both  $\vec{\tau}_T$  and  $\vec{\tau}_B$  are subject to the same symmetry constraints, so it is curious that  $\vec{\tau}_B$  remains zero even when broken symmetries allow  $\vec{\tau}_T \neq 0$ . Furthermore, the result we find in the (presumably strained) NbSe<sub>2</sub>/Py samples ( $\vec{\tau}_T \neq 0, \vec{\tau}_B = 0$ ) is opposite to the results in WTe<sub>2</sub>/Py samples ( $\vec{\tau}_T = 0, \vec{\tau}_B \neq 0$ ) [10, 11] where a similar low-symmetry state is intrinsic to the WTe<sub>2</sub> crystal structure. This suggests that the existence of the torque components  $\vec{\tau}_B$  and  $\vec{\tau}_T$  does not depend solely on the nature of the global broken symmetries, but also on microscopic factors like the interface transparency between the TMD and the ferromagnet, the Berry curvature of the bands involved in the transport, the local atomic point-group symmetries, and the nature of the atomic orbitals that contribute to charge and spin transport. [31–33]

#### 4.4 Dependence on NbSe<sub>2</sub> thickness

We investigated the extent to which the different torque components  $\tau_S, \tau_T, \tau_A$ , and  $\tau_B$  depend on the NbSe<sub>2</sub> thickness,  $t$ , by performing ST-FMR measurements as a function of applied magnetic field angle for a collection of different devices

with different values of  $t$ , while keeping the Py thickness fixed ( $t_{mag} = 6$  nm). These strengths of each torque component are linear in the current and voltage applied to the sample, and because the electric field across the device can be more accurately determined than the separate current densities through each of the individual layers in our devices (NbSe<sub>2</sub> and Py), we express the torque strengths as torque conductivities,  $\sigma_j \equiv d\tau_j/dE$  in units of  $(\hbar/2e)(\Omega m)^{-1}$ , where  $j = A, B, S$ , or  $T$  corresponds to the different torque components,  $E$  is the electric field,  $\hbar$  is the reduced Plank's constant and  $e$  the electron charge. We plot the thickness dependence of  $\sigma_A$ ,  $\sigma_S$ , and  $\sigma_T$  in Fig. 4.3. The component  $\sigma_B$  is zero within experimental error for all of the samples measured.

For the out-of-plane field-like torque conductivity  $\sigma_A$  we observe a clear increase with increasing NbSe<sub>2</sub> thickness (Fig. 4.3a). For our thicker devices the magnitude of  $\sigma_A$  agrees with our estimation of the Oersted-field contribution ( $\sigma_{Oe}$ ) due to the current flowing in the NbSe<sub>2</sub> layer. However, for the thinner ( $t < 5$  nm) devices,  $\sigma_A$  is significantly lower than our estimate for the Oersted contribution  $\sigma_{Oe}$ , and then the sign of  $\sigma_A$  is reversed for the monolayer device (see Fig. 4.1c). This behavior at small NbSe<sub>2</sub> thicknesses suggests the presence of an interfacial field-like SOT that opposes the Oersted contribution. However, the size of the reversed SOT is sufficiently small that it is difficult to rule out possible alternative mechanisms such as a spatially non-uniform current density through the thickness of the Py layer. (Nonzero antisymmetric ST-FMR resonances can be observed even in single-layer Py samples, and have been ascribed to this mechanism [2, 34].)

The in-plane damping-like torque component  $\sigma_S$  (Fig. 4.3b) has at most a weak dependence on  $t$ , and possesses a non-zero value all the way down

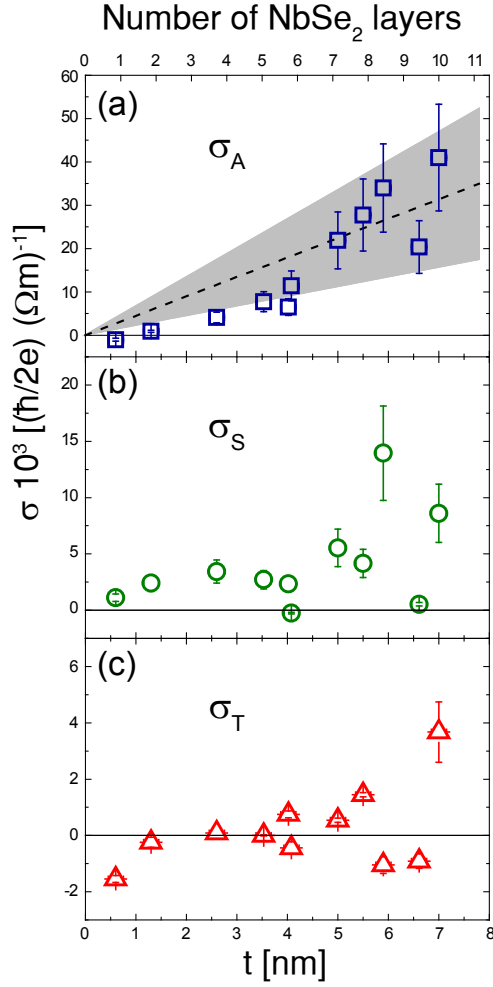


Figure 4.3: Spin-torque conductivities (a)  $\sigma_A$ , (b)  $\sigma_S$ , and (c)  $\sigma_T$  as a function of the NbSe<sub>2</sub> thickness obtained from the angular fits for  $f = 9$  GHz and  $P_{RF} = 5$  dBm. The dashed line in (a) shows the estimated contribution from the Oersted field ( $\sigma_{Oe}$ ) with the gray area representing its standard deviation.

to a single NbSe<sub>2</sub> layer. The small apparent increase of  $\sigma_S$  with increasing  $t$  could arise from a bulk contribution, such as the spin Hall effect. However, the nonzero value of this term down to a single NbSe<sub>2</sub> layer suggests a sizable interfacial SOT. The value of  $\sigma_S$  for the thinnest samples ( $\sigma_S \approx 3 \times 10^3 (\hbar/2e) (\Omega m)^{-1}$ ) has a magnitude similar to reports for other TMDs, such as MoS<sub>2</sub> [7] and WTe<sub>2</sub> [10], but it is significantly below the values for Pt/ferromagnet bilayers [18] and topological insulators at room temperature [6] ( $\sigma_S \approx 10^5 (\hbar/2e) (\Omega m)^{-1}$ ).

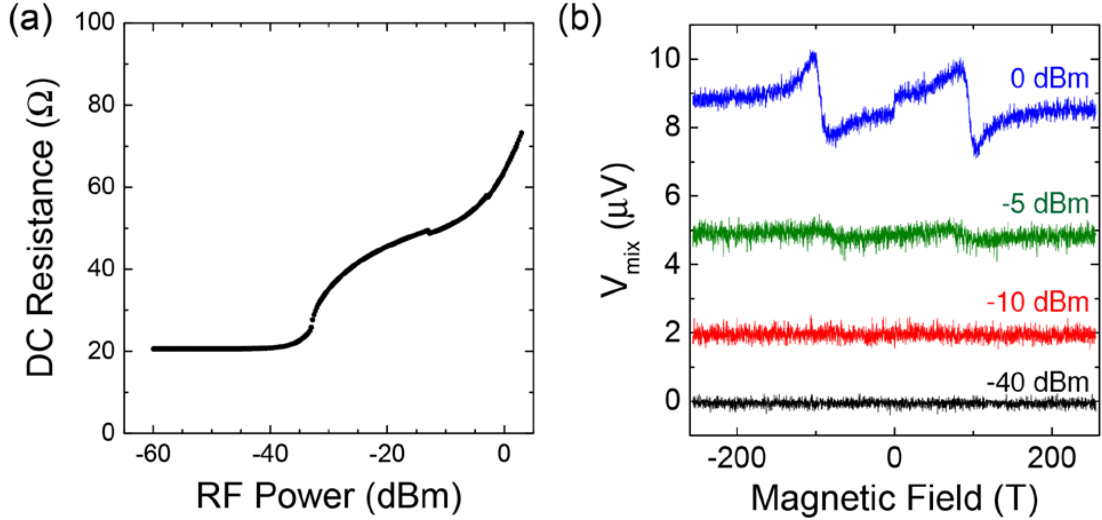


Figure 4.4: Measurements at low temperature (4.2 K) for a sample with  $t = 5.9$  nm. (a) Two-probe DC resistance as a function of applied RF power with  $f = 8$  GHz. (b) ST-FMR mixing voltage as a function of magnetic field at  $\phi = 45^\circ$  and different values of applied RF power with  $f = 8$  GHz.

For the in-plane field-like torque  $\sigma_T$  that is forbidden by symmetry for unstrained NbSe<sub>2</sub> (Fig. 4.3c), we do not observe any systematic trend in the torque conductivity as a function of  $t$ . While  $\sigma_T \approx 0$  for a few of our devices, both the sign and magnitude of this  $\hat{m} \times \hat{z}$  torque term seem uncorrelated with the thickness of the NbSe<sub>2</sub> layer. The lack of correlation between  $\sigma_T$  and  $t$  is in agreement with our assumption that this term arises due to strain in our samples since we do not control this parameter. Strain-controlled experiments [19] could be performed in order to confirm this assumption and better constrain the microscopic origin of this extra torque term.

We also performed temperature dependence measurements for a sample showing all three torque components:  $\sigma_A$ ,  $\sigma_S$ , and  $\sigma_T$  (see Section 4.6.3), with  $\sigma_A \approx \sigma_{Oe}$ . We observe only a weak temperature dependence for the torque ratio  $\sigma_S/\sigma_A$  and a slightly stronger temperature dependence for  $\sigma_T/\sigma_A$ . The weak temperature dependence of the interfacial SOTs in TMD/ferromagnet bilayers

is in agreement with previous studies on semiconducting TMDs [8]. For sufficiently low temperatures ( $T < 7$  K) we observe a superconducting transition if the NbSe<sub>2</sub> layer is sufficiently thick ( $t > 5$  nm). When the devices enter the superconducting state the ST-FMR technique becomes insensitive to spin-orbit torques because the resistance-based ST-FMR signal goes to zero. Upon increasing the RF power above the critical current, the devices transition to the normal state and we recover the ST-FMR resonance signals (see Fig. 4.4).

## 4.5 Conclusion

In summary, we report current induced SOTs in NbSe<sub>2</sub>/Py bilayers. The in-plane antidamping-like term has only a very weak dependence with  $t$ , with values for the spin torque conductivity comparable to other TMDs. For thin NbSe<sub>2</sub> layers, the out-of-plane SOT component for thin NbSe<sub>2</sub> layers is significantly smaller than the estimate Oersted-field contribution, with a sign reversal for a monolayer of NbSe<sub>2</sub>. In addition to these expected torque components, we also observe the presence of a SOT with the form  $\hat{m} \times \hat{z}$  which is forbidden by the bulk symmetry of the NbSe<sub>2</sub> crystal, but can arise in the presence of strain.

We thank R. A. Buhrman for valuable discussions and comments on the manuscript. This work was supported by the Kavli Institute at Cornell for Nanoscale Science, the Netherlands Organization for Scientific Research (NWO Rubicon 680-50-1311), the National Science Foundation (DMR-1406333, DMR-1708499), and the Army Research Office (W911NF-15-1-0447). G.M.S. acknowledges support by a National Science Foundation Graduate Research Fellowship under Grant No. DGE-1144153. This work made use of the NSF-supported

Cornell Nanoscale Facility (ECCS-1542081) and the Cornell Center for Materials Research Shared Facilities, which are supported through the NSF MRSEC Program (DMR-1719875).

## 4.6 Supplemental Information

### 4.6.1 Estimation of spin pumping contributions

When performing ST-FMR experiments in which the resonance signal is weak, it is important to consider that a symmetric component in an ST-FMR experiment might arise not only from an in-plane torque but also by a separate mechanism in which the precessing magnet pumps a spin current into the spin-source material where it is converted to a voltage output by spin-to-charge conversion [35, 36]. Shao *et al.* [8] have questioned whether the symmetric ST-FMR signals observed in MoS<sub>2</sub>/Py devices by Zhang *et al.* [7] might be due to this mechanism rather than to an antidamping spin-orbit torque. The spin-pumping mechanism would produce a signal with the same dependence on the angle of the applied magnetic field ( $\cos(\phi) \sin(2\phi)$ ) as an in-plane antidamping torque  $\vec{\tau}_S$  [6], so the two mechanisms cannot be distinguished on this basis.

We can, however, rule out a dominant contribution to our experiment from the spin-pumping mechanism based on an analysis of the size of the symmetric component of the ST-FMR resonances that we measure. Following the reasoning described in Ref. [6], spin pumping combined with spin-to-charge conver-

sion contributes a symmetric lineshape to the ST-FMR signal with magnitude:

$$V_{SP} = \Theta_{S-C} \frac{ewR\lambda_S}{2\pi} \tanh\left(\frac{t}{2\lambda_S}\right) \text{Re}[g_{\uparrow\downarrow}^{eff}] \langle (\hat{m} \times \frac{\partial \hat{m}}{\partial t})_x \rangle, \quad (4.5)$$

where  $\Theta_{S-C}$  is the spin-to-charge conversion factor,  $e$  is the electron charge,  $w$  is our sample width (3  $\mu\text{m}$  for the sample with  $t = 0.6$  nm and 2.5  $\mu\text{m}$  for  $t = 1.3$  nm),  $t$  is the NbSe<sub>2</sub> thickness  $R$  is the sample resistance (191  $\Omega$  for the sample with  $t = 0.6$  nm and 180  $\Omega$  for  $t = 1.3$  nm),  $\lambda_S$  is the thickness over which spin-to-charge conversion takes place, and  $g_{\uparrow\downarrow}^{eff}$  is the effective spin mixing conductance. For the precession of the magnetic film, we have:

$$\langle (\hat{m} \times \frac{\partial \hat{m}}{\partial t})_x \rangle = 2\pi f \phi_p^2 \sin(\phi) \sqrt{\frac{\mu_0 H}{\mu_0 H + \mu_0 M_{eff}}}, \quad (4.6)$$

where  $\phi_p$  is the maximum precession angle of the ferromagnets magnetization, estimated by  $\phi_p = (dR/d\phi)^{-1} (2/I_{RF}) \sqrt{(V_S)^2 + (V_A)^2}$ . For our samples with  $f = 9$  GHz,  $I_{RF} = 9$  mA,  $\mu_0 H = 0.12$  T and  $\mu_0 M_{eff} = 0.77$  T we have  $\phi_p \approx 0.01$ .

Given the measured magnitude for the symmetric component of our ST-FMR signals, we can estimate a lower bound on the spin-to-charge conversion factor,  $\Theta_{S-C}$ , that would be needed to explain our data by the spin-pumping mechanism. We assume that  $g_{\uparrow\downarrow}^{eff}$  is as large as the value for Pt/Py bilayers:  $g_{\uparrow\downarrow}^{eff} \approx 2 \times 10^{19} \text{ m}^{-2}$  [37]. A slightly smaller upper bound estimated for Co/MoS<sub>2</sub> bilayers:  $g_{\uparrow\downarrow}^{eff} \approx 1.5 \times 10^{19} \text{ m}^{-2}$  [9], but in order to be more conservative in our analysis we will take the larger value. For strong spin-orbit materials,  $\lambda_S$  is ordinarily about 1 nm [6, 38]; we will assume that  $\lambda_S = t$  for our devices with  $t = 0.6$  and 1.3 nm (corresponding to one and two NbSe<sub>2</sub> monolayers). Using the measured values for the symmetric component of the ST-FMR resonances with the  $\cos(\phi) \sin(2\phi)$  dependence on magnetic field angle (6  $\mu\text{V}$  for the  $t = 0.6$  nm sample and 8  $\mu\text{V}$  for the  $t = 1.3$  nm sample), we obtain  $\theta_{S-C} > 39$  for  $t = 0.6$  nm and  $\theta_{S-C} > 49$  for  $t = 1.3$  nm. We consider this too large to be physically

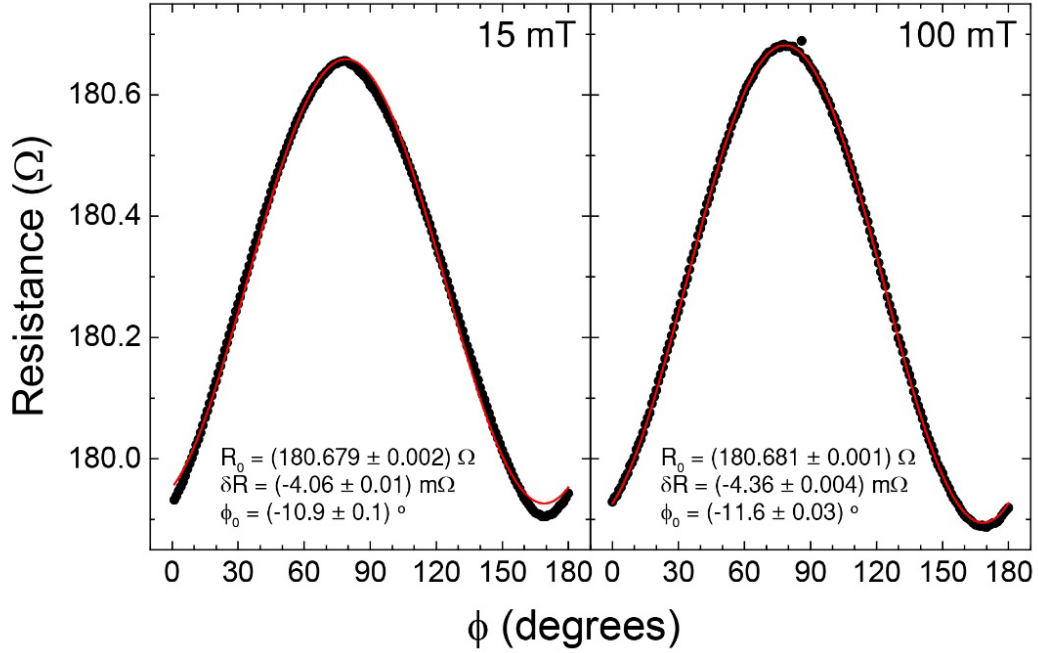


Figure 4.5: Resistance versus magnetic field angle for  $\mu_0 H = 15$  mT (left) and 100 mT (right). The current is applied along  $\phi = 0^\circ$ . The data are shown by the black dots and the fit using Eq. 4.7 is shown in red.

reasonable. This value is larger than the spin-to-charge conversion factor for any known material at room temperature, and if the value were this large the Onsager-reciprocal process (charge-to-spin conversion) would produce an ST-FMR resonance much larger than we measure (corresponding to a spin torque conductance higher than  $10^7 \left(\frac{\hbar}{2e}\right) (\Omega m)^{-1}$ ).

#### 4.6.2 Anisotropic Magnetoresistance Measurements

In order to obtain the torque conductivities, we must determine  $dR/d\phi$  (see Eqs. 4.1 and 4.2). For this purpose we measured the AMR for all our devices. As an example, in Figure 4.5 we plot the AMR measurements ( $R$  vs  $\phi$ ) for the device with  $t = 1.3$  nm for magnetic fields of 15 and 100 mT. The curves can be well

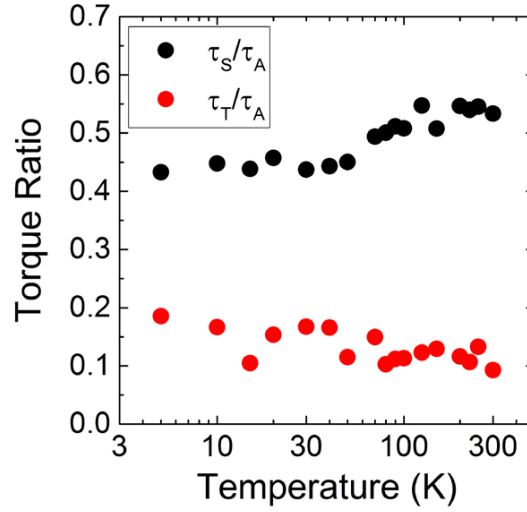


Figure 4.6: Temperature dependence of the ratio of the torque components  $\tau_S/\tau_A$  (black) and  $\tau_T/\tau_A$  (red).

fitted by:

$$R(\phi) = R_0 + \delta R \cos^2(\phi) \quad (4.7)$$

where  $R_0$  is the average resistance and  $\delta R$  the AMR magnitude. To analyze our ST-FMR measurements we use the fitted curves for higher fields, where the magnetization remains better aligned with the applied magnetic field. Even at lower fields the data can be well fitted by Eq. 4.7 with only a small deviation due to shape anisotropy of the Py bar.

### 4.6.3 Temperature Dependence of the Measured Spin-Orbit Torques

We studied the temperature dependence of the SOTs in a sample with  $t = 6$  nm. Our temperature-controlled experimental setup does not allow either for direct calibration of  $I_{RF}$  using a network analyzer (due to the use of wirebonds) nor for sweeps as a function of changing the angle of the magnetic field (though this

has since been remedied). To avoid the need to calibrate  $I_{RF}$ , we chose a sample for which the out-of-plane torque is dominated by the Oersted field so that the ratio  $V_S/V_A$  should be independent of changes in the the sample conductivity. This sample also shows a non-zero  $\tau_T$ , so by measuring the ST-FMR resonances at positive and negative magnetic fields we can we can trace the dependence of this term as a function of temperature. From Eq. 4.3, the difference between positive and negative fields of the symmetric component of the ST-FMR signal gives us the  $S$  fit component:  $V_S(\phi = 45^\circ) - V_S(\phi = -135^\circ) = 2S \cos(45^\circ)$ , and the sum gives us the  $T$  fit component:  $V_S(\phi = 45^\circ) + V_S(\phi = -135^\circ) = 2T$ .

Figure 4.6 shows the temperature dependence of the torque ratios  $\tau_S/\tau_A$  and  $\tau_T/\tau_A$ . Both ratios are only weakly dependent on temperature. The slight decrease in  $\tau_S/\tau_A$  with decreasing temperature is similar to reports regarding the inverse Rashba-Edelstein effect (IREE) in Ag/Bi structures and REE spin torques in TMD/ferromagnet bilayers, which show only a weak temperature dependence with saturation below about 60 K. The ratio  $\tau_T/\tau_A$  displays a slight increase with decreasing temperature.

#### 4.6.4 Resistance as a function of NbSe<sub>2</sub> thickness and the Oersted field contribution

In order to obtain the conductivities of the NbSe<sub>2</sub> and Py layers, we use that the device resistance should scale as  $(R_{sq})^{-1} = \sigma_{Py}t_{mag} + \sigma_{NbSe_2}t$ , where  $R_{sq} = RL/W$  is the resistance per square of the NbSe<sub>2</sub>/Py bilayer, and  $\sigma_{Py}$  and  $t_{mag}$ , and  $\sigma_{NbSe_2}$  and  $t$  are the Py and NbSe<sub>2</sub> conductivities and thicknesses, respectively. Since we keep  $t_{mag} = 6$  nm fixed in all our devices, the conductivities of both layers

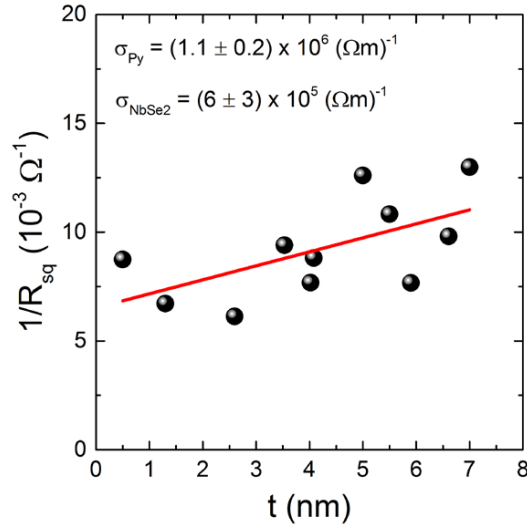


Figure 4.7: Inverse of the resistance per square as a function of the NbSe<sub>2</sub> layer thickness. The dots represent the experimental data for different devices and the red line gives the linear fit.

can be obtained by a linear fit of  $1/R_{sq}$  versus  $t$ , for which the intercept gives  $\sigma_{Py}t_{mag}$  and the slope gives the NbSe<sub>2</sub> conductivity. By fitting the data for all our devices (Fig. 4.7) we obtain:  $\sigma_{Py} = (1.1 \pm 0.2) \times 10^6 (\Omega m)^{-1}$  and  $\sigma_{NbSe_2} = (6 \pm 3) \times 10^5 (\Omega m)^{-1}$ . The Oersted field contribution to the torques is therefore given by:  $\sigma_{Oe} = \left(\frac{e}{\hbar}\right) \mu_0 M_{eff} t_{mag} t \sigma_{NbSe_2} / \hbar$ , where  $\mu_0 M_{eff} \sim 0.8$  T and  $t_{mag} = 6$  nm for our samples.

## References

- [1] M. H. D. Guimares, G. M. Stiehl, D. MacNeill, N. D. Reynolds, and D. C. Ralph. "SpinOrbit Torques in NbSe<sub>2</sub>/Permalloy Bilayers." *Nano Letters* **18**, 1311 (2018).
- [2] L. Liu, T. Moriyama, D. C. Ralph, and R. A. Buhrman. "Spin-Torque Fer-

- romagnetic Resonance Induced by the Spin Hall Effect." *Physical Review Letters* **106**, 036601 (2011).
- [3] I. M. Miron, K. Garello, G. Gaudin, P.-J. Zermatten, M. V. Costache, S. Auffret, S. Bandiera, B. Rodmacq, A. Schuhl, and P. Gambardella. "Perpendicular switching of a single ferromagnetic layer induced by in-plane current injection." *Nature* **476**, 189 (2011).
- [4] C. F. Pai, L. Liu, Y. Li, H. W. Tseng, D. C. Ralph, and R. A. Buhrman. "Spin transfer torque devices utilizing the giant spin Hall effect of tungsten." *Applied Physics Letters* **101**, 122404 (2012).
- [5] Y. Fan, P. Upadhyaya, X. Kou, M. Lang, S. Takei, Z. Wang, J. Tang, L. He, L.-T. Chang, M. Montazeri, G. Yu, W. Jiang, T. Nie, R. N. Schwartz, Y. Tserkovnyak, and K. L. Wang. "Magnetization switching through giant spinorbit torque in a magnetically doped topological insulator heterostructure." *Nature Materials* **13**, 699 (2014).
- [6] A. R. Mellnik, J. S. Lee, A. Richardella, J. L. Grab, P. J. Mintun, M. H. Fischer, A. Vaezi, A. Manchon, E.-A. Kim, N. Samarth, and D. C. Ralph. "Spin-transfer torque generated by a topological insulator." *Nature* **511**, 449 (2014).
- [7] W. Zhang, J. Sklenar, B. Hsu, W. Jiang, M. B. Jungfleisch, J. Xiao, F. Y. Fradin, Y. Liu, J. E. Pearson, J. B. Ketterson, Z. Yang, and A. Hoffmann. "Research Update: Spin transfer torques in permalloy on monolayer MoS<sub>2</sub>." *APL Materials* **4**, 032302 (2016).
- [8] Q. Shao, G. Yu, Y. W. Lan, Y. Shi, M. Y. Li, C. Zheng, X. Zhu, L. J. Li, P. K. Amiri, and K. L. Wang. "Strong Rashba-Edelstein Effect-

- Induced Spin-Orbit Torques in Monolayer Transition Metal Dichalcogenide/Ferromagnet Bilayers." *Nano Letters* **16**, 7514 (2016).
- [9] C. Cheng, M. Collet, J.-C. R. Sánchez, V. Ivanovskaya, B. Dlubak, P. Seineor, A. Fert, H. Kim, G. H. Han, Y. H. Lee, H. Yang, and A. Anane. "Spin to charge conversion in MoS<sub>2</sub> monolayer with spin pumping." arXiv:1510.03451 (2015).
- [10] D. MacNeill, G. M. Stiehl, M. H. D. Guimaraes, R. A. Buhrman, J. Park, and D. C. Ralph. "Control of spinorbit torques through crystal symmetry in WTe<sub>2</sub>/ferromagnet bilayers." *Nature Physics* **13**, 300 (2017).
- [11] D. MacNeill, G. M. Stiehl, M. H. D. Guimarães, N. D. Reynolds, R. A. Buhrman, and D. C. Ralph. "Thickness dependence of spin-orbit torques generated by WTe<sub>2</sub>." *Physical Review B* **96**, 054450 (2017).
- [12] S. Manzeli, D. Ovchinnikov, D. Pasquier, O. V. Yazyev, and A. Kis. "2D transition metal dichalcogenides." *Nature Reviews Materials* **2**, 17033 (2017).
- [13] X. Xi, Z. Wang, W. Zhao, J.-H. Park, K. T. Law, H. Berger, L. Forró, J. Shan, and K. F. Mak. "Ising pairing in superconducting NbSe<sub>2</sub> atomic layers." *Nature Physics* **12**, 139 (2016).
- [14] G. B. Liu, W. Y. Shan, Y. Yao, W. Yao, and D. Xiao. "Three-band tight-binding model for monolayers of group-VIB transition metal dichalcogenides." *Physical Review B* **88**, 085433 (2013).
- [15] X. Xu, W. Yao, D. Xiao, and T. F. Heinz. "Spin and pseudospins in layered transition metal dichalcogenides." *Nature Physics* **10**, 343 (2014).

- [16] A. Kormányos, G. Burkard, M. Gmitra, J. Fabian, V. Zólyomi, N. D. Drummond, and V. Fal'ko. "k · p theory for two-dimensional transition metal dichalcogenide semiconductors." *2D Materials* **2**, 022001 (2015).
- [17] J. Jiang, F. Tang, X. C. Pan, H. M. Liu, X. H. Niu, Y. X. Wang, D. F. Xu, H. F. Yang, B. P. Xie, F. Q. Song, P. Dudin, T. K. Kim, M. Hoesch, P. K. Das, I. Vobornik, X. G. Wan, and D. L. Feng. "Signature of Strong Spin-Orbital Coupling in the Large Nonsaturating Magnetoresistance Material WTe<sub>2</sub>." *Phys. Rev. Lett.* **115**, 166601 (2015).
- [18] M.-H. Nguyen, D. C. Ralph, and R. A. Buhrman. "Spin Torque Study of the Spin Hall Conductivity and Spin Diffusion Length in Platinum Thin Films with Varying Resistivity." *Physical Review Letters* **116**, 126601 (2016).
- [19] J. Lee, Z. Wang, H. Xie, K. F. Mak, and J. Shan. "Valley magnetoelectricity in single-layer MoS<sub>2</sub>." *Nature Materials* **16**, 887 (2017).
- [20] V. P. Amin and M. D. Stiles. "Spin transport at interfaces with spin-orbit coupling: Formalism." *Phys. Rev. B* **94**, 104419 (2016).
- [21] V. P. Amin and M. D. Stiles. "Spin transport at interfaces with spin-orbit coupling: Phenomenology." *Phys. Rev. B* **94**, 104420 (2016).
- [22] K.-W. Kim, K.-J. Lee, J. Sinova, H.-W. Lee, and M. D. Stiles. "Spin-orbit torques from interfacial spin-orbit coupling for various interfaces." *Phys. Rev. B* **96**, 104438 (2017).
- [23] K. Garello, I. M. Miron, C. O. Avci, F. Freimuth, Y. Mokrousov, S. Blügel, S. Auffret, O. Boulle, G. Gaudin, and P. Gambardella. "Symmetry and magnitude of spinorbit torques in ferromagnetic heterostructures." *Nature Nanotechnology* **8**, 587 (2013).

- [24] G. Yu, P. Upadhyaya, Y. Fan, J. G. Alzate, W. Jiang, K. L. Wong, S. Takei, S. A. Bender, L.-T. Chang, Y. Jiang, M. Lang, J. Tang, Y. Wang, Y. Tserkovnyak, P. K. Amiri, and K. L. Wang. "Switching of perpendicular magnetization by spinorbit torques in the absence of external magnetic fields." *Nature Nanotechnology* **9**, 548 (2014).
- [25] A. Chernyshov, M. Overby, X. Liu, J. K. Furdyna, Y. Lyanda-Geller, and L. P. Rokhinson. "Evidence for reversible control of magnetization in a ferromagnetic material by means of spinorbit magnetic field." *Nature Physics* **5**, 656 (2009).
- [26] M. Endo, F. Matsukura, and H. Ohno. "Current induced effective magnetic field and magnetization reversal in uniaxial anisotropy (Ga,Mn)As." *Applied Physics Letters* **97**, 222501 (2010).
- [27] D. Fang, H. Kurebayashi, J. Wunderlich, K. Výborný, L. P. Zárbo, R. P. Campion, A. Casiraghi, B. L. Gallagher, T. Jungwirth, and A. J. Ferguson. "Spinorbit-driven ferromagnetic resonance." *Nature Nanotechnology* **6**, 413 (2011).
- [28] T. D. Skinner, K. Olejník, L. K. Cunningham, H. Kurebayashi, R. P. Campion, B. L. Gallagher, T. Jungwirth, and A. J. Ferguson. "Complementary spin-Hall and inverse spin-galvanic effect torques in a ferromagnet/semiconductor bilayer." *Nature Communications* **6**, 6730 (2015).
- [29] C. Ciccarelli, L. Anderson, V. Tshitoyan, A. J. Ferguson, F. Gerhard, C. Gould, L. W. Molenkamp, J. Gayles, J. Železný, L. Šmejkal, Z. Yuan, J. Sinova, F. Freimuth, and T. Jungwirth. "Room-temperature spinorbit torque in NiMnSb." *Nature Physics* **12**, 855 (2016).

- [30] J. Ribeiro-Soares, R. M. Almeida, E. B. Barros, P. T. Araujo, M. S. Dresselhaus, L. G. Cançado, and A. Jorio. "Group theory analysis of phonons in two-dimensional transition metal dichalcogenides." *Physical Review B* **90**, 115438 (2014).
- [31] X. Zhang, Q. Liu, J.-W. Luo, A. J. Freeman, and A. Zunger. "Hidden spin polarization in inversion-symmetric bulk crystals." *Nature Physics* **10**, 387 (2014).
- [32] H. Kurebayashi, J. Sinova, D. Fang, A. C. Irvine, T. D. Skinner, J. Wunderlich, V. Novák, R. P. Campion, B. L. Gallagher, E. K. Vehstedt, L. P. Zárbo, K. Výborný, A. J. Ferguson, and T. Jungwirth. "An antidamping spinorbit torque originating from the Berry curvature." *Nature Nanotechnology* **9**, 211 (2014).
- [33] J. Železný, H. Gao, A. Manchon, F. Freimuth, Y. Mokrousov, J. Zemen, J. Mašek, J. Sinova, and T. Jungwirth. "Spin-orbit torques in locally and globally noncentrosymmetric crystals: Antiferromagnets and ferromagnets." *Physical Review B* **95**, 014403 (2017).
- [34] S. Emori, T. Nan, A. M. Belkessam, X. Wang, A. D. Matyushov, C. J. Babroski, Y. Gao, H. Lin, and N. X. Sun. "Interfacial spin-orbit torque without bulk spin-orbit coupling." *Phys. Rev. B* **93**, 180402 (2016).
- [35] A. Azevedo, L. H. Vilela Leo, R. L. Rodriguez-Suarez, A. B. Oliveira, and S. M. Rezende. "dc effect in ferromagnetic resonance: Evidence of the spin-pumping effect?" *Journal of Applied Physics* **97**, 10C715 (2005).
- [36] E. Saitoh, M. Ueda, H. Miyajima, and G. Tatara. "Conversion of spin cur-

rent into charge current at room temperature: Inverse spin-Hall effect.” *Applied Physics Letters* **88**, 182509 (2006).

- [37] O. Mosendz, V. Vlaminck, J. E. Pearson, F. Y. Fradin, G. E. W. Bauer, S. D. Bader, and A. Hoffmann. “Detection and quantification of inverse spin Hall effect from spin pumping in permalloy/normal metal bilayers.” *Phys. Rev. B* **82**, 214403 (2010).
- [38] J. C. R. Sánchez, L. Vila, G. Desfonds, S. Gambarelli, J. P. Attané, J. M. De Teresa, C. Magén, and A. Fert. “Spin-to-charge conversion using Rashba coupling at the interface between non-magnetic materials.” *Nature Communications* **4**, 2944 (2013).

## CHAPTER 5

### CURRENT-INDUCED TORQUES IN TANTALUM DITELLURIDE WITH DRESSELHAUS SYMMETRY.

In this chapter, we measure current-induced torques in heterostructures of Permalloy (Py) with TaTe<sub>2</sub>, a transition-metal dichalcogenide material possessing low crystal symmetries. In our TaTe<sub>2</sub>/Py heterostructures, we find torque components with Dresselhaus symmetry, and suggest that the dominant mechanism is simply the Oersted field from a component of current that flows perpendicular to the applied voltage that arises from resistance anisotropy within the TaTe<sub>2</sub>. As the spin-orbit torque community increasingly looks to low-symmetry materials as a way to tune the symmetry allowed spin-orbit torque geometries, there is a strong need to establish the additional torque contributions present in this class of materials. In this work we clarify one such mechanism that does not have its basis in a spin-orbit torque mechanism. This work is adapted from a preprint with the coauthors David MacNeill, Nikhil Sivadas, Ismail El Baggari, Marcos Guimarães, Neal Reynolds, Lena Kourkoutis, Robert Buhrman, Craig Fennie and Dan Ralph.

#### 5.1 Introduction

Current-induced spin-orbit torques are a promising method for efficiently manipulating magnetic devices [1]. Understanding the mechanisms by which the directions of these torques can be manipulated, for example by using crystal symmetries, is important for optimizing them for applications. To date, all observations of spin-orbit torques from centrosymmetric materials – generated through either spin Hall [2, 3], Rashba-Edelstein [4, 5], topological spin-

momentum locking [6, 7], or other spin-orbit effects [8, 9] – can be described as corresponding to a Rashba-like symmetry (Fig. 5.1a). That is, the generated field or spin is perpendicular to the applied current and lies within the sample plane. Torques corresponding to a more general spin symmetry have been observed only in non-centrosymmetric systems, such as torques resulting from the out-of-plane spins in  $WTe_2$  (Chapters 2 and 3), or torques corresponding to a Dresselhaus-like spin polarization (Fig. 5.1b) observed in GaMnAs [10, 11], GaAs/Fe bilayers [12, 13] and NiMnSb [14]. Here, we analyze current-induced torques in bilayers of Permalloy ( $Py = Ni_{81}Fe_{19}$ ) with the low-symmetry material  $TaTe_2$ , a centrosymmetric transition-metal dichalcogenide (TMD). To our surprise, the heterostructures exhibit components of torque for which the dependence on the angle of applied current relative to the crystalline axes reflects a Dresselhaus symmetry, regardless of the fact that  $TaTe_2$  is inversion symmetric. However, we suggest that in the case of  $TaTe_2$  this torque does not originate from a spin-orbit mechanism. Instead, we suggest that this torque is dominated by an Oersted field that mimics a Dresselhaus symmetry due to a resistance anisotropy that causes current to flow non-collinear with the applied electric field. As the spin-orbit torque community increasingly looks to low-symmetry materials as a way to tune the symmetry allowed spin-orbit torque geometries, there is a strong need to establish the additional torque contributions present in this class of materials.

$TaTe_2$  at room temperature has a monoclinic ( $1T'$ ) crystal structure with a centrosymmetric space group  $C2/m$  (# 12) [15, 16]. When integrated into a heterostructure with Py only a single structural symmetry remains, one mirror plane perpendicular to the TMD layers. In  $TaTe_2$ , this mirror is within the  $a$ - $c$  plane, (Fig. 5.1c). The low-symmetry crystal structures of  $TaTe_2$  is clearly vis-

ible in the cross-sectional high-angle annular dark-field scanning transmission electron microscopy (HAADF-STEM) image of one of our devices (Fig. 5.1d).

## 5.2 Device Fabrication

To fabricate our samples we exfoliate TaTe<sub>2</sub> from bulk crystals (supplied by HQ graphene) onto high resistivity silicon / silicon oxide wafers using the scotch tape method, where the final step of exfoliation is carried out in the load lock of our sputtering system under high vacuum ( $< 10^{-6}$  torr). We deposit 6 nm of the ferromagnet permalloy (Py = Ni<sub>81</sub>Fe<sub>19</sub>) by grazing angle sputtering to minimize damage to the TaTe<sub>2</sub> surface (Fig. 5.1d) in an ambient Ar pressure of 5 mtorr. We use a deposition rate well below 0.2 angstroms / second, with the substrate rotating at greater than 10 revolutions per minute. We cap our films with 2 nm Al to prevent oxidation of the ferromagnet. Flakes are selected through optical and atomic force microscopy, where the active region of any device is chosen to be atomically flat, with an RMS surface roughness below 300 pm. The devices are patterned into either a microwave-frequency-compatible ground-signal-ground geometry for resonant measurements, or Hall bars for low-frequency (kHz) 2nd-harmonic Hall measurements using e-beam lithography. The bars are defined by Ar ion milling with SiO<sub>2</sub> used as an etch mask. The etched bars are protected by subsequent sputter coating of SiO<sub>2</sub>. Electrical contacts, Ti (5 nm) / Pt (75 nm), are defined through a lift-off process. Device geometries for the ST-FMR and harmonic Hall measurements are as shown in Chapters 2 and 3 (see Figs. 2.1 and 3.1). The angle  $\phi_{I-mp}$  between the direction of the applied current and the mirror plane of the TMD in the finished devices is determined by measurements of a magnetic easy axis in the Py induced by interaction with the

TMD [17–19], in combination with polarized Raman spectroscopy and HAADF-STEM imaging (see Sections 5.7.4 and 5.7.5). The Py equilibrium magnetization lies within the sample plane. As depicted in Fig. 5.1e, when a current is applied to a TMD/Py bilayer a current-induced torque acts on the magnetic moment. To measure the current-induced torques in our samples, we use two complementary measurement methods, a harmonic Hall technique [18, 20, 21], and spin-torque ferromagnetic resonance (ST-FMR) [2, 6, 17], with all measurements made at room temperature. Both types of measurements gave consistent results. The harmonic Hall measurements are detailed in Section 5.7.2.

### 5.3 ST-FMR measurements

In a ST-FMR measurement, an in-plane RF current (7-12 GHz) is applied to the sample which generates torques on the ferromagnet in phase with the current (Fig. 5.1e). An in-plane magnetic field is applied at an angle of  $\phi$  relative to the applied current, and the magnitude of this field is swept through the ferromagnetic resonance condition. We measure a DC voltage arising from mixing between the RF current and resistance oscillations resulting from magnetization precession together with the anisotropic magnetoresistance (AMR) of the Py (Fig. 5.1f). This mixing voltage,  $V_{\text{mix}}$ , can be fitted as a function of magnetic field as a sum of symmetric and antisymmetric Lorentzians, where the amplitudes of these resonances ( $V_S$  and  $V_A$ ) allow independent measurements of the in-plane ( $\vec{\tau}_{\parallel}$ ) and out-of-plane ( $\vec{\tau}_{\perp}$ ) spin-orbit torques respectively [2, 17]:

$$V_S = -\frac{I_{\text{RF}}}{2} \left( \frac{dR}{d\phi} \right) \frac{1}{\alpha_G \gamma (2B_0 + \mu_0 M_{\text{eff}})} \tau_{\parallel}, \quad (5.1)$$

$$V_A = -\frac{I_{\text{RF}}}{2} \left( \frac{dR}{d\phi} \right) \frac{\sqrt{1 + \mu_0 M_{\text{eff}}/B_0}}{\alpha_G \gamma (2B_0 + \mu_0 M_{\text{eff}})} \tau_{\perp}. \quad (5.2)$$

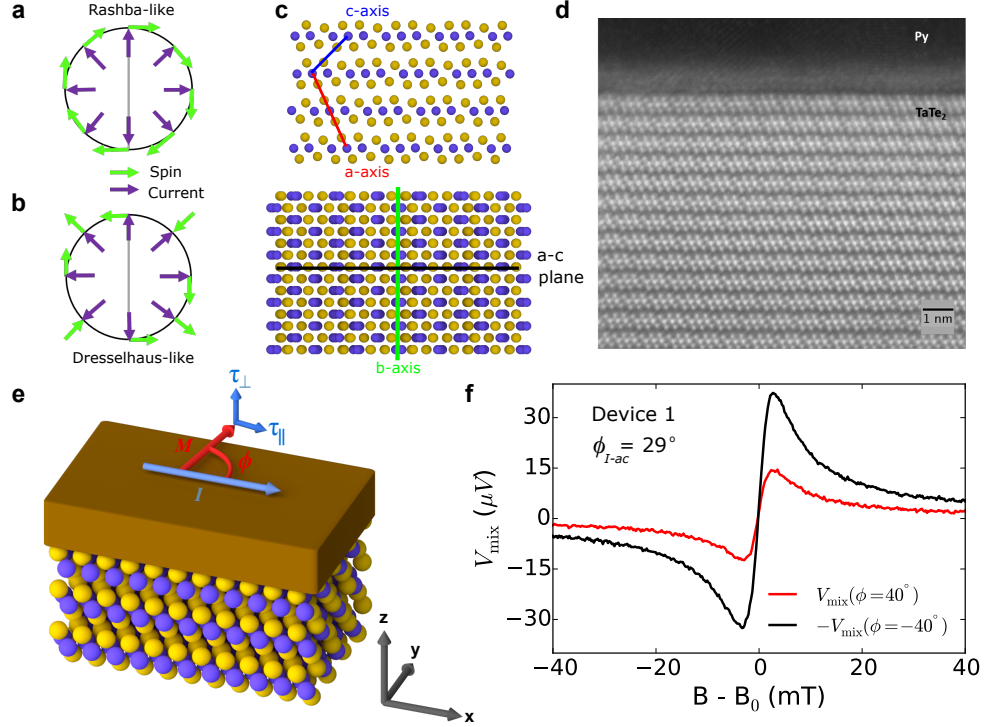


Figure 5.1: (a) Rashba-like and (b) Dresselhaus-like net spin (or field) polarizations, where the spin (green arrow) is generated in response to an applied current (purple arrow). The grey line represents a mirror plane. (c) TaTe<sub>2</sub> crystal structure looking down the b-axis (top) and the exfoliation plane (bottom). The yellow spheres represent Te atoms and the purple spheres represent Ta atoms. (d) A cross-sectional HAADF-STEM image of a TaTe<sub>2</sub>/Permalloy device showing high crystallinity except for one disordered and Te-deficient layer at the interface. The trimerization associated with the low-symmetry room-temperature TaTe<sub>2</sub> crystal structure is clearly visible. (e) Schematic of the bilayer TaTe<sub>2</sub>/Permalloy sample geometry. The x-axis is defined to be parallel to the applied electric field and the z-axis is perpendicular to the sample plane. (f) ST-FMR resonances for a TaTe<sub>2</sub> (19.7 nm) / Py (6 nm) device (Device 1) with the magnetization oriented at 40° and -40° degrees with respect to the current direction. The applied magnetic field,  $B$ , is normalized by the resonance field,  $B_0$ , to account for a small shift in the resonance due to an in-plane uniaxial anisotropy in the Permalloy. The applied microwave power is 2 dBm at a frequency of 9 GHz.

Here  $R$  is the device resistance,  $dR/d\phi$  is due to the AMR in the Py,  $\mu_0 M_{eff}$  is the out-of-plane demagnetization field,  $B_0$  is the resonance field,  $I_{RF}$  is the microwave current in the bilayer,  $\alpha_G$  is the Gilbert damping coefficient, and the

equilibrium magnetization is saturated along the applied field direction.

The magnitude of torques with a conventional Rashba-like symmetry,  $\vec{\tau}_{\parallel} \propto \hat{m} \times (\hat{m} \times \hat{y})$  and  $\vec{\tau}_{\perp} \propto \hat{m} \times \hat{y}$  for current in the  $\hat{x}$  direction, are proportional to  $\cos(\phi)$ . Therefore, in the presence of only Rashba-like torques the magnitude of  $V_{mix}$  is unchanged upon the operation  $\phi \rightarrow -\phi$  but the sign is reversed (as  $dR/d\phi \propto \sin(2\phi)$  in Eqs. 5.1 and 5.2). Figure 5.1f shows resonance curves in  $V_{mix}$  as a function of applied in-plane field magnitude for  $\phi = 40^\circ$  (red) and  $\phi = -40^\circ$  (black, inverted), for one of our TaTe<sub>2</sub>/Py bilayer devices (Device 1). The difference between the two  $V_{mix}$  measurements shows a lack of  $\phi \rightarrow -\phi$  symmetry in the observed torques and suggests the presence of a torque which does not arise entirely from a Rashba-like spin polarization. For all of the TaTe<sub>2</sub>/Py devices, the antisymmetric component of the ST-FMR resonance is by far the dominant contribution, so we will focus on  $\vec{\tau}_{\perp}$  here in the main text. The symmetric ST-FMR component indicates only a weak in-plane antidamping torque with Rashba symmetry  $\vec{\tau}_{\parallel} \propto \hat{m} \times (\hat{m} \times \hat{y})$  and in some cases a small contribution  $\propto \hat{m} \times \hat{z}$  that is not consistent from sample to sample and might arise from strain (see Section 5.7.6).

Figure 5.2a shows  $V_A$  as a function of  $\phi$  for TaTe<sub>2</sub>/Py Device 1. The observed  $V_A(\phi)$  clearly lacks  $\phi \rightarrow -\phi$  symmetry and therefore cannot be described as arising solely from Rashba-like torques  $\propto \cos(\phi)$ . Other symmetries are allowed, however, in low-symmetry samples such as TaTe<sub>2</sub>/Py. Torques associated with Dresselhaus-like spin generation (Fig. 5.1b) can contribute components  $\vec{\tau}_{\parallel} \propto \hat{m} \times [\hat{m} \times [\cos(2\phi_{I-mp})\hat{y} \pm \sin(2\phi_{I-mp})\hat{x}]]$  and  $\vec{\tau}_{\perp} = \hat{m} \times [\cos(2\phi_{I-mp})\hat{y} \pm \sin(2\phi_{I-mp})\hat{x}]$  where  $\hat{x}$  is the direction of applied current. The parts of the Dresselhaus contributions proportional to  $\hat{m} \times (\hat{m} \times \hat{x})$  or  $\hat{m} \times \hat{x}$  will give torque amplitudes

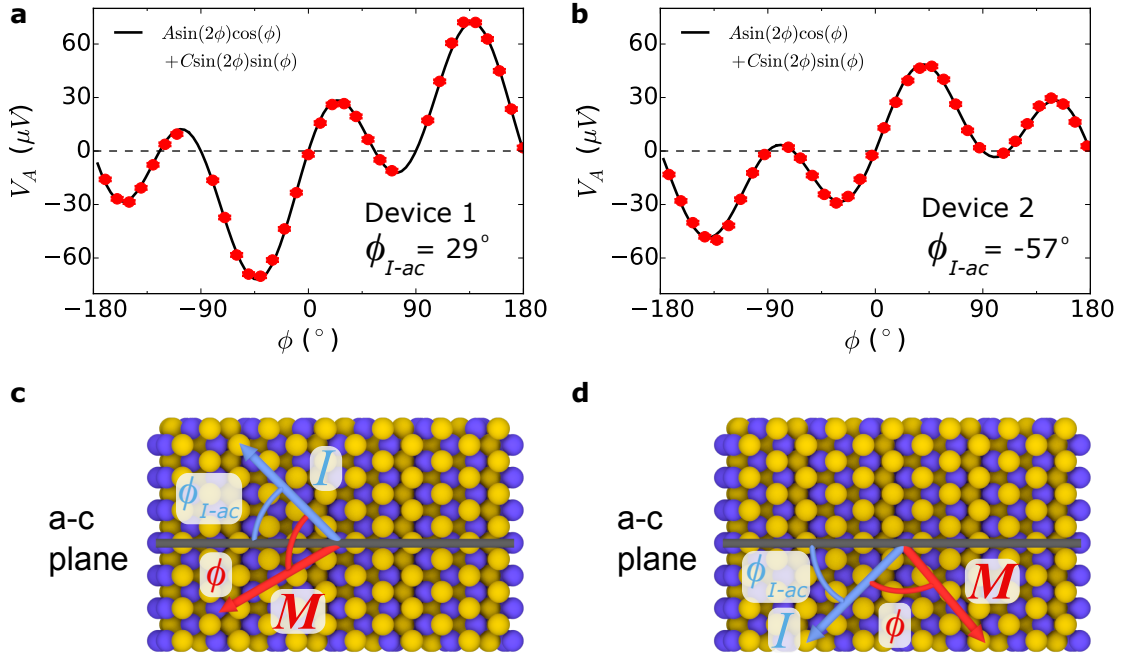


Figure 5.2: (a) and (b) Antisymmetric component of the ST-FMR resonance as a function of applied in-plane magnetic field angle for TaTe<sub>2</sub>/Py Devices 1 and 2 respectively. The applied microwave power is 2 dBm at a frequency of 9 GHz. Device 1 is TaTe<sub>2</sub> (19.7 nm) / Py (6 nm) and Device 2 is TaTe<sub>2</sub> (8.8 nm) / Py (6 nm) with distinct values of  $\phi_{I-mp}$ , the angle between the current and TaTe<sub>2</sub> a-c mirror plane, as specified in the panels.

$\propto \sin(2\phi_{I-ac}) \sin(\phi)$ . We will refer to any current-induced torque of this form as Dresselhaus-like, regardless of its microscopic origin. If we model the out-of-plane torques in our TaTe<sub>2</sub>/Py bilayers as a sum of Rashba-like and Dresselhaus-like terms, we can fit  $V_A$  as:

$$V_A = \sin(2\phi) [A \cos(\phi) + C \sin(\phi)], \quad (5.3)$$

where the  $\sin(2\phi)$  dependence comes from the AMR ( $dR/d\phi$ ) in Eq. 5.2, and both  $A$  and  $C$  might depend on  $\phi_{I-mp}$ . We extract a value of  $C/A = -0.69 \pm 0.01$  for Device 1, in which  $\phi_{I-mp}$  is positive. In Fig. 5.2b we show  $V_A(\phi)$  for TaTe<sub>2</sub>/Py Device 2, in which  $\phi_{I-mp}$  is negative. Positive and negative values of  $\phi_{I-mp}$  are as defined in Fig. 5.2 c and d respectively. In Device 2 the sign

of the  $\phi \rightarrow -\phi$  symmetry breaking is opposite that in Device 1, corresponding to an opposite sign  $C/A = 0.38 \pm 0.01$ . This is consistent with the expectation that in a Dresselhaus-like symmetry the component of spin or field along the current direction changes sign across the mirror plane (Fig. 5.1b). We note that the observation of a torque  $\propto \hat{m} \times \hat{x}$  is distinct from our previously-published work on  $\text{WTe}_2/\text{Py}$ , in which we observed a different non-Rashba component of  $\vec{\tau}_\perp \propto \hat{m} \times (\hat{m} \times \hat{z})$ . A torque proportional to  $\hat{m} \times (\hat{m} \times \hat{z})$  for an in-plane magnetization amounts to adding a term constant in  $\phi$  to Eq. 5.3 (B), such that  $\tau_\perp = A \cos(\phi) + B + C \sin(\phi)$ . We observe no out-of-plane antidamping torque in our  $\text{TaTe}_2/\text{Py}$  devices within experimental uncertainty.

## 5.4 Crystal Axis Dependence

We have performed torque measurements on 19 different  $\text{TaTe}_2/\text{Py}$  devices (4 2nd-harmonic Hall devices and 15 ST-FMR devices), all with distinct values of  $\phi_{I-mp}$  and  $\text{TaTe}_2$  thicknesses,  $t_{TMD}$ . Figure 5.3a shows extracted values of  $C/A$  as a function of  $\phi_{I-mp}$  for both types of samples. The measurements are in good agreement with the dependence on  $\phi_{I-mp}$  expected for a field or spin polarization with Dresselhaus symmetry (Fig. 5.1):  $C/A$  goes to zero when the current is applied either along or perpendicular to a mirror plane ( $\phi_{I-mp} = 0^\circ, 90^\circ$ , and  $180^\circ$ ), and changes sign as  $\phi_{I-mp}$  crosses the  $\text{TaTe}_2$  mirror plane ( $\phi_{I-mp} = 0^\circ$ ). Details for each device are given in Table 5.1.

Our group has previously studied the current-generated torques in the low symmetry TMD  $\text{WTe}_2$ , finding a new component of spin-orbit torque – an out-of-plane antidamping torque – consistent with the  $\text{WTe}_2$  crystal symmetries.

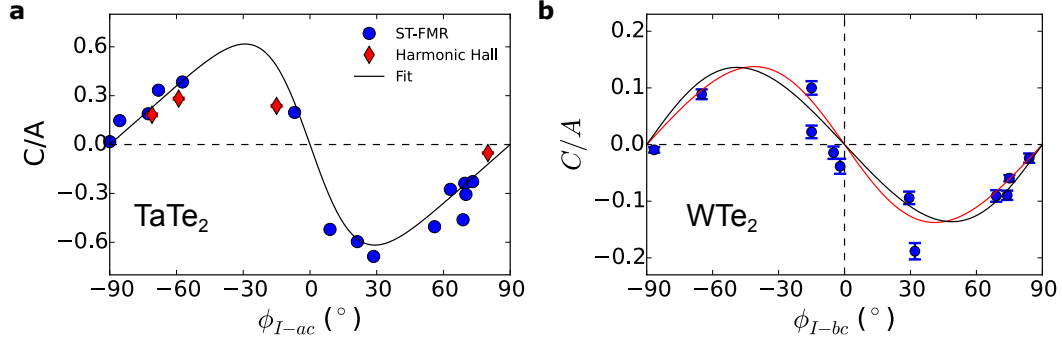


Figure 5.3: a) and b) Ratio of torques  $\propto \hat{m} \times \hat{x}$  to the torques  $\propto \hat{m} \times \hat{y}$ ,  $C/A$ , as a function of the angle between the applied current and the (a)  $\text{TaTe}_2$  a-c mirror plane and (b)  $\text{WTe}_2$  b-c mirror plane for devices studied by either ST-FMR (blue circles) or second harmonic Hall measurements (red diamonds). Fits are discussed in Sections 5.7.7 and 5.7.9.

$\text{WTe}_2$  has an orthorhombic crystal structure that is non-centrosymmetric, with space group  $\text{Pmn}2_1$  (# 31). When interfaced with Py, the heterostructure is reduced to a single mirror plane at the interface (along the  $\text{WTe}_2$  b-c plane). Due to the similarity of symmetries in  $\text{WTe}_2/\text{Py}$  and  $\text{TaTe}_2/\text{Py}$  heterostructures, one might also expect a Dresselhaus-like torque in  $\text{WTe}_2$ . Analysis of the  $\text{WTe}_2/\text{Py}$  devices is slightly more complicated than  $\text{TaTe}_2/\text{Py}$  devices due to the strong out-of-plane antidamping torque  $\vec{\tau}_\perp \propto \hat{m} \times (\hat{m} \times \hat{z})$  in addition to the Rashba and Dresselhaus components. See Section 5.7.9 for more details on the analysis of  $\text{WTe}_2$  devices. In previous work on  $\text{WTe}_2$  devices [17, 18], we studied primarily devices with current applied near high symmetry directions ( $\phi_{I-mp} = 0^\circ$  and  $\pm 90^\circ$ ) and the Dresselhaus contribution was sufficiently small that we did not make note of it. Nevertheless, studies of  $\text{WTe}_2/\text{Py}$  devices at intermediate angles  $\phi_{I-mp}$  allow a clear separation of the different torque components based on their dependence on  $\phi$ , and measurements of the Dresselhaus contribution (see Fig. 5.4). Figure 5.3b shows the extracted values of  $C/A$  as a function of  $\phi_{I-mp}$  for our  $\text{WTe}_2$  devices. Our previous measurements of out-of-plane antidamping torques in  $\text{WTe}_2/\text{Py}$  samples are not affected by the inclusion of the additional

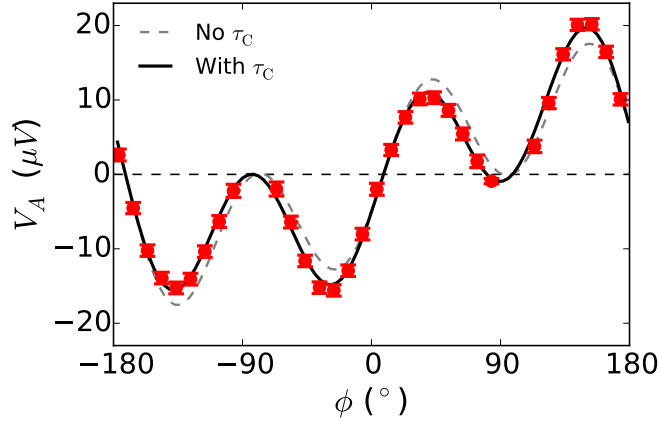


Figure 5.4: Antisymmetric component of the ST-FMR resonance as a function of applied in-plane magnetic field angle for WTe<sub>2</sub>/Py Device 11 in chapter 2. The applied microwave power is 2 dBm at a frequency of 9 GHz. The angle from the current to the mirror plane is 32°.

Dresselhaus term in the fits (see Section 5.7.9).

To obtain a more quantitative estimate for the strength of the Dresselhaus torques, we take into account that a Dresselhaus torque does not point exclusively in the direction  $\vec{\tau}_\perp \propto \hat{m} \times \hat{x}$ , but depending on the value of  $\phi_{I-mp}$  it can also have a component in the perpendicular direction that can add to or subtract from Rashba component (see Fig. 1a,b):

$$\tau_\perp^C = C \sin(\phi) = [D \sin(2\phi_{I-mp})] \sin(\phi),$$

$$\tau_\perp^A = A \cos(\phi) = [R + D \cos(2\phi_{I-mp})] \cos(\phi),$$

where  $R$  is the component of  $\cos(\phi)$  torques arising from a Rashba-like spin polarization, and  $D$  for Dresselhaus-like. The fit lines shown in Fig. 5.3 for TaTe<sub>2</sub>/Py corresponds to a value  $D/R = -0.51 \pm 0.03$  (see Section 5.7.7), and for WTe<sub>2</sub>/Py corresponds to a value  $D/R = -0.13 \pm 0.02$  (see Section 5.7.9).

## 5.5 Microscopic Mechanism

We now turn to consideration of the microscopic mechanism that generates current-induced torques with Dresselhaus symmetry in our system. TaTe<sub>2</sub> cannot generate a torque with a Dresselhaus symmetry through the mechanism present in GaMnAs [10, 11] and NiMnSb [14] (an inverse spin Galvanic effect), since inversion symmetry is intact in the TaTe<sub>2</sub> bulk. An interfacial generation is possible, but this would imply a trivial dependence on the TaTe<sub>2</sub> thickness (see Section 5.7.8), and preliminary first principles modeling of a torque from a “hidden spin-polarization” [22] suggests that this effect is small in our system. One trivial mechanism can arise from resistivity anisotropy within the TMD. Both TaTe<sub>2</sub> and WTe<sub>2</sub> exhibit significant resistance anisotropy, where we show the extracted resistivity of TaTe<sub>2</sub> from our devices as a function of  $\phi_{I-ac}$  in Fig 5.5a (where we have removed contributions from the Py layer and contact resistance as outlined in Section 5.7.8). The extracted in-plane resistivity anisotropy is  $2.6 \pm 0.6$ . When an electric potential is applied away from one of the principle axes in a material with anisotropic resistivity, the electric field and the current are no longer collinear, *i.e.* for a potential along the sample bar the generated current may be tilted. In a bar consisting of just one material, say TaTe<sub>2</sub>, the boundary conditions force the transverse current at the edges of the bar to be zero. However, in a bilayer with Py, the transverse component of current in the TMD will turn into the Py to establish a return current flowing in the reverse transverse direction and result in a circulating transverse current loop. The Oersted field generated by this current loop naturally produces a field-like torque on the Py layer with Dresselhaus symmetry ( $\vec{\tau}_{\perp} \propto \sin(2\phi_{I-mp})\hat{m} \times \hat{x}$ ), in addition to the standard Oersted torque with a Rashba symmetry from the projection

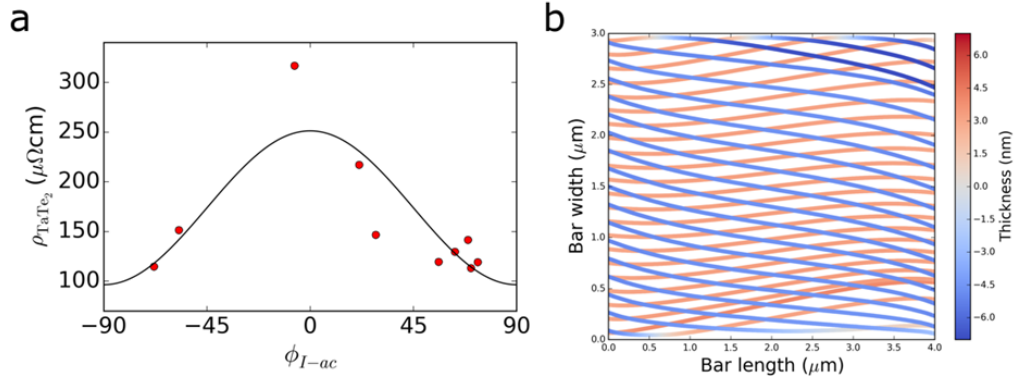


Figure 5.5: a) Measurement of the TaTe<sub>2</sub> resistivity for 10 of our devices as a function of  $\phi_{I-ac}$ , extracted from the two-point resistance. (b) Simulated current paths for a TaTe<sub>2</sub>(10 nm)/Py(6 nm) bilayer bar of length 4  $\mu\text{m}$  and width 3  $\mu\text{m}$  with a  $\phi_{I-ac} = 45^\circ$  for a constant voltage applied across the length of the bar. The color map shows the height of the current streamline, with positive values in the Py layer and negative values in the TaTe<sub>2</sub> layer.

of current flowing along the bar. We have modeled the current pathways and associated Oersted fields in our TaTe<sub>2</sub>/Py bilayers through the finite element analysis software package COMSOL. Figure 5.5b shows the simulated current path for a constant voltage applied across the length of a bar (length 4  $\mu\text{m}$  and width of 3  $\mu\text{m}$ ) with an anisotropy ratio of 2.6. Here, the principle axes tilted at a 45° angle from the length of the bar ( $\phi_{I-mp} = 45^\circ$ ). The blue streamlines show the current within the TaTe<sub>2</sub>, and the red streamlines show the current flowing within the Py.

By taking the ratio of the integrated total current within the TaTe<sub>2</sub> layer going in the y-direction (along the width of the bar) to that in the x-direction (along the length of the bar) we can estimate a value of  $C/A$  due to the Oersted field generated by tilted currents. The result has the same dependence on  $\phi_{I-mp}$  as measured for the TaTe<sub>2</sub>/Py bilayers and the correct overall sign of  $C/A$  vs.  $\phi_{I-mp}$  for TaTe<sub>2</sub>/Py. For an anisotropy ratio of 2.6 we estimate a ratio of  $C/A \sim 0.32$ , within a factor of 2 of the result found in experiment. This quantitative differ-

ence might be explained by an underestimate of the resistivity anisotropy in the TaTe<sub>2</sub> or by spatial non-uniformity in the resistivity as a function of thickness in the Py layer. If such a non-uniformity were due to increased scattering at the TaTe<sub>2</sub>/Py interface, the average effective resistivity of the Py would be higher above the midplane of the Py layer than below. This causes the return current of the transverse current loop flowing in the Py to add to the Oersted field from the transverse current flowing in the TaTe<sub>2</sub>, while the longitudinal current in the Py at the same time subtracts from the Oersted field produced by the longitudinal current in the TaTe<sub>2</sub>. This has the overall effect of increasing  $C$  and decreasing  $A$ , giving an enhanced value of  $C/A$ .

Additional evidence that the Dresselhaus torque in TaTe<sub>2</sub>/Py is due to an Oersted field rather than a spin-orbit torque is that all other components of spin-orbit torque in TaTe<sub>2</sub>/Py are measured to be small or zero (including the in-plane antidamping torque with Rashba symmetry,  $\propto \hat{m} \times (\hat{m} \times \hat{y})$ , that is usually dominant in spin-orbit systems). This may also be the reason that TaTe<sub>2</sub> does not exhibit an out-of-plane antidamping torque  $\propto \hat{m} \times (\hat{m} \times \hat{z})$  even though it is symmetry allowed. Last, the observed Dresselhaus torque  $\propto \hat{m} \times \hat{x}$  and the Oersted torque from the longitudinal current  $\propto \hat{m} \times \hat{y}$  have a similar dependence on the thickness of the TaTe<sub>2</sub> (see Section 5.7.8).

A torque from tilted currents in WTe<sub>2</sub>/Py bilayers also qualitatively explains the Dresselhaus symmetry torques observed in WTe<sub>2</sub>/Py devices, and is discussed in more detail in Section 5.7.9.

## 5.6 Conclusions

In summary, we have measured current-induced torques with Dresselhaus-like symmetry in both TaTe<sub>2</sub>/Py and WTe<sub>2</sub>/Py. This component of torque can likely be explained as due to the Oersted field generated by a component of current transverse to the applied voltage in the sample, arising from the resistivity anisotropy in the low-symmetry TMDs. Understanding the various possible torque generation mechanisms in low-symmetry systems is crucial for potential engineering of the microscopic mechanisms by which crystal symmetries can be used to manipulate spin-orbit torques. It is our hope that this work clarifies one such mechanism that does not have its basis in a spin-orbit torque mechanism.

Acknowledgements: The primary support for this project, including support for G.M.S., came from the US Department of Energy (DE-SC0017671). D.M. was supported in part by the National Science Foundation (NSF) (DMR-1406333), N.S. by the NSF through the Platform for the Accelerated Realization, Analysis, and Discovery of Interface Materials (PARADIM) (DMR-1539918) and the Cornell University Center for Advanced Computing at Cornell University, M.H.D.G. by the Netherlands Organization for Scientific Research (NWO Rubicon 680-50-1311), and N.D.R. by the NSF through the Cornell Center for Materials Research (CCMR) (DMR-1719875). Sample fabrication was performed in the CCMR shared facilities and at the Cornell Nanoscale Science & Technology Facility, a member of the National Nanotechnology Infrastructure Network, which is supported by the NSF (ECCS-1542081). The electron microscopy work was primarily supported by the NSF through PARADIM as part of the Materials for Innovation Platform Program. The FEI Titan Themis 300 was acquired through Grant NSF-MRI-1429155, with additional support from Cornell University, the

Weill Institute, and the Kavli Institute at Cornell.

## 5.7 Supplemental Information

### 5.7.1 Analysis of ST-FMR measurements

The details of our ST-FMR analysis can be found in Section 2.8.2. To determine a quantitative measure of the torques (not just a ratio) from Eqs. 1 and 2, we determine  $\alpha_G$ ,  $R(\phi)$  and  $I_{\text{RF}}$  as discussed in Section 2.8.2, with the exception that  $R(\phi)$  is measured under a 0.1 T field in this work.

The torque conductivity reported in the main text is defined as the angular momentum absorbed by the magnet per second per unit interface area per unit electric field. It provides a measure of the torques produced in a spin source/ferromagnet bilayer independent of geometric factors. For a torque  $\tau_K$  (where  $K = \text{A or C}$ ) we calculate the corresponding torque conductivity as:

$$\sigma_K = \frac{M_S l w t_{\text{magnet}}}{\gamma} \frac{\tau_K}{(l w) E} = \frac{M_S l t_{\text{magnet}}}{\gamma} \frac{\tau_K}{I_{\text{RF}} \cdot Z},$$

where  $M_S$  is the saturation magnetization,  $E$  is the electric field,  $l$  and  $w$  are the length and width of the TaTe<sub>2</sub>/Permalloy bilayer,  $Z$  is the measured RF device impedance, and  $t_{\text{magnet}}$  is the thickness of the Permalloy. We approximate  $\mu_0 M_S \approx \mu_0 M_{\text{eff}} = 0.83$  T, as extracted from the ST-FMR measurements.

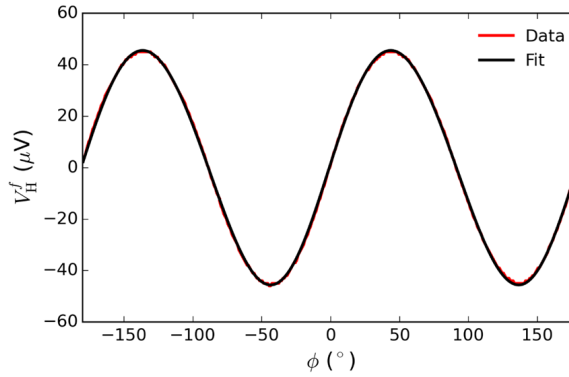


Figure 5.6: First harmonic Hall signal (red) and fit (black) in Device 16 with 20 mT applied in-plane field and a 300 mV RMS excitation across sample and a 50  $\Omega$  bias resistor in series.

### 5.7.2 Second harmonic Hall measurements

Hall bars are fabricated using the same process as our ST-FMR devices, and have a length and width as specified in Table 5.1; the width of the voltage probes used for the Hall measurements are scaled by a ratio of 0.375 times the width of the bar for each device. The active region of the Hall bar has a uniform TaTe<sub>2</sub> thickness, with no monolayer steps as measured by atomic force microscopy. We apply a voltage  $V(t) = V_0 \cos(2\pi ft)$  across the sample and a 50  $\Omega$  bias resistor in series at a frequency  $f=1.3$  kHz, where  $V_0 = 300$  mV or 200 mV root mean square (RMS) for bars of width 3  $\mu\text{m}$  and 2  $\mu\text{m}$  respectively. The first ( $V_H^f$ ) and second ( $V_H^{2f}$ ) harmonic of the Hall signals are measured simultaneously as a function of applied magnetic field angle, where the magnitude of the applied field is held constant throughout a given measurement (ranging from 0.01 to 0.1 T). The current through the Hall bar is measured separately under the same experimental conditions as the Hall measurement. Figure 5.6 shows the first harmonic Hall signal as a function of applied magnetic field angle,  $\phi$ , and is fit

using the equation:

$$V_H^f = I_0 R_{PHE} \sin(2\phi_M),$$

where  $I_0$  is the current applied to the Hall bar,  $R_{PHE}$  is the planar Hall resistance and  $\phi_M$  is the angle of the magnetization with respect to the current direction. In the limit where  $B \gg B_A$ ,  $\phi_M = \phi - (B_A/B) \sin(2\phi - 2\phi_{EA})$ , where  $B_A$  is the magnitude of the in-plane magnetic anisotropy in the Permalloy and  $\phi_{EA}$  is the angle of the magnetic easy-axis with respect to the current direction. The first harmonic Hall measurement is used to determine  $I_0 R_{PHE}$ ,  $B_A$ , and  $\phi_{EA}$ .  $V_H^{2f}$  is related to the out-of-plane ( $\tau_\perp$ ) and in-plane ( $\tau_\parallel$ ) components of the current-generated spin-orbit torques by (see Section 3.6.1 for a derivation<sup>1</sup>):

$$V_H^{2f} \approx I_0 R_{PHE} \cos(2\phi_M) \frac{\tau_\perp/\gamma}{B + B_A \cos(2\phi_M - 2\phi_{EA})} + \frac{I_0 R_{AHE}}{2} \frac{\tau_\parallel/\gamma}{B + \mu_o M_{\text{eff}} + B_A \cos^2(\phi_M - \phi_{EA})}, \quad (5.4)$$

where  $R_{PHE}$  is the planar Hall resistance,  $R_{AHE}$  is the anomalous Hall resistance,  $\mu_o M_{\text{eff}}$  is the effective magnetization field, and  $\gamma$  is the gyromagnetic ratio. In high symmetry systems the spin-orbit torques have a purely Rashba-like spin-symmetry with an out-of-plane component  $\vec{\tau}_\perp \propto \hat{m} \times \hat{y}$  and an in-plane component  $\vec{\tau}_\parallel \propto \hat{m} \times (\hat{m} \times \hat{y})$  where the applied current is the  $\hat{x}$  direction. In this case, both torque magnitudes are proportional to  $\cos(\phi_M)$  and therefore  $V_H^{2f}(\phi) = V_H^{2f}(-\phi)$  for small  $B_A$ . Figure 5.7a shows  $V_H^{2f}$  as a function of  $\phi$  for one of our Hall bar devices (Device 16). As in our ST-FMR measurements, the measured second harmonic Hall signal clearly lacks  $\phi \rightarrow -\phi$  symmetry. This asymmetry cannot be captured by Rashba-like torques and the small in-plane magnetic anisotropy (grey fit in Fig. 5.7a), pointing to the presence of additional torques. If we allow for a Dresselhaus-like component of field-like torque,  $\propto \hat{m} \times \hat{x}$ , and model the out-of-plane torques present in our Hall bar as a sum of Rashba-like and

<sup>1</sup>Note that there is an unfortunate difference in the definition of the in-plane torque direction in Chapter 3 than in the other chapters.

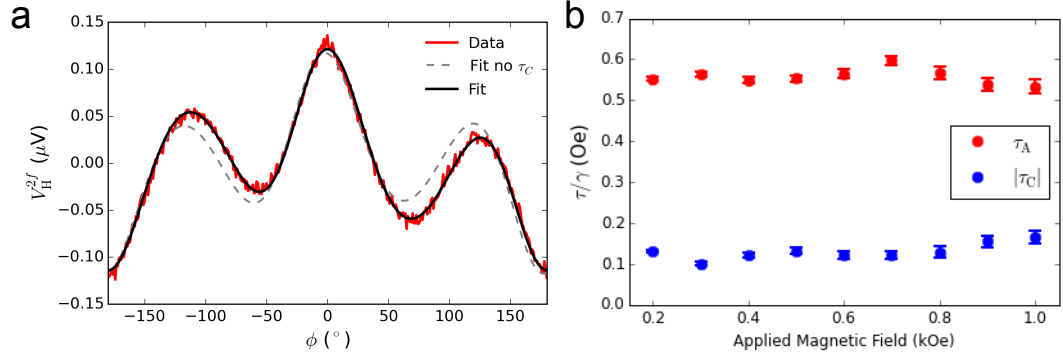


Figure 5.7: (a) Second harmonic Hall voltage for Device 16, where the dashed grey line gives the fit function assuming only Rashba-like torque contributions, and the black curve shows the full fit using Eq. 5.5 . As can be clearly seen, the small uniaxial anisotropy in the Py only weakly breaks  $\phi \rightarrow -\phi$  symmetry and is unable to account for our observations. The applied in-plane magnetic field is 20 mT with a 300 mV excitation across the device and an in series 50 ohm bias resistor. (b) The second harmonic Hall fit values of  $\tau_A$  and  $\tau_C$  as a function of applied in-plane magnetic field for Device 16 under the same excitation conditions.

Dresselhaus-like components:

$$\tau_{\perp} = A \cos(\phi) + C \sin(\phi),$$

we can accurately capture the  $\phi \rightarrow -\phi$  symmetry breaking in the observed  $V_H^{2f}$ .

To fit the second harmonic Hall data, we must consider the effects of magneto-thermal voltages. For an in-plane magnetization, thermal contributions to the second harmonic Hall voltage are dominated by the planar Nernst effect arising from an out-of-plane thermal gradient, which adds a term proportional to  $\cos(\phi)$  to  $V_H^{2f}$ . In the limit of  $\mu_0 M_{\text{eff}} \gg B, B_A$ , the second harmonic Hall voltage arising from  $\tau_{\parallel}$  also has an overall angular dependence of  $\cos(\phi)$  if  $\tau_{\parallel}$  has only a Rashba-like contribution. We therefore combine the terms proportional to  $\cos(\phi)$  into one fit parameter to yield a total fit function of:

$$V_H^{2f} \approx \cos(2\phi_M) \frac{A \cos(\phi_M) + C \sin(\phi_M)}{B + B_A \cos(2\phi_M - 2\phi_E)} + N \cos(\phi_M) + \text{offset}, \quad (5.5)$$

where  $A$  is proportional to the out-of-plane torques with a  $\cos(\phi_m)$  dependence,

$$A = I_0 R_{PHE} \tau_A / \gamma,$$

and  $C$  is proportional to the out-of-plane torques with a  $\sin(\phi_m)$  dependence,

$$C = I_0 R_{PHE} \tau_C / \gamma.$$

$N$  is a combination of an in-plane antidamping torque and the planar Nernst contributions. Figure 5.7a shows the measured  $V_H^{2\omega}$  as a function of  $\phi$  (red) for Device 16 and the fit (black). Figure 5.7b shows  $\tau_A/\gamma$  and  $\tau_C/\gamma$  as a function of applied magnetic field, where  $I_0 R_{PHE}$  extracted from the first harmonic Hall signal is divided from the fit values of  $A$  and  $C$ . The field independence of the extracted terms confirms their origin as current-generated torques.

We determine the individual torque conductivities  $\sigma_A$  and  $\sigma_C$  from the second harmonic Hall measurements according to (here the subscript  $K = A$  or  $C$ ):

$$\sigma_K = \frac{M_s l w t_{\text{magnet}}}{\hbar \gamma / 2e} \frac{\tau_K}{(l w) E} \left( \frac{\hbar}{2e} \right) = \frac{e M_s l t_{\text{magnet}}}{\mu_B} \frac{\tau_K}{V} \left( \frac{\hbar}{2e} \right)$$

To estimate the applied electric field we divide the applied voltage by the length of the Hall device. We estimate the saturation magnetization as the effective magnetization,  $M_s \approx M_{\text{eff}}$ , determined from the average  $M_{\text{eff}}$  of our ST-FMR devices (described below), finding  $\mu_0 M_{\text{eff}} = 0.83\text{T} \pm 0.02\text{T}$ . This is a reasonable approximation given that Hall and ST-FMR devices are made from the same ferromagnetic deposition and fabrication process.

Device Number	Device Type	$t$ (nm) $\pm 0.3$ nm	$L \times W$ ( $\mu\text{m}$ ) $\pm 0.2$ $\mu\text{m}$	$C/A$	$\tau_S/\tau_A$	$B_A$ (0.1 mT)	$\phi_{\text{T-ac}}$	$\phi_{\text{Raman}}$ $\pm 2^\circ$
1	ST-FMR	8.8	5 X 4	-0.687(7)	0.20(2)	23	29	45
2	ST-FMR	19.7	5 X 4	0.384(7)	-0.04(2)	20	-57	-70
3	ST-FMR	6.8	4 X 3	-0.31(1)	0.17(3)	48	70	50
4	ST-FMR	11.3	5 X 4	-0.596(8)	0.30(2)	20	21	25
5	ST-FMR	10.4	5 X 4	-0.238(6)	0.18(2)	29	70	-
6	ST-FMR	9.1	5 X 4	-0.275(6)	0.22(1)	21	63	65
7	ST-FMR	15.4	5 X 4	0.197(6)	0.21(2)	28	-7	-7
8	ST-FMR	16.4	5 X 4	0.147(6)	-0.02(2)	16	-86	-90
9	ST-FMR	9.4	3 X 2	0.189(4)	0.18(1)	17	-72	-
10	ST-FMR	11.0	4 X 3	-0.521(5)	0.18(1)	25	9	-
11	ST-FMR	16.1	4 X 3	0.02(1)	-0.01(4)	53	-90	-90
12	ST-FMR	6	4 X 3	0.334(9)	0.16(3)	48	-68	-55
13	ST-FMR	8.2	4 X 3	-0.46(1)	0.15(3)	43	69	50
14	ST-FMR	17.4	4 X 3	-0.50(1)	0.06(3)	25	56	25
15	ST-FMR	4.5	4 X 3	-0.23(1)	0.27(3)	29	73	20
16	SH	14.2	10.3 X 3	0.237(6)	-	19	-15	-20
17	SH	7.8	7.2 X 2	-0.052(4)	-	31	80	85
18	SH	16.4	4.9 X 2	0.282(5)	-	18	-59	-20
19	SH	5.0	16 X 3	0.182(8)	-	46	-71	-

Table 5.1: Comparison of device parameters, torque ratios, and magnetic anisotropy parameters for TaTe<sub>2</sub>/Py heterostructures.

### 5.7.3 Cross-sectional HAADF-STEM

For electron microscopy measurements, we prepare a thin cross-sectional lamella from the active area of Devices 7 and 11 using the focused ion beam (FIB) lift-out technique. Imaging is performed perpendicular to the current direction of the sample. Aberration-corrected high-angle annular dark-field (HAADF) STEM is performed in an FEI Titan Themis operating at 300 kV. The convergence semi-angle is 21.4 mrad, and the inner collection angle for HAADF is 68 mrad. The probe current is 50-60 pA. To overcome drift and scan noise, we collect stacks of 30 images taken with 1  $\mu\text{s}$ /pixel dwell time and align and average them using rigid registration. Despite the high voltage, we do not observe knock-on damage between frames or during imaging. The sample alignment from the expected crystal axis for devices 7 and 11 differed by only  $\sim 5$  degrees, which is typical for samples prepared using FIB lift-out. STEM imaging cour-

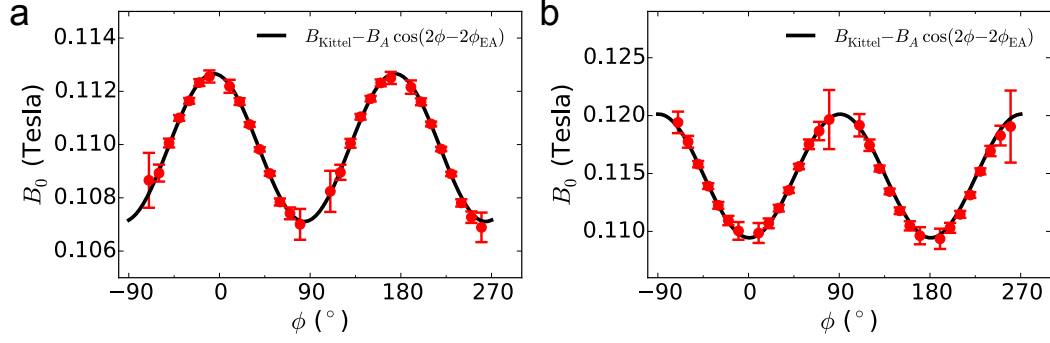


Figure 5.8: Resonant field for ST-FMR devices as a function of applied magnetic field angle for Device 7 (a) and Device 11 (b). The angle at which the resonant field is minimized gives the direction of the magnetic easy axis,  $\phi_{EA}$ , here  $83^\circ$  and  $0^\circ$ , corresponding to  $\phi_{I-ac}$  values of  $-7^\circ$  and  $-90^\circ$ , respectively. The magnitude of the magnetic easy axis,  $B_A$ , can also be directly extracted from the fit. The applied microwave frequency is 9 GHz with applied powers of 2 dBm and 5 dBm respectively.

tesy of Ismail El Baggari.

#### 5.7.4 Measurement of the in-plane magnetic anisotropy

In our ST-FMR devices, measurements of the resonant field ( $B_0$ ) as a function of the applied magnetic field angle ( $\phi$ ) can be used to extract the in-plane magnetic easy-axis direction and magnitude. The angular dependence of  $B_0$  can be described by:

$$B_0 = B_{\text{Kittel}} - B_A \cos(2[\phi - \phi_{EA}]),$$

where  $B_{\text{Kittel}}$  is the resonance field without any in-plane anisotropy and  $\phi_{EA}$  is the angle of the easy-axis with respect to the current direction. Figure 5.8 shows the magnetic field at ferromagnetic resonance as a function of the in-plane magnetization angle for Devices 7 and 11. The data from both samples indicate the presence of a uniaxial magnetic anisotropy within the sample plane, at angles of 83 and 4 degrees from the current direction, respectively. Table 5.1 shows the

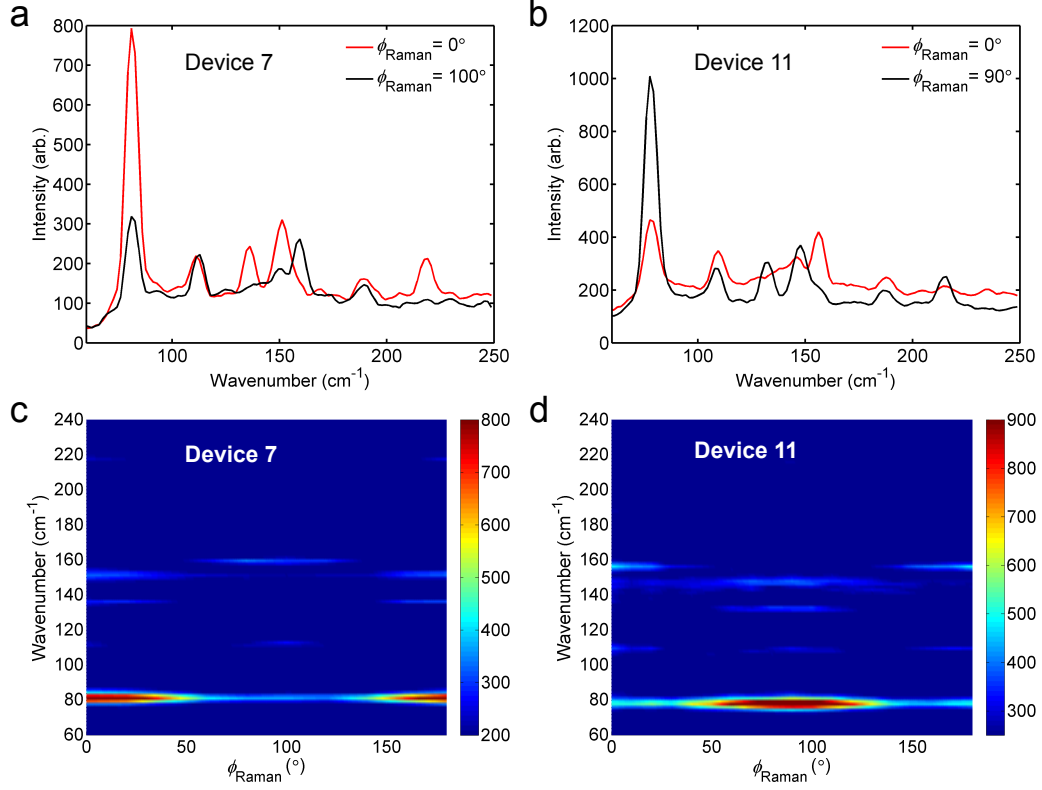


Figure 5.9: (a,b) Raman spectra for Devices 7 and 11, with a 488 nm excitation and with the excitation and detector polarized parallel to each other.  $\phi_{\text{Raman}}$  is the angle between the excitation polarization and the device current direction (along the bar). The red traces show spectra with the polarization parallel to the current and the black traces show spectra with the polarization approximately perpendicular. (c,d) Angular dependence of the Raman spectra for the two devices. The color map represents the peak intensity (with arbitrary units). The maximum of the  $\sim 80 \text{ cm}^{-1}$  peak corresponds to the TaTe<sub>2</sub> a-c mirror plane, where  $\phi_{\text{Raman}} \rightarrow -\phi_{I-ac}$ .

magnitude of  $B_A$  and  $\phi_{EA}$  for all devices.

In our Hall bar devices, measurements of the first harmonic Hall voltage (described in Section 5.7.2) can be used to determine the magnitude and direction of the induced easy-axis in the Permalloy film. The Hall voltage is given by  $V_H = I_0 R_{PHE} \sin(2\phi_M)$ , where  $I_0$  is the current applied to the Hall bar,  $R_{PHE}$  is the planar Hall resistance and  $\phi_M$  is the angle of the magnetization with respect to the current direction. In the limit where  $B \gg B_A$ ,  $\phi_M = \phi - (B_A/B) \sin(2\phi - 2\phi_{EA})$ .

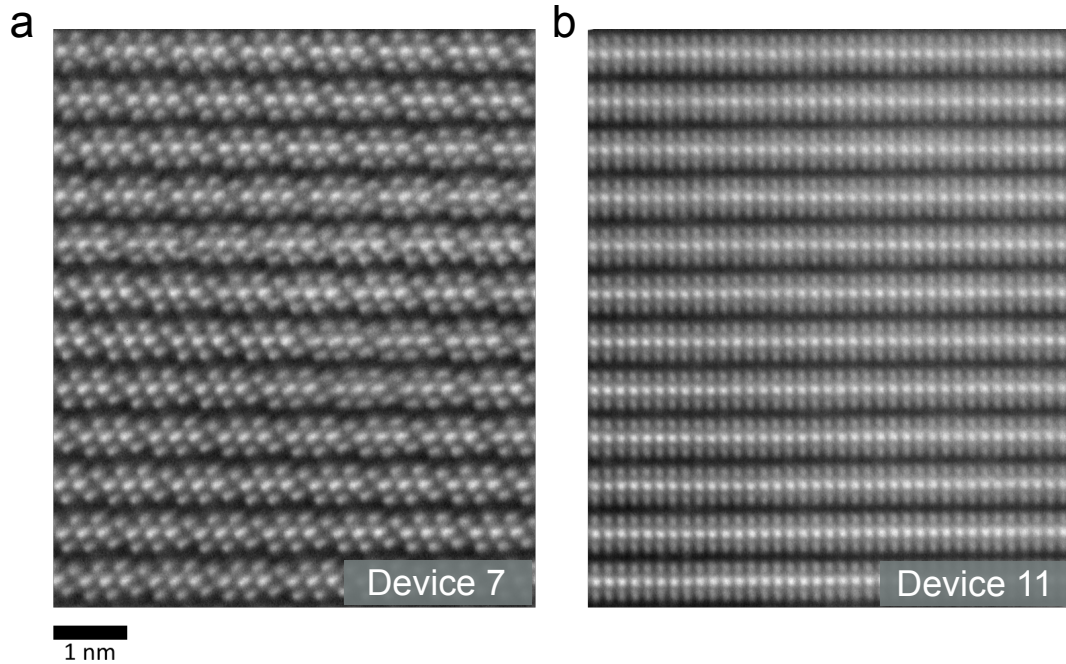


Figure 5.10: (a,b) Cross-sectional HAADF-STEM images of Devices 7 and 11 respectively. The images are taken perpendicular to the current direction for each device (along the ST-FMR sample bar). (a) looks down the TaTe<sub>2</sub> b-axis and (b) looks along the TaTe<sub>2</sub> b-axis, confirming that in each device the induced magnetic easy-axis lies along the TaTe<sub>2</sub> b-axis.

The first harmonic Hall measurement is used to determine  $I_0 R_{PHE}$ ,  $B_A$ , and  $\phi_{EA}$ . Figure 5.6 shows the first harmonic Hall voltage for Device 16.

We find that TaTe<sub>2</sub> and WTe<sub>2</sub> both induce a magnetic easy axis in the adjacent Py, but in opposite directions with respect to their respective crystallographic mirror plane direction (TaTe<sub>2</sub> induces a magnetic easy-axis perpendicular to the a-c mirror plane, whereas WTe<sub>2</sub> induces a magnetic easy-axis along its b-c mirror plane). The magnitude of the induced easy axis is stronger in WTe<sub>2</sub>/Py bilayers (6.2-17.3 mT) as compared to the TaTe<sub>2</sub>/Py bilayers (1.7-5.3 mT). We find no such magnetic easy axis in NbSe<sub>2</sub>/Py or MoTe<sub>2</sub>/Py devices.

### 5.7.5 Determination of TaTe<sub>2</sub> crystal axes

As noted in the previous section, similar to WTe<sub>2</sub>/Py bilayers, TaTe<sub>2</sub> induces a magnetic easy axis in the adjacent Permalloy layer. We use this easy axis to determine the angle between the current direction and the TaTe<sub>2</sub> crystal axes. For TaTe<sub>2</sub>/Py, we found that the alignment of the magnetic easy axis is along the b-axis of the TaTe<sub>2</sub> crystal using a combination of magnetic anisotropy measurements together with polarized Raman spectroscopy and cross-sectional HAADF-STEM imaging. Details of the HAADF-STEM imaging can be found in Section 5.7.3. The Raman measurements are performed using a Renishaw inVia confocal Raman microscope with a linearly polarized 488 nm wavelength excitation and a co-linear polarizer placed in front of the spectrometer entrance slit. The sample is positioned such that the excitation electric field is in the sample plane with a normal angle of incidence.

No previous measurements of a polarization-dependent Raman spectrum in TaTe<sub>2</sub> have been reported to our knowledge, but the symmetry of the polarization dependence is required to be the same as the room temperature monoclinic phase in 1T'-MoTe<sub>2</sub> (space group # 11), which has been studied in detail (see Sections 6.7 and 6.8). This is because the polarization dependence of the Raman signal is governed by the point group (2/m) which is the same for both TaTe<sub>2</sub> and 1T'-MoTe<sub>2</sub>. Raman spectra are shown for two samples (Devices 7 and 11) in the Fig. 5.9. We have verified by cross-sectional HAADF-STEM imaging in both of these devices (Fig. 5.10) that, like in 1T'-MoTe<sub>2</sub>, the  $\sim 80 \text{ cm}^{-1}$  parallel-polarized Raman mode in TaTe<sub>2</sub> is maximized along the crystallographic a-c mirror plane. For each of these devices, the measured magnetic easy-axis corresponds to the TaTe<sub>2</sub> b-axis (Fig. 5.8). The values of  $\phi_{I-ac}$  as measured by Raman

( $\phi_{I-ac} \rightarrow -\phi_{Raman}$ ) are reported in Table 5.1 for 15 of our devices. For 12 of these devices the induced magnetic easy axis lies within  $20^\circ$  of the estimated peak of the Raman  $80 \text{ cm}^{-1}$  mode (the a-c plane). For the remaining three devices there is significant disagreement. A shape anisotropy in the Py bar can account for some of the discrepancy in our ST-FMR samples the etched bar length is  $\sim 40 \mu\text{m}$  long (the majority of the bar is covered by the top leads) leading to an aspect ratio of 3:40 or 4:40 and a shape anisotropy of  $\sim 10 \text{ Oe}$ . In at least one of these samples (Device 18) the discrepancy may be explained by mild damage that occurred to the device between the electronic measurements and Raman characterization.

### 5.7.6 In-plane torques in TaTe<sub>2</sub>/Py bilayers

In the main text we focused on the out-of-plane torques in TaTe<sub>2</sub>/Py bilayers. Here, we will comment on the in-plane torques present in our samples as measured by ST-FMR. The symmetric component of the Lorentzian fit of the mixing voltage (Eq. 5.1) is proportional to the in-plane torques in the bilayers. We observe a small but non-zero torque component with an angular dependence proportional to  $\cos(\phi)$  in our samples, corresponding to a torque  $\propto \hat{m} \times (\hat{m} \times \hat{y})$ , which we call  $\tau_S$ . The angular dependence of the in-plane torques is shown for two different devices in Fig. 5.11 a and b, and the ratio of this torque to  $\tau_A$  is reported in Table 5.1 for all devices measured. The relatively small size of the measured symmetric signals (blue) is evident when plotted with the corresponding anti-symmetric signals (red) on the same scale (Fig. 5.11 c and d). In some of our samples, we also observe a very small in-plane torque  $\propto \hat{m} \times \hat{z}$ , which we call  $\tau_T$ . We therefore fit the dependence of the applied magnetic field angle for the

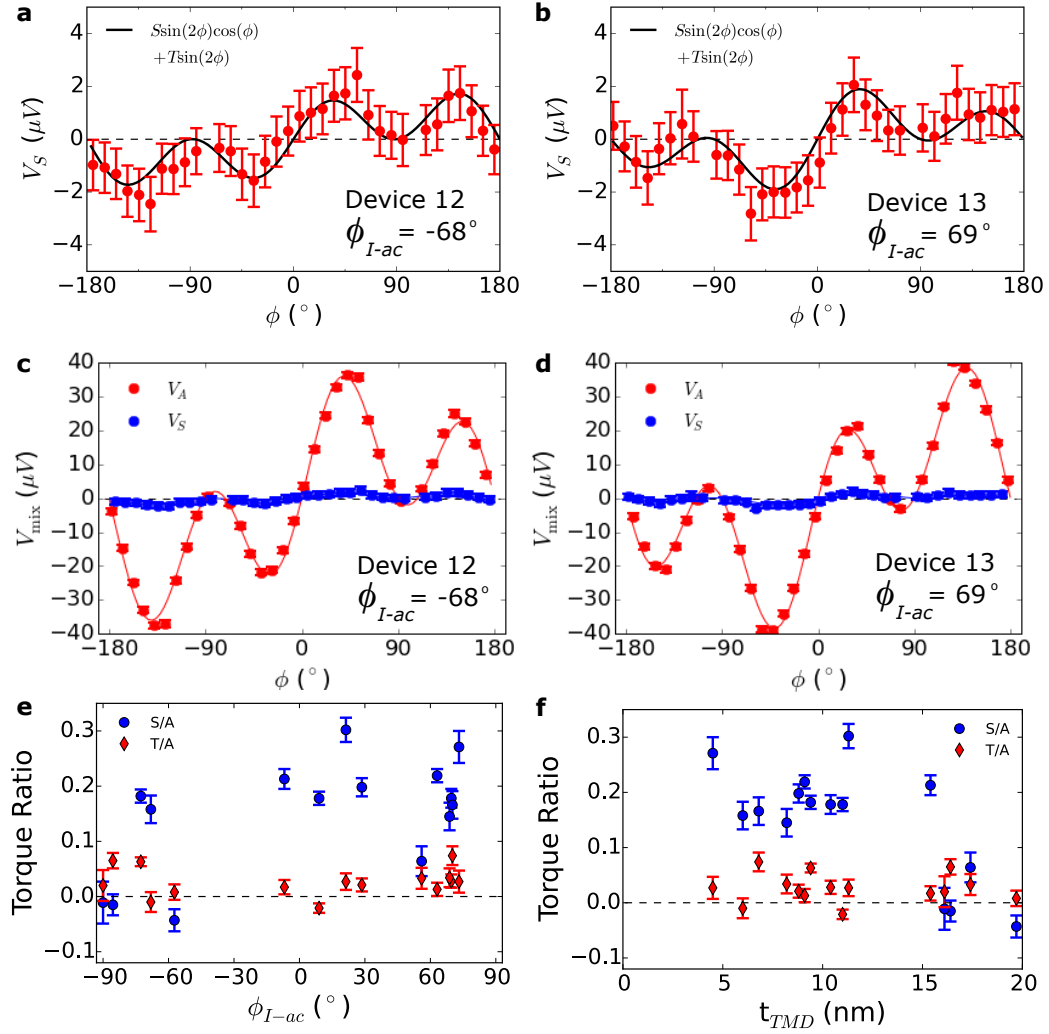


Figure 5.11: (a,b) Symmetric component of the mixing voltage (red points) for ST-FMR devices 12 and 13, corresponding to the in-plane torque. The black curves show fits using Eq. 5.6. (c,d) Symmetric ( $V_S$ , blue) and antisymmetric ( $V_A$ , red) components of the mixing voltage, corresponding to in-plane and out-of-plane torques, plotted on the same scale. (e,f) Ratios of the fit components  $S/A$  and  $T/A$  vs.  $\phi_{I-ac}$  and  $t_{TMD}$ . In (a-f) the applied microwave frequency is 9 GHz.

symmetric component of the ST-FMR mixing voltage,  $V_S$ , as a sum of these two torques:

$$V_S = \sin(2\phi) [S \cos(\phi) + T]. \quad (5.6)$$

The torque  $\tau_T$  is allowed by the symmetry of the TaTe<sub>2</sub> crystal, however, this small component of torque is inconsistent across our devices, and does not show the expected dependence across the a-c mirror plane, *i.e.* it does not always change sign for positive and negative  $\phi_{I-ac}$  as expected by symmetry. We therefore do not report it as a torque ubiquitous to the TaTe<sub>2</sub>/Py system. Figure 5.11 e and f shows  $S/A$  and  $T/A$  as a function of  $\phi_{I-ac}$  and the TMD thickness,  $t_{\text{TMD}}$  for all of our ST-FMR devices. Due to the small size of the in-plane torques in the TaTe<sub>2</sub>/Py bilayer system, we do not report the in-plane torques as measured by the second harmonic Hall technique as it is difficult to separate such a small term from the Nernst voltage present in our samples.

### 5.7.7 Model for C/A

In the main text we have modeled the  $\phi_{I-mp}$  dependence of the torques proportional to  $\hat{m} \times \hat{x}$  as arising solely from a Dresselhaus symmetry and the torques proportional to  $\hat{m} \times \hat{y}$  as a sum of Rashba and Dresselhaus symmetry contributions:

$$\begin{aligned}\tau_{\perp}^C &= C \sin(\phi) = [D \sin(2\phi_{I-mp})] \sin(\phi), \\ \tau_{\perp}^A &= A \cos(\phi) = [R + D \cos(2\phi_{I-mp})] \cos(\phi),\end{aligned}$$

where  $R$  is the component of  $\cos(\phi)$  torques arising from a Rashba symmetry, and  $D$  for Dresselhaus, which can generate both  $\cos(\phi)$  and  $\sin(\phi)$  dependent torques. The fit equation used to extract a ratio of  $D/R$  from the plot of  $C/A$  as a function of  $\phi_{I-mp}$  is:

$$\frac{C}{A} = \frac{D/R \sin(2\phi_{I-mp})}{1 \pm D/R \cos(2\phi_{I-mp})}, \quad (5.7)$$

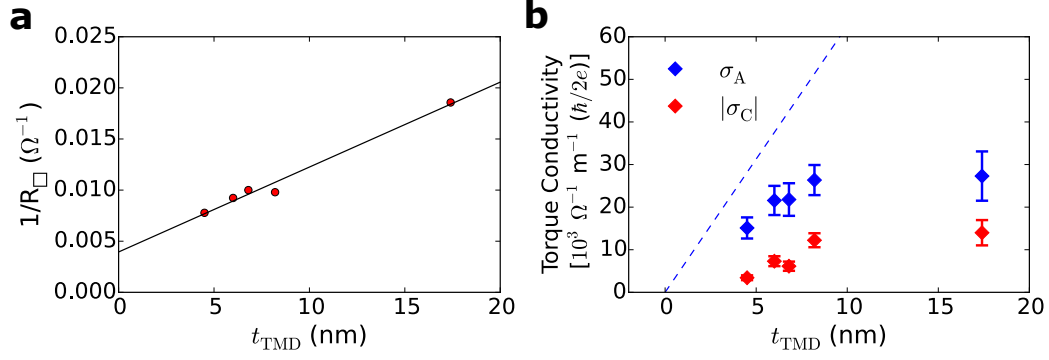


Figure 5.12: (a)  $1/R_{\square}$  as a function of the TaTe<sub>2</sub> thickness for the 5 devices with the same aspect ratio ( $4 \times 3 \mu\text{m}$ ) and within  $\pm 10^\circ$  of  $|\phi_{I-ac}| = 65^\circ$  (red circles). The fit (black line) allows an extraction of the resistivities for TaTe<sub>2</sub> and Py. (b) Torque conductivities for the same 5 devices, as shown in the main text. Here, the dashed blue line gives the estimated Oersted field contribution to  $\sigma_A$ .

where the sign of  $D/R$  sets the relative orientation of the field directions in the Dresselhaus and Rashba symmetries and the  $\pm$  in the denominator sets the overall orientation. Our TaTe<sub>2</sub>/Py bilayers are represented by the scenario shown in Fig. 5.1 a and b, where  $D/R$  is negative and the sign in the denominator is positive, consistent with an Oersted field from tilted currents dominating both contributions. We note that this model does not take into account the possibility that  $D$  and  $R$  may differ in their dependence on the thickness of the TMD.

### 5.7.8 Thickness dependence of the torques

Here we report the thickness dependence of torque conductivities  $\sigma_A$  and  $\sigma_C$  for 5 devices  $\pm 10^\circ$  within  $|\phi_{I-ac}| = 65^\circ$  where all selected devices also have the same aspect ratio of  $4 \times 3 \mu\text{m}$ . In Fig. 5.12a we plot  $1/R_{\square}$  for these 5 devices as a function of TaTe<sub>2</sub> thickness, where  $R_{\square} = wR/l$  is the sheet resistance as determined from the two point resistance of the device,  $R$ , with width  $w$  and length  $l$ . The fit

function is given by:

$$\frac{1}{R_{\square}} = \frac{t_{\text{mag}}}{\rho_{\text{residual}}} + \frac{t_{\text{TMD}}}{\rho_{\text{TMD}}}$$

where  $t_{\text{mag}}$  is the thickness of the Py,  $\rho_{\text{residual}}$  is the residual resistivity at  $t_{\text{TMD}} = 0$  and includes the Py resistance and device contact resistance, and  $\rho_{\text{TMD}}$  is the resistivity of TaTe<sub>2</sub> for  $|\phi_{I-ac}| = 65^\circ$ . We extract values of  $\rho_{\text{TMD}} \sim 120 \pm 10 \mu\Omega\text{cm}$  and  $\rho_{\text{residual}} \sim 150 \pm 20 \mu\Omega\text{cm}$ . Using these values, we can estimate the Oersted field contribution to the torque conductivities. For the torque  $\propto \hat{m} \times \hat{y}$  the estimated Oersted field torque conductivity is given by:

$$\sigma_{\text{Oe}} = \left(\frac{e}{\hbar}\right) \mu_0 M_S t_{\text{mag}} \sigma_{\text{TMD}}^{\text{Charge}} t_{\text{TMD}},$$

where we estimate  $M_s \approx M_{\text{eff}}$  from the ST-FMR measurements and  $\sigma_{\text{TMD}}^{\text{Charge}} \sim 8.3 \pm 0.5 \times 10^5 (\Omega^{-1} \text{m}^{-1})$  from the extracted resistivity. The blue line in Fig. 5.12b gives the estimated  $\sigma_{\text{Oe}}$  contribution for  $\sigma_A$ . Note that this estimate is for a material with an isotropic resistivity and may overestimate the value as it does not capture the effects of tilted current paths, as well as any thickness dependence to the TaTe<sub>2</sub> resistivity. Also, as noted in the main text, if the resistivity of the Py is not uniform across its thickness (for instance due to increased scattering near the TaTe<sub>2</sub>/Py interface) this could have the effect of decreasing the measured value Oersted torque  $\propto \hat{m} \times \hat{y}$  due to competing Oersted torques from the TaTe<sub>2</sub> and current above the midline of the Py thickness.

### 5.7.9 Dresselhaus-like torque in WTe<sub>2</sub>/Py bilayers

As discussed in the main text, the WTe<sub>2</sub> crystal structure allows a Dresselhaus-like spin-polarization based on a symmetry analysis of either the bulk crystal or the WTe<sub>2</sub>/Py surface. A torque arising from such a current-induced spin-

Device Number	$t$ (nm) $\pm 0.3$ nm	$L \times W$ ( $\mu\text{m}$ ) $\pm 0.2$ $\mu\text{m}$	$\tau_B/\tau_A$ w/out $C$	$\tau_B/\tau_A$ w/ $C$	$C/A$	$B_A$ (0.1 mT)	$\phi_{l-bc}$ $\pm 2^\circ$
1	5.5	$4.8 \times 4$	0.373(4)	0.372(3)	-0.010(5)	70.1(7)	-87
2	15.0	$6 \times 4$	0.011(7)	0.011(7)	-0.01(1)	151(2)	-5
5	8.2	$6 \times 4$	0.133(8)	0.132(8)	0.10(1)	150(1)	-15
7	3.4	$4 \times 3$	0.207(8)	0.206(8)	0.02(1)	153(1)	-15
9	6.7	$5 \times 4$	0.278(6)	0.279(6)	0.089(9)	173(1)	-65
11	14.0	$5 \times 4$	-0.13(1)	-0.128(9)	-0.19(1)	138(2)	32
12	5.3	$5 \times 4$	-0.320(6)	-0.319(6)	-0.024(8)	156(3)	84
14	5.3	$5 \times 4$	0.340(7)	0.341(7)	-0.09(1)	140(1)	69
15	5.5	$5 \times 4$	0.332(7)	0.331(6)	-0.060(6)	155(1)	75
16	3.4	$5 \times 4$	0.236(8)	0.236(7)	-0.09(1)	132(1)	29
17	2.6	$5 \times 4$	0.020(8)	0.021(8)	-0.039(1)	20(2)	-2
18	5.0	$5 \times 4$	-0.451(7)	-0.444(6)	-0.090(8)	20(3)	74

Table 5.2: Comparison of device parameters, torque ratios, and magnetic anisotropy parameters for  $\text{WTe}_2/\text{Py}$  bilayers as originally detailed in Chapter 2, but with the addition of a Dresselhaus torque component to the fit for the out-of-plane torques. We find a small but nonzero value for the ratio  $C/A$  for samples in which  $\phi_{l-bc}$  is sufficiently different from  $0^\circ$  or  $\pm 90^\circ$ . We also show that the inclusion of the Dresselhaus-like torque  $\propto \hat{m} \times \hat{x}$  does not affect our previously reported values for the out-of-plane antidamping torque component because the ratio  $B/A$  is unchanged within measurement uncertainty.

polarization is maximized when an in-plane current is applied at an intermediary angle with respect to the  $\text{WTe}_2$  mirror symmetries (b-c mirror plane and a-c glide plane). In our previous work, we did not originally notice a torque component arising from a Dresselhaus-like spin-polarization as we focused on samples with current perpendicular or parallel to the b-c mirror plane ( $\phi_{a-l} = 0^\circ$  and  $\phi_{a-l} = 90^\circ$ ), where the Dresselhaus-like component is expected to be minimal. Adding a Dresselhaus-like component,  $\hat{m} \times \hat{x}$ , to the fit of the out-of-plane torques ( $V_A$ , antisymmetric component of  $V_{mix}$ ) for the  $\text{WTe}_2/\text{Py}$  ST-FMR devices studied in Chapter 2, gives an overall dependence for the applied magnetic field angle,  $\phi$ , of:

$$V_A = \sin(2\phi)[A \cos(\phi) + B + C \sin(\phi)],$$

where  $A$  represents torques  $\propto \hat{m} \times \hat{y}$ ,  $B$  represents torques  $\propto \hat{m} \times (\hat{m} \times \hat{z})$  and  $C$  represents torques  $\propto \hat{m} \times \hat{x}$ . Figure 5.4 shows one such device and fits with and without the  $C$  parameter. Table 5.2 shows the values of  $C/A$  extracted from the

fits from the devices studied in Chapter 2, as well as the values of  $B/A$  determined with and without including the parameter  $C$  in the fits. As can be seen in the table, our previous observations of the out-of-plane antidamping torque in  $WTe_2/Py$  bilayers are not affected by the inclusion of this extra term. Figure 5.3b shows the extracted values of  $C/A$  plotted as a function of  $\phi_{I-bc}$ , the angle of the applied current to the  $WTe_2$  b-c mirror plane ( $\phi_{I-bc} = \phi_{a-I} - 90^\circ$ ). The dependence of  $C/A$  on the direction of current with respect to the  $WTe_2$  crystal axes is similar to our  $TaTe_2/Py$  samples:  $C/A$  goes to zero when current is parallel or perpendicular to a mirror plane ( $\phi_{I-bc} = 0^\circ$  and  $90^\circ$ ), and is maximal when current is applied between these two values. We model the dependence of  $C/A$  using Eq. 5.7, and extract a value of  $D/R = -0.13 \pm 0.02$ . We note that for our  $WTe_2/Py$  samples, we do not have sufficient resolution to accurately determine the sign in the denominator of Eq. 5.7, with both giving the same ratio of  $D/R$  within the fit error and with comparable residuals (+, red curve; -, black curve). Since we know from our previous work (see Chapter 3) that the Rashba component of the out-of-plane torque is dominated by the Oersted field, we can determine that the sign in the denominator should be positive.

Using the two-point sheet resistance of our  $WTe_2/Py$  devices, we have extracted an in-plane resistivity anisotropy of  $\sim 2$  in  $WTe_2$ , with the a-axis being less resistive. We find a value of  $\rho_{a\text{-axis}} = 530 \pm 140 \mu\Omega\text{cm}$  and a value of  $\rho_{b\text{-axis}} = 1160 \pm 100 \mu\Omega\text{cm}$  averaged across devices that have been exfoliated in nitrogen and vacuum. We note that this difference in surface treatment may affect the absolute values of the resistivities, but it would be surprising if it affected the sign of the anisotropy. The resistivity anisotropy for  $WTe_2$  found here is consistent with both  $TaTe_2$  and  $MoTe_2$  [23] in that the metal-atom chain is the low resistance axis for all of these materials. This implies that qualitatively

the torques with Dresselhaus symmetry in  $WTe_2/Py$  heterostructures can be described by the tilted currents induced through the resistivity anisotropy.

## References

- [1] A. Brataas, A. D. Kent, and H. Ohno. "Current-induced torques in magnetic materials." *Nature Materials* **11**, 372 (2012). Review Article.
- [2] L. Liu, T. Moriyama, D. C. Ralph, and R. A. Buhrman. "Spin-Torque Ferromagnetic Resonance Induced by the Spin Hall Effect." *Physical Review Letters* **106**, 036601 (2011).
- [3] L. Liu, C.-F. Pai, Y. Li, H. W. Tseng, D. C. Ralph, and R. A. Buhrman. "Spin-Torque Switching with the Giant Spin Hall Effect of Tantalum." *Science* **336**, 555 (2012).
- [4] I. M. Miron, G. Gaudin, S. Auffret, B. Rodmacq, A. Schuhl, S. Pizzini, J. Vogel, and P. Gambardella. "Current-driven spin torque induced by the Rashba effect in a ferromagnetic metal layer." *Nature materials* **9**, 230 (2010).
- [5] J. C. R. Sánchez, L. Vila, G. Desfonds, S. Gambarelli, J. P. Attané, J. M. De Teresa, C. Magén, and A. Fert. "Spin-to-charge conversion using Rashba coupling at the interface between non-magnetic materials." *Nature Communications* **4**, 2944 (2013).
- [6] A. R. Mellnik, J. S. Lee, A. Richardella, J. L. Grab, P. J. Mintun, M. H. Fischer, A. Vaezi, A. Manchon, E.-A. Kim, N. Samarth, and D. C. Ralph. "Spin-transfer torque generated by a topological insulator." *Nature* **511**, 449 (2014).

- [7] Y. Fan, P. Upadhyaya, X. Kou, M. Lang, S. Takei, Z. Wang, J. Tang, L. He, L.-T. Chang, M. Montazeri, G. Yu, W. Jiang, T. Nie, R. N. Schwartz, Y. Tserkovnyak, and K. L. Wang. "Magnetization switching through giant spinorbit torque in a magnetically doped topological insulator heterostructure." *Nature Materials* **13**, 699 (2014).
- [8] V. P. Amin and M. D. Stiles. "Spin transport at interfaces with spin-orbit coupling: Formalism." *Physical Review B* **94**, 104419 (2016).
- [9] V. P. Amin and M. D. Stiles. "Spin transport at interfaces with spin-orbit coupling: Phenomenology." *Physical Review B* **94**, 104420 (2016).
- [10] D. Fang, H. Kurebayashi, J. Wunderlich, K. Výborný, L. P. Zárbo, R. P. Campion, A. Casiraghi, B. L. Gallagher, T. Jungwirth, and A. J. Ferguson. "Spinorbit-driven ferromagnetic resonance." *Nature Nanotechnology* **6**, 413 (2011).
- [11] H. Kurebayashi, J. Sinova, D. Fang, A. C. Irvine, T. D. Skinner, J. Wunderlich, V. Novák, R. P. Campion, B. L. Gallagher, E. K. Vehstedt, L. P. Zárbo, K. Výborný, A. J. Ferguson, and T. Jungwirth. "An antidamping spinorbit torque originating from the Berry curvature." *Nature Nanotechnology* **9**, 211 (2014).
- [12] T. D. Skinner, K. Olejník, L. K. Cunningham, H. Kurebayashi, R. P. Campion, B. L. Gallagher, T. Jungwirth, and A. J. Ferguson. "Complementary spin-Hall and inverse spin-galvanic effect torques in a ferromagnet/semiconductor bilayer." *Nature Communications* **6**, 6730 (2015).
- [13] L. Chen, M. Decker, M. Kronseder, R. Islinger, M. Gmitra, D. Schuh, D. Bougeard, J. Fabian, D. Weiss, and C. H. Back. "Robust spin-orbit torque

and spin-galvanic effect at the Fe/GaAs (001) interface at room temperature." *Nature Communications* **7**, 13802 (2016). Article.

- [14] C. Ciccarelli, L. Anderson, V. Tshitoyan, A. J. Ferguson, F. Gerhard, C. Gould, L. W. Molenkamp, J. Gayles, J. Železný, L. Šmejkal, Z. Yuan, J. Sinova, F. Freimuth, and T. Jungwirth. "Room-temperature spinorbit torque in NiMnSb." *Nature Physics* **12**, 855 (2016).
- [15] B. E. Brown. "The crystal structures of NbTe<sub>2</sub> and TaTe<sub>2</sub>." *Acta Crystallographica* **20**, 264 (1966).
- [16] T. Srgel, J. Nuss, U. Wedig, R. Kremer, and M. Jansen. "A new low temperature modification of TaTe<sub>2</sub> — Comparison to the room temperature and the hypothetical 1T-TaTe<sub>2</sub> modification." *Materials Research Bulletin* **41**, 987 (2006). Special Issue Dedicated to Prof. Gerard Ferey.
- [17] D. MacNeill, G. M. Stiehl, M. H. D. Guimaraes, R. A. Buhrman, J. Park, and D. C. Ralph. "Control of spinorbit torques through crystal symmetry in WTe<sub>2</sub>/ferromagnet bilayers." *Nature Physics* **13**, 300 (2017).
- [18] D. MacNeill, G. M. Stiehl, M. H. D. Guimarães, N. D. Reynolds, R. A. Buhrman, and D. C. Ralph. "Thickness dependence of spin-orbit torques generated by WTe<sub>2</sub>." *Physical Review B* **96**, 054450 (2017).
- [19] J. Li and P. M. Haney. "Interfacial magnetic anisotropy from a 3-dimensional Rashba substrate." *Applied Physics Letters* **109**, 032405 (2016).
- [20] M. Hayashi, J. Kim, M. Yamanouchi, and H. Ohno. "Quantitative characterization of the spin-orbit torque using harmonic Hall voltage measurements." *Phys. Rev. B* **89**, 144425 (2014).

- [21] C. O. Avci, K. Garello, M. Gabureac, A. Ghosh, A. Fuhrer, S. F. Alvarado, and P. Gambardella. "Interplay of spin-orbit torque and thermoelectric effects in ferromagnet/normal-metal bilayers." *Phys. Rev. B* **90**, 224427 (2014).
- [22] X. Zhang, Q. Liu, J.-W. Luo, A. J. Freeman, and A. Zunger. "Hidden spin polarization in inversion-symmetric bulk crystals." *Nature Physics* **10**, 387 (2014).
- [23] H. P. Hughes and R. H. Friend. "Electrical resistivity anomaly in  $\beta$ -MoTe<sub>2</sub> (metallic behaviour)." *Journal of Physics C: Solid State Physics* **11**, L103 (1978).

## SPIN-ORBIT TORQUES IN MOLYBDENUM DITELLURIDE

## 6.1 Introduction

This chapter explores the spin-orbit torques generated in yet another low symmetry transition metal dichalcogenide (TMD), MoTe<sub>2</sub> [1–3]. What makes MoTe<sub>2</sub> unique among the commonly studied TMDs is that it is polymorphic – it is readily stabilized into three distinct crystal structures: hexagonal ( $\alpha$ ), monoclinic ( $\beta$ ) and orthorhombic ( $\gamma$ ) – and provides a platform for a rich variety of physics in its different phases, ranging from semiconductor physics [4] to superconductivity [5], and quantum spin Hall physics [6] to topological semi-metals [7–12]. Previous work has shown that laser annealing [2], electrostatic gating [3], and strain [13, 14] can all be used to transition from the  $\alpha$  to the  $\beta$  phase, with the latter two being reversible.

The octahedrally coordinated phases ( $\beta$  and  $\gamma$ ) of MoTe<sub>2</sub> provide a particularly unique opportunity to probe the symmetries relevant for the generation of novel spin-orbit torques. The monoclinic phase (space group 11) retains inversion symmetry, with a screw axis along the Mo-chain (in the monoclinic basis, typically called the b-axis) and a mirror plane perpendicular to the screw axis. Whereas the orthorhombic phase lacks inversion symmetry and is, in fact, isostructural to WTe<sub>2</sub> (space group 31) with a c-axis screw symmetry, an a-c glide plane and b-c mirror plane (in the orthorhombic basis). Both phases, however, are limited to the same single mirror plane symmetry at their surface. This motivates MoTe<sub>2</sub> as an ideal test of the symmetry requirements for the generation of an out-of-plane antidamping torque. Will such a torque be present in

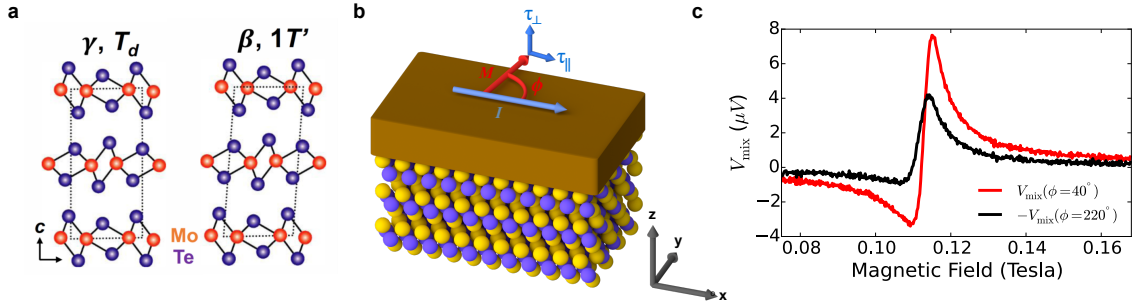


Figure 6.1: a) Octahedrally coordinated MoTe<sub>2</sub> crystal in both the  $\gamma$  ( $T_d$ ) and  $\beta$  ( $1T'$ ) phases with the mirror plane along the page and the Mo chain running into the page. Image adapted from Ref [15]. b) Geometry of the induced spin-orbit torques in our MoTe<sub>2</sub>/Py heterostructures. c) The mixing voltage,  $V_{\text{mix}}$ , as a function of applied magnetic field for Device 1, MoTe<sub>2</sub>(monolayer) / Py(6 nm), where the current is applied perpendicular to the mirror plane and the field applied at an angle of  $40^\circ$  (red) and  $220^\circ$  (black), showing a clear lack of two-fold rotational symmetry in the generated spin-orbit torques. The applied microwave power is 5 dBm at 9 GHz.

both phases of MoTe<sub>2</sub>, implying perhaps that only the symmetries of the interface matter? Or will an out-of-plane antidamping torque only be present in the  $\gamma$  phase, implying that broken inversion symmetry in the spin-generation material is crucial?

Bulk crystals of both the  $\alpha$  and  $\beta$  phases of MoTe<sub>2</sub> can be stabilized at room temperature, with resistivities  $\sim 10^3 \Omega\text{cm}$  and  $\sim 10^{-3} \Omega\text{cm}$  respectively [16]. The  $\gamma$  phase is obtained by a shift in the stacking of the van der Waals layers in  $\beta$ -MoTe<sub>2</sub>, as shown in Fig. 6.1a. Note that an individual layer of octahedrally coordinated MoTe<sub>2</sub> is isostructural to a monolayer of WTe<sub>2</sub> regardless of the bulk phase (space group 11, commonly referred to as  $1T'$ ). The transition between phases occurs as  $\beta$ -MoTe<sub>2</sub> is cooled below 250 K [1], though both pressure [5, 17] and impurity doping [18–20] have been shown to influence the transition temperature. As this first-order transition is predominately a shift in the stacking order of the layers, it is reasonable to suspect that there also be a thickness de-

pendence to the transition in the few-layer limit. In fact, recent work by the Tsen group [15, 21] has suggested this as a viable possibility. Further discussion of the  $\text{MoTe}_2$  crystal phase in our devices can be found in Section 6.8.

The fabrication of our samples is identical to that of the previous chapters. We exfoliate flakes of bulk  $\beta$ - $\text{MoTe}_2$  crystal (provided by HQ graphene) onto Silicon / Silicon Oxide wafers, where the last step of the exfoliation process is carried out under vacuum ( $< 10^{-6}$  torr) in the load lock of our sputtering system. We then use grazing angle sputtering to deposit 6 nm of our ferromagnet, Permalloy ( $\text{Py}=\text{Ni}_{80}\text{Fe}_{20}$ ), and subsequently cap our films with 2 nm of Al by conventional sputtering. The equilibrium direction of the Py magnetic moment is contained within the sample plane. Flakes are identified for patterning by optical and atomic force microscopy, where we select regions of flakes that are clean (no tape residue) and atomically flat ( $< 300$  pm roughness). Samples are patterned into our device structures (either ST-FMR bars or Hall balls) through electron beam lithography and ion mill etching. See Section 2.2 for more details.

For our studies on  $\text{MoTe}_2$ , we will focus on spin-torque ferromagnetic resonance (ST-FMR) measurements, but we have also performed second harmonic Hall measurements and we state here only that they are consistent. At present, we have performed measurements of the spin-orbit torques only at room temperature. Measurements as a function of temperature through the  $\beta$  to  $\gamma$  phase transition are ongoing.

## 6.2 Spin-Torque Ferromagnetic Resonance Measurements

In a ST-FMR measurement, we use a ground-signal-ground type device structure (see Fig. 2.1 for an image of a finished device), in which we apply a GHz frequency current to the MoTe<sub>2</sub>/Py bar through the capacitive branch of a bias tee. We set the angle of the applied magnetic field with respect to the current direction,  $\phi$ , and sweep the magnitude of that field to tune the ferromagnet through its resonance condition while measuring the resultant DC mixing voltage at the inductive end of the bias tee. The mixing voltage,  $V_{mix}$ , can be modeled as the sum of symmetric and antisymmetric Lorentzians (see Section 2.8.2). The amplitudes of those Lorentzians are related to the in-plane ( $\tau_{\parallel}$ ) and out-of-plane ( $\tau_{\perp}$ ) torques on the ferromagnet, respectively, by:

$$V_S = -\frac{I_{RF}}{2} \frac{dR}{d\phi} \frac{1}{\alpha_G \gamma (2B_0 + \mu_0 M_{eff})} \tau_{\parallel} \quad (6.1)$$

$$V_A = -\frac{I_{RF}}{2} \frac{dR}{d\phi} \frac{\sqrt{1 + \mu_0 M_{eff}/B_0}}{\alpha_G \gamma (2B_0 + \mu_0 M_{eff})} \tau_{\perp}, \quad (6.2)$$

where  $R$  is the device resistance,  $\phi$  is the angular orientation of the magnetization relative to the direction of applied current in the sample (since the magnetization is saturated along the applied field direction),  $dR/d\phi$  is due to the anisotropic magnetoresistance in the Py,  $\mu_0 M_{eff}$  is the out-of-plane demagnetization field,  $B_0$  is the resonance field,  $I_{RF}$  is the microwave current in the bilayer,  $\alpha_G$  is the Gilbert damping coefficient and  $\gamma$  is the gyromagnetic ratio.

In high symmetry materials such as Pt, the generated spin-orbit torques are confined to the out of plane field-like torque,  $\vec{\tau}_A \propto \hat{m} \times \hat{y}$ , and in-plane antidamping torque,  $\vec{\tau}_S \propto \hat{m} \times (\hat{m} \times \hat{y})$ , which both have a dependence on the magnetization direction  $\propto \cos(\phi)$ . Note that we define the applied current as always being in the  $\hat{x}$  direction (see Fig. 6.1b). If only torques  $\tau_A$  and  $\tau_S$  are present,  $V_{mix}$  will

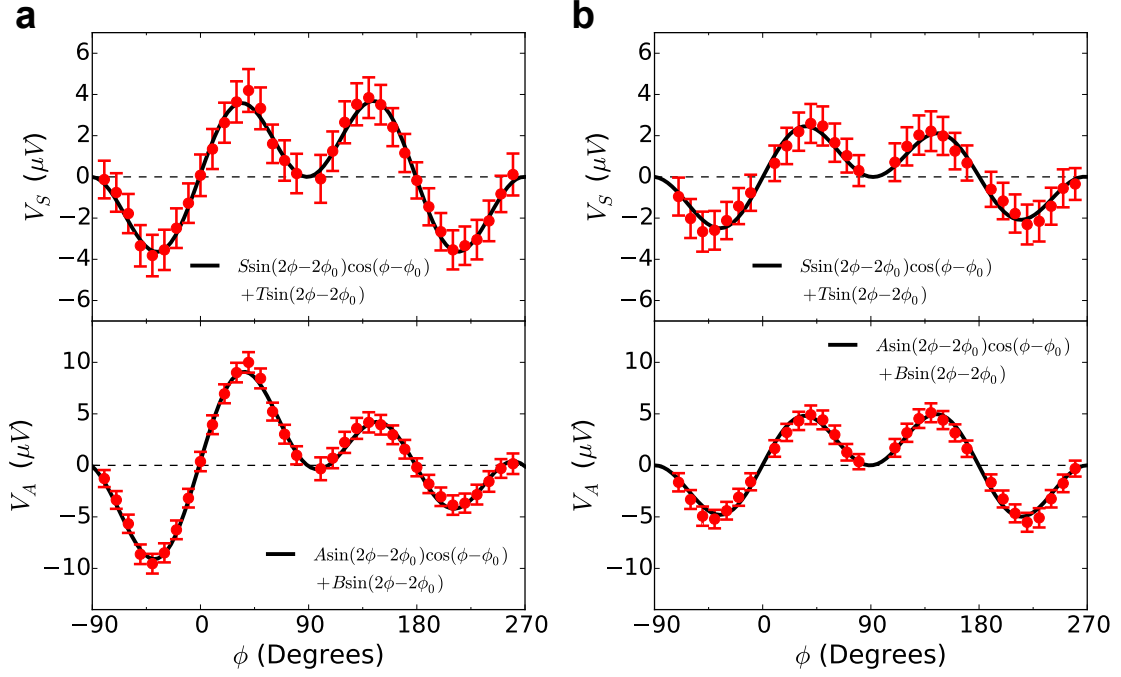


Figure 6.2: a) Dependence on the applied field angle for both the symmetric,  $V_S$ , and antisymmetric,  $V_A$ , component of the mixing voltage for Device 1, MoTe<sub>2</sub>(monolayer) / Py(6 nm) with current applied perpendicular to the MoTe<sub>2</sub> mirror plane. Fits of the angular dependence are made using Eqs. 6.3 and 6.4. An out-of-plane antidamping torque is observed. b) Dependence on the applied field angle for  $V_S$  and  $V_A$  in Device 2, MoTe<sub>2</sub>(5.6 nm) / Py(6 nm) with current applied along the MoTe<sub>2</sub> mirror plane. No out-of-plane antidamping torque is observed, consistent with the symmetry requirements of the MoTe<sub>2</sub> surface. In both samples the applied microwave power is 5 dBm at 9 GHz.

be  $\propto \sin(2\phi) \cos(\phi)$  and exhibit two-fold rotational symmetry up to a minus sign, where the  $\propto \sin(2\phi)$  arises from  $dR/d\phi$  due to the anisotropic magnetoresistance of the Py. Figure 6.1c shows  $V_{\text{mix}}$  at two applied field angles, 40° and 220°, for one of our devices (Device 1) where the applied current in the device is perpendicular to the MoTe<sub>2</sub> mirror plane and the 220° trace has been multiplied by  $-1$  for comparison. Clearly two-fold rotational symmetry is not present in the observed  $V_{\text{mix}}$  signal, suggesting the presence of additional torques.

Figure 6.2a shows the extracted fit parameters  $V_S$  and  $V_A$  as a function of

applied field angle for Device 1. The angular dependence of  $V_A$  (red circles) is not consistent with being  $\propto \sin(2\phi) \cos(\phi)$ . To extract other out-of-plane torques present in the system, we fit the angular dependence of  $V_A$  as:

$$V_A = \sin(2\phi)[A \cos(\phi) + B + C \sin(\phi)]. \quad (6.3)$$

The fit parameter  $B$  is related to torques  $\vec{\tau}_B \propto \hat{m} \times (\hat{m} \times \hat{z})$  – the out-of-plane antidamping torque first observed in  $\text{WTe}_2$  and discussed in chapters 2 and 3. The fit parameter  $C$  is related to torques  $\vec{\tau}_C \propto \hat{m} \times \hat{x}$ , the Dresselhaus-like torque we have discussed in the preceding chapter on  $\text{TaTe}_2$ . For Device 1, we find a ratio  $B/A = 0.30 \pm 0.03$  indicating a sizable out-of-plane antidamping torque, whereas  $C$  is zero to within experimental uncertainty.

We may similarly fit  $V_S$  to extract additional in-plane torques:

$$V_S = \sin(2\phi)[S \cos(\phi) + T + U \sin(\phi)], \quad (6.4)$$

where  $T$  gives torques  $\vec{\tau}_T \propto \hat{m} \times \hat{z}$ , and  $U$  gives torques  $\vec{\tau}_U \propto \hat{m} \times (\hat{m} \times \hat{x})$ . In Device 1,  $T$  and  $U$  are zero within experimental uncertainty.

When current is flowed perpendicular to a single mirror plane (*e.g.* in  $\text{WTe}_2$ , where there are no other symmorphic symmetries present) a net torque generated by an out-of-plane spin  $\propto \hat{m} \times \hat{z}$  and  $\propto \hat{m} \times (\hat{m} \times \hat{z})$  is allowed by symmetry. In the case of Device 1, the presence of a non-zero  $\tau_B$  is consistent with the symmetries of the  $\text{MoTe}_2/\text{Py}$  interface. However, if current is instead flowed along a mirror plane, such a torque is forbidden by symmetry. Figure 6.2b shows  $V_S$  and  $V_A$  for a  $\text{MoTe}_2/\text{Py}$  device in which current is flowed along the  $\text{MoTe}_2$  mirror plane (Device 2). Consistent with this symmetry requirement, fits of  $V_A$  and  $V_S$  using Eqs. 6.3 and 6.4 yield values of  $B$  and  $T$  that are zero within experimental uncertainty. For more details on the symmetry arguments, see the

discussion in Sections 2.8.6 and 2.8.8. For a further discussion of the crystal axis dependence see the subsequent section, Section 6.3.

In Section 2.8.2 we provided a detailed discussion on determining the magnitude of the torques using Eqs. 6.1 and 6.2 as well as associated torque conductivities. Briefly, we must first determine values for  $\alpha_G$ ,  $R(\phi)$ , and  $I_{\text{RF}}$ . The Gilbert damping is estimated from the frequency dependence of the linewidth via  $\Delta = 2\pi f\alpha_G/\gamma + \Delta_0$ , where  $\Delta_0$  is the inhomogeneous broadening.  $R(\phi)$  is determined by measurements of the device resistance as a function applied in-plane magnetic field angle (with a field magnitude of 0.1 T). The RF current is determined by estimating the reflection coefficients of our devices ( $S_{11}$ ) and the transmission coefficient of our RF circuit ( $S_{21}$ ) through vector network analyzer measurements. These calibrations allow calculation of the RF current flowing in the device as a function of applied microwave power and frequency:

$$I_{\text{RF}} = 2 \sqrt{1\text{mW} \cdot 10^{\frac{P_{\text{source}}(\text{dBm}) + S_{21}(\text{dBm})}{10}} (1 - |\Gamma|)^2 / 50\Omega} \quad (6.5)$$

where  $P_{\text{source}}$  is the power sourced by the microwave generator and  $\Gamma = 10^{S_{11}(\text{dBm})/20}$ .

The torque conductivity, defined as the angular momentum absorbed by the magnet per second per unit interface area per unit electric field, provides an absolute measure of the torques produced in a spin source/ferromagnet bilayer nominally independent of geometric factors. For a torque  $\tau_K$  (where  $K = A, B, C, S, T$  or  $U$ ) we calculate the corresponding torque conductivity via

$$\sigma_K = \frac{M_s l w t_{\text{Py}}}{\gamma} \frac{\tau_K}{(l w) E} = \frac{M_s l t_{\text{Py}}}{\gamma} \frac{\tau_K (1 - \Gamma)}{(1 + \Gamma) I_{\text{RF}} \cdot 50\Omega} \quad (6.6)$$

where  $M_s$  is the saturation magnetization,  $E$  is the electric field,  $l$  and  $w$  are the length and width of the MoTe<sub>2</sub>/Permalloy bilayer, and  $t_{\text{Py}}$  is the thickness

of the Permalloy. Here,  $t_{\text{magnet}} = 6$  nm. The factor  $M_s l w t_{\text{magnet}} / \gamma$  is the total angular momentum of the magnet, and converts the normalized torque into units of angular momentum per second. Due to the unavailability of mm-scale MoTe<sub>2</sub>/Permalloy bilayers, we are unable to measure  $M_s$  directly via magnetometry, and instead approximate  $M_s \approx M_{\text{eff}}$ , which we have found to be accurate in other Permalloy bilayer systems. We estimate  $\mu_0 M_{\text{eff}} \sim 0.83$  T as extracted from our ST-FMR measurements.

### 6.3 Dependence on Crystallographic Orientation

We have determined the torque conductivities for 13 MoTe<sub>2</sub>( $t_{\text{TMD}}$ )/Py(6 nm) devices all with distinct thicknesses of MoTe<sub>2</sub>,  $t_{\text{TMD}}$ , and angles between the current direction and the MoTe<sub>2</sub> mirror plane. See Section 6.7 for details on the determination of the crystal axes in our devices. We define  $\phi_I$  as the angle between the current and the crystal axis perpendicular to the MoTe<sub>2</sub> mirror plane (typically called the a-axis in the  $\gamma$  phase and b-axis in the  $\beta$  phase), such that  $\phi_I = 0^\circ$  is perpendicular to the mirror plane and  $\phi_I = 90^\circ$  is parallel. Figure 6.3a shows  $\sigma_B$  as a function of  $\phi_I$  for 12 of our devices (we have excluded our MoTe<sub>2</sub> bilayer,  $t_{\text{TMD}} = 1.4$  nm, device for now, which will be discussed later). We clearly see that, consistent with the symmetry requirements on the torques,  $\tau_B$  is largest when current is applied perpendicular to the MoTe<sub>2</sub> mirror plane and is progressively reduced as current is instead applied along the mirror plane.

In contrast to this strong angular dependence,  $\sigma_S$  (Fig. 6.3b) shows no significant dependence on  $\phi_I$ . This is similar to the  $\sigma_S$  dependence on  $\phi_{a-I}$  observed in WTe<sub>2</sub>/Py heterostructures (see Fig 2.12). We obtain an average value of  $\sigma_S$

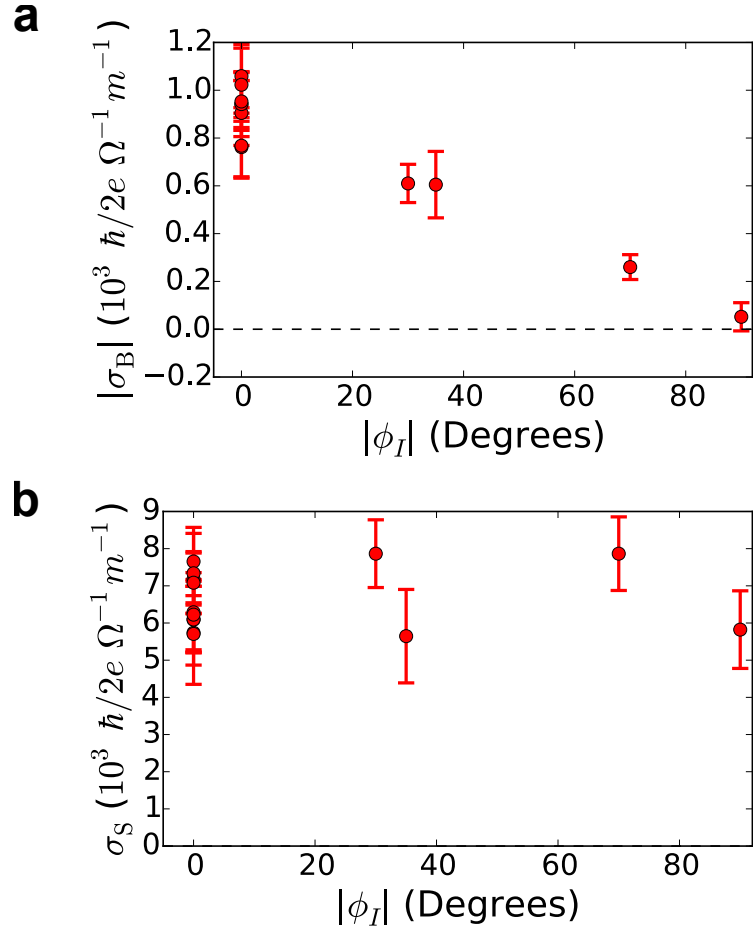


Figure 6.3: a) Torque conductivities for the out-of-plane antidamping torque ( $\vec{\tau}_B \propto \hat{m} \times (\hat{m} \times \hat{z})$  for current in the  $\hat{x}$  direction) as a function of  $|\phi_I|$  for 12 of our MoTe<sub>2</sub>/Py devices, all with distinct MoTe<sub>2</sub> thicknesses. We have excluded our bilayer MoTe<sub>2</sub> device in this plot, which is discussed in detail later. b) Torque conductivities for the standard antidamping torque ( $\vec{\tau}_S \propto \hat{m} \times (\hat{m} \times \hat{y})$  for current in the  $\hat{x}$  direction) as a function of  $|\phi_I|$  in all of our MoTe<sub>2</sub>/Py devices. In both plots the applied microwave power is 5 dBm. Torque conductivities are averaged over measurements at frequencies 8-11 GHz in steps of 1 GHz.

for our MoTe<sub>2</sub>/Py devices of  $6800 \pm 300 \hbar/(2e) (\Omega^{-1}m^{-1})$ , similar to the average value observed in our WTe<sub>2</sub>/Py heterostructures,  $8000 \pm 200 \hbar/(2e) (\Omega^{-1}m^{-1})$  [22, 23], and larger than the  $\approx 3000 \hbar/(2e) (\Omega^{-1}m^{-1})$  observed in our NbSe<sub>2</sub>/Py heterostructures [24].

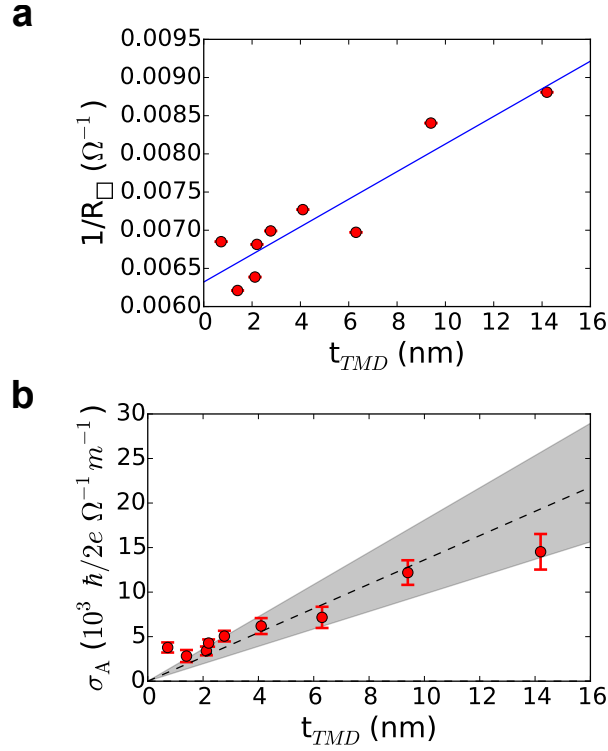


Figure 6.4: a) Inverse sheet resistance of devices with current perpendicular to the MoTe<sub>2</sub> mirror plane (red circles) as a function of MoTe<sub>2</sub> thickness as measured by a two-point method. The blue line gives a fit using Eq. 6.7 to extract the sheet resistances for the Py and MoTe<sub>2</sub>. b) Torque conductivity for the out-of-plane field like torque ( $\propto \hat{m} \times \hat{y}$ ) as a function of thickness for devices with current perpendicular to the MoTe<sub>2</sub> mirror plane (red circles). The dashed line gives the predicted Oersted field contribution from the torques (Eq. 6.8) and the shaded region gives the spread in the expected contribution as given by the error in the measured charge conductivity in MoTe<sub>2</sub>. The applied microwave power is 5 dBm. Torque conductivities are averaged over measurements at frequencies 8-11 GHz in steps of 1 GHz.

## 6.4 MoTe<sub>2</sub> Thickness Dependence

As a probe of the mechanism that drives the spin-orbit torques in our MoTe<sub>2</sub>/Py heterostructures, it is helpful to study the torques as a function of MoTe<sub>2</sub> thickness. We first extract the individual resistivities of the MoTe<sub>2</sub> and Py layers. Using the two-point resistances of our devices, we may plot the inverse of the

sheet resistance as a function of  $t_{\text{TMD}}$ , and using the relation:

$$\frac{1}{R_{\square}} = \frac{l}{wR} = \frac{t_{\text{Py}}}{\rho_{\text{Py}}} + \frac{t_{\text{TMD}}}{\rho_{\text{TMD}}}, \quad (6.7)$$

extract the resistivities  $\rho_{\text{Py}}$  and  $\rho_{\text{TMD}}$ . In Fig. 6.4a we show  $1/R_{\square}$  as a function of  $t_{\text{TMD}}$  for all devices in which the current is aligned perpendicular to the MoTe<sub>2</sub> mirror plane, and fit using Eq. 6.7 (blue line) to extract resistivities  $\rho_{\text{Py}} = 95 \pm 2$  ( $\mu\Omega \text{ cm}$ ) and  $\rho_{\text{TMD}} = 550 \pm 75$  ( $\mu\Omega \text{ cm}$ ). The value obtained for  $\rho_{\text{Py}}$  is similar to that seen in our WTe<sub>2</sub> devices.

Figure 6.4b shows  $\sigma_{\text{A}}$  as a function of  $t_{\text{TMD}}$  (red circles) for devices in which current is aligned perpendicular to the MoTe<sub>2</sub> mirror plane. A strong thickness dependence of the torques is observed. In many material systems the torque  $\propto \hat{m} \times \hat{y}$  (for current in the  $\hat{x}$  direction) is dominated by the Oersted torque – that is, the magnetic field generated from a simple current-carrying wire. For instance, we have previously shown that in the WTe<sub>2</sub>/Py and NbSe<sub>2</sub>/Py systems  $\tau_{\text{A}}$  is dominated by the Oersted torque (see Chapters 3 and 4). We model the torque conductivity generated by the Oersted torque as:

$$\sigma_{\text{Oe}} = \frac{e\mu_0 M_{\text{S}} t_{\text{Py}} \sigma_{\text{TMD}}}{\hbar} t_{\text{TMD}}, \quad (6.8)$$

where  $\sigma_{\text{TMD}}$  is the charge conductivity of the MoTe<sub>2</sub>. The dashed line in Fig. 6.4b shows the predicted Oersted torque using the extracted value of  $\rho_{\text{TMD}}$  and the shaded region about the dashed line gives the error in the predicted torque as given by the spread in  $\rho_{\text{TMD}}$ . All devices with the exception of our monolayer device are well described by the predicted Oersted torque. Deviation from the predicted Oersted torque in our monolayer device suggests a possible interfacial contribution to  $\tau_{\text{A}}$ , as suspected in our NbSe<sub>2</sub>/Py devices, or a strong layer dependence to the MoTe<sub>2</sub> resistivity. Previous work on uncapped MoTe<sub>2</sub> flakes has suggested that a band gap is opened in the few-layer limit [6]; however, more

recent work on capped MoTe<sub>2</sub> devices suggests that flakes remain conducting in this limit when they are not exposed to oxygen [15, 21]. At present, we have only studied one monolayer MoTe<sub>2</sub>/Py device, and require more devices in this few-layer regime before a more concrete conclusion can be drawn.

Figure 6.5 shows the thickness dependence for  $\tau_A$ ,  $\tau_B$  and  $\tau_S$  and associated torque conductivities for devices with current aligned perpendicular to the MoTe<sub>2</sub> mirror plane. The ratio  $\tau_S/\tau_A$ , depicted in panel a, shows a roll-off similar to that of the WTe<sub>2</sub>/Py devices which were exfoliated under vacuum (Fig. 3.8). Figure 6.5b shows the magnitude of the ratio  $\tau_B/\tau_S$  as a function of MoTe<sub>2</sub> thickness. The dependence is largely flat, which implies a similar dependence on thickness for both torques and is qualitatively similar to the WTe<sub>2</sub> dependence observed (see Fig. 3.6). The striking exception in the thickness dependence is from our one device in which the MoTe<sub>2</sub> is just a bilayer (1.4 nm) thick. In this device, no out-of-plane antidamping torque is observed within our experimental error. Note that we plot the absolute value of  $\tau_B$  as the sign of the torque is varied by the orientation of the top MoTe<sub>2</sub> flake, again similar to WTe<sub>2</sub>.

Figure 6.5 c and d show  $|\sigma_B|$  and  $\sigma_S$  respectively. Both are largely independent of MoTe<sub>2</sub> thickness, implying an interfacial origin for the observed antidamping torques. Again, the notable exception in the  $|\sigma_B|$  is the bilayer thick MoTe<sub>2</sub> device. Excluding the bilayer device, we find an average value for  $|\sigma_B| = 930 \pm 50 \hbar/(2e) (\Omega^{-1}m^{-1})$ . The average value of  $\sigma_S$  is  $6800 \pm 300 \hbar/(2e) (\Omega^{-1}m^{-1})$ . It is interesting that while the magnitude of  $\sigma_S$  in MoTe<sub>2</sub> is similar to that observed in our WTe<sub>2</sub> devices, the value of  $|\sigma_B|$  is approximately 1/3 that of WTe<sub>2</sub> [22, 23].

We have measured the spin-orbit torques in MoTe<sub>2</sub>/Py heterostructures in

Device Name	Device Number	$t$ (nm) $\pm 0.3$ nm	$L \times W$ ( $\mu\text{m}$ ) $\pm 0.2$ $\mu\text{m}$	$\tau_B/\tau_A$	$\tau_S/\tau_A$	$\phi_l$ $\pm 5^\circ$
HQ7D11	1	0.7	$5 \times 4$	0.30(3)	1.6(1)	0*
HQ7D1	2	5.6	$5 \times 4$	-0.01(3)	1.3(2)	90*
HQ7D4	3	6.3	$5 \times 4$	0.11(2)	0.82(7)	0*
HQ7D2	4	1.4	$5 \times 4$	0.01(3)	2.0(2)	0
HQ7D3	5	14.2	$5 \times 4$	0.05(1)	0.37(5)	0*
HQ7D6	6	2.1	$5 \times 4$	-0.27(3)	1.71(7)	0*
HQ7D7	7	2.2	$5 \times 4$	0.22(2)	1.6(1)	0*
HQ7D8	8	2.8	$5 \times 4$	0.21(2)	1.4(1)	0*
HQ7D9	9	4.1	$5 \times 4$	-0.16(2)	1.1(1)	0*
HQ7D10	10	9.4	$5 \times 4$	-0.08(1)	0.55(7)	0*
HQ7D5	11	2.2	$5 \times 4$	-0.21(3)	1.8(2)	35
HQ5D5	12	2.3	$4.5 \times 4$	0.10(2)	1.2(1)	30
HQ5D8	13	9.4	$4 \times 3$	-0.023(8)	0.64(3)	-70
HQ5D6	14	8.6	$4 \times 3$	0.075(8)	0.57(4)	-5

Table 6.1: Comparison of device parameters, torque ratios, and magnetic anisotropy parameters for MoTe<sub>2</sub>/Py bilayers. Here  $\phi_l$  is the angle between the current and the crystal axis perpendicular to the MoTe<sub>2</sub> mirror plane as measured by polarized Raman spectroscopy, where “\*” indicates the value has been estimated from the exfoliation direction and has yet to be checked by Raman (though this has proven to be a generally accurate estimate).

monolayer steps from a single MoTe<sub>2</sub> layer to quadlayer MoTe<sub>2</sub> with current perpendicular to the MoTe<sub>2</sub> mirror plane. Though we are at present limited by the number of devices in this thickness regime (we have one monolayer, one bilayer, two trilayer devices and one quadlayer), we can make some interesting preliminary observations on the few-layer dependence and relevant comparisons to WTe<sub>2</sub>. In our monolayer, trilayer and quadlayer MoTe<sub>2</sub> devices, we observe a large out-of-plane antidamping torque. Similarly, our WTe<sub>2</sub> monolayer and trilayer devices show a strong out-of-plane antidamping torque (see Fig. 3.5, no quadlayer WTe<sub>2</sub> has been studied as of yet). However, in bilayer devices, the out-of-plane antidamping torque is significantly reduced. In WTe<sub>2</sub> bilayers (two devices)  $\tau_B$  is  $\sim 1/2$  that of the monolayer and trilayer devices, and in our MoTe<sub>2</sub> device  $\tau_B$  is zero within our experimental uncertainty. The origin of this reduction is unknown. Note that  $\sigma_S$  for the bilayer is not reduced. In WTe<sub>2</sub> and  $\gamma$ -MoTe<sub>2</sub>, the non-symmorphic crystal symmetries (b-c glide plane

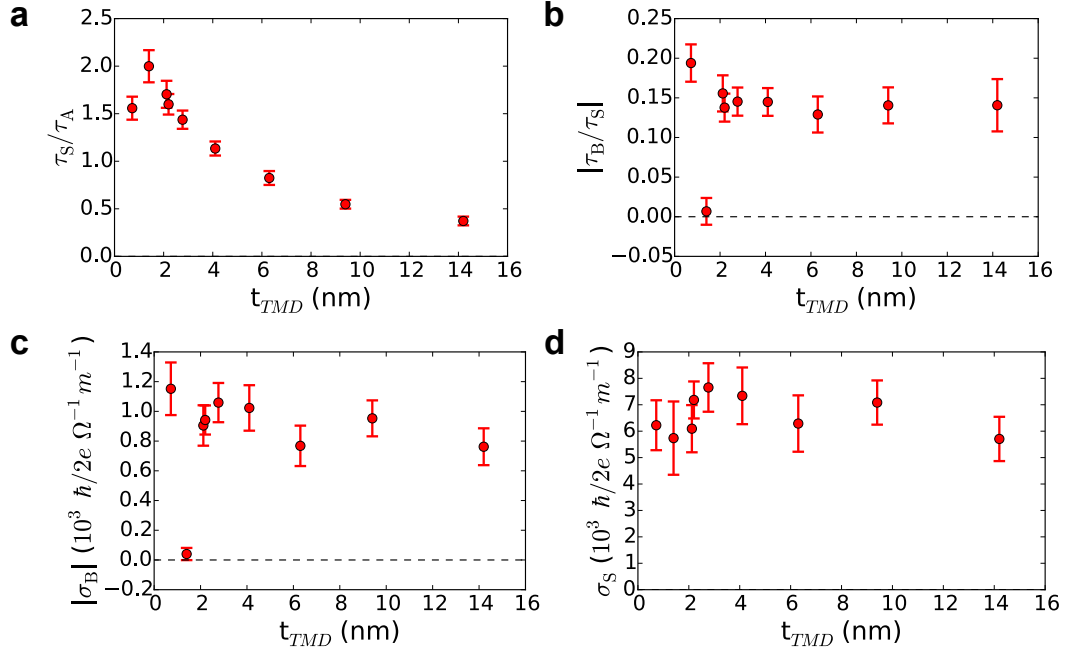


Figure 6.5: a and b) Ratio of (a)  $\tau_S/\tau_A$  and (b)  $\tau_B/\tau_S$  as a function of MoTe<sub>2</sub> thickness for devices with current aligned perpendicular to the MoTe<sub>2</sub> mirror plane. The device that shows a value of zero  $\tau_B/\tau_S$  is bilayer MoTe<sub>2</sub>. The applied microwave power is 5 dBm at 9 GHz. c and d) The torque conductivities (c)  $\sigma_B$  and (d)  $\sigma_S$  as a function of TMD thickness. Both are largely independent of thickness implying an interfacial origin. The device that shows a value of zero  $\sigma_B$  is bilayer MoTe<sub>2</sub>. The applied microwave power is 5 dBm. Torque conductivities are averaged over measurements at frequencies 8-11 GHz in steps of 1 GHz.

and c-axis screw) require the spin responsible for generating  $\tau_B$  to have the opposite sign in adjacent layers, though do not affect the in-plane component of the spin responsible for generating  $\tau_S$ . It is tempting to relate the reduction of  $\tau_B$  in bilayer WTe<sub>2</sub> and MoTe<sub>2</sub> to the symmetry mandated layer dependence for the sign of the generated out-of-plane spins; however, we caution the reader that a standard diffusion type model for the out-of-plane spins would not be consistent with the short spin diffusion length implied by the observed thickness dependence of  $\sigma_S$ .

Perhaps the most plausible explanation lies in the observed few-layer de-

pendence of the band structure in the TMDs. As previously noted, in uncapped MoTe<sub>2</sub> flakes a band gap emerges in the few-layer regime [6]. Although subsequent studies of capped MoTe<sub>2</sub> suggests thin flakes (< 10 nm) may actually be conducting [15, 21], it has been well established that a band gap opens in the few-layer limit for encapsulated WTe<sub>2</sub> [25, 26]. Further, while the few-layer dependence of the TMD band structure should be significantly altered by band bending, doping, or strain type effects that arise from interfacing the TMD with metallic Py, it is reasonable to suspect that some thickness dependence of the band structure will persist in the few-layer limit. This, of course, is not a direct explanation for suppression of  $\tau_B$  in bilayer thick devices, and is merely a suggested starting point. We are actively pursuing further measurements in the few-layer regime.

## 6.5 Dresselhaus-like Torques

Figure 6.6 shows the torque conductivities for the torques  $\propto \hat{m} \times \hat{x}$ ,  $\sigma_C$ , and the torques  $\propto \hat{m} \times (\hat{m} \times \hat{x})$ ,  $\sigma_U$ , as a function of applied current direction,  $\phi_I$ . Again, at  $\phi_I = 0^\circ$  current is directed perpendicular to the MoTe<sub>2</sub> mirror plane. We refer to such torques as Dresselhaus-like, and have discussed these torques in detail in the context of TaTe<sub>2</sub> and WTe<sub>2</sub> (see Chapter 5). In the case of a Dresselhaus-like torque, symmetry requires that the torque be zero when current is either along or perpendicular to a mirror plane. Consistent with that requirement, both  $\sigma_C$  and  $\sigma_U$  are zero when current is flowed along or perpendicular to the MoTe<sub>2</sub> mirror plane, and are maximal at an intermediary angle.

Due to their low-symmetry crystal structure,  $\beta$  and  $\gamma$ -MoTe<sub>2</sub> exhibit an

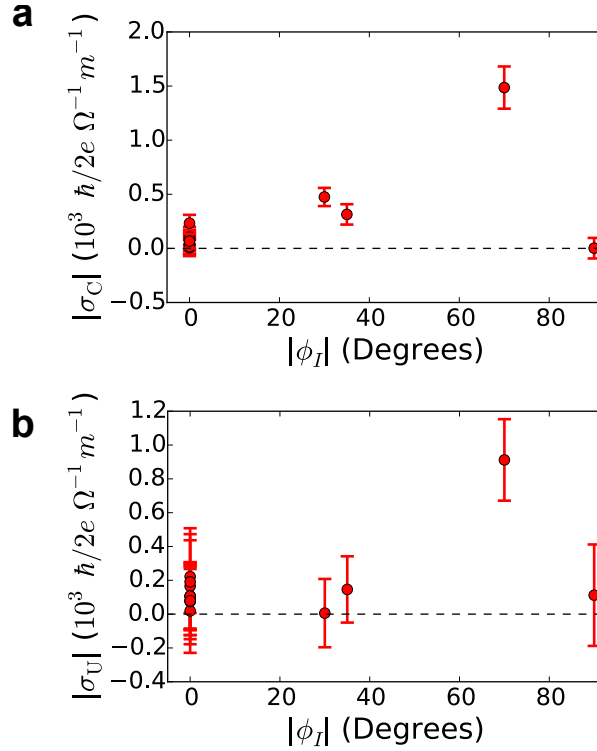


Figure 6.6: a and b) Torque conductivities for the Dresselhaus-like torques (a)  $\propto \hat{m} \times \hat{x}$  and (b)  $\propto \hat{m} \times (\hat{m} \times \hat{x})$  as a function of  $|\phi_I|$  for all of our ST-FMR devices. The applied microwave power is 5 dBm. Torque conductivities are averaged over measurements at frequencies 8-11 GHz in steps of 1 GHz.

anisotropic resistivity within the sample plane [27]. We must therefore be aware of the effect discussed in Section 5.5 – when a voltage is applied across a crystallographic direction that is not one of the principle axes, the resultant current will be tilted. This will cause a component of the Oersted field to instead be oriented along the current direction and generate a torque  $\propto \hat{m} \times \hat{x}$ . Additionally, if there is a standard antidamping component of the torque, typically  $\propto \hat{m} \times (\hat{m} \times \hat{y})$ , the tilting of the current will generate an antidamping torque  $\propto \hat{m} \times (\hat{m} \times \hat{x})$ . At present, we do not have enough devices at intermediary values of  $\phi_I$  to accurately gauge the magnitude of these effects, and ultimately determine whether  $\sigma_C$  and  $\sigma_U$  are dominated by contributions from tilted currents or an intrinsic spin-orbit contribution.

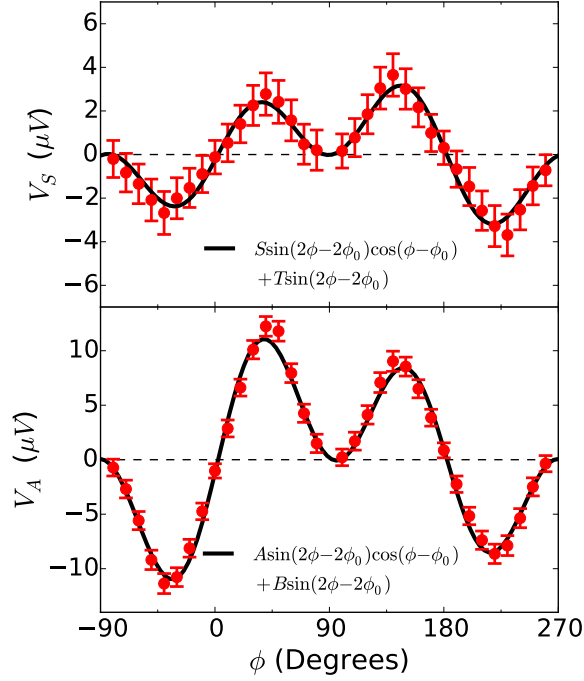


Figure 6.7: Dependence on the applied field angle for both the symmetric,  $V_S$ , and antisymmetric,  $V_A$ , component of the mixing voltage for a device that shows an in-plane field-like torque  $\propto \hat{m} \times \hat{z}$  (Device 3), with MoTe<sub>2</sub>(6.3 nm) / Py(6 nm) and current applied perpendicular to the MoTe<sub>2</sub> mirror plane. Fits of the angular dependence are made using Eqs. 6.3 and 6.4. The applied microwave power is 5 dBm at 9 GHz

## 6.6 In-plane Field-like Torque

The symmetry requirements for  $\tau_B$  are identical to that of the in-plane field-like torque,  $\vec{\tau}_T \propto \hat{m} \times \hat{z}$ . That is, if current is flowed perpendicular to a single mirror plane,  $\tau_T$  is allowed by symmetry. However, in WTe<sub>2</sub> we did not observe any significant value of  $\tau_T$  even though a large  $\tau_B$  was present. The situation in (presumably) strained NbSe<sub>2</sub>/Py devices was exactly the opposite. There we observed a large value of  $\tau_T$ , but no  $\tau_B$ .

In some of our MoTe<sub>2</sub>/Py devices we do observe a small but nonzero value

of  $\tau_T$ . Figure 6.7 shows  $V_S$  and  $V_A$  for one such device (Device 3) for which current is applied perpendicular to the mirror plane. Fitting  $V_A$  and  $V_S$  with Eqs. 6.3 and 6.4 we can extract a ratio of the torques  $\tau_T/\tau_S = -0.12 \pm 0.06$  and  $\tau_T/\tau_B = -0.9 \pm 0.5$ . Note that in all devices with the current perpendicular to the mirror plane, the ratio of  $\tau_T/\tau_B$  is always negative (see Fig. 6.8a), suggesting that to two effects may be correlated.

Interestingly, if we look at  $|\sigma_T|$  as a function of  $\phi_I$ , as shown in Fig. 6.8b, no clear dependence is observed. This suggests that either the fit parameter  $T$  from Eq. 6.4 is non-zero due to an artifact we have not considered, or that the torque is inexplicably not dependent of the symmetries of the  $\text{MoTe}_2$  crystal. Figure 6.8c shows  $|\sigma_T|$  for all of our devices (regardless of  $\phi_I$ ) as a function of  $t_{\text{TMD}}$ , showing that  $|\sigma_T|$  is stronger in thicker samples. This thickness dependence is intriguing and not yet understood.

## 6.7 Determination of Crystal Orientation

Crystals of  $\beta\text{-MoTe}_2$  exfoliate with the c-axis out of plane and are generally elongated in the Mo-chain direction, with sharp and cleanly cleaved edges running parallel to that direction. This is very similar to  $\text{WTe}_2$ , and can be used as a first-order approximation of the in-plane crystal axis during device fabrication. The following two subsections discuss our additional methods for verifying the  $\text{MoTe}_2$  crystal alignment with our devices.

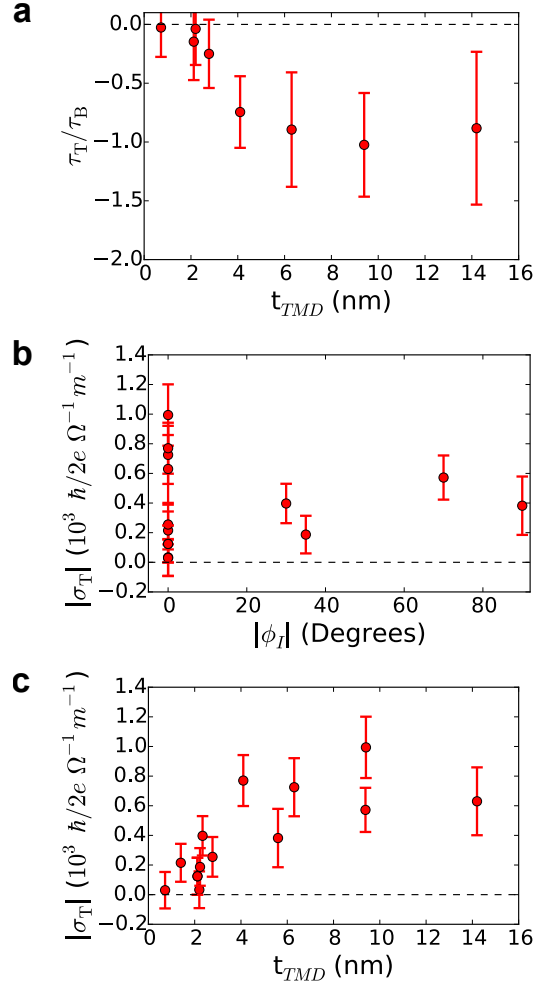


Figure 6.8: a) The torque ratio  $\tau_T/\tau_B$  as a function of thickness for devices with the current applied perpendicular to the MoTe<sub>2</sub> mirror plane direction. Note that the ratio is always negative. We have excluded the bilayer device as  $\tau_B \sim 0$ . The applied microwave power is 5 dBm at 9 GHz. b and c) Torque conductivity  $\sigma_T$  as a function of (b)  $|\phi_I|$  and (c) TMD thickness for all devices. No clear dependence on  $|\phi_I|$  is observed in contrast with  $\sigma_B$  and the MoTe<sub>2</sub> crystal symmetries. Interestingly, a clear dependence on  $t_{TMD}$  is observed, with only thick flakes showing a significant effect. The applied microwave power is 5 dBm. Torque conductivities are averaged over measurements at frequencies 8-11 GHz in steps of 1 GHz.

### 6.7.1 Magnetic Easy Axis

In WTe<sub>2</sub>/Py bilayers, the WTe<sub>2</sub> induced a strong in-plane magnetic easy axis that corresponded with the b-axis of the crystal, regardless of the applied current di-

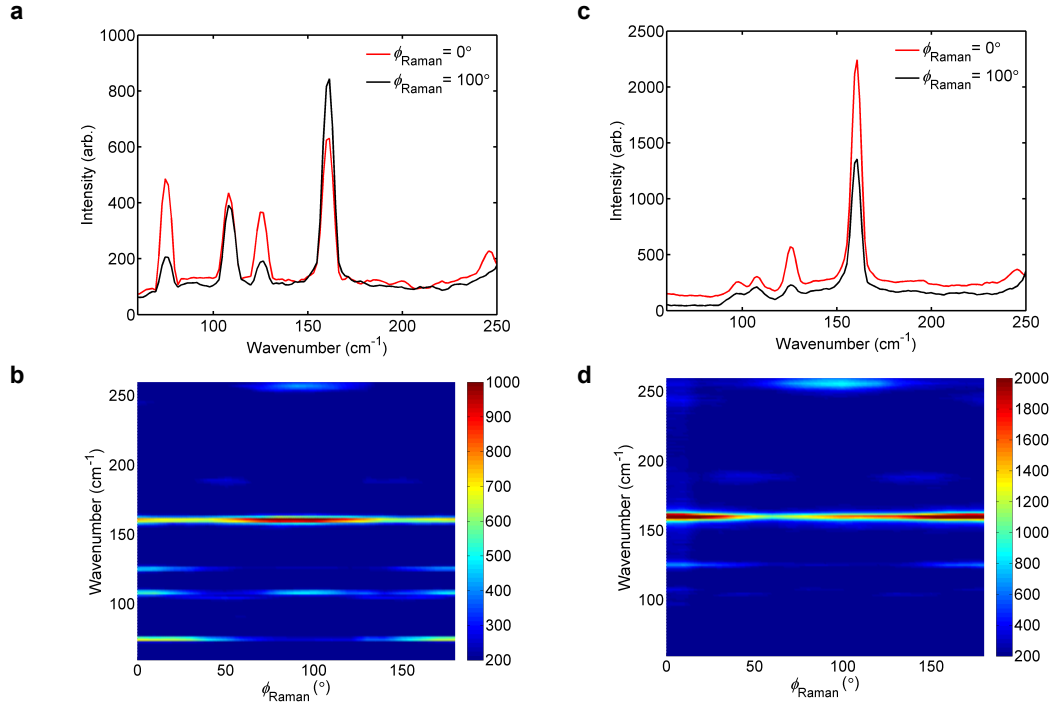


Figure 6.9: Parallel polarized Raman spectra for a thick MoTe<sub>2</sub> flake (~50 nm) using (a) and (b) 488 nm and (c) and (d) 532 nm wavelength excitation taken at room temperature. For the 488 nm excitation, the ~78 cm<sup>-1</sup> mode is maximized when the excitation polarization is perpendicular to the MoTe<sub>2</sub> mirror plane. The observed angular dependence of the modes in both (a) and (c) are consistent with the symmetries of either the  $\beta$  and  $\gamma$  phase of MoTe<sub>2</sub>.

rection. This correlation (checked through polarized Raman spectroscopy, see Section 2.2) provided an efficient means for extracting the angle between the WTe<sub>2</sub> crystal axes and the current direction through electrical measurements. TaTe<sub>2</sub> also generated a similar effect, though the magnitude of the easy-axis was weaker. In contrast to WTe<sub>2</sub> and TaTe<sub>2</sub>, MoTe<sub>2</sub> does not induce any measurable magnetic easy-axis within the Py. We note that NbSe<sub>2</sub>/Py devices also showed no measurable induced magnetic easy-axis. This is an interesting contrast in and of itself, perhaps suggesting a weaker coupling between the TMD and ferromagnet. It also means that we must use an alternative method of determining the alignment of the current with respect to the MoTe<sub>2</sub> crystal.

## 6.7.2 Raman Spectroscopy

The Raman spectra of MoTe<sub>2</sub> has been well characterized in all three crystal phases [2, 3, 15, 28–31]. We use polarized Raman spectroscopy to determine the crystal axis orientation of our MoTe<sub>2</sub> devices. Raman measurements are performed with the CCMR inVia confocal Raman microscope with a linearly polarized excitation and a parallel polarizer placed in front of the spectrometer. The sample is aligned to the linear polarization direction (along the length of the device) and spectra are taken as the sample is rotated in steps of 10°.

Most of the literature regarding Raman spectroscopy on MoTe<sub>2</sub> has used a 532 nm wavelength excitation; however, we have found that the intensity of that excitation in our Raman microscope can damage thin flakes. Instead, we use a 488 nm excitation which does not damage our devices when properly attenuated (~10%). In order to compare our Raman measurements with those of the literature, we have calibrated our 488 nm excitation with measurements using a 532 nm excitation on a thick flake ( $\approx 50$  nm), which is not appreciably damaged by the beam. Figure 6.9 shows the measured Raman spectrum for (a and b) 488 nm and (c and d) 532 nm on the same flake. Our Raman measurements are consistent with either  $\beta$ -MoTe<sub>2</sub> and  $\gamma$ -MoTe<sub>2</sub> phases, which cannot be distinguished with the measurements sensitivity of this Raman spectrometer (see the following section). The  $\sim 78$  cm<sup>-1</sup> peak is maximized when the excitation polarization is aligned perpendicular to the MoTe<sub>2</sub> mirror plane for the 488 nm excitation (Fig. 6.9a), *i.e.* along the Mo-chain direction.

## 6.8 Determining the Crystal Phase in the Few-Layer Limit

The majority of published studies on  $\gamma$ -MoTe<sub>2</sub> have focused on bulk crystals [1, 9–12, 29, 31] although a handful of reports have studied the phase transition between the  $\beta$  and  $\gamma$  phase in the thin-film limit [15, 28–30]. The  $\beta$  and  $\gamma$  phase can be distinguished through polarized Raman by the presence of one additional peak at  $\sim 11$  cm<sup>-1</sup> and a small peak splitting in the  $\sim 130$  cm<sup>-1</sup> mode [29, 31]. These peaks emerge in  $\gamma$ -MoTe<sub>2</sub> as bulk crystals are cooled below the transition temperature of 250 K, showing a temperature hysteresis of about 20 K. Resolving this ultra low frequency peak and the small peak splitting at  $\sim 130$  cm<sup>-1</sup> is beyond the resolution capabilities of the CCMR inVia confocal Raman microscope.

The studies on thin-film  $\beta$ -MoTe<sub>2</sub> have used both polarized Raman spectroscopy [15, 29, 30] and second harmonic generation (SHG) [28] to characterize their films. SHG can provide an additional probe of the crystal phase in few-layer thick films – SHG is strongly sensitive to the presence or lack of inversion symmetry. Odd layer number  $\beta$  films retain total bulk inversion symmetry, whereas even number  $\beta$ - and any few-layer  $\gamma$ -MoTe<sub>2</sub> beyond monolayer have broken global inversion symmetry. These studies, and in particular Beams *et al.*, have conclusively shown that their uncapped few-layer films are consistent with the  $\beta$  phase at room temperature.

However, recent reports on few-layer capped MoTe<sub>2</sub>, where the flakes are exfoliated in a nitrogen glove box and capped with hexagonal boron nitride to protect the films from oxidation, have found a contrasting result [15, 21]. In these capped MoTe<sub>2</sub> samples, they find that the transition temperature from  $\beta$

to  $\gamma$  is increased to 400 K in the few-layer limit, and that  $\gamma$ -MoTe<sub>2</sub> is stabilized at room temperature.

Our films are similarly protected from oxidation by the ferromagnet and additional capping layers (2 nm of Al<sub>2</sub>O<sub>3</sub> and ~60 nm of SiO<sub>2</sub>), implying that our few layer devices may be stabilized in the  $\gamma$  phase at room temperature. Unfortunately, the presence of the metallic Py layer makes SHG characterization difficult. We are currently working to make measurements using a specialized Raman microscope with the ability to resolve the  $\sim 11$  cm<sup>-1</sup> mode and the peak splitting at  $\sim 130$  cm<sup>-1</sup>.

## 6.9 Discussion and Concluding Remarks

In summary, we have studied the current-induced spin-orbit torques in MoTe<sub>2</sub>/Py heterostructures at room temperature. We have observed an out-of-plane antidamping torque,  $\tau_B$ , qualitatively similar to the  $\tau_B$  observed in WTe<sub>2</sub>/Py heterostructures. This torque is consistent with the symmetries of the MoTe<sub>2</sub> surface – at the interface of MoTe<sub>2</sub> and Py the structural symmetries are limited to a single mirror plane, and consistent with that symmetry,  $\tau_B$  is only observed when a component of the current is flowed perpendicular to that mirror plane. The magnitude of the observed torque is  $\sim 1/3$  that observed in similar devices using WTe<sub>2</sub> as the spin source layer, and in both materials,  $\tau_B$  is largely independent of the TMD thickness. The standard antidamping torque,  $\tau_S$ , is also independent of thickness indicating that both torques are likely generated by an interfacial mechanism. The notable exception in the thickness dependence of  $\tau_B$  is the bilayer thick MoTe<sub>2</sub> device, in which no  $\tau_B$  is observed.

This again is qualitatively similar to our observations on similar  $\text{WTe}_2$  devices, but the origin of this effect is unknown. Unlike  $\text{WTe}_2$ , we observe an in-plane field-like torque,  $\tau_T$ , in  $\text{MoTe}_2/\text{Py}$  heterostructures. We find that this torque is largely independent of the crystal orientation, in tension with the symmetry requirements for the torques. Instead,  $\tau_T$  seems to depend more on the thickness of the TMD, being larger in thicker films.

We note that at present, we do not know whether our  $\text{MoTe}_2$  devices are stabilized in the  $\gamma$  phase or the  $\beta$  phase at room temperature. We are actively pursuing measurements to determine the phase of our devices in the few-layer limit. Additionally, we will soon perform measurements as a function of temperature in the hope of determining the dependence of the spin-orbit torques on the crystal phase. It is our hope that those temperature dependent measurements will help to illuminate some of the mysteries outlined in this chapter. Is inversion symmetry breaking in the bulk of the spin-generation material a necessary requirement for the generation of  $\tau_B$ ? Why is there no  $\tau_B$  in bilayer  $\text{MoTe}_2$ , and is the attenuation of  $\tau_B$  in bilayer dependent on the crystal phase? And similarly, what is the effect driving the observed  $\tau_T$ ? Is it a genuine torque? If so, what is breaking the relevant symmetry since it does not seem to depend on the crystalline orientation?

## References

- [1] R. Clarke, E. Marseglia, and H. P. Hughes. "A low-temperature structural phase transition in  $-\text{MoTe}_2$ ." *Philosophical Magazine B* **38**, 121 (1978).
- [2] S. Cho, S. Kim, J. H. Kim, J. Zhao, J. Seok, D. H. Keum, J. Baik, D.-H. Choe,

- K. J. Chang, K. Suenaga, S. W. Kim, Y. H. Lee, and H. Yang. "Phase patterning for ohmic homojunction contact in MoTe<sub>2</sub>." *Science* **349**, 625 (2015).
- [3] Y. Wang, J. Xiao, H. Zhu, Y. Li, Y. Alsaied, K. Yan Fong, Y. Zhou, S. Wang, W. Shi, Y. Wang, A. Zettl, E. Reed, and X. Zhang. "Structural phase transition in monolayer MoTe<sub>2</sub> driven by electrostatic doping." *Nature* **550** (2017).
- [4] C. Ruppert, O. B. Aslan, and T. F. Heinz. "Optical Properties and Band Gap of Single- and Few-Layer MoTe<sub>2</sub> Crystals." *Nano Letters* **14**, 6231 (2014).
- [5] Y. Qi, P. G. Naumov, M. N. Ali, C. R. Rajamathi, W. Schnelle, O. Barkalov, M. Hanfland, S.-C. Wu, C. Shekhar, Y. Sun, V. Süß, M. Schmidt, U. Schwarz, E. Pippel, P. Werner, R. Hillebrand, T. Förster, E. Kampert, S. Parkin, R. J. Cava, C. Felser, B. Yan, and S. A. Medvedev. "Superconductivity in Weyl semimetal candidate MoTe<sub>2</sub>." *Nature Communications* **7**, 11038 (2016).
- [6] D. H. Keum, S. Cho, J. H. Kim, D.-H. Choe, H.-J. Sung, M. Kan, H. Kang, J.-Y. Hwang, S. W. Kim, H. Yang, K. J. Chang, and Y. H. Lee. "Bandgap opening in few-layered monoclinic MoTe<sub>2</sub>." *Nature Physics* **11**, 482 (2015).
- [7] Y. Sun, S.-C. Wu, M. N. Ali, C. Felser, and B. Yan. "Prediction of Weyl semimetal in orthorhombic MoTe<sub>2</sub>." *Phys. Rev. B* **92**, 161107 (2015).
- [8] Z. Wang, D. Gresch, A. A. Soluyanov, W. Xie, S. Kushwaha, X. Dai, M. Troyer, R. J. Cava, and B. A. Bernevig. "MoTe<sub>2</sub>: A Type-II Weyl Topological Metal." *Phys. Rev. Lett.* **117**, 056805 (2016).
- [9] A. Tamai, Q. S. Wu, I. Cucchi, F. Y. Bruno, S. Riccò, T. K. Kim, M. Hoesch, C. Barreteau, E. Giannini, C. Besnard, A. A. Soluyanov, and F. Baumberger. "Fermi Arcs and Their Topological Character in the Candidate Type-II Weyl Semimetal MoTe<sub>2</sub>." *Phys. Rev. X* **6**, 031021 (2016).

- [10] J. Jiang, Z. K. Liu, Y. Sun, H. F. Yang, C. R. Rajamathi, Y. P. Qi, L. X. Yang, C. Chen, H. Peng, C.-C. Hwang, S. Z. Sun, S.-K. Mo, I. Vobornik, J. Fujii, S. S. P. Parkin, C. Felser, B. H. Yan, and Y. L. Chen. "Signature of type-II Weyl semimetal phase in MoTe<sub>2</sub>." *Nature Communications* **8**, 13973 (2017).
- [11] K. Deng, G. Wan, P. Deng, K. Zhang, S. Ding, E. Wang, M. Yan, H. Huang, H. Zhang, Z. Xu, J. Denlinger, A. Fedorov, H. Yang, W. Duan, H. Yao, Y. Wu, S. Fan, H. Zhang, X. Chen, and S. Zhou. "Experimental observation of topological Fermi arcs in type-II Weyl semimetal MoTe<sub>2</sub>." *Nature Physics* **12**, 1105 (2016).
- [12] L. Huang, T. M. McCormick, M. Ochi, Z. Zhao, M.-T. Suzuki, R. Arita, Y. Wu, D. Mou, H. Cao, J. Yan, N. Trivedi, and A. Kaminski. "Spectroscopic evidence for a type II Weyl semimetallic state in MoTe<sub>2</sub>." *Nature Materials* **15**, 1155 (2016).
- [13] K.-A. N. Duerloo, Y. Li, and E. J. Reed. "Structural phase transitions in two-dimensional Mo- and W-dichalcogenide monolayers." *Nature Communications* **5**, 4214 (2014).
- [14] S. Song, D. H. Keum, S. Cho, D. Perello, Y. Kim, and Y. H. Lee. "Room Temperature SemiconductorMetal Transition of MoTe<sub>2</sub> Thin Films Engineered by Strain." *Nano Letters* **16**, 188 (2016).
- [15] R. He, S. Zhong, H. H. Kim, G. Ye, Z. Ye, L. Winford, D. McHaffie, I. Rikl, F. Chen, X. Luo, Y. Sun, and A. W. Tsen. "Dimensionality-driven orthorhombic MoTe<sub>2</sub> at room temperature." *Phys. Rev. B* **97**, 041410 (2018).
- [16] E. Revolinsky and D. Beerntsen. "Electrical properties of  $\alpha$ - and  $\beta$ -MoTe<sub>2</sub> as

- affected by stoichiometry and preparation temperature." *Journal of Physics and Chemistry of Solids* **27**, 523 (1966).
- [17] C. Heikes *et al.* "Mechanical control of crystal symmetry and superconductivity in Weyl semimetal MoTe<sub>2</sub>." arXiv:1804.09093 (2018).
- [18] D. Rhodes, D. A. Chenet, B. E. Janicek, C. Nyby, Y. Lin, W. Jin, D. Edelberg, E. Mannebach, N. Finney, A. Antony, T. Schiros, T. Klarr, A. Mazzoni, M. Chin, Y. c. Chiu, W. Zheng, Q. R. Zhang, F. Ernst, J. I. Dadap, X. Tong, J. Ma, R. Lou, S. Wang, T. Qian, H. Ding, R. M. Osgood, D. W. Paley, A. M. Lindenberg, P. Y. Huang, A. N. Pasupathy, M. Dubey, J. Hone, and L. Balicas. "Engineering the Structural and Electronic Phases of MoTe<sub>2</sub> through W Substitution." *Nano Letters* **17**, 1616 (2017).
- [19] S. M. Oliver, R. Beams, S. Krylyuk, I. Kalish, A. K. Singh, A. Bruma, F. Tavazza, J. Joshi, I. R. Stone, S. J. Stranick, A. V. Davydov, and P. M. Vora. "The structural phases and vibrational properties of Mo<sub>1-x</sub>W<sub>x</sub>Te<sub>2</sub> alloys." *2D Materials* **4**, 045008 (2017).
- [20] H.-J. Kim, S.-H. Kang, I. Hamada, and Y.-W. Son. "Origins of the structural phase transitions in MoTe<sub>2</sub> and WTe<sub>2</sub>." *Phys. Rev. B* **95**, 180101 (2017).
- [21] S. Zhong, A. Tiwari, G. Nichols, F. Chen, X. Luo, Y. Sun, and A. W. Tsen. "Origin of magnetoresistance suppression in thin  $\gamma$ -MoTe<sub>2</sub>." *Phys. Rev. B* **97**, 241409 (2018).
- [22] D. MacNeill, G. M. Stiehl, M. H. D. Guimaraes, R. A. Buhrman, J. Park, and D. C. Ralph. "Control of spinorbit torques through crystal symmetry in WTe<sub>2</sub>/ferromagnet bilayers." *Nature Physics* **13**, 300 (2017).

- [23] D. MacNeill, G. M. Stiehl, M. H. D. Guimarães, N. D. Reynolds, R. A. Buhrman, and D. C. Ralph. "Thickness dependence of spin-orbit torques generated by  $\text{WTe}_2$ ." *Physical Review B* **96**, 054450 (2017).
- [24] M. H. D. Guimares, G. M. Stiehl, D. MacNeill, N. D. Reynolds, and D. C. Ralph. "SpinOrbit Torques in  $\text{NbSe}_2$ /Permalloy Bilayers." *Nano Letters* **18**, 1311 (2018).
- [25] Z. Fei, T. Palomaki, S. Wu, W. Zhao, X. Cai, B. Sun, P. Nguyen, J. Finney, X. Xu, and D. H. Cobden. "Edge conduction in monolayer  $\text{WTe}_2$ ." *Nature Physics* **13**, 677 (2017).
- [26] S. Wu, V. Fatemi, Q. D. Gibson, K. Watanabe, T. Taniguchi, R. J. Cava, and P. Jarillo-Herrero. "Observation of the quantum spin Hall effect up to 100 kelvin in a monolayer crystal." *Science* **359**, 76 (2018).
- [27] H. P. Hughes and R. H. Friend. "Electrical resistivity anomaly in  $\beta\text{-MoTe}_2$  (metallic behaviour)." *Journal of Physics C: Solid State Physics* **11**, L103 (1978).
- [28] R. Beams, L. G. Canado, S. Krylyuk, I. Kalish, B. Kalanyan, A. K. Singh, K. Choudhary, A. Bruma, P. M. Vora, F. Tavazza, A. V. Davydov, and S. J. Stranick. "Characterization of Few-Layer 1T  $\text{MoTe}_2$  by Polarization-Resolved Second Harmonic Generation and Raman Scattering." *ACS Nano* **10**, 9626 (2016).
- [29] S.-Y. Chen, T. Goldstein, D. Venkataraman, A. Ramasubramaniam, and J. Yan. "Activation of New Raman Modes by Inversion Symmetry Breaking in Type II Weyl Semimetal Candidate T- $\text{MoTe}_2$ ." *Nano Letters* **16**, 5852 (2016).

- [30] L. Zhou, S. Huang, Y. Tatsumi, L. Wu, H. Guo, Y.-Q. Bie, K. Ueno, T. Yang, Y. Zhu, J. Kong, R. Saito, and M. Dresselhaus. "Sensitive Phonon-Based Probe for Structure Identification of 1T MoTe<sub>2</sub>." *Journal of the American Chemical Society* **139**, 8396 (2017).
- [31] K. Zhang, C. Bao, Q. Gu, X. Ren, H. Zhang, K. Deng, Y. Wu, Y. Li, J. Feng, and S. Zhou. "Raman signatures of inversion symmetry breaking and structural phase transition in type-II Weyl semimetal MoTe<sub>2</sub>." *Nature Communications* **7**, 13552 (2016).

## CHAPTER 7

### FINAL THOUGHTS AND FUTURE DIRECTIONS

This dissertation has focused on studying the novel spin-orbit torques generated in low-symmetry spin-source materials. Our primary work describes the first observation of an out-of-plane antidamping spin-orbit torque in  $WTe_2/Py$  heterostructures, as well as the generation of this torque in heterostructures where we have replaced  $WTe_2$  with a similar material,  $MoTe_2$ . We have shown that this novel torque, as well as the accompanying in-plane antidamping torque, is generated by an interfacial mechanism such as the Rashba-Edelstein effect or an alternative surface scattering spin-orbit effect [1, 2]. However, the details of such a microscopic mechanism have yet to be identified. Questions such as: “What physical parameter controls the size of the observed torques (atomic dipole moments, spin-orbit coupling, Berry curvature, spin-polarization of the conduction bands, etc.), and can that parameter be manipulated (gating, strain, different materials, etc.)?”, “Can an out-of-plane antidamping torque be generated through a bulk mechanism given the right material?”, and, “What role, if any, does the adjacent ferromagnet and associated interface play in the out-of-plane spin-generation?” will need to be addressed if the work presented in this dissertation is to truly inform the design of novel materials for potential memory applications.

Using those questions as a guide, we can pose several potentially fruitful experiments. Perhaps the most straightforward idea, though technically challenging, is to study a pure van der Waals heterostructure system in which the metallic ferromagnet  $Py$  is replaced with a material such as  $CrI_3$ ,  $CrBr_3$  or  $CrCl_3$ . This is advantageous for several reasons: (1) disorder at the interface associated

with the deposition of the Py is removed from the system. This makes modeling of any torques through first principles calculations infinitely more achievable. (2) If the van der Waals ferromagnet used is insulating, the spin-source material would no longer be pinned to the Py fermi level and could be studied as a function of gate voltage and doping in the few-layer regime. (3) It allows for a straightforward study of several different van der Waals ferromagnets, probing the effects of an in-plane vs. out-of-plane magnetization, as well as conducting vs. insulating ferromagnets. One could even imagine making a trilayer stack, in which  $WTe_2$  and a conducting 2D ferromagnet, such as  $Fe_3GeTe_2$ , are separated by an insulating hexagonal boron nitride tunnel barrier for spin-dependent tunneling spectroscopy measurements [3].

Our work on  $NbSe_2$  discussed in Chapter 4 suggests another approach. Instead of starting with a low symmetry material, we can start with a material of higher symmetry and systematically lower the symmetries constraints through the application of a strain [4]. By studying the response of the spin-orbit torques to the application of a known strain (both in magnitude and crystallographic direction), one might gain further insights into the physical parameter behind the generation of torques  $\propto \hat{m} \times \hat{z}$  and  $\propto \hat{m} \times (\hat{m} \times \hat{z})$ . Further, one could imagine applying a dynamic strain (not just a fixed, static strain set during fabrication) to such a system, perhaps by use of a four-point-bend apparatus [5], that effectively turns these novel torques on and off throughout a measurement. Would the novel torques be linear with the applied strain? Or would there be some peak or jump as strain stabilizes a new state in  $NbSe_2$  (perhaps one of the charge density states)?

One might also venture into the vast number of other low-symmetry mate-

rials in an attempt to learn more about what exactly makes  $\text{WTe}_2$  and  $\text{MoTe}_2$  special. Here, one will find the Inorganic Crystal Structure Database (ICSD) to be an invaluable resource. We have started such an exploration by limiting our search to materials that might have a bulk spin-generation effect (*i.e.*, are monoclinic or lower), have large spin-orbit coupling, and can be exfoliated for ease of device fabrication, such as  $\text{ReSe}_2$  or  $\text{TaTe}_2$ , but this approach has not guaranteed results. As discussed in Chapter 5, no out-of-plane antidamping torque was observed in  $\text{TaTe}_2$ , even though it is symmetry allowed. It is not yet clear whether  $\text{TaTe}_2$  does not show such a torque simply because no sizable (in-plane or out-of-plane) antidamping torques were observed at all, or if there is a deeper reason related to the band structure, crystal structure, etc. that specifically limits an out-of-plane antidamping torque. Further, our work on  $\text{TaTe}_2$  provides a valuable lesson for those who choose to study other low-symmetry materials – artifacts such the Oersted field generated by tilted currents will be present in all low-symmetry systems!

In looking into materials that require an epitaxial growth, one must try to control, or at the very least be aware of, the domain structure and crystallographic twins in the material. Ferroelectric materials might be one way in which the grain boundaries and the “symmetry-breaking” direction of the material could be tuned after growth.

As a means of studying the effects of a low-symmetry surface on torque generation, one might also look into the available low-symmetry single crystal substrates, where a polycrystalline ferromagnet could be simply deposited on top. When the low-symmetry substrate is insulating, spins generated in the metallic ferromagnet might scatter off the low-symmetry surface and induce a

novel torque [1, 2, 6]. Upon last looking, crystal vendors such as MTI supply only two monoclinic substrates:  $\text{Ga}_2\text{O}_3$  and  $\text{CdWO}_4$ . We have made very preliminary torque measurements on  $\text{CdWO}_4/\text{Py}$  heterostructures, and it is worth pursuing these measurements further.

It is worth noting that there are a plethora of other interesting effects in these low-symmetry heterostructure systems, such as the induced in-plane magnetic easy-axis observed in  $\text{WTe}_2/\text{Py}$  and  $\text{TaTe}_2/\text{Py}$ . This effect is in line with the theoretical predictions made by Li and Haney [6]. We have also made preliminary measurements of the induced uniaxial magnetic anisotropy in  $\text{CdWO}_4/\text{Py}$  and  $\text{CdWO}_4/\text{Fe}$  heterostructures, finding that the magnetic anisotropy increases to  $\sim 300$  Oe at 10 K and that the insertion of 2 nm MgO or a thin dusting of W (0.5 nm) between the layers completely destroys the effect. If this effect could be tuned to be just a factor of 5 larger, this could effectively be used to stabilize in-plane magnetic moments for memory technologies.

There is much to do. Good luck!

## References

- [1] V. P. Amin and M. D. Stiles. "Spin transport at interfaces with spin-orbit coupling: Phenomenology." *Physical Review B* **94**, 104420 (2016).
- [2] V. P. Amin and M. D. Stiles. "Spin transport at interfaces with spin-orbit coupling: Formalism." *Physical Review B* **94**, 104419 (2016).
- [3] L. Liu, C.-T. Chen, and J. Z. Sun. "Spin Hall effect tunnelling spectroscopy." *Nature Physics* **10**, 561 (2014).

- [4] J. Lee, Z. Wang, H. Xie, K. F. Mak, and J. Shan. "Valley magnetoelectricity in single-layer MoS<sub>2</sub>." *Nature Materials* **16**, 887 (2017).
- [5] P. G. Gowtham, G. M. Stiehl, D. C. Ralph, and R. A. Buhrman. "Thickness-dependent magnetoelasticity and its effects on perpendicular magnetic anisotropy in Ta/CoFeB/MgO thin films." *Phys. Rev. B* **93**, 024404 (2016).
- [6] J. Li and P. M. Haney. "Interfacial magnetic anisotropy from a 3-dimensional Rashba substrate." *Applied Physics Letters* **109**, 032405 (2016).